TU Delft

Delft University of Technology

On the powder metallurgy, additive manufacturing and welding of oxide dispersion strengthened Eurofer steel

Fu, J.

DOI
10.4233/uuid:b9fbf8e5-dc31-4da0-b560-79c05ebc00a2

Publication date
2021

Document Version
Final published version

Citation (APA)
Fu, J. (2021). *On the powder metallurgy, additive manufacturing and welding of oxide dispersion strengthened Eurofer steel*. [Dissertation (TU Delft), Delft University of Technology]. https://doi.org/10.4233/uuid:b9fbf8e5-dc31-4da0-b560-79c05ebc00a2

Important note
To cite this publication, please use the final published version (if applicable).
Please check the document version above.

Copyright
Other than for strictly personal use, it is not permitted to download, forward or distribute the text or part of it, without the consent of the author(s) and/or copyright holder(s), unless the work is under an open content license such as Creative Commons.

Takedown policy
Please contact us and provide details if you believe this document breaches copyrights.
We will remove access to the work immediately and investigate your claim.

This work is downloaded from Delft University of Technology.
For technical reasons the number of authors shown on this cover page is limited to a maximum of 10.

On the powder metallurgy, additive manufacturing and welding of oxide dispersion strengthened Eurofer steel

On the powder metallurgy, additive manufacturing and welding of oxide dispersion strengthened Eurofer steel

Dissertation

for the purpose of obtaining the degree of doctor
at Delft University of Technology
by the authority of the Rector Magnificus, Prof.dr.ir. T.H.J.J van der Hagen,
chair of the Board for Doctorates
to be defended publicly on
Thursday 16 December 2021 at 12:30 o'clock

by

Jia FU
Master of Engineering in Materials Science and Engineering,
Beihang University, China
born in Qitaihe, China

This dissertation has been approved by the promotors.

Composition of the doctoral committee:

Rector Magnificus,	Chairman
Prof.dr. I.M. Richardson	Delft University of Technology, Promotor
Dr.ir. M.J.M. Hermans	Delft University of Technology, Copromotor

Independent members:

Prof.dr. M. de Baar	Dutch Institute for Fundamental Energy Research
Prof.dr.ir. J. Sietsma	Delft University of Technology
Prof.dr.ir. S. van der Zwaag	Delft University of Technology
Prof.dr. R. Petrov	Ghent University
Prof.dr. Y. Pei	Groningen University

This research was carried out under project number T16010f in the framework of the Partnership Program of the Materials innovation institute M2i (www.m2i.nl) and the Netherlands Organisation for Scientific Research (www.nwo.nl).

Keywords: Oxide dispersion strengthened steel, microstructural analysis, mechanical properties, powder metallurgy, additive manufacturing, welding
Printed by: ProefschriftMaken || www.proefschriftmaken.nl

Copyright © 2021 by Jia Fu
ISBN 978-94-6423-565-4
An electronic version of this dissertation is available at
http://repository.tudelft.nl

Contents

Summary ..... **ix**

Samenvatting ..... **xiii**

1 Introduction **1**

1.1 Introduction 2

1.2 Aim of the study 4

1.3 Outline of the thesis 4

References 6

2 Background **7**

2.1 Introduction of ODS steels 8

2.1.1 Nuclear fission and fusion reactors 8

2.1.2 High performance structural materials 10

2.2 Powder metallurgy 12

2.2.1 Mechanical alloying 13

2.2.2 Consolidation techniques 15

2.3 Additive manufacturing 20

2.3.1 Selective laser melting 20

2.3.2 Direct metal deposition 22

2.3.3 Binder jetting 23

2.3.4 Summary 24

2.4 Welding of ODS steels 25

2.4.1 Fusion welding 25

2.4.2 Solid-state welding 28

2.5 Summary 29

References 30

3 Experimental details **41**

3.1 Powder metallurgy 42

3.2 Direct metal deposition 45

3.3 Welding techniques 46

3.3.1 Spark plasma sintering (SPS) joining 46
3.3.2 Pulsed laser beam welding 47
3.4 General characterisation techniques 48
3.4.1 Microstructural characterisation techniques 48
3.4.2 Mechanical properties 50
References 51
4 Fabrication of ODS Eurofer via mechanical alloying and spark plasma sintering 53
4.1 Introduction 54
4.2 Experimental details 55
4.2.1 Materials and preparation 55
4.2.2 Analysis methods 55
4.2.3 Property tests 56
4.3 Results and discussion 56
4.3.1 Effect of mechanical alloying time 56
4.3.2 Effect of spark plasma sintering 61
4.3.3 Microstructure characterisation 65
4.3.4 Mechanical properties 67
4.4 Conclusions 72
References 72
5 Microstructure and mechanical properties of SPS-produced and heat-treated ODS Eurofer 75
5.1 Introduction 76
5.2 Experimental details 76
5.2.1 Materials 76
5.2.2 Methods 76
5.3 Results and discussion 77
5.3.1 Design of a heat treatment route 77
5.3.2 Microstructure characterisation 79
5.3.3 Dislocation density measurement 92
5.3.4 Tensile properties investigation 93
5.4 Conclusions 98
References 99
6 Additive manufacturing of ODS Eurofer by direct metal deposition 105
6.1 Introduction 106
6.2 Experimental details 107

6.3 Results and discussion 107
6.3.1 Powder characterisation 107
6.3.2 Microstructure characterisation 109
6.3.3 Nanoindentation measurement 115
6.4 Conclusions 116
References 117
7 Welding of ODS Eurofer via solid state diffusion bonding and non-traditional fusion welding 121
7.1 Introduction 122
7.2 Experimental details 123
7.2.1 Material preparation 123
7.2.2 Material characterisation 123
7.3 Results and discussion 124
7.3.1 Joining by SPS 124
7.3.2 Joining by pulsed laser beam welding 128
7.4 Conclusions 145
References 146
8 Conclusions and recommendations for future work 149
8.1 General conclusions 150
8.2 Recommendations for future work 152
Acknowledgements 153
List of publications 155
Curriculum Vitae 157

Summary

Oxide dispersion strengthened (ODS) steels are promising candidates for use as structural materials in the next generation fission and fusion reactors. Compared to conventional ferritic or martensitic steels, ODS steels exhibit improved high-temperature creep properties and irradiation resistance. Favourable properties are mainly attributed to the fine grain features and the high number density of nanosized oxide particles in the steel matrix. These nanoparticles can act as pinning sites for dislocations and stable sinks for irradiation introduced defects, leading to significantly enhanced mechanical properties.

In order to be employed in nuclear systems with large, complex structures, the fabrication and welding of ODS steels with reproducible and superior properties are inevitable and essential. However, after 10–20 years of studying since the emergence of ODS steels, these issues remain the major bottlenecks limiting further development. This thesis is concerned with ODS Eurofer steel, which is one of the representatives of ODS steels and has been the research focus in terms of promising nuclear materials within the European Union. With the aim to develop suitable and effective methods for the fabrication and welding of ODS Eurofer, the result of this study should help to extend the use of ODS steels in future nuclear applications.

In this study, ODS Eurofer steel was initially prepared via mechanical alloying and spark plasma sintering (SPS). Different combinations of mechanical alloying and SPS parameters were adopted in order to optimise the fabrication process. The experimental results show that lattice strain and deformation stress in the powders increase with the milling time, indicating a continuous refinement during the intensive milling process. A sample milled for 30 h, SPS-sintered at 1373 K at a pressure of 60 MPa had the highest density and microhardness among all the results obtained. The yield and tensile strengths were higher while the elongation was lower in the top and bottom surfaces compared to the middle area of the SPS produced sample. This is due to a higher amount of carbon, resulting from carbon diffusion from the mould material.

In order to homogenise the microstructure and improve the mechanical performance of the SPS-produced steel, a heat treatment route including normalising and tempering was designed based on differential scanning calorimetry measurements. The microstructure was characterised by scanning electron microscopy, electron backscattered diffraction, electrolytic extraction, X-ray diffraction and transmission electron microscopy. Thermodynamic calculations conducted using Thermo-Calc software were used to determine the precipitation conditions. The results show that the Vickers microhardness of the sample after the designed heat treatment is more uniform compared to the SPS-produced condition. A dual phase and bimodal microstructure was formed in the SPS-produced and tempered steels. $M_{23}C_6$ and M_6C carbides were found in

the SPS-produced sample while only $M_{23}C_6$ carbides were observed in the tempered sample. The carbides dissolve and reprecipitated during the heat treatment, preferentially located at the grain boundaries. Nanosized Y_2O_3 particles were found to be inhomogenously distributed in the steel matrix in both conditions. The dislocation density in the material decreased significantly after the normalising and tempering treatment. A yield strength model was developed that includes the strengthening contributions of solid solutes, grain size, dislocation density and nanoparticles. It shows that oxide dispersion strengthening, dislocation strengthening and grain boundary strengthening are the major contributions to the yield strength of the SPS-produced ODS Eurofer, while oxide dispersion strengthening and grain boundary strengthening are the dominant strengthening mechanisms in the tempered material. Yielding properties were comparable to hot isostatic pressing or hot extrusion as reported in the literature. The powder metallurgy route presented by this study shows potential to be used as a cost-effective method to produce high performance ODS Eurofer.

Understanding the nature of nano-oxide particles in ODS steels is vital for a better control of the microstructure and mechanical properties to extend their applications. Electron microscopy and atom probe tomography were used to investigate the nanocluster features in ODS Eurofer steel. With the addition of V and Ta in ODS Eurofer, the nanoclusters exhibit a higher number density with a decreased average diameter, indicating that V and Ta are beneficial for the formation of small clusters. Irrespective of the composition of the base material, the smaller particles (< 4 nm) have a variable stoichiometry while the larger particles (around 5–15 nm) are likely to have a Y_2O_3 stoichiometry. The nanoclusters were found to have a core/shell structure, where Y, O and Ta are enriched in the core and Cr and V are predominant in the shell. The formation of the complex structure is possibly the result of a competing effect between Ta, Y, V and Cr binding with O. It is deduced that Ta tends to combine with O in the core of the clusters due to a higher affinity, pushing V and Cr to the surrounding shell during the formation of the nanoclusters.

The production of ODS Eurofer via an alternative route was realised by direct metal deposition and hot isostatic pressing. A laser power of 800 W was found to be a suitable parameter, which guaranteed a sufficient heat input while avoiding a depletion of Y_2O_3 in the steel. The nanoparticles in the produced steel were coarsened to 5–30 nm, leading to a deterioration (around 14%) in the microhardness compared to the SPS-produced steel. After a normalising and tempering treatment, the grain size of ODS Eurofer grew significantly (around 50%) due to a partial loss of Y_2O_3 pinning, indicating a compromised microstructural stability. Compared to SPS prepared ODS Eurofer, the hardness of martensite and ferrite in the direct metal deposition produced steel was lower, associated with grain growth and nano-oxide distribution.

The welding behaviour study of ODS Eurofer started with solid-state diffusion bonding realised by SPS. ODS Eurofer was successfully joined below the melting temperature at 1373 K with a heating rate of 100 K/min and a pressure of 80 MPa. An almost defect-free joint was obtained with a holding time of 40 min and a powder layer of 1.27 g cm^{-2} between the steel disks. The fine-grained microstructure and finely dispersed nanoparticles in the material show no significant change after the joining process. The tensile properties of the joint material are

comparable to the base material. Therefore, SPS has been proven to be a promising technique to join ODS Eurofer without destroying the microstructure and thereby degrading the mechanical performance.

A number of spot-on-plate experiments were initially conducted to study the effect of a pulsed laser beam on the microstructure of ODS Eurofer. The results show that with a laser power of 2500 W and a pulse duration of 200 ms, full penetration can be obtained in a 5 mm thick plate. This condition is favourable for the elimination of trapped gas in the spot, although showing a highly modified microstructure, a severe material loss and a complete depletion of Y_2O_3 nanoparticles. In the case of a 1 mm thick plate with the use of filler material, with a laser power of 2500 W and a pulse duration of 5 ms, the material loss was fully compensated and the nano-Y_2O_3 dispersion was retained. Subsequently, ODS Eurofer was successfully welded using optimised parameters and a distributed pulse pattern to minimise local heat accumulation. The solidified fusion zone consisted of an elongated dual phase microstructure with microvoids. Nano-oxide particles were found to be dispersed in the steel, with higher number densities located in smaller grains. Electron backscattered diffraction analysis showed that after a normalising and tempering heat treatment, the microstructure of the joint is recovered, with substantially unaltered grain size, which is beneficial for the mechanical performance of the joint. However, the tensile properties of the joints are marginally compromised compared to those of the base material, which is associated with welding defects and a slightly deteriorated microstructure. The experimental results indicate that ODS Eurofer joints with reasonable microstructures and mechanical properties can be achieved via pulsed laser beam welding and post weld heat treatments.

In summary, the outcome of this study highlights various aspects regarding the microstructural evolution and mechanical properties of ODS Eurofer subjected to different processing techniques. The powder metallurgy, additive manufacturing and welding behaviour of ODS Eurofer have been presented and discussed in detail. With a similar chemical composition and strengthening mechanisms compared to other ODS steel variants, this research will contribute to the further development and application of the ODS steel family.

Samenvatting

Staalsoorten versterkt met gedispergeerde oxiden (ODS staal) zijn veelbelovende kandidaten voor gebruik als constructiemateriaal in splijtings- en fusiereactoren van de volgende generaties. Vergeleken met conventionele ferritische of martensitische staalsoorten, vertonen ODS-staalsoorten verbeterde kruipeigenschappen bij hoge temperaturen en zijn beter bestand tegen straling. Gunstige eigenschappen worden voornamelijk toegeschreven aan de fijne korrelstructuur en de hoge deeltjesdichtheid van oxidedeeltjes in de staalmatrix met een grootte in de orde van nanometers. Deze nanodeeltjes kunnen dislocaties pinnen en dienen als locaties voor opslag van straling geïntroduceerde defecten. Dit leidt tot aanzienlijk verbeterde mechanische eigenschappen.

Om toegepast te kunnen worden in nucleaire systemen met grote, complexe structuren, is de fabricage en het lassen van ODS-staal met reproduceerbare en superieure eigenschappen noodzakelijk en essentieel. Sinds de opkomst van ODS-staal blijven deze aspecten na 10-20 jaar studie nog steeds de belangrijkste knelpunten die verdere ontwikkeling belemmeren. Dit proefschrift richt zich op ODS Eurofer staal, één van de vertegenwoordigers van ODS staal. Binnen de Europese Unie is hierop het onderzoek gericht en wordt het gezien als veelbelovende materiaal in nucleaire toepassingen. Met als doel om geschikte en effectieve methoden te ontwikkelen voor de fabricage en het lassen van ODS Eurofer, kunnen de resultaten van deze studie bijdragen om het gebruik van ODS-staal in toekomstige nucleaire toepassingen uit te breiden.

ODS Eurofer-staal is in deze studie aanvankelijk geproduceerd via de route van mechanische legeren (mechanical alloying, MA) en 'spark-plasma-sintering' (SPS). Er zijn verschillende procesparametercombinaties van mechanische legeren en SPS toegepast om het fabricageproces te optimaliseren. De experimentele resultaten laten zien dat de spanning in het rooster en spanning ten gevolge van de deformatie, in de poeders toenemen als functie de MA procestijd, wat wijst op een continue verfijning tijdens het intensieve deformatieproces. Het specimen dat gedurende 30 uur mechanisch gelegeerd is en gesinterd bij een temperatuur van 1373 K en een druk van 60 MPa, heeft de hoogste dichtheid en microhardheid van alle verkregen resultaten. De vloei- en treksterkten zijn hoger en de rek is lager aan het oppervlak in vergelijking tot het middengedeelte van het SPS-geproduceerde proefstuk. Dit komt door een hoger gehalte aan koolstof, als gevolg van koolstofdiffusie uit het grafieten mal.

Het begrip van het karakter van nano-oxidedeeltjes in ODS-staalsoorten is van vitaal belang voor een betere controle over de microstructuur en mechanische eigenschappen om hun toepassingen uit te breiden. Elektronenmicroscopie en atom probe tomography zijn toegepast

om de kenmerken van de nanoclusters in ODS Eurofer-staal te onderzoeken. Met de toevoeging van V en Ta in ODS Eurofer vertonen de nanoclusters een hogere deeltjesdichtheid met een kleinere gemiddelde diameter. Dit geeft aan dat V en Ta gunstig zijn voor de vorming van kleine clusters. Ongeacht de samenstelling van het basismateriaal hebben de kleinere deeltjes (< 4 nm) een variabele stoichiometrie, terwijl de grotere deeltjes (5–15 nm) waarschijnlijk een Y_2O_3-stoichiometrie hebben. De nanoclusters bleken een kern/schil-structuur te hebben, waarbij Y, O en Ta verrijkt zijn in de kern terwijl Cr en V voornamelijk in de schil aanwezig zijn. De vorming van de complexe structuur is mogelijk het resultaat van de concurrentie tussen Ta, Y, V en Cr om een binding met O aan te gaan. Uit de samenstellingsverdeling kan worden afgeleid dat Ta zich in de kern van de (Y_2O_3) clusters bindt aan O vanwege een hogere affiniteit, waarbij tijdens de vorming van nanoclusters V en Cr naar de omringende schil wordt verdreven.

Om de microstructuur te homogeniseren en de mechanische eigenschappen van het SPS-geproduceerde staal te verbeteren, is op basis van differentiële scanning-calorimetriemetingen een warmtebehandelingsprocedure ontworpen, bestaande uit normaalgloeien en ontlaten. De microstructuur is ook na deze behandeling gekarakteriseerd door scanning-elektronenmicroscopie, elektron backscattered diffraction, elektrolytische extractie, röntgendiffractie en transmissie-elektronenmicroscopie. Thermodynamische berekeningen uitgevoerd met behulp van Thermo-Calc-software zijn uitgevoerd om de precipitatie condities te bepalen. De resultaten laten zien dat de Vickers-microhardheid in het specimen na de warmtebehandeling uniformer is in vergelijking met de SPS-geproduceerde toestand. Een tweefase en bimodale microstructuur wordt gevormd in de SPS-geproduceerde en getemperde staalsoorten. $M_{23}C_6$- en M_6C-carbiden zijn waargenomen in het met SPS geproduceerde proefstuk, terwijl alleen $M_{23}C_6$-carbiden zijn gevonden in het getemperde specimen. De carbiden lossen op en precipiteren weer, bij voorkeur aan de korrelgrenzen, tijdens de warmtebehandeling. In beide condities bleken de Y_2O_3-deeltjes inhomogeen verdeeld in de staalmatrix. De dislocatiedichtheid in het materiaal is aanzienlijk verminderd na de normaalgloei- en ontlaatbehandeling. Een vloeigrensmodel is opgesteld waarin de bijdragen van oplossingsharding, korrelgrootte, dislocatiedichtheid en nanodeeltjes zijn opgenomen. Het laat zien dat de dispersie van oxiden, de dislocatiedichtheid en aanwezigheid van korrelgrenzen de belangrijkste bijdragen leveren aan de vloeigrens van de SPS-geproduceerde ODS Eurofer, terwijl de dispersie van oxiden en het korrelgrenseffect de dominante verstevigingsmechanismen zijn in het geharde materiaal. Eigenschappen worden verkregen, vergelijkbaar met, in de literatuur gerapporteerde waarden, door middel van heet isostatisch persen of extrusie. De poedermetallurgische route die in deze studie is gepresenteerd, toont aan dat het proces potentieel gebruikt kan worden om hoogwaardig ODS Eurofer te produceren op een kosteneffectieve manier.

De productie van ODS Eurofer via een alternatieve route werd gerealiseerd door direct metal deposition en heet isostatisch persen. Een laservermogen van 800 W bleek een geschikte parameter te zijn, die een voldoende warmte-inbreng garandeerde, maar tegelijkertijd een verlies van Y_2O_3 in het staal voorkwam. De nanodeeltjes in het geproduceerde staal groeiden tot 5–30 nm, wat leidde tot een afname (ongeveer 14%) in microhardheid in vergelijking met het SPS-geproduceerde staal. Na een normaalgloei en temper behandeling nam de korrelgrootte

van ODS Eurofer aanzienlijk toe (ongeveer 50%), als gevolg van een gedeeltelijk verlies van het Y_2O_3-pinning effect, wat wijst op een verminderde stabiliteit van de microstructuur. Vergeleken met het SPS bereide ODS Eurofer, was de hardheid van martensiet en ferriet in het staal geproduceerd via direct metal deposition lager, hetgeen gerelateerd is aan korrelgroei en de verdeling van de nano-oxide deeltjes.

Het onderzoek naar het lasgedrag van ODS Eurofer is gestart met het diffusie door middel van het SPS proces. ODS Eurofer werd met succes verbonden op een temperatuur van 1373 K met een opwarmsnelheid van 100 K/min en een druk van 80 MPa. Er werd een bijna defectvrije verbinding verkregen na een procestijd van 40 min en een poederlaag van 1.27 g cm^{-2} tussen de stalen schijven. De fijnkorrelige microstructuur en de fijn verdeelde nanodeeltjes in het materiaal vertonen geen significante verandering na het verbindingsproces. De mechanische eigenschappen van de verbinding zijn vergelijkbaar met het basismateriaal. Hiermee is bewezen dat SPS een veelbelovende techniek is om ODS Eurofer te lassen, zonder de microstructuur nadelig te beïnvloeden en daarmee de mechanische prestaties.

Om het effect van pulserend laserlassen op de microstructuur van ODS Eurofer te bestuderen zijn in eerste instantie een aantal puntlas experimenten uitgevoerd. De resultaten laten zien dat met een laservermogen van 2500 W en een pulsduur van 200 ms volledige penetratie kan worden verkregen in een 5 mm dikke plaat. Deze voorwaarde is gunstig voor de eliminatie van porievorming door ingesloten gas in het lasmetaal. Echter de lassen vertonen een sterk gewijzigde microstructuur, een aanzienlijk materiaalverlies en een volledige verdwijning van de Y_2O_3-nanodeeltjes. Bij een 1 mm dikke plaat met gebruik van toevoegmateriaal, met een laservermogen van 2500 W en een pulsduur van 5 ms, werd het materiaalverlies volledig gecompenseerd en bleven de nano-Y_2O_3-dispersie behouden. Vervolgens is ODS Eurofer met succes gelast met behulp van geoptimaliseerde parameters en een gedistribueerde lassequentie om lokale warmteaccumulatie te minimaliseren. De gestolde fusiezone bestaat uit een langwerpige tweefase microstructuur waarin microholtes aanwezig zijn. Nano-oxidedeeltjes bleken verspreid te zijn in het staal maar met een hogere dichtheid in de kleinere korrels. Electron backscattered diffraction analyse toont aan dat na een normaalgloei en temper warmtebehandeling, de microstructuur van de las wordt hersteld, met een ongewijzigde korrelgrootte en kleinere misoriëntaties van de korrels in verschillende zones. Dit is gunstig voor de mechanische eigenschappen van de las. De sterkte-eigenschappen van de verbindingen zijn echter licht afgenomen in vergelijking met die van het basismateriaal, wat te wijten is aan lasdefecten en een enigszins verslechterde microstructuur. De experimentele resultaten geven aan dat ODS Eurofer-verbindingen met een relatief goede microstructuur kunnen worden bereikt via gepulseerd laserlassen met een daarop volgende warmtebehandeling.

Samenvattend: De uitkomsten van deze studie belichten verschillende aspecten met betrekking tot de ontwikkeling van de microstructuur en de mechanische eigenschappen van ODS Eurofer onderworpen aan verschillende verwerkingstechnieken. Poedermetallurgie, additive manufacturing en lasgedrag van ODS Eurofer zijn in detail gepresenteerd en besproken. In vergelijking met andere ODS-staalvarianten, met een vergelijkbare chemische samenstelling en versterkingsmechanismen, zal dit onderzoek bijdragen aan de verdere ontwikkeling en toepassing van de ODS-staalfamilie.

1

Introduction

1.1 Introduction

Due to the rapidly growing energy demand and concerns about climate change, nuclear energy now provides over 10% of the world's electricity [1]. In the near future, the next generation fission and fusion reactors are expected to be designed and built to replace existing nuclear power plants or to augment the nuclear production capacity [2].

The core of a nuclear reactor is subjected to a combination of high temperatures, high stresses, chemically aggressive coolants and intense radiation fluxes [3]. Such core conditions require candidate materials possessing good thermal, chemical and mechanical properties to withstand the harsh environment. In particular, materials should have very low dimensional changes (creep and void swelling) under irradiation of high doses up to 150 dpa (displacements per atom).

Oxide dispersion strengthened (ODS) ferritic/martensitic steels are known to have good high-temperature mechanical properties as well as high resistance to neutron irradiation and void swelling [4]. The finely dispersed nano-sized oxide particles in the steel matrix hinder the motion of dislocations and grain boundaries, acting as trapping sites for both point defects and helium atoms generated during irradiation [5]. As seen in Figure 1.1 [2], compared to conventional austenitic steels used in current fission reactors, ODS steels exhibit very low dimensional changes in service, even at displacement doses above 150 dpa. From that perspective, ODS steels are considered as leading candidate structural materials for future fission and fusion reactors. Within the European Union, the development of ODS steels has essentially been focused on ODS Eurofer, which is based on a ferritic/martensitic steel Eurofer 97 reinforced with 0.3 wt% Y_2O_3 [6].

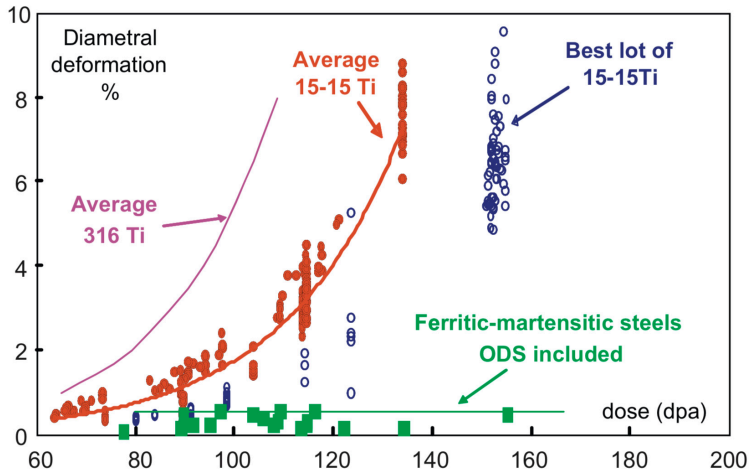


Figure 1.1. Maximum deformation of austenitic steels and ODS ferritic/martensitic steels versus irradiation dose. 15-15 Ti refers to a Ti-stabilised austenitic stainless steel [2].

As appealing as ODS steels are for nuclear applications, the fabrication and welding of high-performance ODS steels are major impediments limiting their application [7]. Conventionally, ODS steels are produced through a complex and inflexible powder metallurgy route. This starts with mechanical alloying where powder composites of metal and oxide particles are subjected

to repeated fracturing and cold welding, leading to dissolution of alloying elements. Subsequently, consolidation of powders is usually conducted by hot isostatic pressing or hot extrusion. The consolidation process is followed by thermomechanical treatments to improve the mechanical performance of the material. Although ODS steels with dispersed nanoscale oxides and desired mechanical properties can be obtained by this route, it comes along with high costs, long manufacturing times and limitations in terms of material shapes [8]. Details of the individual steps need to be further understood and optimised to obtain reproducible and high-performance materials.

The rapid development of additive manufacturing provides a potential alternative to produce ODS alloys. Additive manufacturing has many advantages over conventional techniques, including high material utilisation, short manufacturing cycle, low manufacturing costs and high flexibility in terms of manufacturing materials with large and complex shapes. In particular, due to the high solidification rate and the surface tension gradients generated in the laser-induced melt pool, laser additive manufacturing is a promising technique to fabricate ODS steels with a homogeneous distribution of the second-phase particles [7]. Figure 1.2 [9] presents an overview of tensile properties of various steels fabricated by conventional processing and additive manufacturing from previous studies. In most cases, additive manufacturing can produce steels with equally good tensile properties when compared to conventional processing. However, the study and application of additive manufacturing on ODS steels is still in an early stage. In order to be applied in the harsh working environment of nuclear systems, research efforts are required to improve the mechanical properties of additive manufactured ODS steels.

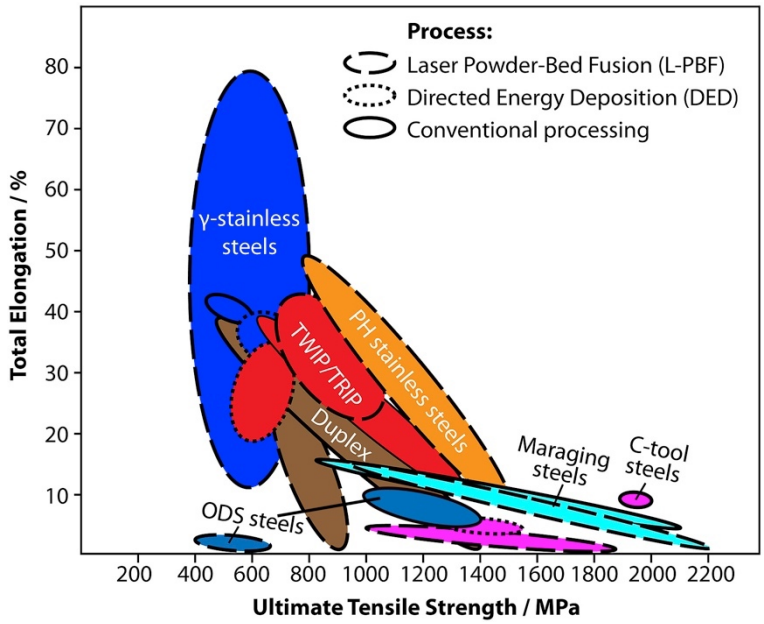


Figure 1.2. An overview of tensile properties of steels fabricated by conventional processing and additive manufacturing. Generally, the properties in the heat-treated condition are given, if applicable. ODS: oxide dispersion-strengthened, c-tool: carbon-bearing tool, TWIP/TRIP: twinning/transformation-induced plasticity, PH: precipitation hardening [9].

For a broader application of ODS steels to nuclear systems with large and complex structures, reliable welding techniques are essential and inevitable. However, ODS steels were generally considered to be non-fusion weldable [10]. As soon as a molten pool is created during fusion welding, the nano-oxide particles in the steel will quickly agglomerate and float on the top of the molten pool, causing oxide-depletion as well as significant degradation of mechanical properties in the joint. Owing to a similar thermal condition in the fusion zone of laser additive manufacturing, laser beam welding may have potential as a joining method for ODS steels. Employing filler materials and a pulsed spot welding strategy could be beneficial to obtain joints with an acceptable microstructure. In addition, diffusion bonding is a promising method to join ODS steels with retained microstructural features due to its solid-state characteristic.

1.2 Aim of the study

The primary aim of the study is to generate a better understanding of the response of ODS Eurofer steel in powder metallurgy, additive manufacturing and welding process conditions. A large number of factors involved in these processes should be incorporated in the research programme, including the thermal effect of various processes, the behaviour of powders subjected to different treatments, a multiscale characterisation of the microstructural features, investigations of mechanical properties of deposited steels, etc. By this means, this research will contribute to the optimisation of the fabrication and welding of ODS steels.

It should be mentioned that this thesis is part of the research program of material behaviour under extreme particle and radiation loading. While the research in this study focuses on the fabrication and welding aspects of ODS Eurofer, the behaviour of ODS Eurofer in irradiation and plasma environments will be addressed in another project within this program and will be presented in the thesis of Viviam Marques Pereira.

In this study, ODS Eurofer was fabricated via two routes to clarify the effects of the manufacturing process on its microstructure and mechanical behaviour. The first is the traditional powder metallurgy route. However, instead of using conventional hot isostatic pressing or hot extrusion, spark plasma sintering (SPS) is investigated in an attempt to consolidate nanometric powders to near theoretical density with minimum grain growth. The second alternative fabrication route examined is additive manufacturing, with laser-based direct metal deposition. Finally, the weldability of ODS Eurofer is studied based on the microstructural evolution and mechanical properties evaluation. Solid-state diffusion bonding, as well as non-traditional fusion welding realised by pulsed laser beam welding are assessed for their suitability to join ODS Eurofer.

1.3 Outline of the thesis

In chapter 2, an overview of the powder metallurgy, additive manufacturing and welding of ODS steels is provided, along with the research progressions and challenges in these fields. Various powder metallurgy techniques including mechanical alloying, hot isostatic pressing, hot extrusion and spark plasma sintering (SPS) are reviewed. This is followed by an introduction of different additive manufacturing techniques and their applications on ODS

steels. Finally, potential welding techniques including fusion welding and solid-state welding of ODS steels are presented. Research questions addressed in this thesis are defined based on the literature review.

The experimental procedures employed in this study are described in chapter 3. Details regarding the powder metallurgy processes and conditions, additive manufacturing techniques as well as SPS joining and laser welding conditions are elaborated. Subsequently, general microstructural characterisation techniques and mechanical property measurements are introduced.

The production of ODS Eurofer via powder metallurgy, *i.e.* mechanical alloying and SPS is presented in chapter 4. In this chapter, the aim is to assess the potential of the proposed powder metallurgical route to fabricate ODS Eurofer, engineered for high strength combined with reasonable ductility. Individual steps of the processing route are optimised based on the microstructure and properties of the steel. The characterisation of the milled powders and produced steels is conducted to understand the effect of mechanical alloying and SPS on ODS Eurofer.

Subsequently, the effects of heat treatment on the microstructure and mechanical properties of ODS Eurofer prepared by powder metallurgy are provided in chapter 5. The aim is to gain a thorough understanding of the microstructure and mechanical properties of powder metallurgy prepared and heat-treated ODS Eurofer. The microstructural features are investigated by multiscale characterisations via optical microscopy (OM), scanning electron microscopy (SEM), electron backscattered diffraction (EBSD), X-Ray diffraction (XRD), transmission electron microscopy (TEM) and atom probe tomography (APT). Moreover, the tensile properties of the as-produced and heat-treated specimens are investigated. Specifically, a yield strength model is proposed to evaluate the contributions of solute atoms, grain size, dislocation density and nanosized particles.

Additive manufacturing of ODS Eurofer realised by direct metal deposition is presented in chapter 6. In order to reveal the feasibility of direct metal deposition, the results are compared with those obtained from the powder metallurgy route. A standard heat treatment route proposed in chapter 5 is applied to investigate the microstructural stability of the steels produced. Nanoindentation experiments are conducted to study the relationship between microstructural components (martensite and ferrite) and localised hardness of ODS Eurofer processed by different conditions.

A comprehensive joining study on ODS Eurofer is given in chapter 7. Solid-state diffusion bonding realised by SPS is conducted to join ODS Eurofer. Results of microscopic analysis and mechanical properties of the SPS joints are presented and discussed. In addition, to study the effect of a pulsed laser beam welding on the microstructure of ODS Eurofer, a number of spot-on-plate experiments with varying parameters are carried out. A pulsed laser beam welding method is proposed based on optimised welding parameters, to minimise local heat accumulation and microstructure deterioration. Filler materials and post weld heat treatment procedures are applied to improve the final quality of the joints.

Finally, conclusions derived from this study and recommendations for the future work are presented in chapter 8.

References

[1] J. Cobb, Highlights of the World Nuclear Performance Report 2020, (2020).
[2] P. Yvon, F. Carré, Structural materials challenges for advanced reactor systems, J. Nucl. Mater. 385(2) (2009) 217-222.
[3] S.J. Zinkle, G. Was, Materials challenges in nuclear energy, Acta Mater. 61(3) (2013) 735-758.
[4] A. Aleev, N. Iskandarov, M. Klimenkov, R. Lindau, A. Möslang, A. Nikitin, S. Rogozhkin, P. Vladimirov, A. Zaluzhnyi, Investigation of oxide particles in unirradiated ODS Eurofer by tomographic atom probe, J. Nucl. Mater. 409(2) (2011) 65-71.
[5] H. Sandim, R. Renzetti, A. Padilha, D. Raabe, M. Klimenkov, R. Lindau, A. Möslang, Annealing behavior of ferritic–martensitic 9% Cr–ODS–Eurofer steel, Mater. Sci. Eng., A 527(15) (2010) 3602-3608.
[6] R. Lindau, A. Möslang, M. Schirra, P. Schlossmacher, M. Klimenkov, Mechanical and microstructural properties of a hipped RAFM ODS-steel, J. Nucl. Mater. 307 (2002) 769-772.
[7] C. Doñate-Buendía, F. Frömel, M.B. Wilms, R. Streubel, J. Tenkamp, T. Hupfeld, M. Nachev, E. Gökce, A. Weisheit, S. Barcikowski, Oxide dispersion-strengthened alloys generated by laser metal deposition of laser-generated nanoparticle-metal powder composites, Mater. Des. 154 (2018) 360-369.
[8] I. Hilger, X. Boulnat, J. Hoffmann, C. Testani, F. Bergner, Y. De Carlan, F. Ferraro, A. Ulbricht, Fabrication and characterization of oxide dispersion strengthened (ODS) 14Cr steels consolidated by means of hot isostatic pressing, hot extrusion and spark plasma sintering, J. Nucl. Mater. 472 (2016) 206-214.
[9] P. Bajaj, A. Hariharan, A. Kini, P. Kürnsteiner, D. Raabe, E.A. Jägle, Steels in additive manufacturing: A review of their microstructure and properties, Mater. Sci. Eng., A 772 (2020) 138633.
[10] B. Baker, L. Brewer, Joining of oxide dispersion strengthened steels for advanced reactors, JOM 66(12) (2014) 2442-2457.

2

Background

2.1 Introduction of ODS steels

2.1.1 Nuclear fission and fusion reactors

The Covid-19 virus caused a global pandemic that has brought about a temporary hiatus. As a result, current forecasts project a decline in energy demand [1]. However, energy demand generally rebounds after global shocks and catastrophic events [2] and it is likely that the upward trend in energy demand will resume after the pandemic. The requirement of meeting the increasing demand for energy production due to urbanisation, while maintaining environmental acceptability, has motivated a rapid growth in the share of green power generation in the global electricity energy matrix.

Nuclear power, an established part of the world's electricity matrix, is currently providing over 10% of world electricity. In an annual report published by the US Energy Information Administration in 2016, nuclear power and renewable energy are forecast to be the world's fastest-growing energy sources from 2012 to 2040 [3]. Due to its high reliability and predictability, nuclear power is especially suited to meet the large-scale, continuous electricity demand.

Although nuclear power is a promising energy source, its operational safety and management are of fundamental importance. For instance, toxic nuclear waste must be isolated within safe containers, which are stored for approximately 50 years before disposal [4]. Moreover, the final disposal of the nuclear waste requires a full isolation from the environment for a very long time (~1000 years).

In general, nuclear energy is generated by nuclear fission or fusion reactors. The development of fission reactors has followed an evolutionary path through generation I, II and III starting from the 1950s, constantly building upon the experience acquired from previous generations. Generation IV fission reactors are a set of theoretical designs currently under investigation in order to use advanced fuels and operate at higher burn-up rates. They are expected to minimise nuclear waste and operating costs, and improve safety, sustainability and efficiency.

Fuel cladding is one of the most important features in generation IV fission reactors. The cladding forms the outer layer of the fuel rods, keeping the radioactive materials isolated from the coolant. The material for fuel cladding is usually selected after other design aspects of the reactor’s core are decided, such as the nuclear fuel and the coolant materials, which determine multiple design constraints for the selection of the material. For instance, there are constraints regarding mechanical properties of the material which include creep resistance, mechanical strength, toughness, neutron radiation resistance. Furthermore, the selection is complicated by constraints imposed by the requirement for chemical compatibility with coolant and fuel materials. Moreover, thermal challenges need to be overcome such as maximum service temperature, thermal expansion and thermal conductivity [5, 6]. Overall, the development and selection of structural materials of advanced fission reactors are challenging. For example, as the most mature technology of Generation IV systems [7], the cladding material of Sodium-cooled Fast Reactors (Figure 2.1 [8]) will experience high temperatures, intense radiation fluxes, and corrosive environments that exclude the use of existing generation (II/III) fuel cladding

materials such as zirconium alloys [9]. The extreme operating conditions for these nuclear power systems are beyond those experienced in current nuclear power plants, and require the development of new high-performance structural materials.

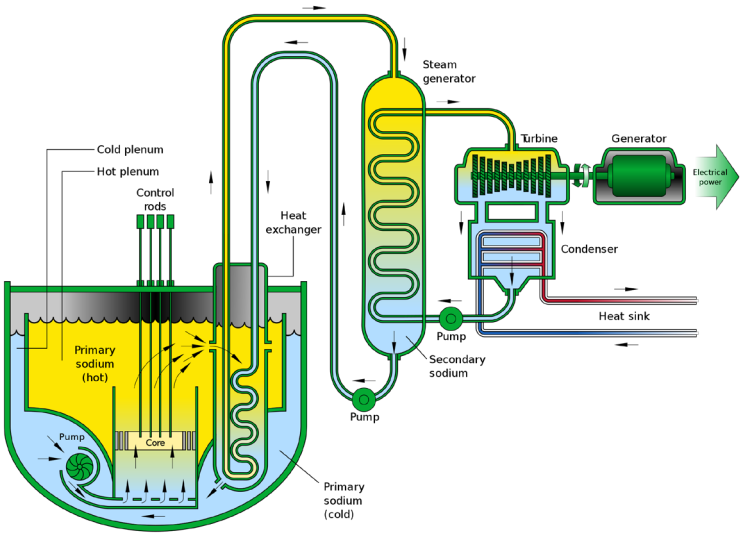


Figure 2.1. A schematic of sodium-cooled fast reactor [8].

In addition to nuclear fission, nuclear fusion also promises clean and safe energy in a very efficient way. A schematic of a prototypic magnetic fusion energy reactor is shown in Figure 2.2 [10]. The fusion reactions are induced within a toroidal-shaped high temperature ionised plasma which is shaped by powerful toroidal and poloidal field magnets. The major function of the blanket region in the figure is to efficiently capture the energy produced by the fusion reactions and transfer the heat for electricity generation. In addition, the blanket can create and extract fresh tritium fuel, allowing continuous operation of the system [11].

High-performance structural materials are expected to be required for advanced fusion reactors, which are subjected to intense fluxes of high-energy neutrons along with high temperature coolants that may induce a corrosive environment [12]. Steady-state heat fluxes for the blanket component in magnetically-confined fusion energy reactors are estimated to be in the range of 1–10 MW/m^2, which is substantially higher than the highest heat flux for structural materials in fission reactors (~1 MW/m^2 for the fuel cladding). Compared to fission, the average neutron energy associated with the deuterium-tritium fusion reaction tends to produce much higher levels of transmutant solutes such as H and He in the structural materials that generally magnify radiation-induced degradation processes. In addition, the design lifetime for the blanket structural materials is about five times higher than that for the core internal structures of fission reactors, indicating strict restrictions on material selection.

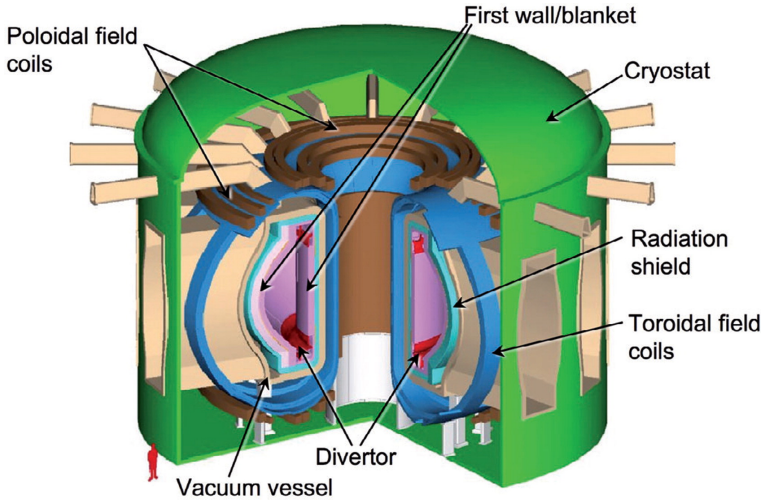


Figure 2.2. A schematic of key components in a magnetically-confined fusion reactor [10].

2.1.2 High performance structural materials

The worldwide research and development for fuel cladding in advanced fission reactors as well as the blanket/first wall in fusion reactors has been focused on low radiation-induced activation materials. Low activation means that the radioactive activation when exposed to neutron irradiation should be as low and quickly decaying as possible, which facilitates re-use, maintenance and disposal of the material. Consequently, it is achieved by replacing elements that decay slowly after capturing one or more extra neutrons (*e.g.* Nb, Mo, Al and Ni) by others that exhibit a higher decay rate of induced radioactivity (*e.g.* Cr, Ti, V, Fe, W, Si, Ta and C) [13].

One of the most promising candidate materials is reduced-activation ferritic–martensitic (RAFM) steels. RAFM steels have a large number of superior properties for nuclear applications, including reduced void swelling, a higher thermal conductivity, a lower thermal expansion and a lower tendency to helium embrittlement when compared to the austenitic steels [14]. Extensive development and investigation of RAFM steels including OPTIFER (optimised ferritic alloys [15]), MANET (martensitic alloys for nuclear fusion facilities [16]) and F82H (steels with 8% Cr and 2% W [17]) has been undertaken. Based on the physical, mechanical and structural data gained with these steels, a slightly modified RAFM steel was developed within the European Union, which was designated as Eurofer 97. Similar to other RAFM steels, Eurofer 97 possesses good mechanical properties even at high temperatures and is therefore considered to be a promising candidate for use as a structural material in nuclear applications. However, the irradiation embrittlement at low temperatures and inferior long-term creep rupture strength at high temperatures limit the applications of Eurofer 97 in advanced nuclear systems to an upper operating temperature of about 823 K [18].

An important way to improve the radiation resistance and thermal creep resistance of RAFM steels is through the addition of fine oxide particles to form so-called oxide dispersion strengthened (ODS) steels. The addition of nanoscale oxide particles (mainly pure Y_2O_3 [19, 20] or Y_2O_3 + Ti [21]) is multifunctional. Firstly, these nanoscale oxide particles inhibit the

migration of dislocations and grain boundaries to improve strength. Secondly, the particles can act as nucleation sites for helium bubbles to suppress/retard the formation of large bubbles at grain boundaries and therefore aging at high temperatures. Lastly, they can act as stable sinks for irradiation induced defects such as vacancies and interstitial atoms such as Cr, Nb, Mo and V, which otherwise might be the origin of alloy dissolution and aging embrittlement, even at a low volume fraction (<1 vol%) [22, 23]. By optimising their chemical compositions, ODS steels with desired microstructures and mechanical properties can be produced via appropriate manufacturing processes.

According to the Fe–Cr constitution diagram, the binary Fe–Cr steels are ferritic over the whole temperature range at above approximately 12 wt% Cr [24]. Steels that contain 9–11 wt% Cr undergo phase transformations during heating and cooling. They are usually referred as dual-phase steels due to a martensite and ferrite microstructure [25]. Studies have demonstrated that dual-phase steels tend to have a good combination of high strength and good ductility. The high strength is due to interfacial hardening of martensite by resisting dislocation slip. Good ductility is attributed to the strain hardening behaviour of ferrite through pronounced dislocation activities, strain partitioning, or strain-induced phase transformation [26]. In particular, ODS steels containing 9 wt% of Cr are known to be most advantageous regarding high-temperature mechanical properties. Additionally, the shift in ductile-to-brittle transition-temperature after irradiation is minimised at Cr contents around 9 wt%. [27]. However, as candidate structural materials for future nuclear applications, the radiation resistance of ODS steels is another important factor to be considered. BCC ferritic alloys are known to exhibit better radiation resistance than FCC austenitic alloys [28]. Furthermore, increasing the Cr content is favourable for the corrosion–oxidation resistance [22]. Hence, both 9 wt% Cr and >12 wt% Cr ODS steels have been developed extensively in recent years. Table 2.1 lists the chemical compositions of typical ODS steels developed in different countries. Within the European Union, the research on ODS steels has essentially been focused on ODS Eurofer, which is based on Eurofer 97 steel and reinforced with 0.3 wt% Y_2O_3.

In addition to Cr, the composition of ODS steels should be carefully designed to fulfil their application requirements. It is known that Ta stabilises the grain size by carbide formation and improves strength of the material. The addition of W is beneficial for a good compromise regarding low activation, as well as good ductility and creep strength [29]. Vanadium has been commonly used as an alloying element for ferritic steels due to the effect of refining prior austenite grain structure and carbide size, and therefore improving tensile strength, creep and Charpy impact fracture resistance. The addition of a small amount of Ti has proven to further reduce the size of the oxide particles [22]. Manganese can be added for phase control [30]. Carbon is a strong austenite stabilising element, and has a very small solubility in ferrite, resulting in the formation of carbides for precipitation strengthening [31].

Table 2.1. Nominal composition of various ODS steels (wt%).

ODS steels	Cr	C	Ti	W	Mn	Mo	Al	Ni	V	Ta	Y_2O_3	Fe	Ref.
MA754	20	0.05	0.5	–	–	–	0.3	77.55	–	–	0.6	1	[32]
MA956	20	0.05	0.5	–	–	–	4.5	–	–	–	0.5	Bal.	[33]
MA957	14	–	0.9	–	–	0.3	–	–	–	–	0.25	Bal.	[33]
12YWT	12.6	0.05	0.35	2.4	0.05	–	–	0.3	–	–	0.25	Bal.	[33]
14YWT	14	–	0.4	3	–	–	–	–	–	–	0.3	Bal.	[34]
PM2000	20	<0.04	0.5	–	–	–	5.5	–	–	–	0.5	Bal.	[35]
DT2203 YO5	13	–	2.2	–	–	1.5	–	–	–	–	0.5	Bal.	[36]
ODS Eurofer	9	0.1	–	1.1	0.4	–	–	–	0.2	0.12	0.3	Bal.	[20]
MB18A	9.04	0.13	0.2	1.93	0.04	–	–	0.02	–	–	0.36	Bal.	[37]
1DK	12.9	0.05	0.52	2.8	–	–	–	0.16	–	–	0.5	Bal.	[38]
M93	9	2	0.2	–	–	–	–	–	–	–	0.35	Bal.	[39]
K1	19	0.3	0.3	–	–	–	–	–	–	–	0.35	Bal.	[39]
F82H	7.66	0.1	–	1.95	0.16	–	–	0.02	0.16	0.02	0.34	Bal.	[40]

Compared with RAFM steels, ODS Eurofer/steels have shown superior performance, especially high creep resistance in the 773–973 K temperature range and low swelling under irradiation [41]. They have considerable potential to be employed as high performance structural materials for the next generation fission reactors as well as advanced fusion reactors; however, the fabrication and welding of ODS Eurofer/steels are very challenging, due to the complex nature of the material. There have been extensive investigations on these subjects by multiple methods and techniques in recent years. An overview of powder metallurgy, additive manufacturing and welding of ODS Eurofer/ODS steels, is presented in section 2.2, 2.3 and 2.4 respectively, together with a brief discussion of various possibilities and challenges facing the fabrication and welding of ODS Eurofer/ODS steels.

2.2 Powder metallurgy

Conventional methods such as melting and casting are not suitable to produce ODS steels because of a clustering and coarsening of oxide particles at the ingot surface [41]. The primary reason is the high thermal stability of Y_2O_3 at casting temperatures and the poor wettability between Y_2O_3 particles and molten Fe. The melting point of Y_2O_3 is around 2683 K, and the contact angle of steel drops with Y_2O_3 particles is over 90° [42]. This prevents the metallurgical bonding of Y_2O_3 with other alloying elements in the material. In addition, with a lower density than liquid steel, Y_2O_3 particles will float on the liquid surface and accumulate in the cast risers, leading to a Y_2O_3-depleted bulk material.

Instead, ODS steels are usually produced by powder metallurgy techniques. This starts with mechanical alloying (MA) of a blend of either elemental or atomised powders to obtain a homogenous dispersion of nanoparticles in the steel powders. The mechanically alloyed powder is then consolidated at high temperatures and pressures to produce the bulk material. Afterwards,

different thermal/mechanical treatments are applied to optimise its microstructure and mechanical properties. Powder metallurgy is known to have high material utilisation and energy efficiency, it is therefore particularly suitable for the production of expensive materials [43].

2.2.1 Mechanical alloying

Mechanical alloying, also referred to as ball milling, is considered to be the most mature processing route for the synthesis of elemental powders and non-equilibrium structures. It has been used to produce a variety of alloys and composites, including intermetallics, quasicrystalline alloys, amorphous alloys, nanocrystalline alloys, and dispersion-strengthened alloys at near ambient temperature [44, 45]. Mechanical alloying is a powder metallurgy process where elemental powders in either equilibrium or metastable phases are mixed in a high-energy ball mill (Figure 2.3(a) [46]). The mechanism of MA is anchored on repeated cold welding, fracturing, and rewelding of powder particles. The repeated collision of the milling balls and powder particles induces intense plastic deformation and particle fracture (Figure 2.3(b)). Repeated fracturing causes formation of composite particles with desired compositions. Subsequently, small agglomerations of particles form the final morphology of the powder in the welding phase (Figure 2.3(c)). By this means, chemical elements can form micro- or nanostructured powders with defined stoichiometry and crystalline order.

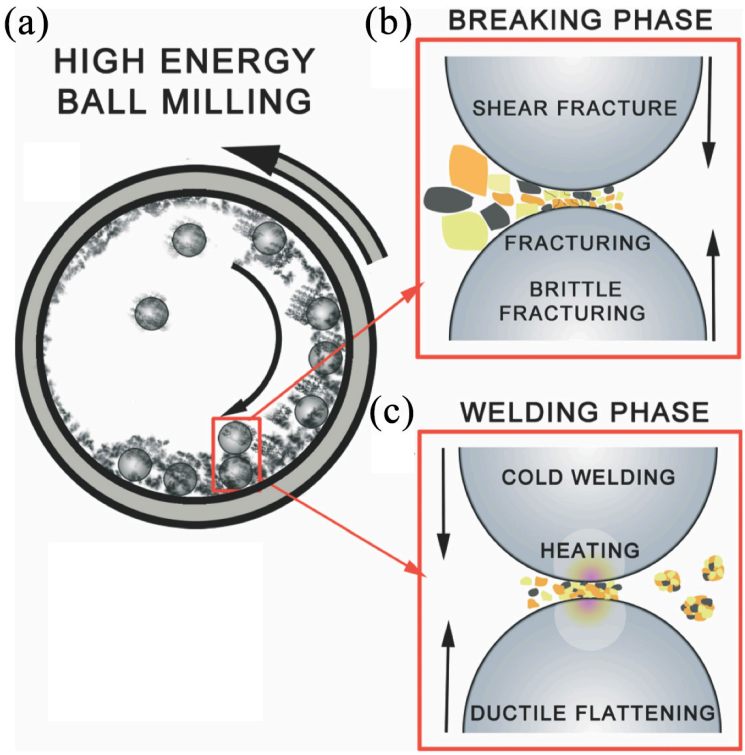


Figure 2.3. (a) schematic illustration of a high energy ball mill, (b) breaking phase and (c) welding phase [46].

Since MA is a completely solid-state technique, it is not affected by the limitations of typical manufacturing methods that include melting and the associated pitfalls of non-homogenous distribution and porosity, which makes it an ideal technique to fabricate ODS steels. Mechanical alloying is believed to be the most successful technology to add oxides to steel matrix and can obtain ultrafine oxide powders (1–4 nm) and high number densities (~10^{24} m^{-3}) [47]. However, powder contamination during MA is a significant concern for the production of high-purity bulk steels. The small particle size, large exposed surface area, and formation of new surfaces during ball milling all contribute to powder contamination. The primary methods to prevent powder contamination are the use of high-purity powders, a high-purity atmosphere (usually argon), milling containers of similar material to the powders, and the minimisation of milling time. Therefore, a clean and efficient milling process is a necessary condition to achieve homogeneous and reproducible microstructures of ODS steels.

Additionally, the appropriate selection of MA parameters is imperative to achieve homogenous steel powders. These parameters include rotation speed, ball to powder ratio (BPR) and milling time, which play an important role in the structural evolution of the synthesised powders [48]. Therefore, it is crucial to optimise these milling parameters to ensure a homogeneous chemical composition and more importantly, a uniform dispersion of Y_2O_3 in the steel powders. A large number of studies have been conducted by researchers so far, aiming at understanding the roles of chemical compositions [49], milling parameters [50] and operating environment [51] on the quality of fabricated ODS steels in terms of homogeneity, anisotropy, reproducibility and mechanical properties [52, 53].

The production of 9 wt% Cr ODS steel powder via mechanical alloying was reported by Zhou *et al.* [25]. The starting material was gas atomised powders with a nominal composition of Fe–9Cr–0.1C–2W–0.2V–0.07Ta (wt%) blended with 0.35 wt% yttrium oxide (Y_2O_3) nanoparticles. The mechanical alloying was performed in a planetary ball mill with a 15:1 ball to powder ratio at 400 rpm for 5–45 h. SEM morphologies of the powders under different milling times are shown in Figure 2.4. As can be seen in Figure 2.4 (a), the atomised pre-alloyed powder exhibited a spherical morphology. During the first 5 h, the powders almost remained the original shape. The powders became flattened after milling for 10 h. As the milling time was increased to 20 h, the morphology of the powders evolved into the round thin-plate shape. Due to intense collisions between balls and powders, the brittle plates were fragmented into pieces. Granular particles with irregular shape were produced after 45 h (Figure 2.4 (e)), resulting from repeated interactions between fragment and cold welding. The refinement effect of the ball milling process on the powders is manifested in Figure 2.4 (f). It can be seen that after milling for 45 h, the powder size was decreased from 130 μm to 45 μm.

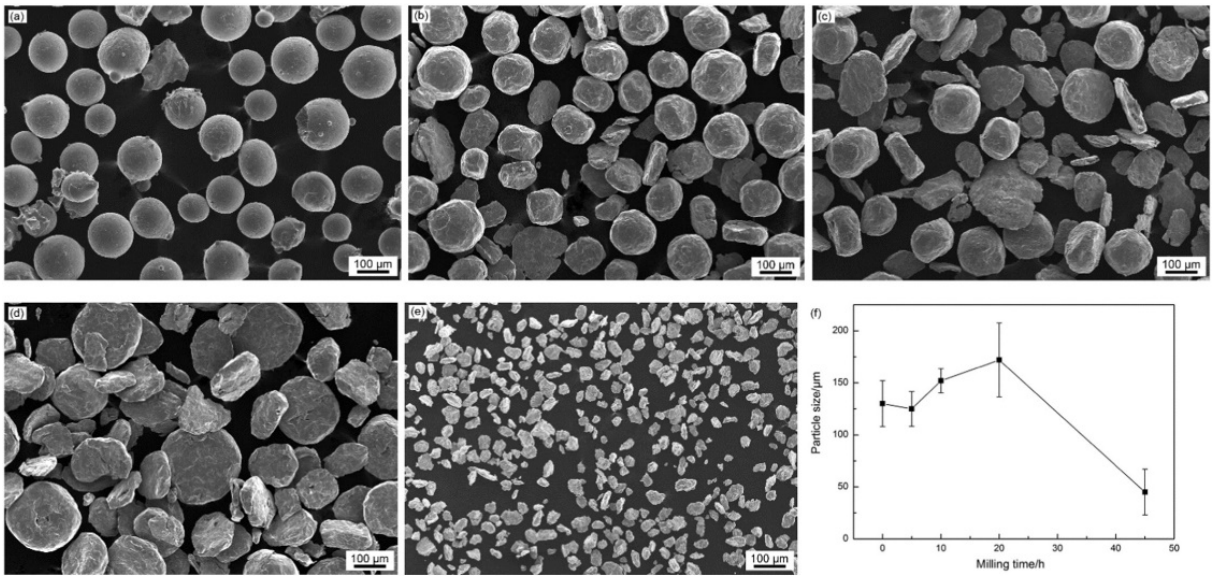


Figure 2.4. SEM micrographs of (a) the pre-alloyed 9Cr powder and the blended powder milled for (b) 5 h, (c) 10 h, (d) 20 h, (e) 45 h, and (f) the variation of powder size as a function of milling time [25].

Apart from gas atomised powders, elemental powders can also be used as raw material for mechanical alloying. Kuma *et al.* [54] used high-purity elemental powders to produce an ODS steel with a nominal composition of Fe–18Cr–2W–0.2Ti–0.35 Y_2O_3 (wt%). The powders were mixed thoroughly and mechanically alloyed at 1000 rpm for 7 h with a ball to powder ratio of 10:1 under an argon atmosphere. Even though the precursor powders had different sizes (Fe: 50 μm, Cr: 45 μm, W: 12 μm, Ti: 44 μm and Y_2O_3: 25–50 nm), the powders obtained after mechanical alloying had a narrow size distribution of 25–35 μm, which was assumed to be suitable for the following consolidation process.

2.2.2 Consolidation techniques

Mechanical alloying is usually followed by hot isostatic pressing (HIP) or hot extrusion (HE) to consolidate the powders. Hot isostatic pressing has the characteristic of employing isostatic pressure and elevated temperatures to ensure an efficient processing [55]. It is mainly used for the consolidation of metal powders, cladding of similar and dissimilar alloys, and elimination of porosities as a post-treatment after casting or additive manufacturing [56]. In particular, HIP is an important tool for the densification of powder metallurgy prepared products. During HIP, powders are encapsulated in a gas-tight container and consolidated in the capsule to their full density. Hot extrusion, in comparison, is a process by which products are formed by forcing a heated billet through a die with a desired cross-section. The main advantage of HE lies in the fabrication of materials with complex shapes, and materials that are brittle, since only compressive and shear stresses are applied during the HE process [57].

The consolidation of mechanically alloyed ODS powders at laboratory scale is mainly performed by HIP [20, 58, 59], while for industrial productions such as MA956, MA957 or PM2000 alloys, HE is often favoured [60]. Hot isostatic pressing usually yields a more isotropic

microstructure but a lower ductility and fracture toughness compared to the materials produced by HE [61].

As reported by Unifantowicz *et al.* [62], an ODS ferritic steel processed by either HIP or HE was investigated in order to assess the influence of the consolidation technique on the microstructure and mechanical properties of the obtained ingots. The results showed that both materials contained equiaxed grains with an average diameter of 40–80 nm and a high number density of nano-oxide particles. The HE steel exhibited a higher tensile strength at low to moderate temperatures than the HIP steel, due to the deformed microstructure and substantial work hardening effects. At higher temperatures, although both steels had a similar tensile strength, the HE steel showed higher uniform elongation, indicating better mechanical properties over a wide temperature range.

As mentioned above, HIP and HE are the most commonly used consolidation processes for ODS steels. However, high processing costs due to long processing times and anisotropic properties of produced ingots are issues to be considered. As a result, an alternative route *i.e.* spark plasma sintering (SPS) has been explored and developed, by which a lower cost to produce materials with enhanced properties can be established.

Spark plasma sintering, also known as pulsed electric current sintering or field assisted sintering technology, employs a pulsed direct electrical current to heat up an electrically conductive tool with powder inside to perform fast consolidation. A schematic of the SPS device is shown in Figure 2.5 [63]. The heat generation during SPS is internal, in contrast to the conventional hot pressing, where the heat is provided by external heating elements. This facilitates a very high heating rate (up to 1000 K min^{-1}), hence significantly shortening the sintering process (within a few minutes) and energy costs [64]. Owing to the short duration of the process, SPS is able to consolidate powders with nanosize or nanostructure meanwhile maintain the intrinsic properties of the powders in fully dense products. Standard cooling rates of SPS can reach as high as 150 K min^{-1}, which is realised by direct contact with water-cooled rods. A higher cooling rate up to 400 K min^{-1} is possible by additional active cooling using gas flow. Simultaneously, the application of a uniaxial pressure facilities the bonding of adjacent powders and enhances densification. The sintering process is carried out under vacuum or protective gas at atmospheric pressure. Control of the processing cycle is usually done by temperature measurement (using either thermocouples or axial/radial pyrometers), but can also be achieved by power, current or displacement control. It is interesting to point out that even though the technique was named as "Spark Plasma Sintering", it is debatable whether there is any plasma discharge during the process. Nonetheless, it seems to be widely accepted that occasional electric discharges may take place on a microscopic level [65].

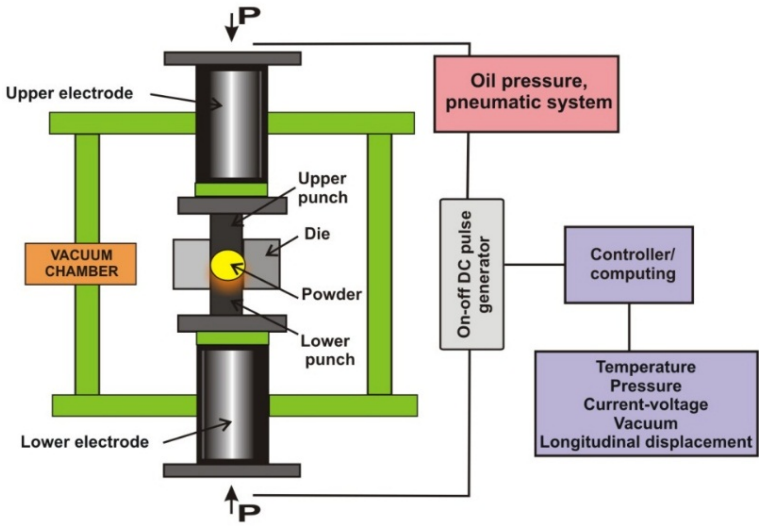


Figure 2.5. A schematic of the SPS device [63].

Spark plasma sintering offers many advantages over conventional systems like HIP, HE or atmospheric furnaces, including ease of operation, accurate control of any stage of sintering, as well as high reproducibility, safety and reliability [66]. In particular, the Joule heating and short holding times applied have made it possible to efficiently sinter nanometric powders to near theoretical densities with minimum grain growth. The mechanisms of grain evolution during SPS were reported by Xie *et al.* [67] and are schematically described in Figure 2.6. Nanosized grains are initially formed in the powders after MA (Figure 2.6(a)). Subsequently, the powders are heated by the applied pulsed current during SPS (Figure 2.6(b)). The current preferentially flows along the surfaces of the powders due to a lower resistance, resulting in a higher local temperature at the surface area. Due to the effect of applied pressure, sintering necks can be quickly formed at the touch point. Consequently, the grains at sintering neck areas are larger due to a higher local temperature. Meanwhile, the grains inside the powders recrystallise and form fine grains as a result of the heterogeneous temperature and short sintering times [68, 69]. Finally, the powders are nearly fully consolidated, with a microstructure of ultrafine grains surrounded by coarse grains, as shown in Figure 2.6(c).

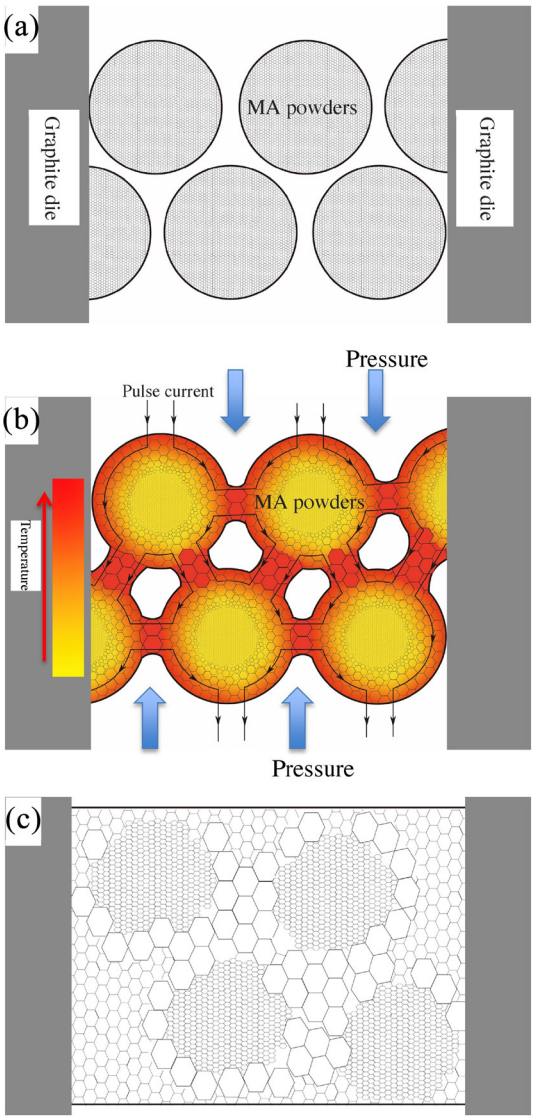


Figure 2.6. Schematic of grain evolution during SPS, (a) grains in MA powders, (b) grains during SPS and (c) grains after SPS [67].

Spark plasma sintering is by far the most widely used ultrarapid sintering technique. Its success has been highlighted by significant applications. SPS has been used to produce functionally graded materials, thermoelectric materials, ferroelectric materials, magnetic materials, nanostructured materials, amorphous materials, intermetallic compound, metal matrix and ceramic matrix composites, highly refractory metals and ceramics, etc [70]. Recently, it has been used to consolidate different types of ODS steels. For comparison, the synthesis parameters of various ODS steels by HIP, HE and SPS are summarised in Table 2.2. The applied pressure and time needed for the production of ODS steels via SPS are significantly lower than those for HIP and HE, demonstrating that SPS is a promising and cost-effective method for the fabrication of ODS steels.

Table 2.2. Synthesis parameters of various ODS steels (wt%) by mechanical alloying and different consolidation techniques.

Alloys and techniques	Milling time/h	Speed/ rpm	BPR	Consolidation time/h	Temperature/ K	Pressure/ MPa	Ref.
ODS 16.5Cr HIP	12	200	10:1	1	1423	103	[71]
ODS 18Cr HIP	30	300	5:1	2	1373	100	[72]
ODS 18Cr HIP	30	300	5:1	2	1373	100	[73]
ODS 16.7Cr HIP	60	380	10:1	3	1373	120	[74]
ODS 18Cr HIP	60	380	10:1	3	1423	200	[75]
ODS 25Cr HIP	30	300	5:1	2	1373	100	[76]
ODS 16.8Cr HIP	30	300	5:1	3	1423	100	[76]
ODS 17Cr HIP	30	300	5:1	3	1423	100	[77]
ODS 18Cr HE	48	250	15:1	–	1423	–	[78]
ODS 18Cr HE	–	–	–	–	1423	620	[79]
ODS 18Cr HE	6	550	7.5:1	–	1423	620	[80]
ODS 14Cr HE	–	–	–	–	1173	990	[81]
ODS 17Cr SPS	5	600	5:1	0.08	1223	50	[82]
ODS 14Cr SPS	50	260	10:1	0.08	1298	40	[83]
ODS 14Cr SPS	60	300	10:1	0.07	1373	36	[84]
ODS 9Cr SPS	50	260	10:1	0.08	1223	40	[67]
ODS 14Cr SPS	60	150	10:1	0.08	1423	50	[85]

In summary, SPS is a versatile processing method for consolidation and synthesis of numerous structural or functional materials including ODS steels. It enables the development of electrically conductive and non-conductive materials at both lab and industrial scale. The important features of the SPS process and their influences on densification and properties of materials have been critically examined and reviewed by researchers [86, 87]. However,

research and development efforts are still continuing to lead SPS to maturity. For instance, the effects of electrical current/field on mass transport, reactivity, microstructure evolution, formability and properties need to be better understood. In addition, upscaling to large products and improved flexibility regarding product geometries are required, which could be studied with the help of finite element modelling computations. Finally, the underlying sintering mechanisms need to be fully understood, considering the complicated mechanical, electrical, and thermal phenomena associated with SPS.

2.3 Additive manufacturing

As stated above, ODS steels are usually fabricated through powder metallurgical processes. However, issues posed by the complicated route are to be considered: the fabrication process is generally time-consuming and expensive due to complex variables. Mechanisms of the individual steps are not yet fully understood due to limited and scattered results of the end products. Besides, scaling-up towards an industrial scale may pose problems [88]. In addition, powder metallurgy techniques do not offer the possibility of near-net-shape manufacturing. Thus, current research interest in this subject has been focused on the development and evaluation of alternative production routes for ODS steels, since this would significantly increase their widespread use.

Laser additive manufacturing (LAM) is principally capable of producing ODS steels by offering high solidification rates in combination with strong Maragoni effects within a small scaled melt pool, potentially leading to a homogenous distribution of oxide particles in the material [89]. It has the advantages of high material utilisation, short manufacturing cycle and low manufacturing cost. In particular, unlike traditional fabrication techniques, LAM allows the manufacturing of near-net-shaped parts; therefore, complex geometries can be produced efficiently with minimum subsequent subtractive machining [90]. Laser additive manufacturing mainly falls into two categories: powder-bed printing system, such as selective laser melting (SLM), and blown-powder printing system, such as direct metal deposition (DMD). Although the development of LAM techniques for ODS steels is still in the early stage, both SLM and DMD have been demonstrated to be promising in fabricating a variety of high-performance ODS steels [91-96].

2.3.1 Selective laser melting

Selective laser melting is a layer-wise powder bed fusion additive manufacturing process [97]. The SLM process enables the rapid production of complex geometry components without the time-consuming mould design and further machining. A schematic of the SLM process can be seen in Figure 2.7(a) [98]. A high energy laser beam selectively scans and melts a thin layer of a metal powder bed under a protective atmosphere. The molten powder rapidly solidifies and forms a layer of consolidated powder. Subsequently, a new layer of metal powder is deposited on the top of the previous layer and the process repeats until the desired build is achieved [99]. Similar to other rapid prototyping technologies, SLM fabrication uses computer-aided design, which allows a high level of design freedom and flexibility [100]. A number of complex designs

can be produced with SLM, including thin-walled structures, coatings, solid builds, meshes and porous structures.

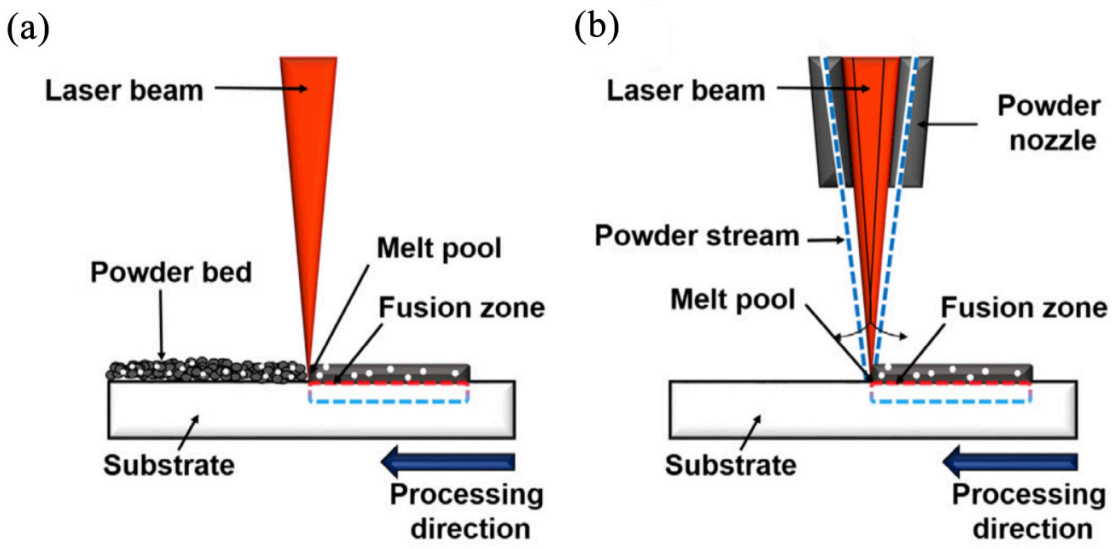


Figure 2.7. Representative scheme of the (a) SLM and (b) DMD manufacturing technologies [98].

Recently, a number of studies have been reported on successful attempts of SLM fabricating different kinds of ODS steels. Walker *et al.* [101] studied SLM on PM2000 alloy and demonstrated that a relative fine distribution of Y_2O_3 with a mean size of 50–60 nm was retained in the built walls. The coarsening and agglomeration of oxide particles appeared to be influenced by the laser scanning speed. Another attempt on printing PM2000 thin-walled structures using the SLM process was reported by Boegelein *et al.* [91]. The yield strength of as-grown walls (330 MPa) was inferior to the conventionally produced PM2000 alloy (500 MPa), due to porosity in the build. Yet, the yield strength could be increased to 450 MPa by post heat treatments because of the presence of atomic Y in the matrix and precipitation of fine Y-enriched oxide particles.

Nearly fully dense austenitic 304L ODS steel builds were manufactured using optimised parameters in an SLM machine [92]. In order to avoid severe alloying of the gas atomised powders, a light mixing approach with a low rotation speed of 100 rpm and a short mixing time of 4 h was employed to prepare the precursor powder. The alloy produced exhibited a tensile strength of 700 MPa and a ductility of 32%, which is better than conventionally manufactured austenitic ODS alloys. The improvement of strength was mainly attributed to the fine dispersion of nanoparticles, while enhanced ductility was caused by a pronounced work hardening effect in large grains due to the high dislocation accumulation capacity.

Vasquez *et al.* [93] studied the effect of powder characteristics on the properties of SLM builds. ODS Fe–14Cr powders produced by mechanical alloying (non-spherical) and gas atomisation (spherical) were used as raw material for comparison. It was found that spherical particles allowed SLM builds with higher densities than those made with non-spherical particles.

Moreover, the chemical composition of the powders strongly influenced the final microstructure of SLM parts. Due to the exothermic reactions when forming oxides, the presence of Y and Ti promoted the formation of large and shallow molten pools, leading to the growth of columnar grains along the building direction.

2.3.2 Direct metal deposition

Direct metal deposition is another type of LAM process, which is accomplished by simultaneously delivering metallic powder and focused laser energy. A schematic of DMD can be seen in Figure 2.7(b). While both SLM and DMD are based on similar principles, their differences lie in the depositing methodology of the powders, which can affect the dynamics of the process. In DMD, the metal powder is injected or blown through a nozzle and into the melt pool [91]. Direct metal deposition provides a high deposition rate and a relatively wide process window to fabricate large items compared to other metal-based AM methods.

According to Shi *et al.* [94], an ODS Fe–9Cr (wt%) alloy was manufactured by DMD followed by HIP. It was found that with the increase of laser power, the density of alloys increased, while the number density of nanoscale oxides decreased significantly. Hot isostatic pressing effectively increased the density of the material as well as the number density of nanoscale oxides, which significantly improved the mechanical properties. Further research demonstrated that a post heat treatment was an efficient way for the precipitation of more oxides in the matrix of the as-built ODS alloy [95].

A new method was proposed by Donate-Buendia *et al.* [96] for the production of ODS powders as feedstock materials for LAM. The technique was intended to replace mechanical alloying, which tend to produce deformed powder particles that have non-spherical morphologies and cause unstable powder injections in DMD. The scheme of the powder generation is shown in Figure 2.8. A colloidal suspension of Y_2O_3 nanoparticles was fragmented and generated by pulsed laser irradiation [96] (Figure 2.8(a)). Subsequently, Y_2O_3 particles were adsorbed on ferritic steel powder, which was subjected to pH-controlled electrostatic interactions to create ODS steel powders (Figure 2.8(b)). Afterwards, an ODS ferritic steel was produced by DMD under selected conditions. The results showed that about half of the Y_2O_3 particles were fragmented from an average size of 28 nm to 3.2 nm. The compression strength of the DMD prepared material was significantly enhanced compared to non-ODS steel, due to an effective strengthening of nano-Y_2O_3.

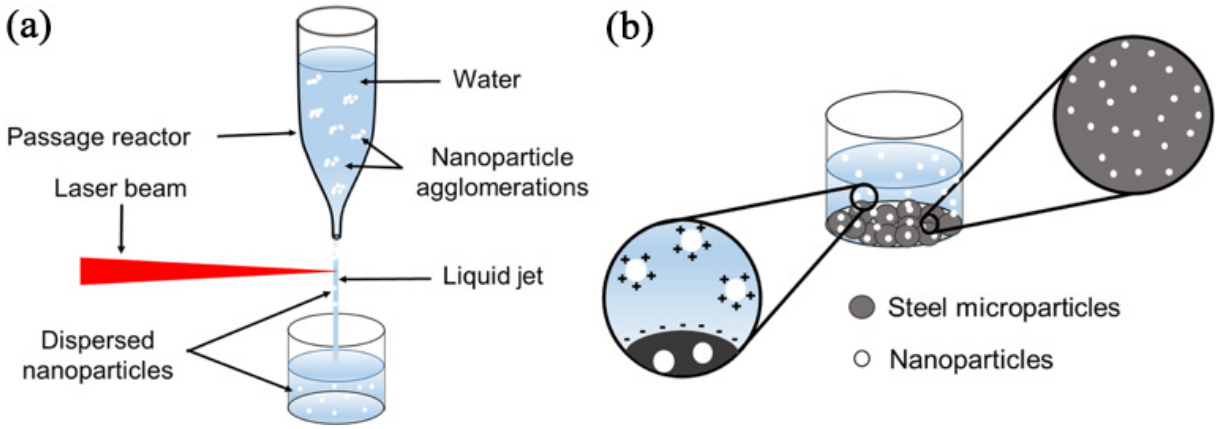


Figure 2.8. (a) Scheme of the experimental setup used for the generation of nanoparticles by pulsed laser irradiation in a passage reactor: Agglomerated nanoparticles flowed through a passage reactor and were irradiated by a laser beam, producing deagglomerated and/or fragmented nanoparticles; (b) Creating steel powders with nanoparticles by pH-controlled electrostatic interaction [96].

2.3.3 Binder jetting

Due to the use of laser as a heat source, both SLM and DMD have a very localised heat input. The processed material presumably undergoes rapid solidification, phase transformations and repeated thermal cycles and heat treatments. Rapid solidification can induce residual stresses and metastable phases and, in some cases, heat is extracted directionally, resulting in preferential directional grain growth [102]. In addition, processing defects such as porosity and rough surface finish significantly affect the integrity of the produced part, resulting in anisotropic performances [103].

Binder jetting is the only powder bed additive manufacturing process that is not fusion-based, thus manufactured parts have no melting-associated problems, unlike LAM processes [99]. A schematic overview of the binder jetting process is shown in Figure 2.9 [99]. A suspension that consists of the desired powders and suitable binders is prepared through ball milling. Printing begins with the spreading of a thin layer of the suspension on a transparent film. After the layer is rapidly patterned on the holder by the light source, the holder moves up and a new layer of suspension is spread on the film. The printing process is repeated layer-by-layer until the build is complete. After printing, the green body is exposed to a debinding process to burn out all the organic binder components. Finally, the porous body undergoes a sintering process to obtain a fully densified specimen.

As described above, the photosensitive slurry-based stereolithography technique of binder jetting can obtain parts with high dimensional accuracy and good surface finishing [104]. The decoupling between the printing and consolidation processes enables the consolidation of powders in a homogeneous environment, resulting in a uniform microstructure of the products. More importantly, due to its solid-state characteristic, binder jetting would be beneficial for the retaining of featured microstructures of ODS steels. So far, binder jetting has been widely used in producing ceramic structures, medical and biomedical applications and metal matrix

composites [99]. However, to the author's knowledge, it has not been used to produce ODS steels.

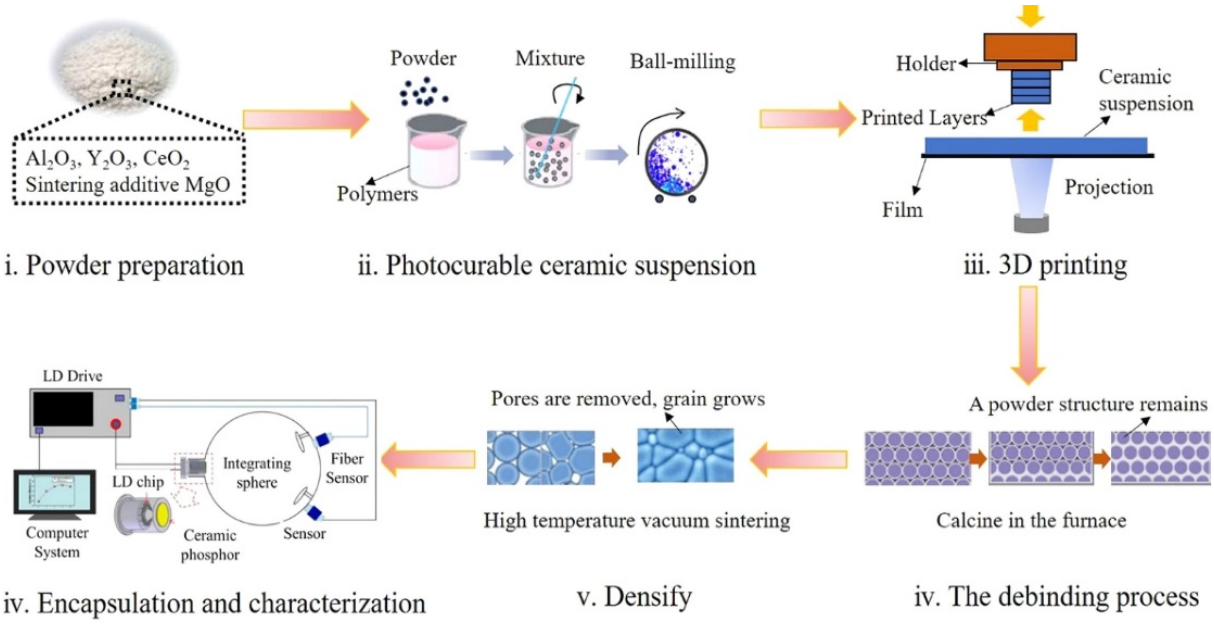


Figure 2.9. A schematic of the binder jetting printing procedure [99].

2.3.4 Summary

Additive manufacturing (AM) is a relatively new manufacturing technology and far from fully matured. The development of AM techniques producing ODS steels is still at the laboratory stage. Most performed studies are focused on optimisation of process parameters, microstructure characterisation and mechanical properties evaluation. The ultimate goal would be producing ODS steels via AM with equally good or even superior properties compared to conventionally prepared parts. Improving the performance of AM-produced ODS steels rests on careful optimisation and implementation of tailored microstructures through controlled processes and appropriate composition manipulations that can promote and stabilise new microstructures. Rapid manufacturing, formation of substructures and increased dislocation densities characterise the LAM processes; Solid-state processing, residual-stress free and good integrity of final parts describe the binder jetting process. These features provide promising perspectives to further extend the applications of AM-produced ODS steels. Nonetheless, associated AM processing defects such as porosity and cracks pose a challenge. Research on understanding these defects and finding ways to suppress or circumvent them during processing deserve more attention.

Nowadays, AM research studies, especially those on parameter optimisation, are still based on trial-and-error efforts, which require extensive time and costs. With the rapid development of machine learning and artificial intelligence, experimental efforts to produce AM parts can be significantly reduced. Machine learning and artificial intelligence assisted AM equipment linked with high throughput synthesis, rapid automatic characterisation tools, and appropriate

robotics will be promising for real time manufacturing and novel material process optimisation [105].

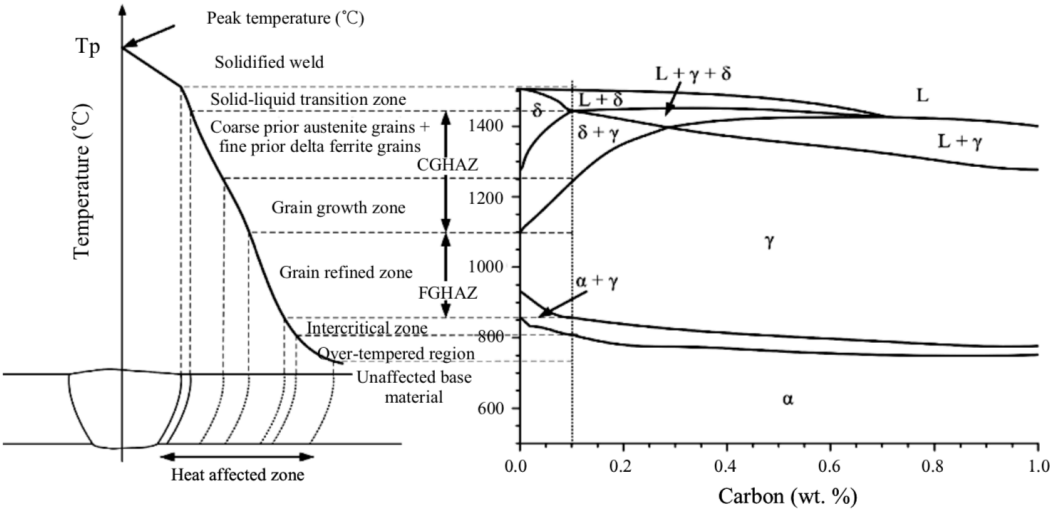
2.4 Welding of ODS steels

In order to employ ODS steels in advanced nuclear systems having large, complex structures, reliable welding techniques are inevitable and essential. However, welding of ODS steels is a major technical bottleneck limiting their use and has been identified by many researchers [9, 106, 107]. The difficulties lie in the retention of strength and prevention of agglomeration of oxide particles in the joint. Overcoming these obstacles would further increase their utility in advanced nuclear applications. The most commonly used techniques for welding ODS steels generally include fusion welding and solid-state welding techniques. So far, there have been a large number of studies on welding ODS steels by different techniques with varying degrees of success.

2.4.1 Fusion welding

Fusion welding techniques use a variety of heat sources (plasma arc, laser beam, etc.) to melt materials which subsequently become welded upon cooling and solidification. These techniques usually create good, strong welds for austenitic or ferritic steels. However, fusion welding of ODS steels is problematic. Once the material is molten, the finely distributed oxide particles will quickly agglomerate and form a slag on the molten pool surface due to a lower density compared to the Fe matrix, leaving a dispersion-free weld zone. This will lead to a significant loss in mechanical performance in the weld zone due to the lack of dispersion strengthening. In addition, fusion welding tends to significantly modify the carefully-designed microstructure and texture of ODS steels, causing a reduction or complete loss of their high-temperature properties. Moreover, fusion welding may release or entrap gases either from the base metal or the protective atmosphere, which can result in porosity in the fusion zone or heat-affected zone (HAZ). Such void formation is a problem especially for Al-containing ODS alloys [108].

As shown in Figure 2.10, Pandey *et al.* [109] illustrated the effect of fusion welding on the HAZ metallurgy in a 9 wt% Cr steel. The microstructure evolution in the HAZ is mainly influenced by the temperature, heating and cooling rate, dwell time, number of welding passes and post weld heat treatment. Based on peak temperature experienced, the HAZ can be divided into a coarse grained HAZ, a fine grained HAZ, an intercritical HAZ and an over-tempered HAZ. In particular, traditional fusion welding techniques generally create a relatively large HAZ that often has inferior strength and degraded material properties, leading to an early failure upon mechanical loading.



Sub-zones	Temperature experienced	Transformation reactions	Microstructure characteristics	Mechanical properties
CGHAZ	$T_m>T_p>T_{\gamma\delta}$	$\gamma+\delta \rightarrow M+\delta$	Untempered martensite, undissolved NbX, dissolved $M_{23}C_6$	Poor toughness and high strength
	$T_{\gamma\delta}>T_p>A_{c3}$	Coarse $\gamma \rightarrow M$	Untempered martensite, undissolved NbX, dissolved $M_{23}C_6$	Poor toughness and high strength
FGHAZ	$T_{\gamma\delta}>T_p>A_{c3}$	Fine $\gamma \rightarrow M$	Untempered martensite, dissolved find $M_{23}C_6$, undissolved MX and coarse $M_{23}C_6$	Adequate toughness and strength
IC-HAZ	$A_{c3}>T_p>A_{c1}$	$\gamma \rightarrow M+OM$	Untempered martensite, tempered martensite, dissolved very fine $M_{23}C_6$, undissolved MX and coarse $M_{23}C_6$	High toughness and poor strength
Over-tempered base zone	$T_p<A_{c1}$	OM	Tempered martensite, Undissolved MX and coarse $M_{23}C_6$	High toughness and poor strength

Where,T_p=temperature experienced during welding; T_m= melting point of steel; $T_{\gamma\delta}$ =temperature at which γ to δ transformation completed during heating; A_{C3}=upper critical temperature at which α to γ transformation completed on heating; A_{c1}=lower critical temperature at which α to γ transformation started on heating; γ =austenite; δ =ferrite; M=martensite; OM=overtempered martensite.

Figure 2.10. Schematic of the sub-zones of the HAZ of 9 wt% Cr steel weldments and corresponding transformation reaction [109].

Various traditional fusion welding techniques have been employed to join ODS steels, however, with limited success. Both gas tungsten arc welding (GTAW) and gas metal arc welding (GMAW) were found to cause melting which disrupted both the oxide distribution and grain structure of MA 758 alloy [110]. Using electro-spark deposition (ESD) welding on MA957, Miao *et al.* [111] reported that ESD welding produced substantial porosity in the weld region. The oxide particles were severely disturbed during the melting–solidification process, causing a significant reduction of strength of the weld metal.

In comparison, electron beam welding (EBW) and laser beam welding (LBW) can possibly provide a solution for welding ODS steels, due to a very local heat input accompanied by a small HAZ. Both EBW and LBW have a much higher power density (~10^{11} W m^{-2} for EBW and 10^9–10^{11} W m^{-2} for LBW) compared to the traditional fusion welding techniques mentioned above. Figure 2.11 presents a schematic of the fusion zone created by various technologies [112]. In general, the EBW joint has the smallest fusion zone due to the high power density as well as high heating and cooling rates, followed by the LBW joint. The workpiece deformations caused by EBW and LBW are reduced compared to tungsten inert gas (TIG), metal inert gas (MIG) and plasma welding. However, because of the very high temperature gradient inside the EBW and LBW weld, there is a strong fluid flow in the melt pool [113]. The fluid flow is

expected to have a large influence on the distribution of the yttrium oxide particles [114]. Additionally, the rapid cooling of EBW and LBW tends to cause undesirable metallurgical structures, although this could be improved by the subsequent post weld heat treatment.

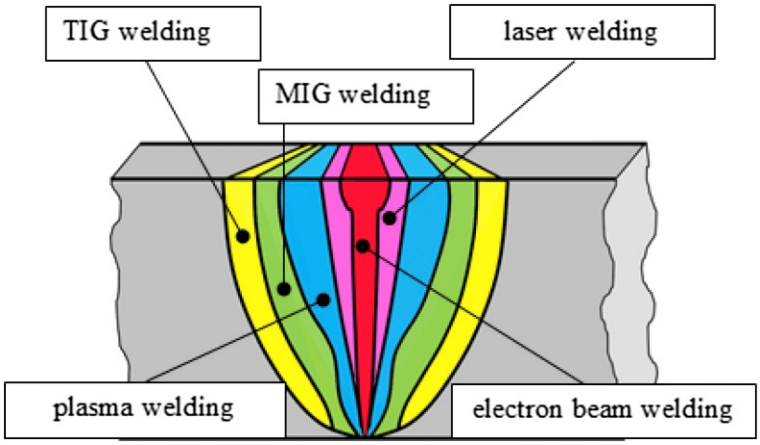
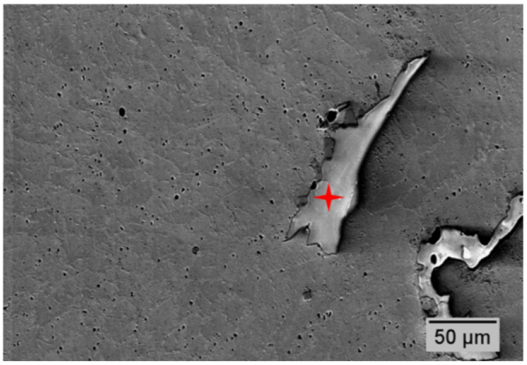


Figure 2.11. Geometry of the fusion zone created by various welding technologies [112].

Unfortunately, studies on EBW and LBW of ODS steels did not provide successful results, either. Lindau *et al.* [115] used EBW to weld ODS Eurofer steel. It was concluded that EBW led to weak weld seams, and that deterioration of mechanical properties was related to the oxide-disrupted microstructure in the weld zone. A ferritic ODS steel INCOLOY MA956 was welded via EBW by Jan *et al.* [116]. The experimental results showed that oxide particles formed large oxygen-rich slag particles in the weld metal (Figure 2.12), which would be detrimental to the mechanical properties of the material. Similarly, using LBW on PM2000 steel, Muangiunburee [117] observed an agglomeration of Y_2O_3 in the joint and in particular at the top of the weld surface. Lemmen *et al.* [114] employed LBW to weld PM1000 steel and observed clustering of oxide particles and consequently, a reduction of strength in the weld.



element	Y	Al	Ti	Fe	Cr	O
Wt %	66.7	16.8	2.0	0.9	0.7	12.9

Figure 2.12. Weld material microstructure with an oxide slag particle, the composition of the particle is presented in the table [116].

In summary, ODS steels do not seem to be fusion-weldable because of the inevitable clustering behaviour of the oxide particles when in the liquid state. Part of the reason for the significant disruption of the oxide particles is related to the long duration of the melt pool before solidification. Electron beam welding and LBW provide better chances for welding ODS steels due to the very high power density and associated high heating/cooling rates. In addition, in order to obtain a high quality joint between materials characterised by limited or difficult weldability, a filler material is advisable or necessary for EBW and LBW. The addition of filler material has been found to be effective in eliminating underfill and enhancing the mechanical properties of the joint. Liang *et al.* [118] studied the effect of filler powders on a laser welded ODS ferritic steel. The tensile strength of the joint with filler powders was increased from 312 MPa to 708 MPa. The benefits of filler material on the enhancement of mechanical properties was clearly manifested, despite the fact that the yttrium oxides in the joint were found to be severely coarsened and formed submicron oxide particles.

2.4.2 Solid-state welding

In solid-state welding processes, the workpieces are joined under a pressure providing an intimate contact and at a temperature essentially below the melting temperature of the parent material. Bonding of the materials is the result of atom diffusion instead of melting [119]. Solid-state welding techniques are attractive for joining ODS steels, as they do not create a molten zone at the joining area and the degradation of featured microstructures can be avoided or minimised. Therefore, solid-state welding techniques realised by diffusion bonding and friction stir welding (FSW) have been successfully developed and applied to join various ODS steels in recent years.

Diffusion bonding typically involves heat (reaching 50–80% of the melting temperature [120]) and pressure to perform solid-state bonding with a minimum of macroscopic deformation. Since no melting is involved in the process, the oxide particles stay essentially the same during an optimised diffusion bonding procedure [21]. However, even though no distinct HAZ is formed in the joint, the whole workpiece is subjected to a heat treatment. For transformable ODS steels like ODS Eurofer, development of high-quality diffusion bonds requires careful control over the recrystallisation behaviour of the material.

A 9 wt% Cr ODS steel was successfully joined via diffusion bonding in a hydrostatic vacuum hot-press furnace at 1473 K for 1 h [121]. Microstructure observations revealed no welding defects and homogenously distributed nano-oxide particles in the joint. The joints exhibited nearly the same tensile behaviour as the base metal at room temperature and at a high temperature of 973 K. Krishnardula *et al.* [122] examined diffusion bonding parameters for MA956 and PM2000 in both the unrecrystallised (fine-grained) and secondary-recrystallised (coarse-grained) conditions. It was found that bonding occurred only when unrecrystallised surfaces were involved. This was assumed to be due to the high stored energy in the fine-grained material. Noto *et al.* [123] studied a dissimilar joint of tungsten and ODS 15 wt% Cr steel established by diffusion bonding. Pure iron was inserted in between these materials to reduce the thermal stress caused by different thermal expansion coefficients. The bonding was carried

out at 1513 K for 1 h in a vacuum of 8.0×10^{-4} Pa with a hot press machine. A bond strength of 265 MPa was obtained with an equiaxed structure. The fracture was found to occur at tungsten grain boundaries. It is notable that SPS can also be used as a diffusion bonding technique. As mentioned in section 2.2.2, SPS has the major advantage of fast processing that can finish joining within a few minutes. Despite its great potential, little information is yet available on using SPS to join ODS steels.

The results from the literature indicate that diffusion bonding can be used to join ODS steels with minor microstructure and property deterioration. Unfortunately, diffusion bonding is usually conducted in vacuum or inert gas atmosphere. Therefore, it is not practical or cost-effective for all applications. For this reason, FSW has been considered as an alternative and promising method for joining ODS steels.

Friction stir welding is a solid-state welding process in which coalescence of materials is achieved by frictional heat combined with pressure. Due to its solid-state characteristic, FSW-welded ODS steel joints usually exhibit good mechanical strength at room temperature and elevated temperatures. There have been a large number of FSW studies on ODS alloys in recent years, demonstrating that joints can be produced with ODS 12 wt% Cr steel [124], ODS 15 wt% Cr steel [125], ODS 20 wt% Cr steel [126], MA956 [127], MA957 [111], PM2000 [128], etc. However, several studies [126, 129] on microstructural evolution during FSW of ODS steels agree that a large strain tended to be generated in the stir zone of the joint, where deformation heterogeneities facilitated the onset of recrystallisation. A further consideration was that the flow of the material near the joint had a distinct directionality by the rotating tool, which promoted the formation of high angle grain boundaries upon secondary recrystallisation. Furthermore, modifications of the size, shape, and composition of the oxide dispersoids were observed in the FSW joints of ODS 19 wt% Cr steel [130] and ODS 40 wt% Al steel [131]. Accordingly, the elevated-temperature creep resistance of FSW joints was found to be degraded and similar to that of the fusion-welded parts [110]. In addition, the application of FSW is limited due to geometrical restrictions [115]. The tool wear in FSW may also reduce the tool life and deteriorate the microstructure and mechanical properties of the joints [132].

In summary, solid-state welding techniques generally create reasonable joints in ODS steels. Their advantages include minimal metallurgical defects and disruption of oxide particles, largely or fully retained mechanical properties compared to base material, few consumable materials (filler material, fluxes and shielding gas) required as well as the possibilities of joining dissimilar materials [133]. However, the disadvantages lie in the high costs due to long bonding durations and expensive equipment. The applications of some techniques for joining ODS steels on site are limited due to a critical working environment.

2.5 Summary

An overview of the development, fabrication and welding of ODS steels is provided in this chapter. Various fabrication and welding techniques regarding feasibility, parameter optimisation as well as microstructure and mechanical property investigations have been reviewed and discussed. A few important observations can be summarised as follows:

(1) ODS steels are one of the most promising candidate structural materials for future fission and fusion reactors. Superior properties are attributed to the fine grains and finely dispersed nano-oxide particles. Development of suitable fabrication and welding techniques for ODS steels can further increase their widespread use.

(2) ODS steels are usually fabricated by a powder metallurgy route. In particular, SPS shows the advantage of rapid processing as a consolidation technique compared to hot isostatic pressing and hot extrusion. A number of studies on powder metallurgy have been carried out aiming at understanding the roles of composition, milling parameters, consolidation process and post-processing on the quality of ODS steels. In order to develop ODS steels with demanded microstructure and mechanical properties, the manufacturing route still needs to be optimised. The link between the initial powder features and the final compacts needs to be better understood by utilising advanced characterisation techniques.

(3) The complexity and high cost of powder metallurgy lead to the development of an alternative route for producing high-performance ODS steels. Selective laser melting and direct metal deposition have been successfully applied on several kinds of ODS steel components. Binder jetting shows potential to produce ODS steels owing to its solid-state characteristic. However, there are still many issues need to be solved, including processing parameter optimisation, thermal stress, defects like porosity and cracks, oxide particle size and distribution, microstructure and mechanical properties, etc.

(4) For traditional fusion-based welding of ODS steels, the nanoparticles in the joint inevitably agglomerate and grow due to melting, leading to degraded properties of the joint. Electron beam welding and laser beam welding have shown potential to weld ODS steels due to their high power density and localised heat input. Joining of ODS steels by solid-state welding such as diffusion bonding and FSW has been shown to be effective to produce reasonable welds while maintain most of the base material strength. However, the applicability of the solid-state welding techniques on site is a major issue to be considered.

The development and study of ODS steels, especially on manufacturing and welding, is still at an early stage. This thesis is focused on the investigation of manufacturing and welding behaviour of ODS Eurofer. With the aim of establishing a link between the microstructural evolution and mechanical properties of ODS Eurofer, processed by different techniques, this thesis will contribute to a better understanding of ODS Eurofer and ultimately ODS steels.

References

[1] M.A. Aktar, M.M. Alam, A.Q. Al-Amin, Global economic crisis, energy use, CO_2 emissions, and policy roadmap amid COVID-19, Sustainable Production and Consumption (2020).

[2] F. Jotzo, P.J. Burke, P.J. Wood, A. Macintosh, D.I. Stern, Decomposing the 2010 global carbon dioxide emissions rebound, Nature Climate Change 2(4) (2012) 213-214.

[3] A. Sieminski, U. Administrator, Energy information administration, International Energy Outlook (2016).

[4] C. Azevedo, Selection of fuel cladding material for nuclear fission reactors, Eng. Failure Anal. 18(8) (2011) 1943-1962.

[5] G. Wikmark, L. Hallstadius, K. Yueh, Cladding to sustain corrosion, creep and growth at high burn-ups, Nucl. Eng. Technol 41(2) (2009) 143.
[6] A.T. Motta, A. Yilmazbayhan, M.J.G. da Silva, R.J. Comstock, G.S. Was, J.T. Busby, E. Gartner, Q. Peng, Y.H. Jeong, J.Y. Park, Zirconium alloys for supercritical water reactor applications: Challenges and possibilities, J. Nucl. Mater. 371(1-3) (2007) 61-75.
[7] I. Pioro, Handbook of generation IV nuclear reactors, Woodhead Publishing2016.
[8] T. Abram, S. Ion, Generation-IV nuclear power: A review of the state of the science, Energy Policy 36(12) (2008) 4323-4330.
[9] S.J. Zinkle, G. Was, Materials challenges in nuclear energy, Acta Mater. 61(3) (2013) 735-758.
[10] F. Najmabadi, A. Abdou, L. Bromberg, T. Brown, V. Chan, M. Chu, F. Dahlgren, L. El-Guebaly, P. Heitzenroeder, D. Henderson, The ARIES-AT advanced tokamak, advanced technology fusion power plant, Fusion Eng. Des. 80(1-4) (2006) 3-23.
[11] S.J. Zinkle, J.T. Busby, Structural materials for fission & fusion energy, Mater. Today 12(11) (2009) 12-19.
[12] D.L. Smith, M. Billone, S. Majumdar, R. Mattas, D.-K. Sze, Materials integration issues for high performance fusion power systems, J. Nucl. Mater. 258 (1998) 65-73.
[13] J.-L. Boutard, A. Alamo, R. Lindau, M. Rieth, Fissile core and Tritium-Breeding Blanket: structural materials and their requirements, Comptes Rendus Physique 9(3-4) (2008) 287-302.
[14] K. Ehrlich, Materials research towards a fusion reactor, Fusion Eng. Des. 56 (2001) 71-82.
[15] K. Ehrlich, S. Kelzenberg, H.-D. Röhrig, L. Schäfer, M. Schirra, The development of ferritic-martensitic steels with reduced long-term activation, J. Nucl. Mater. 212 (1994) 678-683.
[16] R. Klueh, K. Ehrlich, F. Abe, Ferritic/martensitic steels: promises and problems, J. Nucl. Mater. 191 (1992) 116-124.
[17] E. Daum, K. Ehrlich, M. Schirra, Proceedings of the second milestone meeting of European laboratories on the development of ferritic/martensitic steels for fusion technology, Karlsruhe, September 9-10, 1996, (1997).
[18] S. Jitsukawa, M. Tamura, B. Van der Schaaf, R. Klueh, A. Alamo, C. Petersen, M. Schirra, P. Spaetig, G. Odette, A. Tavassoli, Development of an extensive database of mechanical and physical properties for reduced-activation martensitic steel F82H, J. Nucl. Mater. 307 (2002) 179-186.
[19] C. Cayron, E. Rath, I. Chu, S. Launois, Microstructural evolution of Y_2O_3 and $MgAl_2O_4$ ODS EUROFER steels during their elaboration by mechanical milling and hot isostatic pressing, J. Nucl. Mater. 335(1) (2004) 83-102.
[20] R. Lindau, A. Möslang, M. Schirra, P. Schlossmacher, M. Klimenkov, Mechanical and microstructural properties of a hipped RAFM ODS-steel, J. Nucl. Mater. 307 (2002) 769-772.
[21] M. Miller, K. Russell, D. Hoelzer, Characterization of precipitates in MA/ODS ferritic alloys, J. Nucl. Mater. 351(1-3) (2006) 261-268.
[22] G. Odette, M. Alinger, B. Wirth, Recent developments in irradiation-resistant steels, Annu. Rev. Mater. Res. 38 (2008) 471-503.

[23] H. Sandim, R. Renzetti, A. Padilha, D. Raabe, M. Klimenkov, R. Lindau, A. Möslang, Annealing behavior of ferritic–martensitic 9% Cr–ODS–Eurofer steel, Mater. Sci. Eng., A 527(15) (2010) 3602-3608.
[24] H. Zhu, T. Wei, R. Harrison, L. Edwards, K. Maruyama, Development of oxide dispersion strengthened steels for high temperature nuclear structural applications, Engineering Asset Management and Infrastructure Sustainability, Springer2012, pp. 1147-1160.
[25] X. Zhou, Y. Liu, L. Yu, Z. Ma, Q. Guo, Y. Huang, H. Li, Microstructure characteristic and mechanical property of transformable 9Cr-ODS steel fabricated by spark plasma sintering, Mater. Des. 132 (2017) 158-169.
[26] R. Maeda, Z.-L. Wang, T. Ogawa, Y. Adachi, Stress–strain partitioning behavior and mechanical properties of dual-phase steel using finite element analysis, Materials Today Communications 25 (2020) 101658.
[27] A. Kohyama, A. Hishinuma, D. Gelles, R. Klueh, W. Dietz, K. Ehrlich, Low-activation ferritic and martensitic steels for fusion application, J. Nucl. Mater. 233 (1996) 138-147.
[28] K. Murty, I. Charit, Structural materials for Gen-IV nuclear reactors: Challenges and opportunities, J. Nucl. Mater. 383(1-2) (2008) 189-195.
[29] R. Lindau, A. Möslang, M. Rieth, M. Klimiankou, E. Materna-Morris, A. Alamo, A.-A. Tavassoli, C. Cayron, A.-M. Lancha, P. Fernandez, Present development status of EUROFER and ODS-EUROFER for application in blanket concepts, Fusion Eng. Des. 75 (2005) 989-996.
[30] M. Inoue, T. Kaito, S. Ohtsuka, Research and development of oxide dispersion strengthened ferritic steels for sodium cooled fast breeder reactor fuels, Materials Issues for Generation IV Systems, Springer2008, pp. 311-325.
[31] R. Klueh, Elevated temperature ferritic and martensitic steels and their application to future nuclear reactors, Int. Mater. Rev. 50(5) (2005) 287-310.
[32] J. Wang, W. Yuan, R.S. Mishra, I. Charit, Microstructural evolution and mechanical properties of friction stir welded ODS alloy MA754, J. Nucl. Mater. 442(1-3) (2013) 1-6.
[33] M.S. El-Genk, J.-M. Tournier, A review of refractory metal alloys and mechanically alloyed-oxide dispersion strengthened steels for space nuclear power systems, J. Nucl. Mater. 340(1) (2005) 93-112.
[34] D.A. McClintock, D.T. Hoelzer, M.A. Sokolov, n. Nanstad, Mechanical properties of neutron irradiated nanostructured ferritic alloy 14YWT, J. Nucl. Mater. 386 (2009) 307-311.
[35] A. Czyrska-Filemonowicz, B. Dubiel, Mechanically alloyed, ferritic oxide dispersion strengthened alloys: structure and properties, J. Mater. Process. Technol. 64(1-3) (1997) 53-64.
[36] R. Evans, J. Preston, B. Wilshire, E. Little, Creep and creep fracture of an oxide-dispersion-strengthened 13% chromium ferritic steel, Mater. Sci. Eng., A 167(1-2) (1993) 65-72.
[37] S. Ukai, S. Ohtsuka, T. Kaito, H. Sakasegawa, N. Chikata, S. Hayashi, S. Ohnuki, High-temperature strength characterization of advanced 9Cr-ODS ferritic steels, Mater. Sci. Eng., A 510 (2009) 115-120.
[38] S. Ukai, M. Harada, H. Okada, M. Inoue, S. Nomura, S. Shikakura, K. Asabe, T. Nishida, M. Fujiwara, Alloying design of oxide dispersion strengthened ferritic steel for long life FBRs core materials, J. Nucl. Mater. 204 (1993) 65-73.

[39] J.P. Wharry, M.J. Swenson, K.H. Yano, A review of the irradiation evolution of dispersed oxide nanoparticles in the bcc Fe-Cr system: Current understanding and future directions, J. Nucl. Mater. 486 (2017) 11-20.
[40] B. Li, Z. Wang, K. Wei, T. Shen, C. Yao, H. Zhang, Y. Sheng, X. Lu, A. Xiong, W. Han, Evaluation of helium effect on irradiation hardening in F82H, ODS, SIMP and T91 steels by nano-indentation method, Fusion Eng. Des. 142 (2019) 6-12.
[41] M. Dadé, J. Malaplate, J. Garnier, F. De Geuser, F. Barcelo, P. Wident, A. Deschamps, Influence of microstructural parameters on the mechanical properties of oxide dispersion strengthened Fe-14Cr steels, Acta Mater. 127 (2017) 165-177.
[42] K. Verhiest, S. Mullens, J. Paul, I. De Graeve, N. De Wispelaere, S. Claessens, A. DeBremaecker, K. Verbeken, Experimental study on the contact angle formation of solidified iron–chromium droplets onto yttria ceramic substrates for the yttria/ferrous alloy system with variable chromium content, Ceram. Int. 40(1) (2014) 2187-2200.
[43] H. Danninger, C. Gierl-Mayer, Advanced powder metallurgy steel alloys, Advances in Powder Metallurgy, Elsevier2013, pp. 149-201.
[44] C. Suryanarayana, Mechanical alloying and milling, Prog. Mater Sci. 46(1-2) (2001) 1-184.
[45] C. Suryanarayana, E. Ivanov, V. Boldyrev, The science and technology of mechanical alloying, Mater. Sci. Eng., A 304 (2001) 151-158.
[46] V.-I. Merupo, S. Velumani, K. Ordon, N. Errien, J. Szade, A.-H. Kassiba, Structural and optical characterization of ball-milled copper-doped bismuth vanadium oxide (BiVO 4), CrystEngComm 17(17) (2015) 3366-3375.
[47] M. Yamamoto, S. Ukai, S. Hayashi, T. Kaito, S. Ohtsuka, Reverse phase transformation from α to γ in 9Cr-ODS ferritic steels, J. Nucl. Mater. 417(1-3) (2011) 237-240.
[48] M. Enayati, F. Mohamed, Application of mechanical alloying/milling for synthesis of nanocrystalline and amorphous materials, Int. Mater. Rev. 59(7) (2014) 394-416.
[49] J. Hoffmann, M. Rieth, R. Lindau, M. Klimenkov, A. Möslang, H.R.Z. Sandim, Investigation on different oxides as candidates for nano-sized ODS particles in reduced-activation ferritic (RAF) steels, J. Nucl. Mater. 442(1-3) (2013) 444-448.
[50] I. Bogachev, E. Grigoryev, O.L. Khasanov, E. Olevsky, Fabrication of 13Cr-2Mo ferritic/martensitic oxide-dispersion-strengthened steel components by mechanical alloying and spark-plasma sintering, JOM 66(6) (2014) 1020-1026.
[51] M. Sivakumar, A. Dasgupta, C. Ghosh, D. Sornadurai, S. Saroja, Optimisation of high energy ball milling parameters to synthesize oxide dispersion strengthened Alloy 617 powder and its characterization, Adv. Powder Technol. 30(10) (2019) 2320-2329.
[52] M. Serrano, M. Hernández-Mayoral, A. García-Junceda, Microstructural anisotropy effect on the mechanical properties of a 14Cr ODS steel, J. Nucl. Mater. 428(1-3) (2012) 103-109.
[53] J.R. Rieken, I.E. Anderson, M.J. Kramer, G. Odette, E. Stergar, E. Haney, Reactive gas atomization processing for Fe-based ODS alloys, J. Nucl. Mater. 428(1-3) (2012) 65-75.
[54] D. Kumar, U. Prakash, V. Dabhade, K. Laha, T. Sakthivel, Mechanical alloying and powder forging of 18% Cr oxide dispersion-strengthened steel produced using elemental powders, J. Mater. Eng. Perform. 28(1) (2019) 242-253.

[55] N. Loh, K. Sia, An overview of hot isostatic pressing, J. Mater. Process. Technol. 30(1) (1992) 45-65.
[56] P. Samal, J. Newkirk, Powder metallurgy processing by hot isostatic pressing, (2015).
[57] C. Ramesh, A. Hirianiah, K. Harishanad, N.P. Noronha, A review on hot extrusion of Metal Matrix Composites (MMC's), International Journal of Engineering and Science 1(10) (2012) 30-35.
[58] Z. Oksiuta, N. Baluc, Effect of mechanical alloying atmosphere on the microstructure and Charpy impact properties of an ODS ferritic steel, J. Nucl. Mater. 386 (2009) 426-429.
[59] V. De Castro, T. Leguey, M. Monge, A. Munoz, R. Pareja, D. Amador, J. Torralba, M. Victoria, Mechanical dispersion of Y_2O_3 nanoparticles in steel EUROFER 97: process and optimisation, J. Nucl. Mater. 322(2-3) (2003) 228-234.
[60] S. Ukai, T. Narita, A. Alamo, P. Parmentier, Tube manufacturing trials by different routes in 9CrW-ODS martensitic steels, J. Nucl. Mater. 329 (2004) 356-361.
[61] P. Olier, A. Bougault, A. Alamo, Y. De Carlan, Effects of the forming processes and Y_2O_3 content on ODS-Eurofer mechanical properties, J. Nucl. Mater. 386 (2009) 561-563.
[62] P. Unifantowicz, Z. Oksiuta, P. Olier, Y. De Carlan, N. Baluc, Microstructure and mechanical properties of an ODS RAF steel fabricated by hot extrusion or hot isostatic pressing, Fusion Eng. Des. 86(9-11) (2011) 2413-2416.
[63] I. Sulima, Consolidation of AISI316L austenitic steel–TiB2 composites by SPS and HP-HT technology, Sintering Techniques of Materials, Rijeka, InTech-Open Access Publisher 1 (2015) 125-153.
[64] M. Suárez, A. Fernández, J. Menéndez, R. Torrecillas, H. Kessel, J. Hennicke, R. Kirchner, T. Kessel, Challenges and opportunities for spark plasma sintering: a key technology for a new generation of materials, Sintering applications 13 (2013) 319-342.
[65] J.R. Groza, A. Zavaliangos, Sintering activation by external electrical field, Mater. Sci. Eng., A 287(2) (2000) 171-177.
[66] C. Zhang, A. Kimura, R. Kasada, J. Jang, H. Kishimoto, Y. Yang, Characterization of the oxide particles in Al-added high-Cr ODS ferritic steels, J. Nucl. Mater. 417(1-3) (2011) 221-224.
[67] R. Xie, Z. Lu, C. Lu, Z. Li, X. Ding, C. Liu, Microstructures and mechanical properties of 9Cr oxide dispersion strengthened steel produced by spark plasma sintering, Fusion Eng. Des. 115 (2017) 67-73.
[68] U. Anselmi-Tamburini, S. Gennari, J. Garay, Z. Munir, Fundamental investigations on the spark plasma sintering/synthesis process: II. Modeling of current and temperature distributions, Mater. Sci. Eng., A 394(1-2) (2005) 139-148.
[69] K. Vanmeensel, A. Laptev, J. Hennicke, J. Vleugels, O. Van der Biest, Modelling of the temperature distribution during field assisted sintering, Acta Mater. 53(16) (2005) 4379-4388.
[70] R. Orru, R. Licheri, A.M. Locci, A. Cincotti, G. Cao, Consolidation/synthesis of materials by electric current activated/assisted sintering, Materials Science and Engineering: R: Reports 63(4-6) (2009) 127-287.

[71] T.-K. Kim, C.-S. Bae, D.-H. Kim, J.-S. Jang, S.-H. Kim, C.-B. Lee, D.-H. Hahn, Microstructural observation and tensile isotropy of an austenitic ODS steel, Nuclear Engineering and Technology 40(4) (2008) 305-310.
[72] Y. Miao, K. Mo, Z. Zhou, X. Liu, K.-C. Lan, G. Zhang, M.K. Miller, K.A. Powers, J. Almer, J.F. Stubbins, In situ synchrotron tensile investigations on the phase responses within an oxide dispersion-strengthened (ODS) 304 steel, Mater. Sci. Eng., A 625 (2015) 146-152.
[73] M. Wang, Z. Zhou, H. Sun, H. Hu, S. Li, Microstructural observation and tensile properties of ODS-304 austenitic steel, Mater. Sci. Eng., A 559 (2013) 287-292.
[74] Z. Zhou, S. Yang, W. Chen, L. Liao, Y. Xu, Processing and characterization of a hipped oxide dispersion strengthened austenitic steel, J. Nucl. Mater. 428(1-3) (2012) 31-34.
[75] Y. Xu, Z. Zhou, M. Li, P. He, Fabrication and characterization of ODS austenitic steels, J. Nucl. Mater. 417(1-3) (2011) 283-285.
[76] M. Wang, Z. Zhou, H. Sun, H. Hu, S. Li, Effects of plastic deformations on microstructure and mechanical properties of ODS-310 austenitic steel, J. Nucl. Mater. 430(1-3) (2012) 259-263.
[77] H.K. Zhang, Z. Yao, Z. Zhou, M. Wang, O. Kaitasov, M.R. Daymond, Radiation induced microstructures in ODS 316 austenitic steel under dual-beam ions, J. Nucl. Mater. 455(1-3) (2014) 242-247.
[78] J.H. Lee, Development of oxide dispersion strengthened ferritic steels with and without aluminum, Frontiers in Energy 6(1) (2012) 29-34.
[79] M.K. Dash, S. Saroja, R. Mythili, A. Dasgupta, Influence of texture on deformation mechanism of hot extruded oxide dispersion strengthened 18Cr ferritic steel, J. Mater. Eng. Perform. 29(10) (2020) 6881-6889.
[80] M. Nagini, R. Vijay, K.V. Rajulapati, K.B.S. Rao, M. Ramakrishna, A. Reddy, G. Sundararajan, Effect of process parameters on microstructure and hardness of oxide dispersion strengthened 18Cr ferritic steel, MMTA 47(8) (2016) 4197-4209.
[81] Z. Oksiuta, M. Lewandowska, K. Kurzydlowski, N. Baluc, Reduced activation ODS ferritic steel–recent development in high speed hot extrusion processing, physica status solidi (a) 207(5) (2010) 1128-1131.
[82] P. Koncz, Á. Horváth, K. Balázsi, F.Ç. Şahin, G. Göller, Y. Onüralp, C. Balázsi, Correlation between milling parameters, structural and mechanical properties of nanostructured austenitic Y_2O_3 strengthened steels, Mater. Sci. Forum, Trans Tech Publ, 2013, pp. 409-414.
[83] Z. Li, Z. Lu, R. Xie, C. Lu, C. Liu, Effect of spark plasma sintering temperature on microstructure and mechanical properties of 14Cr-ODS ferritic steels, Mater. Sci. Eng., A 660 (2016) 52-60.
[84] M.A. Auger, V. De Castro, T. Leguey, A. Muñoz, R. Pareja, Microstructure and mechanical behavior of ODS and non-ODS Fe–14Cr model alloys produced by spark plasma sintering, J. Nucl. Mater. 436(1-3) (2013) 68-75.
[85] H. Zhang, Y. Huang, H. Ning, C.A. Williams, A.J. London, K. Dawson, Z. Hong, M.J. Gorley, C.R. Grovenor, G.J. Tatlock, Processing and microstructure characterisation of oxide dispersion strengthened Fe–14Cr–0.4 Ti–0.25Y_2O_3 ferritic steels fabricated by spark plasma sintering, J. Nucl. Mater. 464 (2015) 61-68.

[86] S. Grasso, Y. Sakka, G. Maizza, Electric current activated/assisted sintering (ECAS): a review of patents 1906–2008, Science and Technology of Advanced Materials 10(5) (2009) 053001.
[87] N. Saheb, Z. Iqbal, A. Khalil, A.S. Hakeem, N. Al Aqeeli, T. Laoui, A. Al-Qutub, R. Kirchner, Spark plasma sintering of metals and metal matrix nanocomposites: a review, Journal of Nanomaterials 2012 (2012).
[88] I. Hilger, X. Boulnat, J. Hoffmann, C. Testani, F. Bergner, Y. De Carlan, F. Ferraro, A. Ulbricht, Fabrication and characterization of oxide dispersion strengthened (ODS) 14Cr steels consolidated by means of hot isostatic pressing, hot extrusion and spark plasma sintering, J. Nucl. Mater. 472 (2016) 206-214.
[89] R. Streubel, M.B. Wilms, C. Doñate-Buendía, A. Weisheit, S. Barcikowski, J.H. Schleifenbaum, B. Gökce, Depositing laser-generated nanoparticles on powders for additive manufacturing of oxide dispersed strengthened alloy parts via laser metal deposition, Jpn. J. Appl. Phys. 57(4) (2018) 040310.
[90] H. Fayazfar, M. Salarian, A. Rogalsky, D. Sarker, P. Russo, V. Paserin, E. Toyserkani, A critical review of powder-based additive manufacturing of ferrous alloys: Process parameters, microstructure and mechanical properties, Mater. Des. 144 (2018) 98-128.
[91] T. Boegelein, S.N. Dryepondt, A. Pandey, K. Dawson, G.J. Tatlock, Mechanical response and deformation mechanisms of ferritic oxide dispersion strengthened steel structures produced by selective laser melting, Acta Mater. 87 (2015) 201-215.
[92] M. Ghayoor, K. Lee, Y. He, C.-h. Chang, B.K. Paul, S. Pasebani, Selective laser melting of austenitic oxide dispersion strengthened steel: Processing, microstructural evolution and strengthening mechanisms, Mater. Sci. Eng., A 788 (2020) 139532.
[93] E. Vasquez, P.-F. Giroux, F. Lomello, M. Nussbaum, H. Maskrot, F. Schuster, P. Castany, Effect of powder characteristics on production of oxide dispersion strengthened Fe14Cr steel by laser powder bed fusion, Powder Technol. 360 (2020) 998-1005.
[94] Y. Shi, Z. Lu, H. Xu, R. Xie, Y. Ren, G. Yang, Microstructure characterization and mechanical properties of laser additive manufactured oxide dispersion strengthened Fe-9Cr alloy, J. Alloys Compd. 791 (2019) 121-133.
[95] Y. Shi, Z. Lu, L. Yu, R. Xie, Y. Ren, G. Yang, Microstructure and tensile properties of Zr-containing ODS-FeCrAl alloy fabricated by laser additive manufacturing, Mater. Sci. Eng., A 774 (2020) 138937.
[96] C. Doñate-Buendía, F. Frömel, M.B. Wilms, R. Streubel, J. Tenkamp, T. Hupfeld, M. Nachev, E. Gökce, A. Weisheit, S. Barcikowski, Oxide dispersion-strengthened alloys generated by laser metal deposition of laser-generated nanoparticle-metal powder composites, Mater. Des. 154 (2018) 360-369.
[97] B. Mueller, Additive manufacturing technologies–Rapid prototyping to direct digital manufacturing, AsAut (2012).
[98] C. Doñate-Buendia, R. Streubel, P. Kürnsteiner, M. Wilms, F. Stern, J. Tenkamp, E. Bruder, S. Barcikowski, B. Gault, K. Durst, Effect of nanoparticle additivation on the microstructure and microhardness of oxide dispersion strengthened steels produced by laser powder bed fusion and directed energy deposition, Procedia CIRP 94 (2020) 41-45.

[99] S. Mirzababaei, S. Pasebani, A review on binder jet additive manufacturing of 316L stainless steel, Journal of Manufacturing and Materials Processing 3(3) (2019) 82.
[100] N.B. Dahotre, S. Harimkar, Laser fabrication and machining of materials, Springer Science & Business Media2008.
[101] J.C. Walker, K.M. Berggreen, A.R. Jones, C.J. Sutcliffe, Fabrication of Fe–Cr–Al oxide dispersion strengthened PM2000 alloy using selective laser melting, Adv. Eng. Mater. 11(7) (2009) 541-546.
[102] L.E. Murr, E. Martinez, S. Gaytan, D. Ramirez, B. Machado, P. Shindo, J. Martinez, F. Medina, J. Wooten, D. Ciscel, Microstructural architecture, microstructures, and mechanical properties for a nickel-base superalloy fabricated by electron beam melting, MMTA 42(11) (2011) 3491-3508.
[103] W.E. Frazier, Metal additive manufacturing: a review, J. Mater. Eng. Perform. 23(6) (2014) 1917-1928.
[104] J. Schmidt, H. Elsayed, E. Bernardo, P. Colombo, Digital light processing of wollastonite-diopside glass-ceramic complex structures, J. Eur. Ceram. Soc. 38(13) (2018) 4580-4584.
[105] E. Périgo, J. Jacimovic, F.G. Ferré, L. Scherf, Additive manufacturing of magnetic materials, Additive Manufacturing 30 (2019) 100870.
[106] R.J. Kurtz, A. Alamo, E. Lucon, Q. Huang, S. Jitsukawa, A. Kimura, R. Klueh, G.R. Odette, C. Petersen, M.A. Sokolov, Recent progress toward development of reduced activation ferritic/martensitic steels for fusion structural applications, J. Nucl. Mater. 386 (2009) 411-417.
[107] E. Bloom, S. Zinkle, F. Wiffen, Materials to deliver the promise of fusion power–progress and challenges, J. Nucl. Mater. 329 (2004) 12-19.
[108] I.G. Wright, G.J. Tatlock, H. Badairy, C. Chen, Summary of prior work on joining of oxide dispersion-strengthened alloys, Oak Ridge National Laboratory, 2009.
[109] C. Pandey, M.M. Mahapatra, P. Kumar, N. Saini, Some studies on P91 steel and their weldments, J. Alloys Compd. 743 (2018) 332-364.
[110] M. McKimpson, D. O'Donnell, Joining ODS materials for high-temperature applications, JOM 46(7) (1994) 49-51.
[111] P. Miao, G. Odette, J. Gould, J. Bernath, R. Miller, M. Alinger, C. Zanis, The microstructure and strength properties of MA957 nanostructured ferritic alloy joints produced by friction stir and electro-spark deposition welding, J. Nucl. Mater. 367 (2007) 1197-1202.
[112] M.S. Węglowski, S. Błacha, A. Phillips, Electron beam welding–techniques and trends–review, Vacuu 130 (2016) 72-92.
[113] G. Haidemenopoulos, Coupled thermodynamic/kinetic analysis of diffusional transformations during laser hardening and laser welding, J. Alloys Compd. 320(2) (2001) 302-307.
[114] H. Lemmen, K. Sudmeijer, I. Richardson, S. van der Zwaag, Laser beam welding of an Oxide Dispersion Strengthened super alloy, J. Mater. Sci. 42(13) (2007) 5286-5295.
[115] R. Lindau, M. Klimenkov, U. Jäntsch, A. Möslang, L. Commin, Mechanical and microstructural characterization of electron beam welded reduced activation oxide dispersion strengthened–Eurofer steel, J. Nucl. Mater. 416(1-2) (2011) 22-29.

[116] V. Jan, J. Čupera, P. Sohaj, P. Havlik, Microstructure Evaluation of Heterogeneous Electron Beam Weld between Stabilised Austenitic and ODS Ferritic Steel, Mater. Sci. Forum, Trans Tech Publ, 2017, pp. 185-189.
[117] P. Muangjunburee, H-7 Investigation of laser welding of high temperature ODS alloys Ferritic Stainless Steels (Session: Welding/Joining), The Proceedings of the Asian Symposium on Materials and Processing 2006, The Japan Society of Mechanical Engineers, 2006, p. 143.
[118] S. Liang, Y. Lei, Q. Zhu, The filler powders laser welding of ODS ferritic steels, J. Nucl. Mater. 456 (2015) 206-210.
[119] H. Kreye, Melting phenomena in solid state welding processes, WeldJ 56(5) (1977) 154-158.
[120] B. Derby, E. Wallach, Theoretical model for diffusion bonding, Metal Science 16(1) (1982) 49-56.
[121] S. Noh, R. Kasada, A. Kimura, Solid-state diffusion bonding of high-Cr ODS ferritic steel, Acta Mater. 59(8) (2011) 3196-3204.
[122] V. Krishnardula, V. Krishnardula, D. Clark, T. Totemeier, Joining Techniques For Ferritic ODS Alloys, Idaho National Laboratory (INL), 2005.
[123] H. Noto, S. Taniguchi, H. Kurishita, S. Matsuo, A. Kimura, Diffusion Bonding of W/ODS Steel Using Pure Iron Insert for Fusion Reactor Applications, Proceedings of the 8th Pacific Rim International Congress on Advanced Materials and Processing, Springer, 2013, pp. 129-135.
[124] H. Serizawa, M. Murakami, Y. Morisada, H. Fujii, S. Nogami, T. Nagasaka, H. Tanigawa, Influence of friction stir welding conditions on joinability of oxide dispersion strengthened steel/F82H ferritic/martensitic steel joint, Nucl. Mater. Energy 9 (2016) 367-371.
[125] S. Noh, R. Kasada, A. Kimura, S.H.C. Park, S. Hirano, Microstructure and mechanical properties of friction stir processed ODS ferritic steels, J. Nucl. Mater. 417(1-3) (2011) 245-248.
[126] C.-L. Chen, G. Tatlock, A. Jones, Microstructural evolution in friction stir welding of nanostructured ODS alloys, J. Alloys Compd. 504 (2010) S460-S466.
[127] L.N. Brewer, M.S. Bennett, B. Baker, E.A. Payzant, L. Sochalski-Kolbus, Characterization of residual stress as a function of friction stir welding parameters in oxide dispersion strengthened (ODS) steel MA956, Mater. Sci. Eng., A 647 (2015) 313-321.
[128] C. Chen, P. Wang, G. Tatlock, Phase transformations in yttrium–aluminium oxides in friction stir welded and recrystallised PM2000 alloys, Mater. High Temp. 26(3) (2009) 299-303.
[129] K. Yabuuchi, N. Tsuda, A. Kimura, Y. Morisada, H. Fujii, H. Serizawa, S. Nogami, A. Hasegawa, T. Nagasaka, Effects of tool rotation speed on the mechanical properties and microstructure of friction stir welded ODS steel, Mater. Sci. Eng., A 595 (2014) 291-296.
[130] F. Legendre, S. Poissonnet, P. Bonnaillie, L. Boulanger, L. Forest, Some microstructural characterisations in a friction stir welded oxide dispersion strengthened ferritic steel alloy, J. Nucl. Mater. 386 (2009) 537-539.
[131] B. Inkson, P. Threadgill, Friction welding of FeAl40 Grade 3 ODS alloy, Mater. Sci. Eng., A 258(1-2) (1998) 313-318.

[132] U. Acharya, B.S. Roy, S.C. Saha, A study of tool wear and its effect on the mechanical properties of friction stir welded AA6092/17.5 Sicp composite material joint, Materials Today: Proceedings 5(9) (2018) 20371-20379.
[133] E. Akca, A. Gürsel, Solid state welding and application in aeronautical industry, Periodicals of Engineering and Natural Sciences (PEN) 4(1) (2016).

3

Experimental details

This chapter provides an overview of all experimental techniques used in this study. The approaches of powder metallurgy, additive manufacturing and welding of ODS Eurofer are given in detail in section 3.1, 3.2 and 3.3, respectively. In addition, section 3.4 shows general characterisation techniques employed in the study including microstructure characterisation and mechanical property investigations.

3.1 Powder metallurgy

The reference ODS Eurofer material was produced via a powder metallurgy route, *i.e.* mechanical alloying/ball milling and spark plasma sintering (SPS). The starting powders used in this study were commercially available Cr, W, Mn, V, Ta, Y_2O_3 and Fe powders, supplied by Goodfellow, Germany. All of them were weighted according to the nominal composition of ODS Eurofer indicated in Table 3.1. This table also shows the particle size of the powders provided by the manufacturer. It is worth mentioning that carbon powder was not included into the mechanical alloying process, since 1) most of the provided powders have carbon impurities (around 0.02 wt%) and 2) the SPS process will introduce extra carbon into the material due to the use of a graphite mould.

Mechanically alloying was conducted with a Retsch PM 100 ball mill machine, shown in Figure 3.1. The grinding bowl and balls were cleaned with 100 ml isopropanol for 6 h at a speed of 300 rpm before use. The grinding bowl, which is a 250 ml hardened steel bowl, was fastened by the clamping arrangement and protected by the safety glider. The counter balance was adjusted to the total weight of the grinding bowl and the material inside. The grinding media were hardened steel balls to avoid the contamination of powders during ball milling. A combination of 50 x 5 mm diameter, 20 x 10 mm diameter and 3 x 20 mm diameter balls were used to reduce the powder size effectively. The powder used per batch was 61 g. The ball to powder mass ratio was around 3.4:1. The ball milling program was set by the display unit. The powders were milled for 6–36 h at a speed of 300 rpm in an argon atmosphere. A time interval of 10 min after a rotation of 10 min was applied throughout the process to avoid a significant increase of temperature during the intensive milling. These milling conditions were selected based on the study of Suryanarayana [1] on mechanical alloying and milling.

Table 3.1 Chemical composition of ODS Eurofer and the powder size used for powder metallurgy.

	Cr	W	Mn	V	Ta	Y_2O_3	C	Fe
wt./%	9.0	1.1	0.4	0.2	0.12	0.3	0.1	Bal.
Size/µm	38–45	45–75	45–115	Max 45	Max 75	0.025–0.05	–	Max 60

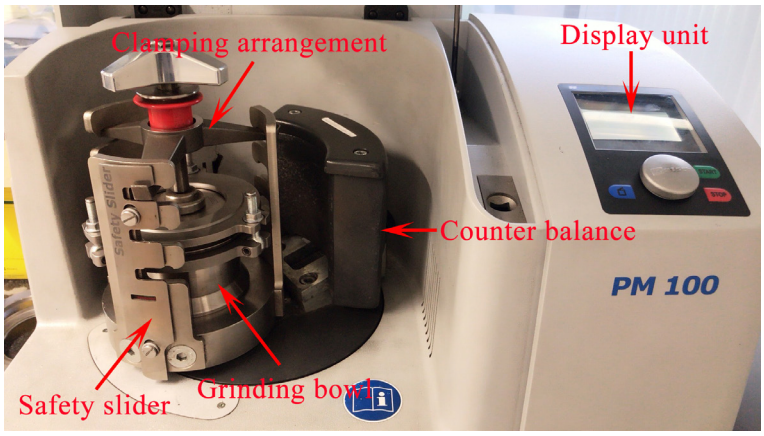


Figure 3.1 PM 100 Ball mill machine.

The as-milled powders were then compacted in a Spark Plasma Sintering (SPS, FCT group, Germany) machine, shown in Figure 3.2. A graphite die and punch assembly was used to hold around 100 g of powder. Graphite foil was used as a release agent for facilitating lubrication and lining the inner surface of the die. Boron nitride spray was used inside the mould chamber to reduce carbon diffusion into the sample. The temperature and pressure profiles used for the consolidation process are shown in Figure 3.3. Since the minimum temperature that could be detected by the optical pyrometer was 673 K, there is an apparent plateau temperature of 673 K at the beginning of the temperature profile. The SPS chamber was pumped two times to ensure a high vacuum of 5–10 Pa. The compacts were then heated at a heating rate of 50 to 400 K min^{-1} up to the sintering temperature, which was chosen as either 1323 K or 1373 K or 1423 K. The holding time at maximum temperature was 30 min to ensure a sufficient sintering. As for the pressure profile, a pre-force of 5 kN was applied to the compacts to align the die and punch assembly. Within 1 min, an axial pressure ranging from 50 and 80 MPa was applied and maintained until the consolidation was finished. The processing conditions used in the study are summarised in Table 3.2. Finally, the compacts were allowed to cool to room temperature by direct contact with the water cooled punches. The cooling rate was set to be 50 K min^{-1} until reaching 673 K. Following this procedure, disks with a diameter of 40 mm and a thickness of approximately 10 mm were produced.

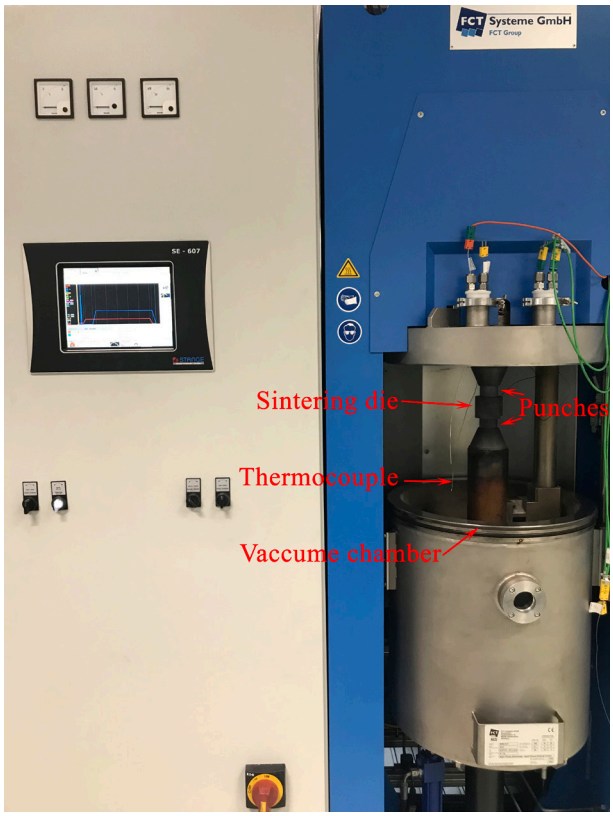


Figure 3.2 An overview of the spark plasma sintering system.

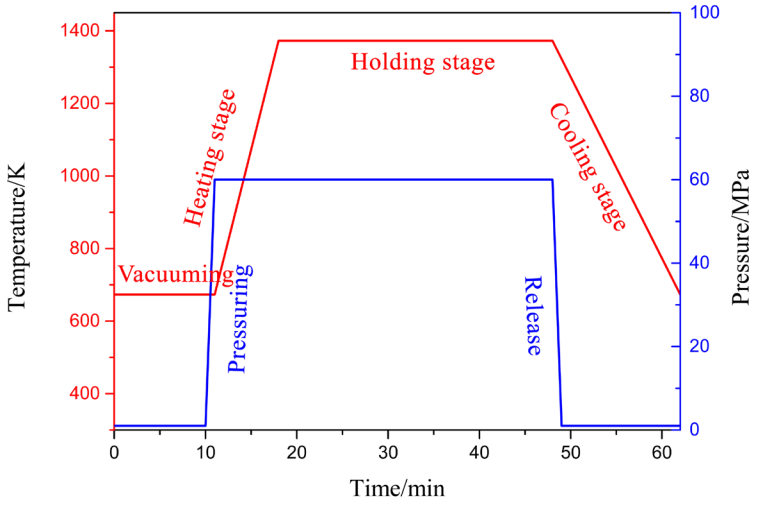


Figure 3.3 Temperature and pressure profiles of the SPS consolidation process.

Table 3.2 Processing conditions used in this study.

	Milling time /h	Pressure /MPa	Heating rate /(K min^{-1})	Sintering temperature/K
A	0	50	100	1373
B	24	50	100	1373
C	30	50	100	1373
D	36	50	100	1373
E	30	40	100	1373
F	30	60	100	1373
G	30	80	100	1373
H	30	60	50	1373
I	30	60	200	1373
J	30	60	400	1373
K	30	60	100	1323
L	30	60	100	1423

A following heat treatment was conducted on the produced disks to homogenise the microstructure and restore ductility. Different heat treatment routes were examined to study the effect on the microstructure and mechanical properties, in order to determine a suitable heat treatment route. The steel was subjected to a normalisation treatment for 1 h at 1323 K, 1423 K or 1523 K, respectively. In the case of a normalisation treatment at 1423 K, a tempering treatment was followed at 873 K, 973 K or 1073 K for 1 h, respectively. All specimens were air cooled to room temperature.

3.2 Direct metal deposition

The raw material for the direct metal deposition (DMD) process is ODS Eurofer powder prepared by mechanical alloying. Elemental powders were weighed according to the nominal composition of ODS Eurofer. The size of different powders is summarised in Table 3.3. The powders were milled in a Retsch planetary ball milling machine under an argon atmosphere for 16 h at 300 rpm. Afterwards, the powders were sieved and had a size distribution within the range of 50–100 μm.

Table 3.3. The size of different powders for direct metal deposition.

	Cr	W	Mn	V	Ta	Y_2O_3	C	Fe
Size/μm	Max 150	45–75	Max 250	Max 325	Max 75	0.025–0.05	Max 45	45–150

ODS Eurofer blocks with dimensions of around 15×15×10 mm^3 were fabricated by the DMD technique. Figure 3.4 (a) is a schematic drawing of the DMD process used in this study [2]. The device is mainly composed of a fibre laser system, a numerical control system, a coaxial powder feeder and an inert gas dynamic protection system. The printing was conducted with

the condition of a laser spot size of 1.6 mm, a laser beam incidence angle of 60°, a scanning speed of 15 mm/s and a powder feeding rate of 5.5 g/min. Three different laser powers were used, which are 600 W, 800 W and 1000 W, respectively. The scanning strategy is shown in Figure 3.4 (b). The deposition went in one direction in the first layer and changed to the opposite direction in the next layer. The process repeated until the z increment was achieved and a total of 40 layers were built. An overlap of around 50% of the bead width was adopted. A 304 stainless steel plate was used as the substrate. In order to consolidate the internal pores and relieve the residual stress within the build, the alloy produced by a laser power of 800 W was further treated by hot isostatic pressing (HIP) at a temperature of 1373 K and a pressure of 100 MPa for 2 h.

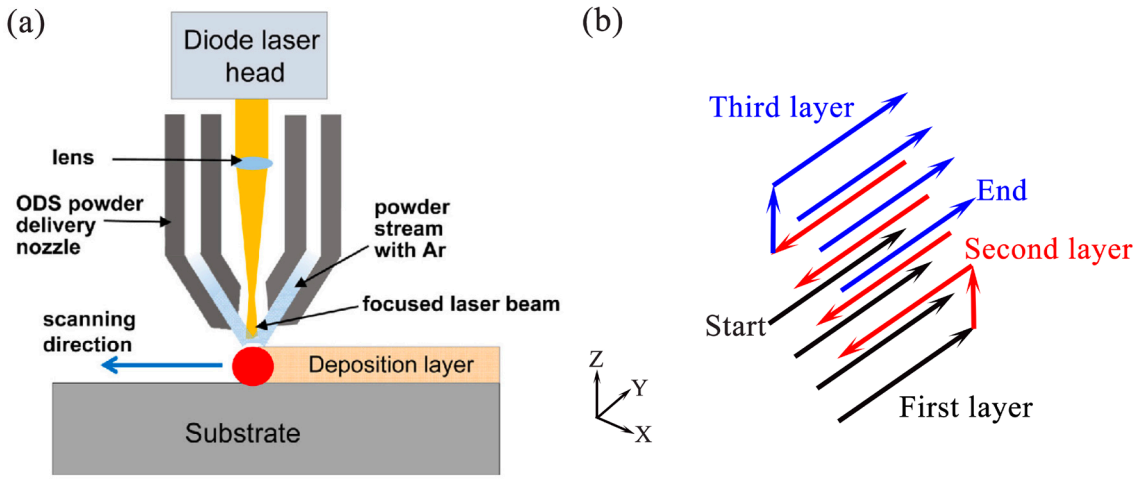


Figure 3.4. (a) schematic of the DMD process and (b) scanning strategy.

3.3 Welding techniques

3.3.1 Spark plasma sintering (SPS) joining

ODS Eurofer disks with 20 mm diameter and 17 mm thickness were produced by the powder metallurgy route, *i.e.* mechanical alloying and spark plasma sintering, for SPS joining. The hardness of the surface area of the produced material (around 650 $HV_{0.3}$) is higher than that of the middle area (around 450 $HV_{0.3}$) due to a higher carbon content and a more rapid cooling [3]. To remove the harder material and ensure a flat surface, the bottom surface was ground and polished. Afterwards, two disks with a thickness of 15 mm were placed against each other with a layer of 1 to 4 g of mechanical alloyed ODS Eurofer powder added in between (Figure 3.5(b)). The specimens were joined by sintering at 1373 K with a heating rate of 100 K min^{-1} and a pressure of 80 MPa with holding times in the range of 10–40 min. A post heat treatment was conducted to improve the mechanical performance by normalising at 1423 K for 1 h, air cooling to room temperature and then tempering at 973 K for 1 h, followed by air cooling to room temperature.

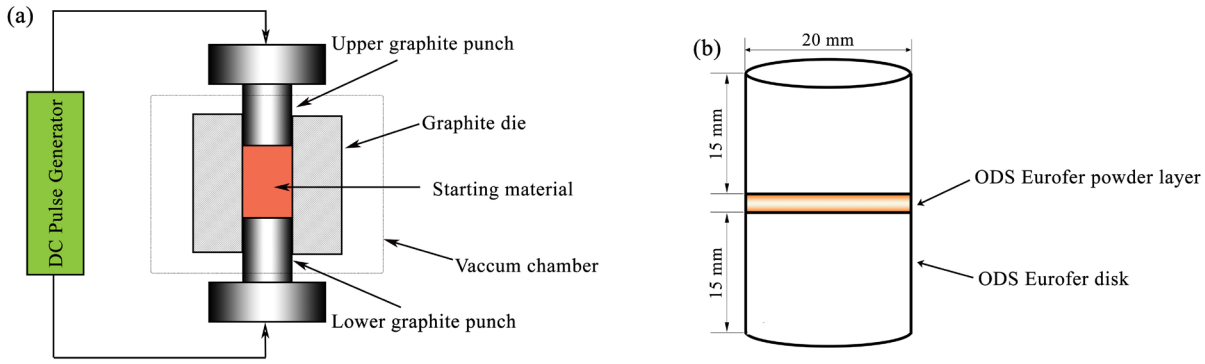


Figure 3.5. (a) Schematic of the SPS device and (b) schematic of the preparation of ODS Eurofer joints by SPS joining.

3.3.2 Pulsed laser beam welding

A 6 kW Yb:YAG laser was used for the laser welding experiments. The focusing optic has a focal length of 223 mm and projects a laser spot with a diameter of 0.4 mm or 0.6 mm for different purposes. The work pieces with a thickness of 1 mm or 5 mm machined from the SPS prepared disks (40 mm diameter and 10 mm thickness) were treated by a pulsed laser beam with a power (P) of 2500 W and pulse durations (t) ranging from 2 ms to 200 ms. A shielding gas of argon was delivered to the work piece at a flow rate of 8 L/min. Instead of moving straight in one direction, the laser beam was moved following the sequence indicated in Figure 3.6 in order to minimise the heat accumulation in the material and therefore shorten the melt pool lifetime. The time interval between each point is around 30 s. The distance between the centres of adjacent spots was 0.5 mm to ensure a continuous weld. Similar to SPS joining, an identical post heat treatment route was conducted to recover the microstructure and release the residual stress generated during welding.

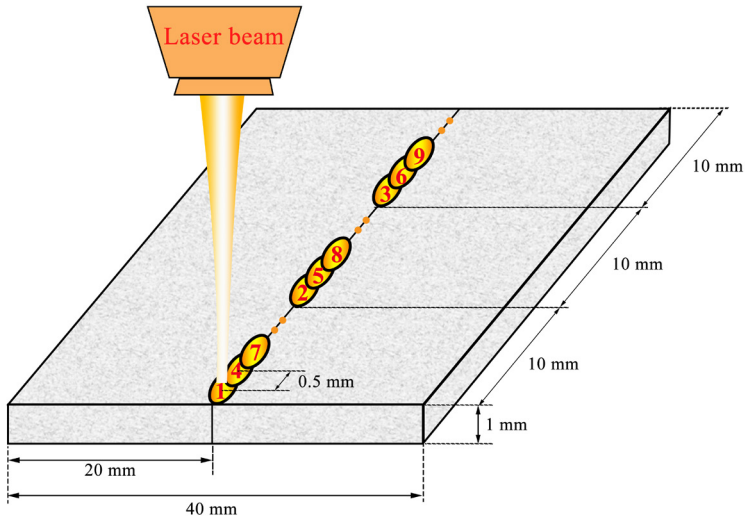


Figure 3.6. Schematic illustration of pulsed laser beam welding strategies.

3.4 General characterisation techniques

Details of the general techniques used in this study to characterise the microstructure and mechanical properties of ODS Eurofer under various conditions are provided in this section. Detailed approaches of each technique applied for different investigations can be found in relevant chapters.

3.4.1 Microstructural characterisation techniques

3.4.1.1 Optical Microscopy (OM) and Scanning Electron Microscopy (SEM)

For optical microscopy (OM) and scanning electron microscopy (SEM) analysis, the materials were ground with 80, 180, 320, 800, 1200 and 2000 grit SiC paper and polished with 3 µm and 1 µm diamond paste. Optical microscopy was conducted using a Keyence Digital Microscope VHX-5000. Scanning electron microscopy was performed using a JEOL 6500F scanning electron microscope equipped with a field emission gun and an energy dispersive spectrometer (EDS) system. To reveal the microstructure for OM and SEM observations, the samples were etched in a solution of 5 g ferric chloride, 50 ml HCl and 100 ml distilled water for 20 s.

3.4.1.2 Electron backscatter diffraction (EBSD)

Specimens for electron backscatter diffraction (EBSD) measurements were first ground and mirror polished. Subsequently, a colloidal silica suspension polishing step was realised by a VibroMet 2 vibratory polisher to obtain stress-free polished surfaces. EBSD scans were acquired using the same SEM facilities mentioned in 3.4.1.1. The EBSD measurements were conducted at an accelerating voltage of 20 kV, a specimen tilt angle of 70°, a working distance of 25 mm and a scan step size of 0.1 µm. FCC (austenite) and BCC iron (ferrite) were chosen as the input phases. The orientation data was post processed with the TSL-orientation image microscopy (OIM) software. Post processing omitted the points with confidence index (CI) lower than 0.1 from the EBSD maps. Inverse pole figure (IPF), grain average image quality (GAIQ), kernel average misorientation (KAM), and kernel average image quality (KAIQ) maps were obtained for analysis.

3.4.1.3 Transmission electron microscopy (TEM)

For transmission electron microscopy (TEM) characterisation, conventional thin foils were extracted from the investigated steel samples. Small disks (diameter 3 mm and thickness 0.1 mm) were cut by wire electrical discharge machining (WEDM). They were first mechanically ground down to a thickness of around 80 µm using a Gatan Disc Grinder. The thickness of TEM specimens were further reduced by electropolishing in a twin-jet electropolisher using 4% perchloric acid and 96% ethanol as electrolyte at room temperature. Once the optical sensor in the polisher detected a hole in the sample, the polishing was stopped. The samples were immersed in ethanol to remove the residual electrolyte. TEM analysis was conducted using a JEOL JEM-2200FS transmission electron microscope equipped with a field emission gun. Energy dispersive X-ray spectrometry (EDS) was used to distinguish carbides

and oxide particles from the steel matrix. The indexation of the diffraction patterns was performed with a TEMIDEA software.

3.4.1.4 X-ray diffraction (XRD)

X-Ray diffraction (XRD) analysis was performed using a Bruker D8-Advanced diffractometer in Bragg-Brentano geometry equipped with a Lynxeye position sensitive detector using Cu Kα target (1.5406 Å). Measurements were conducted in the 2θ range of 10° to 145° with a voltage of 45 kV and a current of 40 mA. A step size of 0.02° (2θ) and a counting time of 2 s per step were employed. The instrumental contributions to the peak width was determined and corrected using LaB_6 powder. The XRD patterns obtained were analysed with DIFFRAC.EVA software for peak evaluation and phase determination.

3.4.1.5 X-ray fluorescence (XRF) and combustion analysis

The chemical composition of the steel produced by powder metallurgy and additive manufacturing was determined by X-ray fluorescence (for heavy elements) and combustion analysis (for carbon). XRF measurements were performed with a Panalytical Axios Max WD-XRF spectrometer. The data evaluation was realised by a SuperQ5.0i/Omnian software. Combustion experiments were conducted to determine the carbon content using a LECO CS744. Pre-weighed samples of approximately 1 g were combusted in a stream of oxygen using an induction heater to heat the sample. Carbon in the sample was oxidised to carbon dioxide (CO_2), and swept by the oxygen carrier through a non-dispersive infrared cell to determine the carbon content.

3.4.1.6 Atom probe tomography (APT)

Atom probe tomography (APT) analysis was conducted with a CAMECA LEAP® 5000XR at the Department of Materials, University of Oxford. Atom probe specimens were prepared by the lift-out technique [4] using a Zeiss Crossbeam 540 Analytical Focused Ion Beam (FIB)-SEM. Cleaning of the specimens was performed using 2 kV Ga ions to minimise FIB-induced damage. The atom probe tips were cooled down to 55 K. A 355 nm wavelength, frequency tripled Nd:YAG laser at 40 pJ and 200 kHz was used to sputter atoms from the tip under ultra-high vacuum, at an average detection rate of 1.0%. The detection efficiency of the LEAP 5000XR is 52% [5]. CAMECA IVAS® 3.8.4 software was used to reconstruct the 3D chemical atomic maps. SEM micrographs of the final tip shape and crystallographic pole indexing were used for reconstruction of the APT maps. The size, number density and composition of nanoclusters were calculated using the solute ions of VN, YO, Y, O and TaO_2. A maximum separation method [6] was used to define the nanoclusters with the following parameters: N_{min} = 10, order = 1, d_{max} ranging from 0.8–1.5 nm and L = $d_{erosion}$ = 0.5d_{max}. N_{min} is the minimum number of atoms in a cluster. d_{max} is the maximum distance between atoms in a cluster. The atoms within a distance of L are included in the particle. The atoms at the interface of the clusters are eroded if they are within a distance of $d_{erosion}$ from the nearest atom.

3.4.1.7 Differential scanning calorimetry (DSC)

Thermal analysis of the steel was conducted by means of differential scanning calorimetry (DSC) to obtain the DSC profile. The test was operated in an argon atmosphere with a flow rate of 100 ml/min. The applied thermal cycle was designed as follows: the specimen was heated to 1523 K at a heating rate of 10 K min^{-1} and held at this temperature for 10 min, and then cooled to room temperature at a cooling rate of 10 K min^{-1}. The base line determination and subtraction were performed using an empty crucible with identical heating and cooling rates. Determination of the phase transformation start and finish temperatures was realised by determining the onset and offset temperatures for featured peaks, using the software package provided by the instrument manufacturer.

3.4.2 Mechanical properties

3.4.2.1 Density measurements

The density of the investigated samples was measured by the Archimedes method using distilled water as the immersion medium. The density was determined using the following equation:

$$\rho = \frac{m}{m - m_1}\rho_w, \tag{3.1}$$

where ρ is the density of the sample, m the weight in air, m_1 the weight in distilled water and ρ_w the density of distilled water.

3.4.2.2 Vickers hardness measurements

The Vickers hardness of the studied material was measured using a DuraScan microhardness tester. The measurements were performed under a load of 0.3 kg and repeated at least five times on the ground and polished surface to determine the effect of microstructure on material hardness.

3.4.2.3 Tensile testing measurements

The specimens for tensile testing were machined by wire electrical discharge machining (WEDM) from the studied material. The specimens with a gauge length of 10 mm and a cross-section area of 3×1 mm^2 are shown in Figure 3.7. Tensile testing was conducted by an Instron 5500R testing machine at a nominal strain rate of 2.5×10^{-4} s^{-1} at room temperature, according to ASTM E8/E8M-16a [7]. An extensometer was attached to the specimens to measure the strain during testing. The measurements were made at least three times for each condition to verify the reproducibility of the results. The fracture surfaces were investigated by SEM to determine the failure mechanism.

.

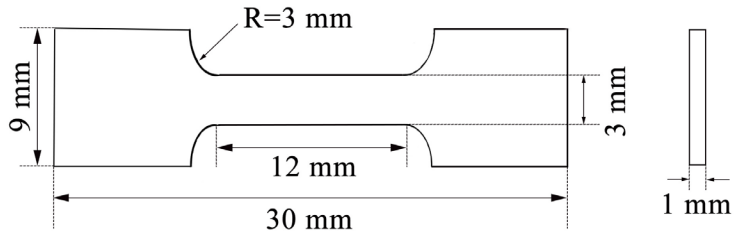


Figure 3.7 Dimensions of tensile samples.

References

[1] C. Suryanarayana, Mechanical alloying and milling, Prog. Mater. Sci. 46(1-2) (2001) 1-184.
[2] K. Euh, B. Arkhurst, I.H. Kim, H.-G. Kim, J.H. Kim, Stability of Y-Ti-O nanoparticles during laser deposition of oxide dispersion strengthened steel powder, Metals and Materials International 23(6) (2017) 1063-1074.
[3] J. Fu, J.C. Brouwer, I.M. Richardson, M.J.M. Hermans, Effect of mechanical alloying and spark plasma sintering on the microstructure and mechanical properties of ODS Eurofer, Mater. Des. 177 (2019) 107849.
[4] M.K. Miller, K.F. Russell, K. Thompson, R. Alvis, D.J. Larson, R. Anderson, S. Klepeis, J. Cairney, D. Saxey, D. Mcgrouther, Review of atom probe FIB-based specimen preparation methods, Microsc. Microanal. 13(6) (2007) 428-436.
[5] T.L. Martin, A.J. London, B. Jenkins, S.E. Hopkin, J.O. Douglas, P.D. Styman, P.A. Bagot, M.P. Moody, Comparing the consistency of atom probe tomography measurements of small-scale segregation and clustering between the LEAP 3000 and LEAP 5000 instruments, Microsc. Microanal. 23(2) (2017).
[6] J. Hyde, C. English, Symposium R: Microstructural Processes in Irradiated Materials, Mater. Res. Soc. Symp. Proc, 2000, p. R6.
[7] I. Astm, ASTM E8/E8M-16a: Standard Test Methods for Tension Testing of Metallic Materials, West Conshohocken, PA, USA: ASTM International (2016).

4

Fabrication of ODS Eurofer via mechanical alloying and spark plasma sintering[1]

[1] This chapter is based on the scientific paper:

J. Fu, J. Brouwer, I. Richardson, M. Hermans, Effect of mechanical alloying and spark plasma sintering on the microstructure and mechanical properties of ODS Eurofer, Mater. Des. 177 (2019) 107849.

4.1 Introduction

As mentioned in chapter 1, oxide dispersion strengthened (ODS) reduced activation ferritic/martensitic (RAFM) steels are promising high-performance structural materials for advanced fusion and fission reactors [1-6]. Compared to Eurofer 97, ODS Eurofer shows a pronounced increase in tensile strength, yield strength and creep strength from room temperature to high temperature up to 973 K [7, 8]. This behaviour is mainly attributed to the presence of the highly dispersed and extremely stable Y_2O_3 particles, which act as obstacles for the movement of dislocations and trapping sites for point defects induced by radiation displacement [9, 10].

A powder metallurgy route is generally applied to produce ODS steels, involving mechanical alloying (MA), consolidation techniques and thermal/mechanical treatments. To add oxides to the steel matrix, mechanical alloying (MA) is believed to be the most successful technique to obtain the ultrafine oxides with a high number density (10^{19}–10^{24} m^{-3}) [11]. The steel powder is blended with yttrium oxide powder in this solid-state processing technique involving repeated welding, fracturing and rewelding of powder particles in a high-energy ball mill [12]. Hot isostatic pressing (HIP) or hot extrusion (HE) are the commonly used techniques to consolidate the mechanically alloyed powders. However, anisotropic and textured grains and relatively high costs due to long hold times are detrimental to the adoption of these alloys [13, 14]. Therefore, an alternative and more cost-effective consolidation method is currently being explored. Spark Plasma Sintering (SPS), also known as Pulsed Electric Current Sintering (PECS) or Field Assisted Sintering Technology (FAST), is a sintering technique employing a pulsed direct electrical current and uniaxial pressure simultaneously to perform high speed consolidation of the powder [15]. This facilitates very high heating (up to 1000 K min^{-1}) and cooling rates (up to 150 K min^{-1}), hence enhancing densification but limiting grain growth, leading to a fully dense product with small grain size [16]. Spark plasma sintering offers many advantages over conventional consolidation techniques such as HIP and HE, including short processing time, ease of operation and the ability to control all stages of sintering [17, 18].

In recent years, MA and SPS have been employed to produce different types of ODS steels, however the application on ODS RAFM steels, especially ODS Eurofer is very limited. Sun *et al.* [19] fabricated Fe–9Cr–1.5W–0.45Mn–0.1Ta–0.2V–0.01Si–0.2Ti–0.3Y_2O_3–0.1/0.2C (wt.%) steels by MA and SPS. Chemical reduction was used to synthesise Fe–0.3Y_2O_3 powders and the tensile properties of the as-produced and annealed samples were studied. Poor elongations were obtained after tensile testing, indicating the brittle nature of the material. Xie *et al.* [20] reported the grain morphology and nano–particle characterisation of Fe–9Cr–1.5W–0.4Mn–0.2V–0.1Ta–0.3Ti–0.3Y_2O_3 (wt.%) prepared by MA and SPS. By proposing a yield strength model considering the contributions of solid solutes, grain size and nanoparticles, it was found that dispersion strengthening by $Y_2Ti_2O_7$ nanoparticles was the major strengthen mechanism in the material. Ukai [21] investigated phase transformations and the mechanical response of Fe–9Cr–2W–0.2Ti–0.35Y_2O_3–0.13C (wt.%) steel produced by MA and SPS. However, process optimisation was lacking in this study. To sum up, limited information is available in the literature concerning the microstructural evolution and mechanical behaviour

of MA and SPS prepared ODS Eurofer, in particular the relationship between microstructure, properties and processing conditions.

The aim of this study is to assess the potential of MA and SPS to fabricate ODS Eurofer engineered for high strength combined with reasonable ductility. Steel powders were milled and consolidated under various conditions. Processing parameters were optimised based on the effect on the microstructure and mechanical properties.

4.2 Experimental details

4.2.1 Materials and preparation

ODS Eurofer was produced via a powder metallurgy route, *i.e.* mechanical alloying and spark plasma sintering. Detailed processing parameters can be found in chapter 3. Different combinations of processing conditions (Table 4.1) were adopted to study their effect on the as-produced material and obtain the optimal processing condition.

Table 4.1 Processing conditions used for the powder metallurgy process.

	Milling time/h	Pressure/ MPa	Heating rate/(K/min)	Sintering temperature/K
A	0	50	100	1373
B	24	50	100	1373
C	30	50	100	1373
D	36	50	100	1373
E	30	40	100	1373
F	30	60	100	1373
G	30	80	100	1373
H	30	60	50	1373
I	30	60	200	1373
J	30	60	400	1373
K	30	60	100	1323
L	30	60	100	1423

4.2.2 Analysis methods

The powders with different milling times were characterised by scanning electron microscopy (SEM) and X-Ray diffraction (XRD). The crystallite size D and lattice strain ε of the powders after mechanical alloying were calculated from the XRD spectrum by the Williamson-Hall equation: [22]

$$\beta cos\theta = \frac{K\lambda}{D} + 4\varepsilon sin\theta, \tag{4.1}$$

where β is the full width at the half maximum height (FWHM), θ is the Bragg angle, K is the Scherrer constant taken as 0.9 [23], and λ is the X-Ray wavelength.

The as-produced specimens were prepared for microstructure characterisation by cutting across the centre of the sample and analysed by optical microscopy (OM), scanning electron microscopy (SEM) and energy dispersive X-ray spectroscopy (EDS). The content of carbon was determined with a LECO CS744.

4.2.3 Property tests

The densities of the produced disks were measured by the Archimedes method. Vickers microhardness was measured from the top surface to the bottom surface of the samples, with a load of 0.3 kg and a step size of 0.5 mm (Figure 4.1 (a)). The specimens for tensile testing were machined by wire electrical discharge machining (WEDM) according to Figure 4.1 (b). Specimens cut from the top to bottom were labelled from 1 to 7.

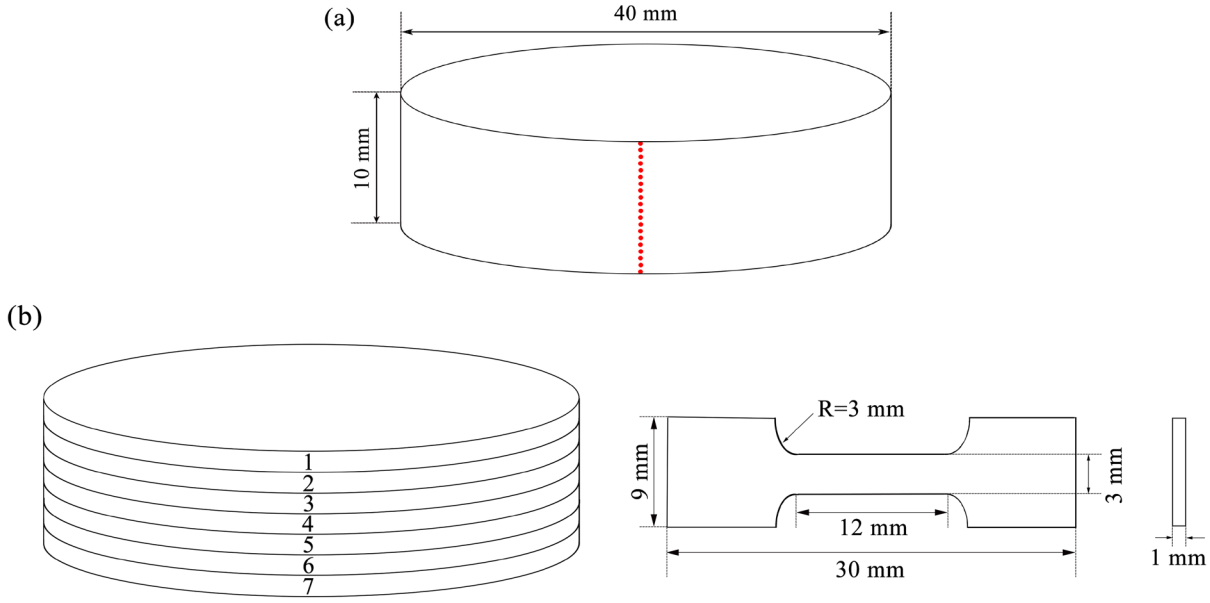


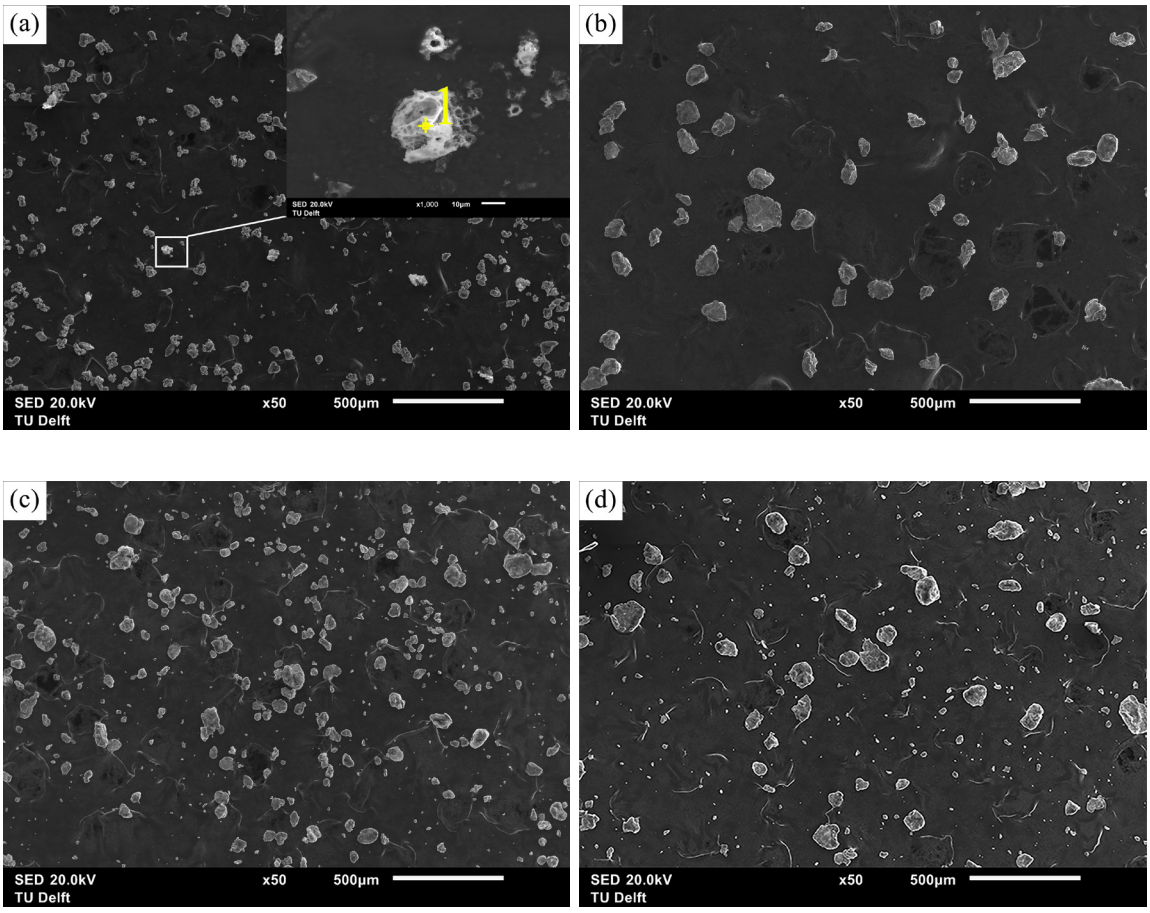
Figure 4.1. (a) the position of the hardness measurements and (b) the position, shape and dimensions of tensile samples.

4.3 Results and discussion

4.3.1 Effect of mechanical alloying time

Figure 4.2 presents the morphology and average size of the powders with different milling times investigated by SEM. It can be seen that the as-delivered powders have an irregular shape (Figure 4.2 (a)), while the particles after the ball milling show distorted shapes due to severe amount of deformation applied (Figure 4.2 (b)–(g)). Figure 4.2 (h) summarises the variation of the powder size as a function of milling time. Around 7600 particles were extracted and measured from the SEM images. It can be seen that the whole milling process can be divided into three stages: cold welding, fracturing and a steady-state stage [24]. In the cold welding stage (0–6 h), as the particles are relatively soft, they tend to weld together and generate large particles. This is the reason that the average diameter of the particles is increased after milling

for 6 h compared to the as-delivered powders. The particle size distribution at this stage is wide, with some particles three to five times larger than the initial size. After that, in the fracturing stage (12–18 h), the powders are fragmented by intense collision and the mean size of the particles is decreased significantly. Finally, in the steady-state stage (24–36 h), it can be seen that the morphology and mean size of the powders show no significant change. This indicates that a dynamic equilibrium is attained where a balance between the rate of welding and fracturing is achieved. A narrow range of particle sizes develops at this stage, as the particles smaller than the mean size are agglomerated at about the same rate as the particles larger than the mean size are reduced. The average size of the particles reaches a minimum of 10.7 ± 2.0 µm after milling for 30 h. After a milling time of 36 h, a slight raise in the particles size up to 11.7 µm can be seen, which may be caused by the agglomeration of the small sized particles.



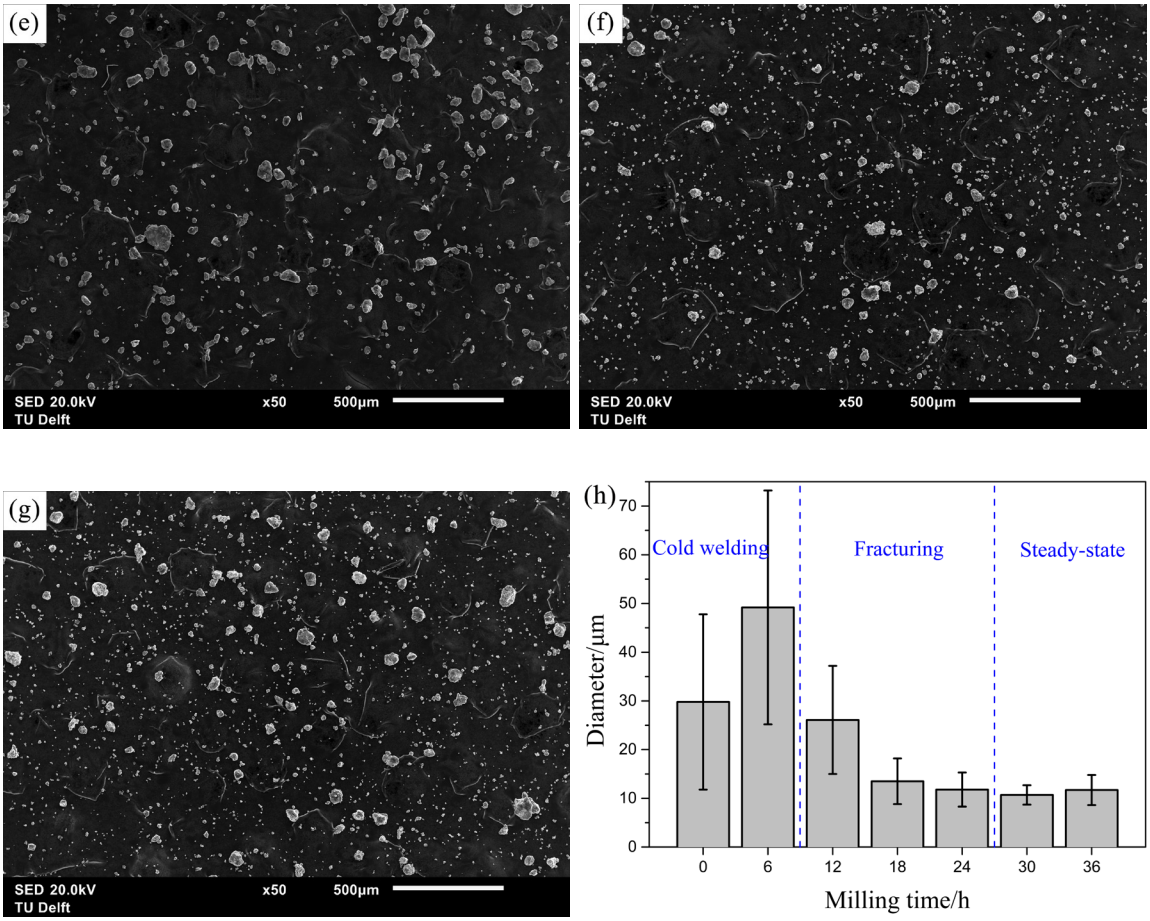


Figure 4.2. SEM micrographs of (a) the as-delivered powders and the powders milled for (b) 6 h, (c) 12 h, (d) 18 h, (e) 24 h, (f) 30 h, (g) 36 h and (h) the variation of the powder size as a function of milling time.

The XRD patterns of the mechanical alloyed powders are shown in Figure 4.3. Fe–Cr mixture and W diffraction peaks can be clearly observed. Some peaks corresponding to yttria are observed in the case of the as-delivered powders due to yttria particle clusters. For instance, an yttria cluster of around 20 µm is identified by EDS, shown in Figure 4.2 (a). It is notable that all of the yttria peaks are invisible when the powders have been milled for 6 h. This is probably due to the yttria clusters breaking up into nano-scale yttria particles during the mechanical alloying process [25]. The absence of the yttria peaks also indicates that they have been incorporated into the steel matrix. Moreover, peak broadening with increasing milling time can be observed from the spectrum, ascribed to the decrease in the crystallite size and the increase in the lattice strain according to Eq. (4.1). Figure 4.4 (a) shows an example of Williamson-Hall equation plot for the powders milled for 12 h. The estimated results of powders milled for different times are illustrated in Figure 4.4 (b). By increasing the milling time to 24 h, the crystallite size is decreased from 38 nm to 23 nm showing an obvious refinement effect, after which, it does not change significantly. Meanwhile, the lattice strain is increased to 0.2 % when the milling time is increased to 36 h, which indicates that the dislocation density in the particles has been increased remarkably due to mechanical alloying.

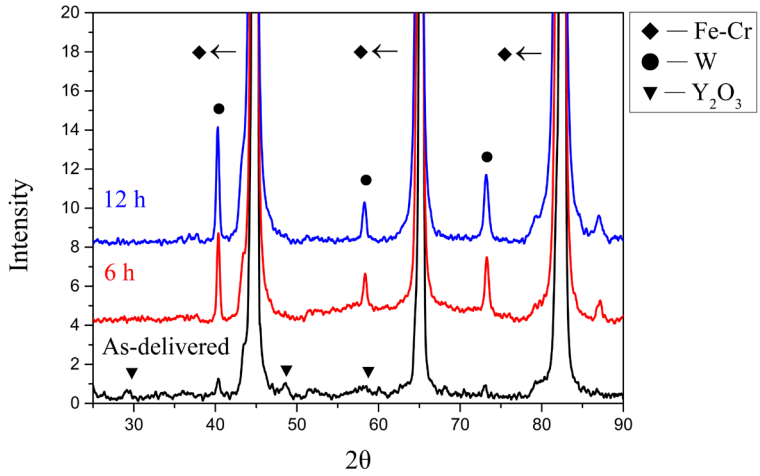


Figure 4.3. XRD patterns for mechanical alloyed powders.

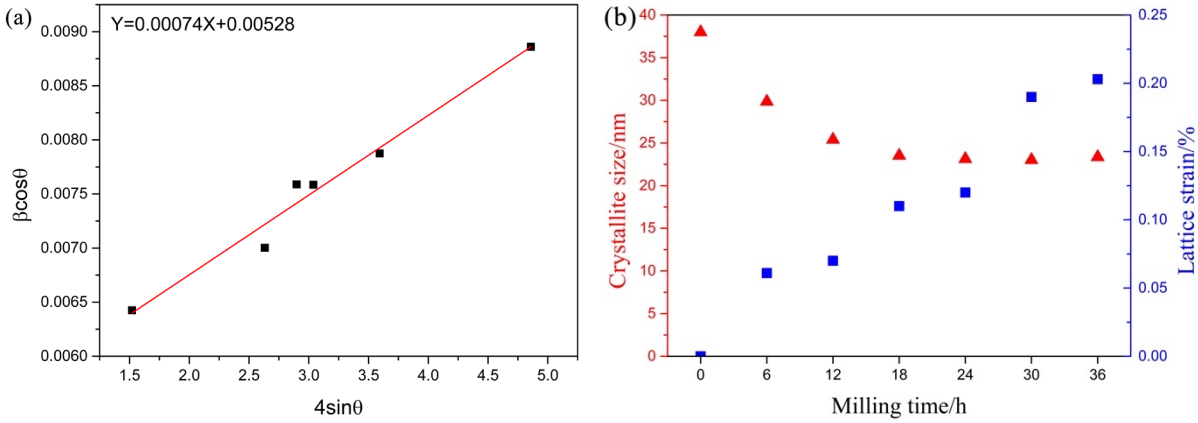


Figure 4.4. (a) Williamson-Hall equation plot for powders milled for 12 h. (b) crystallite size and lattice strain as a function of milling time.

A uniform stress deformation model (USDM) is used in order to estimate the deformation stress introduced by mechanical alloying [26]. In the USDM, the lattice deformation is assumed to be uniform in all the crystallographic directions. According to Hooke's law, $\sigma = E_{hkl}\varepsilon$, where σ is the stress of the crystal and E_{hkl} is the Young's modulus in the [hkl] direction. By using this approach, the Williamson-Hall equation (equation (4.1)) can be modified to

$$\beta cos\theta = \frac{K\lambda}{D} + \frac{4\sigma sin\theta}{E_{hkl}}, \qquad (4.2)$$

where E_{hkl} is given by

$$\frac{1}{E_{hkl}} = S_{11} - 2\left[(S_{11} - S_{12}) - \frac{1}{2}S_{44}\right](\alpha^2\beta^2 + \alpha^2\gamma^2 + \beta^2\gamma^2), \qquad (4.3)$$

S_{11}, S_{12} and S_{44} are components of the compliance tensor and their estimated values for iron are 7.57×10^{-12}, -2.8×10^{-12} and 8.6×10^{-12} Pa^{-1}, respectively [27]; α, β, and γ are the direction cosines of the [hkl] direction and the [100], [010], and [001] directions, respectively.

By plotting βcosθ on the y-axis and $4\sin\theta/E_{hkl}$ on the x-axis, the deformation stress can be estimated based on the slope of the fitting line. The results of deformation stress as a function of milling time are presented in Figure 4.5. It can be clearly seen that the deformation stress increases with the milling time. The stress within the particles accumulates because of the intense collision between the powders and balls. The increasing deformation stress indicates that the powders were crushed continuously during the intensive milling process.

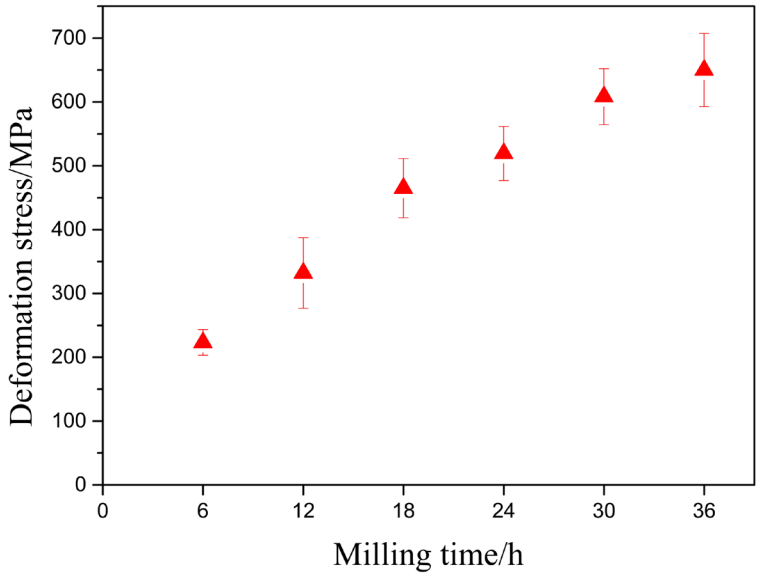


Figure 4.5. Deformation stress as a function of milling time

Figure 4.6 shows the EDS map scanning results of single particles taken from batches milled for 6 h, 18 h and 30 h. Only Fe and Cr are presented here as they account for approximately 98 % of the ingredients of ODS Eurofer. From the results, it can be observed that Fe and Cr started to blend after milling for 6 h (Figure 4.6 (a)–(c)). However, the chemical composition presented in Table 4.2 indicates a large deviation from the targeted composition, although it should be emphasised that the presented composition is based on the characterisation of a single powder particle. After milling for 18 h, although the deviation of the chemical composition has been partially eliminated, Fe and Cr still did not blend very well. For instance, the left-hand side of the particle is rich in Cr, while the right-hand side shows the absence of Cr (Figure 4.6 (d)–(f)). After milling for 30 h, it appears that Fe and Cr were homogenously distributed in the powder due to repeated welding and fracturing (Figure 4.6 (g)–(i)). The chemical composition is very close to the intended composition, showing a sufficient blending.

In conclusion, the effect of mechanical alloying is not only refinement of the (grain) size of the powders and introduction of high deformation stresses and a high dislocation density, but also the homogenous incorporation of the alloying elements into the steel matrix [28]. Considering the above findings, we can conclude that milling for more than 18 h is required to

obtain refined powders with a homogeneously distributed composition, which is favourable for the following SPS process.

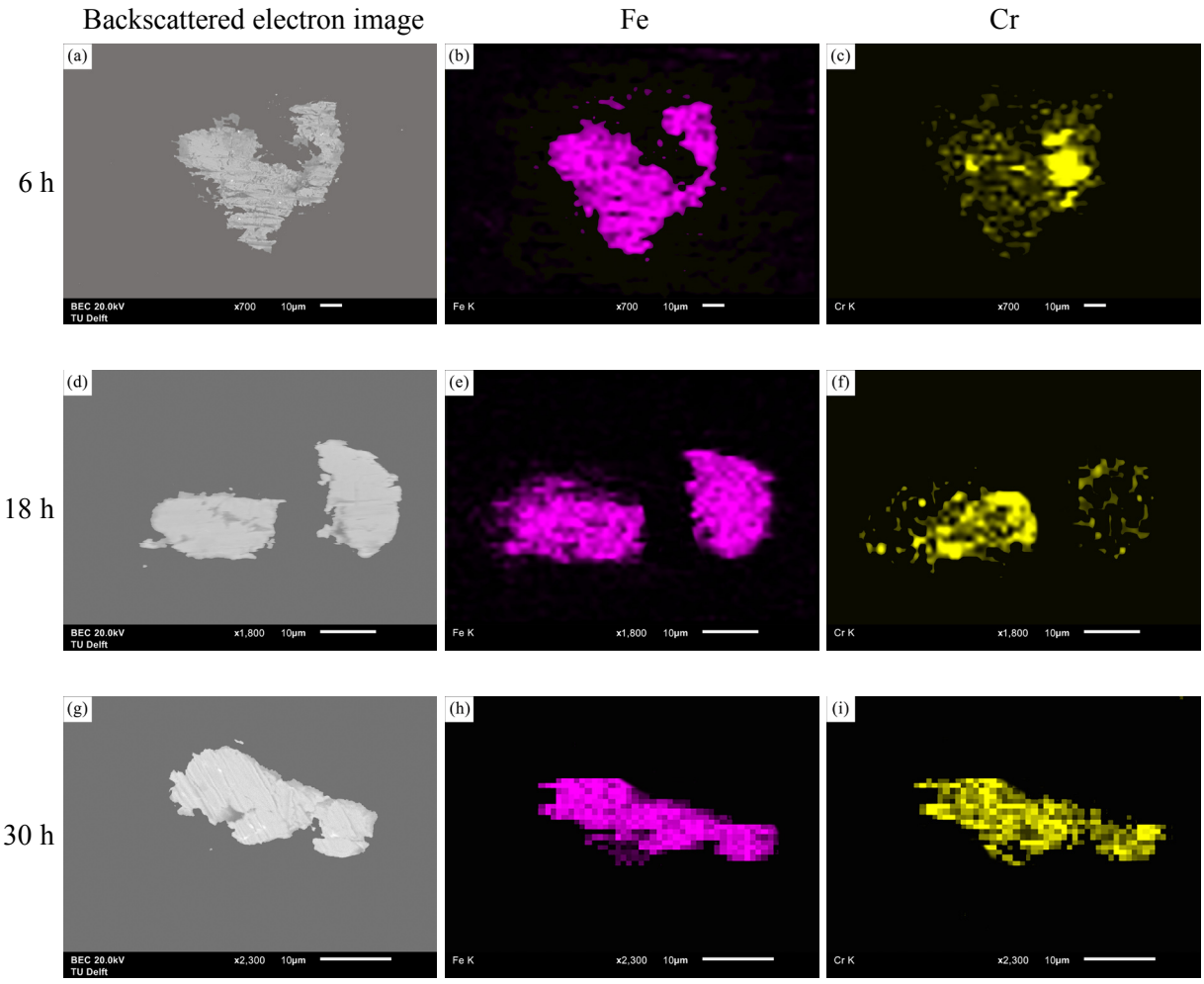


Figure 4.6. EDS map scanning result of cross section of one powder particle milled for 6, 18 and 30 h. (a), (d) and (g) backscattered electron image; (b), (e) and (h) distribution map of Fe; (c), (f) and (i) distribution map of Cr.

Table 4.2 Chemical composition of one powder particle for 6, 18 and 30 h obtained from EDS.

Elements (wt./%)	Cr	W	Mn	Y	V	Ta	Fe
Targeted	9.00	1.10	0.40	0.24	0.20	0.12	88.78
6 h	2.56	1.55	0.72	0.79	0.28	–	94.00
18 h	6.75	1.24	0.54	0.37	0.26	1.40	89.34
30 h	8.54	1.05	0.37	0.22	0.20	0.89	88.63

4.3.2 Effect of spark plasma sintering

Based on the previous results, the powders milled for 24 h, 30 h and 36 h were chosen as the raw material for SPS to produce bulk steels. A specimen prepared from the as-delivered

powders was used as a reference. The temperature of SPS is the first parameter to be determined because it is crucial for the efficiency of the sintering process. Taking the powders milled for 30 h as an example (sample K in Table 3.2), at sintering temperature of 1323 K (with a heating rate of 100 K/min and a pressure of 60 MPa), large pores in the microstructure are visible (Figure 4.7 (a)) suggesting limited sintering. When the sintering temperature was increased to 1373 K (sample F in Table 3.2), almost all pores were eliminated indicating the powders were sintered more efficiently (Figure 4.7 (b)). Local melting occurred when the temperature was increased to 1423 K (sample L in Table 3.2), revealing that the maximum applicable process temperature was exceeded. Thus, it appears that 1373 K is a suitable sintering temperature for the SPS process of ODS Eurofer.

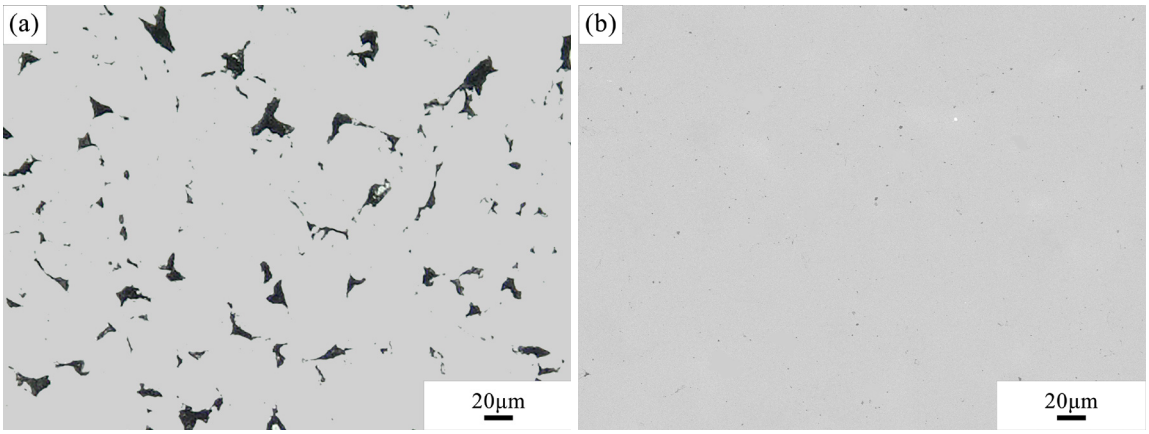


Figure 4.7. Optical micrographs of SPS prepared samples: (a) milled 30 h SPS at 1323 K and (b) milled 30 h SPS at 1373 K.

The EDS mapping results of the SPS prepared samples (sintered at 1373 K) are shown in Figure 4.8. It can be clearly seen that without ball milling, Fe and Cr are non-uniformly distributed due to lack of blending of the powders (Figure 4.8 (a)–(c)). Large cavities can be seen in the microstructure due to the size difference of the initial powders. Table 4.3 gives information about the chemical composition. The chromium content of the scanned area (180×240 µm^2) is 32.24 %, which is significantly higher than that of the targeted composition, indicating that homogenisation has not taken place. After 24 h of ball milling, some of the powders blended together, but there was still an uneven distribution in some areas as indicated in the white frames in Figure 4.8 (e) and (f). A small deviation of the chemical composition from the intended average composition still exists, showing insufficient blending. After 30 h and 36 h of milling, Fe and Cr blended well and became homogeneously distributed (Figure 4.8 (g)–(l)). Moreover, in both cases, the chemical compositions of the scanned areas are in good agreement with that of the targeted composition. Therefore, it can be concluded that a sufficient and efficient mechanical alloying is of importance to accomplish homogeneous and consistent chemical composition of ODS Eurofer, which is crucial to ensure the reproducibility required for the intended nuclear applications.

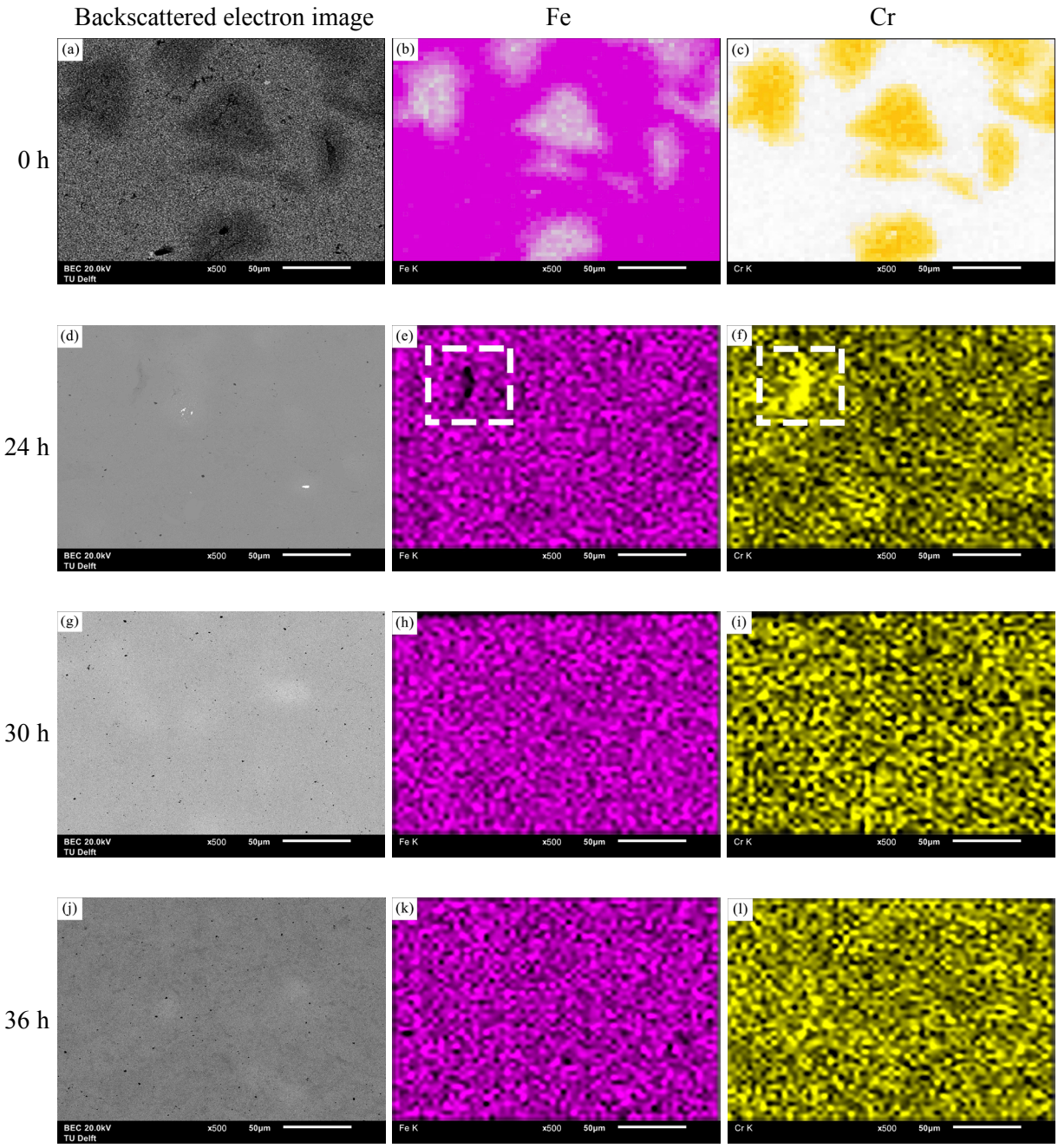


Figure 4.8. EDS map scanning result of the sample produced by milling for 0 h, 24 h, 30 h and 36 h and SPS at 1373 K. (a), (d), (g) and (j) backscattered electron image; (b), (e), (h) and (k) distribution map of Fe; (c), (f), (i) and (l) distribution map of Cr. The inserted dashed rectangles indicate areas with uneven distributions of elements.

Table 4.3 Chemical composition of the sample produced by milling for 0 h, 24 h, 30 h and 36 h and SPS at 1373 K obtained from EDS.

Elements (wt./%)	Cr	W	Mn	Y	V	Ta	Fe
Targeted	9.00	1.10	0.40	0.24	0.20	0.12	88.78
0 h	32.24	0.28	0.65	0.13	0.02	0.49	66.09
24 h	9.96	0.92	0.46	0.28	0.15	–	88.13
30 h	9.19	1.11	0.33	0.19	0.20	0.16	88.72
36 h	8.72	1.18	0.72	0.29	0.24	0.18	88.57

The milled powders were sintered at different pressures combined with different heating rates as indicated in Table 3.2. The density of the bulk steel was evaluated in order to find the optimal processing parameters to produce the bulk steel with the best properties. Figure 4.9 presents the density of the samples (sintered at 1373 K) under different processing conditions. From A, B, C and D, one can observe that the sample milled for 30 h (sample C) has the highest density. This can be attributed to two factors; compared to the samples milled for 0 h and 24 h, the elements were distributed more homogenously and the Y_2O_3 was introduced into the matrix of the base powder after sufficient ball milling, resulting in a harder material. In addition, the average size of the powders milled for 30 h is finest compared to the other conditions. This will cause the generation of fewer and smaller pores between the powders or grains. In addition, according to Diouf and Molinari [28], the sintered material "remembers" the size of the starting powder. Smaller particles tend to form smaller grains, leading to a higher density and probably a higher microhardness based on an extrapolation of the Hall-Petch relationship.

From C, E, F and G in Figure 4.9, it can be seen that the density of the SPS prepared samples increases with the applied pressure up to 60 MPa. The relative density reaches 99.2 % considering the theoretical density for ODS Fe–9Cr steels is 7.82 g/cm^3 [29], revealing a highly compacted bulk steel. When the pressure was further increased to 80 MPa, the density shows no significant change, indicating the best possible properties have been obtained. The role of pressure in SPS is not only to rearrange the particles and break up the agglomerates, but also to provide an extra driving force for densification [19]. With higher pressure applied, the particles are sintered more efficiently, resulting in limited grain growth and less porosity.

The densities of samples processed with different heating rates are exhibited in F, H, I and J in Figure 4.9. A density of 98.0 % at the heating rate of 50 K/min shows a limited sintering during SPS. With a heating rate of 100 K/min, the density was significantly increased. This may be due to a higher electric current density passing through the powders, leading to the generation of higher Joule heat and an improved sintering [30]. Further increase of the heating rate above 100 K/min does not have an obvious effect on the final properties. The processing condition F is therefore determined as the optimum condition for the production of ODS Eurofer.

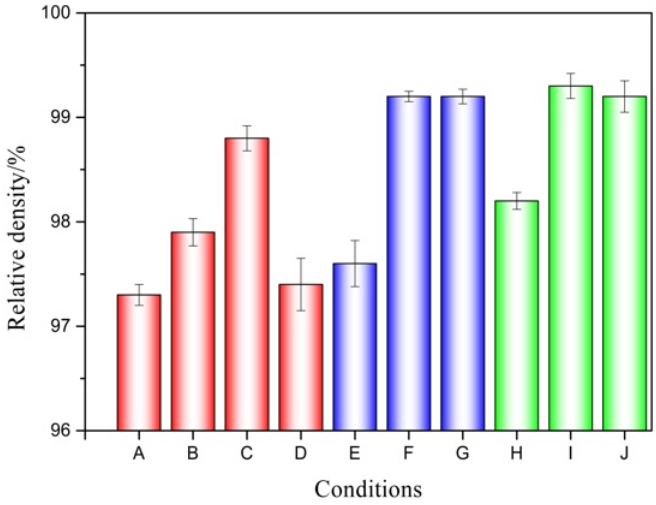


Figure 4.9. Relative density of as-sintered samples in various processing conditions. A, B, C and D were milled for 0 h, 24 h, 30 h and 36 h, respectively, pressed at 50 MPa, sintered with heat rate at 100 K/min. E, F and G were milled for 30 h, pressed at 40 MPa, 60 MPa and 80 MPa, respectively, sintered with heat rate at 100 K/min. H, I and J were milled for 30 h, pressed at 60 MPa, sintered with heating rates at 50 K/min, 200 K/min and 400 K/min, respectively.

4.3.3 Microstructure characterisation

An optical micrograph of the as-produced steel (condition F in Figure 4.9) can be seen in Figure 4.10. Martensite (dark regions) and residual δ-ferrite (white regions) are revealed in the microstructure. The martensitic microstructure of the as-produced steel is probably due to sintering at a high temperature of 1373 K, above Ac1 (around 1096 K), hence martensite is formed during the cooling process. The residual ferrite formation is related to a competition between the pinning force of oxide particles on the δ-ferrite/γ-austenite interface movement and the driving force for the δ–γ transformation.

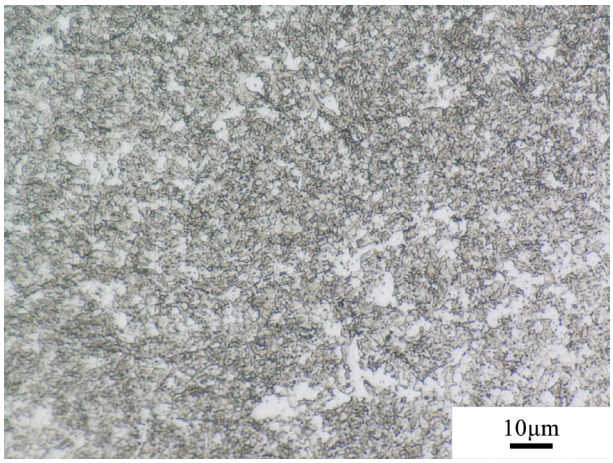


Figure 4.10. Optical micrographs of the as-produced steel (condition F).

The morphology of as-produced sample (condition F) was observed by SEM and is shown in Figure 4.11. It is found that a mixed microstructure with ultrafine grains (UFG, ~200 nm) and coarse grains (CG, ~5 μm) is formed in the as-produced alloy (Figure 4.11 (a)). This feature can also be described as a core-shell microstructure, where the UFG zone acts as the core and the CG zone acts as the shell. Bimodal grain size distributions were also reported in other studies on ODS steels produced by powder metallurgy [20, 31-33]. This microstructure is usually attributed to the milling process: 1) As the nanometre scale Y_2O_3 precipitates tend to impede grain growth through a Zener-type pinning effect on subgrain boundaries [31], the formation of fine grains is presumably due to the resistance to recovery and growth in the regions with a higher density of nanoprecipitates [32]. 2) Heterogenous recrystallisation due to unevenly stored energy after milling, causes rapid growth of some grains at the expense of their more deformed neighbours [33]. In some studies, the SPS process was also seen as one of the causes of the bimodal microstructure [20]. In SPS, electric current passes more easily along the particle surfaces than through the cores due to a lower electrical resistance. The temperature distribution in the powder particles is heterogeneous as the Joule heating is more intensive in the area of sintering necks. The grains in these areas will grow to a larger size due to the higher temperature. Meanwhile, the grains inside the severely deformed powders will recrystallise and form ultrafine grains [34]. All of these factors might contribute to the bimodal nature of the microstructure.

As indicated in the red circle in Figure 4.11 (b), coarse precipitates with sizes of 50–200 nm were found in the microstructure. The chemical composition of the precipitates was determined by EDS, as shown in Table 4.4. They are identified to be $M_{23}C_6$ carbides (M = Fe, Cr, W) based on their size and chemical composition. In addition, it was observed that a large number of precipitates with sizes around 10 nm were present in the as-produced alloy, shown in the blue circle. They are assumed to be Y_2O_3-rich nano-particles, based on their size and density in the matrix. Characterisation of $M_{23}C_6$ and Y_2O_3 precipitates will be addressed in detail in the next chapter.

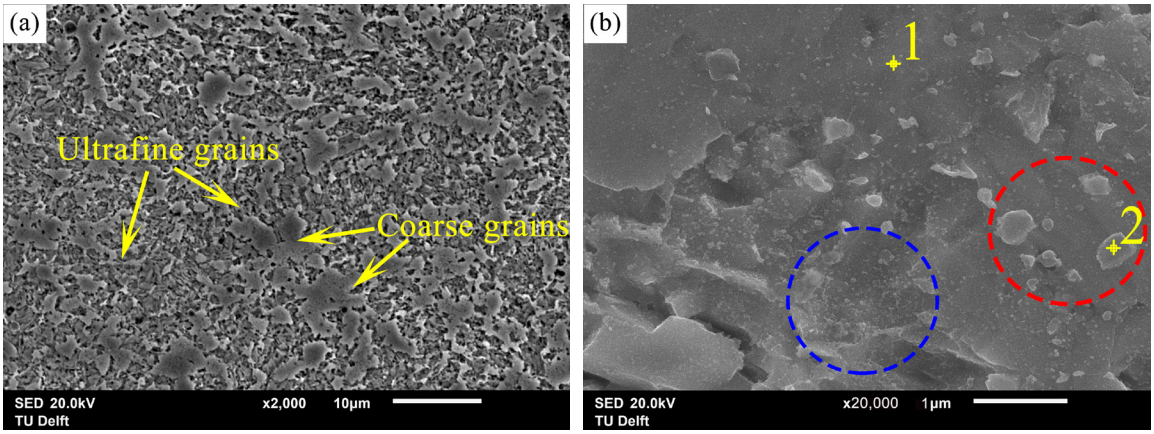


Figure 4.11. SEM morphology of etched as-produced sample F. The inserted circles indicate the locations of precipitates.

Table 4.4 Chemical composition of the points indicated in Figure 4.11 (b).

Elements (wt./%)	Cr	W	Mn	Y	V	Ta	C	Fe
Point 1	9.65	1.01	0.28	0.12	0.05	0.43	0.56	87.8
Point 2	30.65	4.38	0.10	–	–	–	1.59	63.18.

4.3.4 Mechanical properties

Figure 4.12 shows the Vickers hardness profile of a cross section of the as-produced sample F in Figure 4.9, with the maximum value at the top and bottom surfaces and minimum in the centre. This can be ascribed to two reasons: 1) different cooling rates in the surface and the core of the material during SPS and 2) an inhomogeneous distribution of carbon in the as-produced sample. The carbon in the graphite mould diffused into the sample during SPS even though boron nitride spray was used to reduce the diffusion. As a result, compared to the middle area of the sample, the carbon content in the surface area is higher, leading to the formation of a larger number of carbides. As the $M_{23}C_6$ carbides have a strong pinning effect on the migration of dislocations and subgrains, the top and bottom surfaces will have a higher hardness.

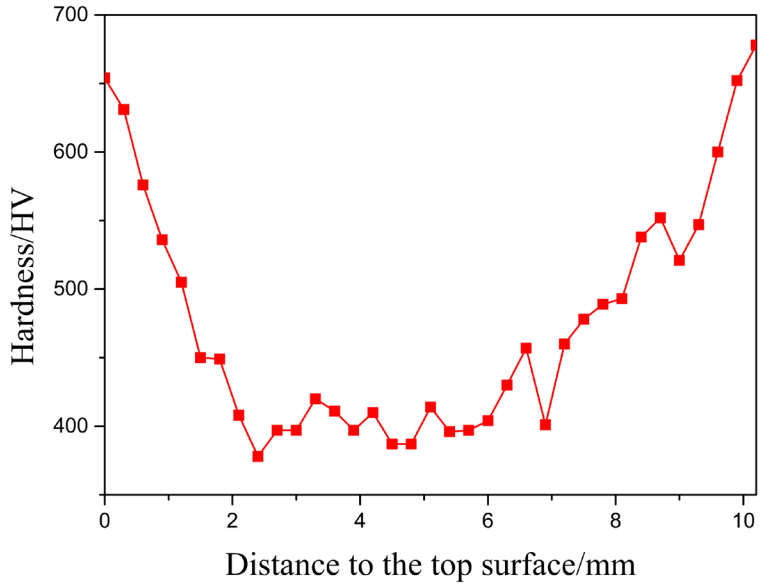


Figure 4.12. Vickers hardness profile of the cross section of the as-produced sample.

The tensile properties of the as-produced sample F at different locations indicated in Figure 4.1 (b) are presented in Figure 4.13. It can be seen that higher tensile strength and yield strength were found in the specimens close to the surface area, associate with a harder material. In addition, the elongations of specimen 1 and 7 (surface area) are 3.02% and 3.95%, respectively, while that of specimen 4 (core area) is as high as 9.85%, indicating a more ductile material in the centre and inhomogeneous properties in the as-produced specimen.

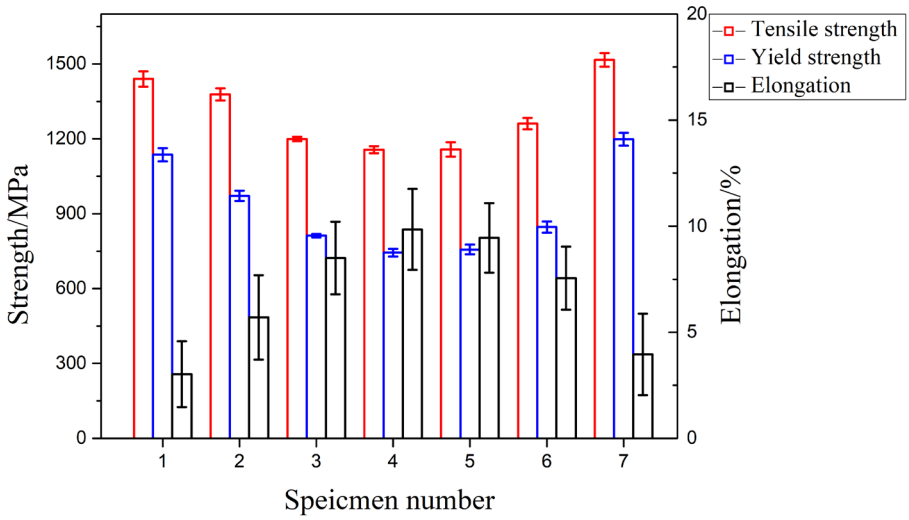
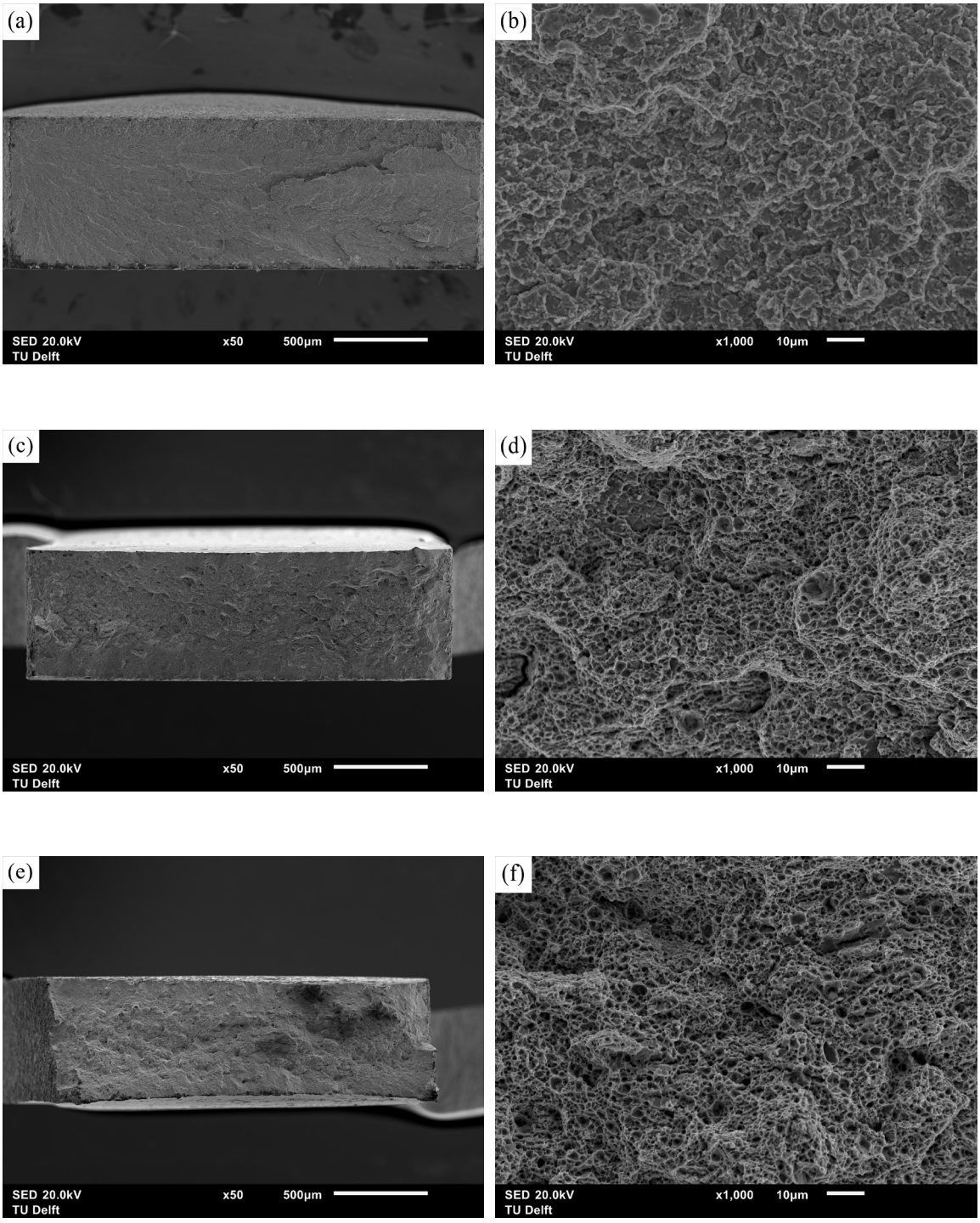
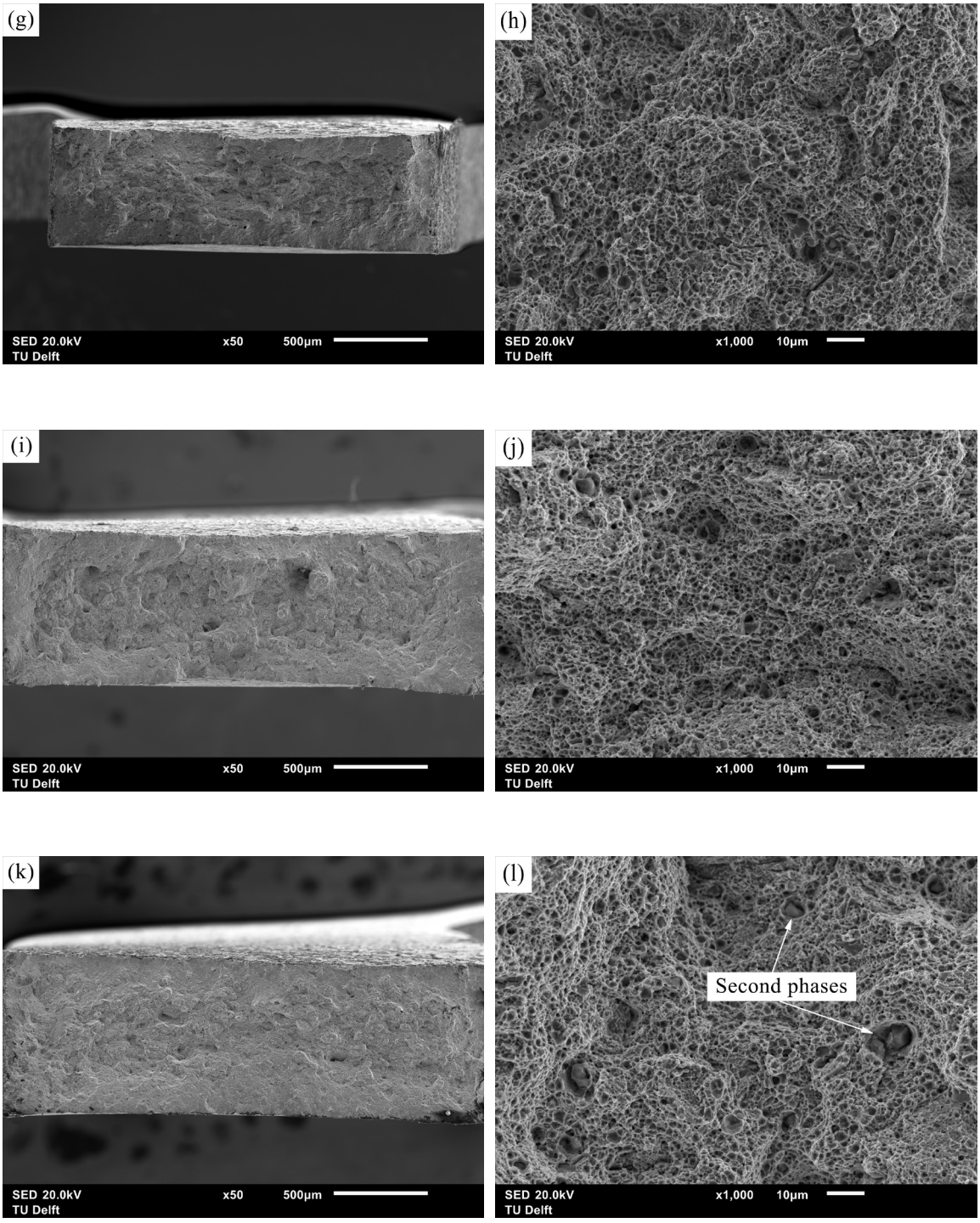


Figure 4.13. Ultimate tensile strength, yield strength and elongation of the as-produced sample F at the location indicated in Figure 4.1 (b).

Fractographic examinations were performed on the fracture surfaces from tensile testing by SEM to understand the failure mechanisms (Figure 4.14). The area reduction of each sample was measured and is presented in Figure 4.15. It can be seen that sample 1 and 7 exhibit an intergranular fracture mode. Failure occurred perpendicular to the direction of the tensile force applied, with virtually no necking. The area reduction of sample 1 and 7 are 2.6 % and 3.0 %, respectively. In contrast, the other samples show a typical ductile fracture mode with numerous dimple features. The area reduction is significantly increased compared to sample 1 and 7. For instance, the area reduction of sample 4 is 37.1 %, suggesting significant necking and a more ductile fracture. At higher magnification, coarse second phase particles (approximately 8 µm) were observed inside the dimples (Figure 4.14(l)). These particles are rich in Fe, Cr, W and C, confirmed by EDS analysis. Second phase particles are known to promote void nucleation, growth and coalescence, which facilitate crack initiation and propagation and reduce the ductility.

Combustion analyse were performed to characterise the carbon content of the tensile specimens more accurately. The results are shown in Figure 4.15. It can be seen that the carbon content of specimen 1 and 7 are 0.18 % and 0.15 %, respectively, much higher than that of the specimen in the middle section, which is 0.04 %. A higher content of carbon causes not only a strength increment but also a reduction in elongation, as carbides in chromium containing steel usually act as preferential sites for cavity nucleation due to stress concentration [35]. Reduced ductility and elongation will therefore be obtained before rupture. The thickness of the carbon diffusion zone in the sintered sample depends on the diffusivity of carbon in the material and sintering temperature. For instance, as described in Ref. [36], only a thin layer of titanium carbide—10 µm thick—formed on a flat surface of a metallic titanium plate treated in the SPS for 1 h with carbon powder poured into the sintering die. In our study, however, it seems that the whole sample was affected by carbon diffusion, although no carbon was added to the precursor powders before mechanical alloying.


(a)
SED 20.0kV
TU Delft
x50
500µm
(b)
SED 20.0kV
TU Delft
x1,000
10µm
(c)
SED 20.0kV
TU Delft
x50
500µm
(d)
SED 20.0kV
TU Delft
x1,000
10µm
(e)
SED 20.0kV
TU Delft
x50
500µm
(f)
SED 20.0kV
TU Delft
x1,000
10µm


(g)
SED 20.0kV
TU Delft
x50
500µm
(h)
SED 20.0kV
TU Delft
x1,000
10µm
(i)
SED 20.0kV
TU Delft
x50
500µm
(j)
SED 20.0kV
TU Delft
x1,000
10µm
(k)
SED 20.0kV
TU Delft
x50
500µm
(l)
Second phases
SED 20.0kV
TU Delft
x1,000
10µm

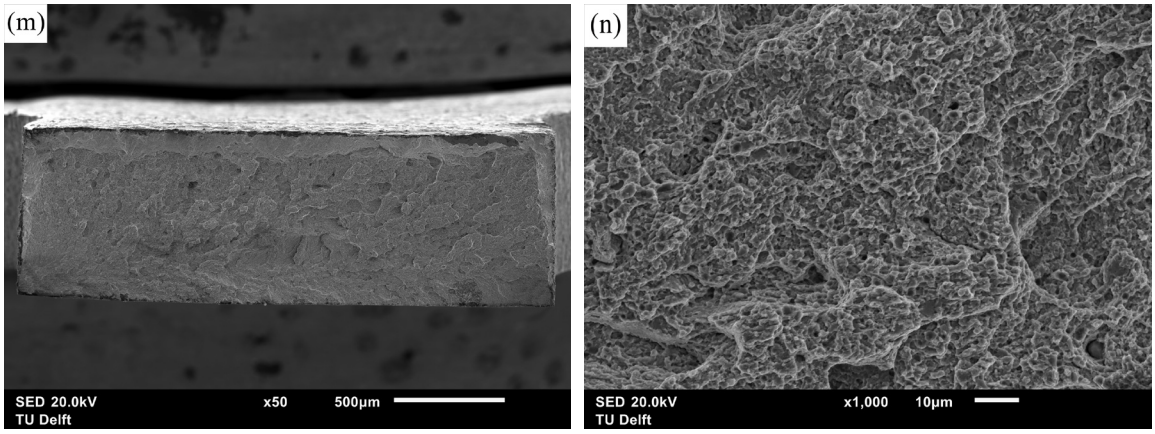


Figure 4.14. SEM micrographs of fracture surfaces of SPS prepared samples after tensile testing. As-produced sample 1: (a) and (b), sample 2: (c) and (d), sample 3: (e) and (f), sample 4: (g) and (h), sample 5: (i) and (j), sample 6: (k) and (l) and sample 7: (m) and (n).

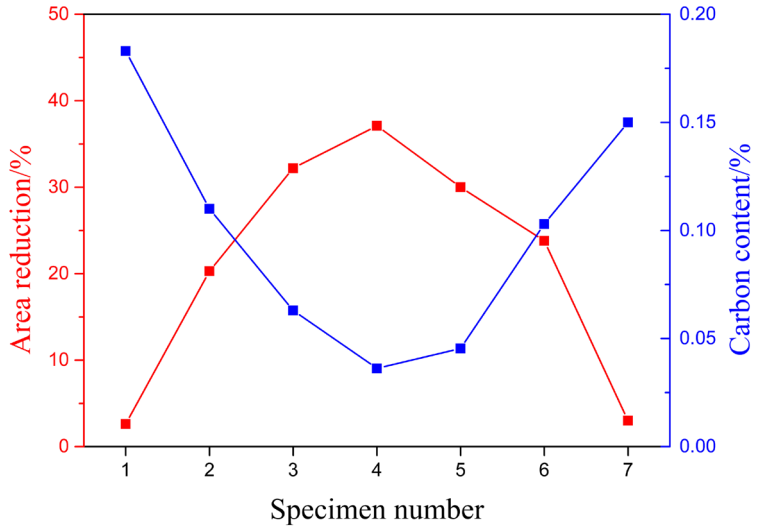


Figure 4.15. Area reduction and carbon content of the as-produced sample

Based on the above findings, it can be seen that ODS Eurofer produced via mechanical alloying and spark plasma sintering shows a high strength and reasonable ductility. However, the homogeneity of the microstructure and mechanical properties needs to be improved by a subsequent heat treatment. It is known that heat treatment is a necessary step to control the properties of the final material, such as microhardness, strength and ductility. It is notable that the mechanical properties of powder metallurgy prepared components are determined by many factors. The powder size and composition as well as processing parameters used are important to the quality of the final part, but heat treatment offers a way to control the final properties more accurately. In addition, for dual phase steels like ODS Eurofer, the application of a heat treatment is crucial to obtain a desired microstructure of martensite and ferrite through phase transformations. The effect of heat treatment on the microstructure and mechanical properties of as-produced ODS Eurofer will be addressed in detail in the next chapter.

4.4 Conclusions

ODS Eurofer was produced by mechanical alloying and spark plasma sintering. The influence of MA and SPS parameters on the microstructure and mechanical properties was studied in detail. The following conclusions are drawn:

1. Mechanical alloying is a necessary step in the process chain to achieve consistent and reproducible microstructures of ODS Eurofer. The lattice strain and deformation stress in the powders increase with the milling time, indicating a continuous refinement during the intensive milling process. After 30 h of milling, the powders have a minimum average size (approximately 10.7 μm) and a homogeneous chemical composition.

2. The powder size, sintering temperature, pressure and heating rate play an important role in the relative density of the produced steel. SPS prepared ODS Eurofer steel shows the highest density when milled for 30 h, sintered at 1373 K with a heating rate of 100 K min^{-1} at a pressure of 60 MPa.

3. The morphology of SPS prepared ODS Eurofer displays a dual phase and bimodal microstructure with coarse grains and ultrafine grains. Coarse $M_{23}C_6$ carbides are found to be present in the microstructure. A high density of nanosized Y_2O_3 is dispersed in the steel matrix.

4. The top and bottom surfaces of the as-produced sample present a higher microhardness and tensile strength and a lower elongation associated with a higher carbon content. Fracture analysis shows an intergranular fracture mode in the surface region and a ductile failure mode with well-defined dimples in the middle region. Spark plasma sintering in combination with MA is a very promising technique to produce ODS Eurofer with good mechanical properties.

References

[1] T. Gräning, M. Rieth, J. Hoffmann, A. Möslang, Production, microstructure and mechanical properties of two different austenitic ODS steels, J. Nucl. Mater. 487 (2017) 348-361.

[2] Y. Yano, T. Tanno, H. Oka, S. Ohtsuka, T. Inoue, S. Kato, T. Furukawa, T. Uwaba, T. Kaito, S. Ukai, Ultra-high temperature tensile properties of ODS steel claddings under severe accident conditions, J. Nucl. Mater. 487 (2017) 229-237.

[3] L. Zhang, L. Yu, Y. Liu, C. Liu, H. Li, J. Wu, Influence of Zr addition on the microstructures and mechanical properties of 14Cr ODS steels, Mater. Sci. Eng., A 695 (2017) 66-73.

[4] R. Lindau, A. Möslang, M. Rieth, M. Klimiankou, E. Materna-Morris, A. Alamo, A.-A. Tavassoli, C. Cayron, A.-M. Lancha, P. Fernandez, Present development status of EUROFER and ODS-EUROFER for application in blanket concepts, Fusion Eng. Des. 75 (2005) 989-996.

[5] H. Dong, L. Yu, Y. Liu, C. Liu, H. Li, J. Wu, Effect of hafnium addition on the microstructure and tensile properties of aluminum added high-Cr ODS steels, J. Alloys Compd. 702 (2017) 538-545.

[6] M. Klimenkov, R. Lindau, U. Jäntsch, A. Möslang, Effect of irradiation temperature on microstructure of ferritic-martensitic ODS steel, J. Nucl. Mater. 493 (2017) 426-435.

[7] R. Lindau, A. Möslang, M. Schirra, P. Schlossmacher, M. Klimenkov, Mechanical and microstructural properties of a hipped RAFM ODS-steel, J. Nucl. Mater. 307 (2002) 769-772.

[8] R. Schaeublin, T. Leguey, P. Spätig, N. Baluc, M. Victoria, Microstructure and mechanical properties of two ODS ferritic/martensitic steels, J. Nucl. Mater. 307 (2002) 778-782.
[9] J. Shen, H. Yang, Y. Li, S. Kano, Y. Matsukawa, Y. Satoh, H. Abe, Microstructural stability of an as-fabricated 12Cr-ODS steel under elevated-temperature annealing, J. Alloys Compd. 695 (2017) 1946-1955.
[10] R. Gao, B. Cheng, L. Zeng, S. Miao, J. Hou, T. Zhang, X. Wang, Q. Fang, C. Liu, Microstructure, hardness and defect structure of the He irradiated ODS ferritic steel, J. Alloys Compd. 691 (2017) 653-658.
[11] Q.X. Sun, Y. Zhou, Q.F. Fang, R. Gao, T. Zhang, X.P. Wang, Development of 9Cr-ODS ferritic-martensitic steel prepared by chemical reduction and mechanical milling, J. Alloys Compd. 598 (2014) 243-247.
[12] C. Suryanarayana, Mechanical alloying and milling, Prog. Mater. Sci. 46(1-2) (2001) 1-184.
[13] P. Miao, G. Odette, T. Yamamoto, M. Alinger, D. Hoelzer, D. Gragg, Effects of consolidation temperature, strength and microstructure on fracture toughness of nanostructured ferritic alloys, J. Nucl. Mater. 367 (2007) 208-212.
[14] Y. Li, J. Shen, F. Li, H. Yang, S. Kano, Y. Matsukawa, Y. Satoh, H. Fu, H. Abe, T. Muroga, Effects of fabrication processing on the microstructure and mechanical properties of oxide dispersion strengthening steels, Mater. Sci. Eng., A 654 (2016) 203-212.
[15] O. Guillon, J. Gonzalez-Julian, B. Dargatz, T. Kessel, G. Schierning, J. Räthel, M. Herrmann, Field-assisted sintering technology/spark plasma sintering: mechanisms, materials, and technology developments, Adv. Eng. Mater. 16(7) (2014) 830-849.
[16] M. Suárez, A. Fernández-Camacho, J.L. Menéndez, R. Torrecillas, Challenges and opportunities for spark plasma sintering: a key technology for a new generation of materials, InTech2013.
[17] C. Zhang, A. Kimura, R. Kasada, J. Jang, H. Kishimoto, Y. Yang, Characterization of the oxide particles in Al-added high-Cr ODS ferritic steels, J. Nucl. Mater. 417(1-3) (2011) 221-224.
[18] Z. Munir, U. Anselmi-Tamburini, M. Ohyanagi, The effect of electric field and pressure on the synthesis and consolidation of materials: A review of the spark plasma sintering method, J. Mater. Sci. 41(3) (2006) 763-777.
[19] Q. Sun, Y. Zhou, Q. Fang, R. Gao, T. Zhang, X. Wang, Development of 9Cr-ODS ferritic–martensitic steel prepared by chemical reduction and mechanical milling, J. Alloys Compd. 598 (2014) 243-247.
[20] R. Xie, Z. Lu, C. Lu, Z. Li, X. Ding, C. Liu, Microstructures and mechanical properties of 9Cr oxide dispersion strengthened steel produced by spark plasma sintering, Fusion Eng. Des. 115 (2017) 67-73.
[21] S. Ukai, Microstructure and High-Temperature Strength of 9CrODS Ferritic Steel, Metal, ceramic and polymeric composites for various uses, InTech2011.
[22] G. Williamson, W. Hall, X-ray line broadening from filed aluminium and wolfram, Acta Metall. 1(1) (1953) 22-31.

[23] Y. Kimura, S. Takaki, S. Suejima, R. Uemori, H. Tamehiro, Ultra grain refining and decomposition of oxide during super-heavy deformation in oxide dispersion ferritic stainless steel powder, ISIJ Int. 39(2) (1999) 176-182.
[24] P.-Y. Lee, J.-L. Yang, H.-M. Lin, Amorphization behaviour in mechanically alloyed Ni—Ta powders, J. Mater. Sci. 33(1) (1998) 235-239.
[25] A. Ramar, Z. Oksiuta, N. Baluc, R. Schäublin, Effect of mechanical alloying on the mechanical and microstructural properties of ODS EUROFER 97, Fusion Eng. Des. 82(15-24) (2007) 2543-2549.
[26] A. Pandey, K. Jayasankar, P. Parida, M. Debata, B. Mishra, S. Saroja, Optimization of milling parameters, processing and characterization of nano-crystalline oxide dispersion strengthened ferritic steel, Powder Technol. 262 (2014) 162-169.
[27] H. Abelson, The creation of OpenCourseWare at MIT, J Sci. Educ. Technol. 17(2) (2008) 164-174.
[28] S. Diouf, A. Molinari, Densification mechanisms in spark plasma sintering: Effect of particle size and pressure, Powder Technol. 221 (2012) 220-227.
[29] M.A. Auger, V. De Castro, T. Leguey, A. Muñoz, R. Pareja, Microstructure and mechanical behavior of ODS and non-ODS Fe–14Cr model alloys produced by spark plasma sintering, J. Nucl. Mater. 436(1-3) (2013) 68-75.
[30] M. Staltsov, I. Chernov, I. Bogachev, B. Kalin, E. Olevsky, L. Lebedeva, A. Nikitina, Optimization of mechanical alloying and spark-plasma sintering regimes to obtain ferrite–martensitic ODS steel, Nucl. Mater. Energy 9 (2016) 360-366.
[31] K.D. Zilnyk, H.R.Z. Sandim, R.E. Bolmaro, R. Lindau, A. Möslang, A. Kostka, D. Raabe, Long-term microstructural stability of oxide-dispersion strengthened Eurofer steel annealed at 800 °C, J. Nucl. Mater. 448(1-3) (2014) 33-42.
[32] H. Kishimoto, M.J. Alinger, G.R. Odette, T. Yamamoto, TEM examination of microstructural evolution during processing of 14CrYWTi nanostructured ferritic alloys, J. Nucl. Mater. s 329–333(1) (2004) 369-371.
[33] X. Boulnat, M. Perez, D. Fabregue, T. Douillard, M.H. Mathon, Y.D. Carlan, Microstructure evolution in nano-reinforced ferritic steel processed by mechanical alloying and spark plasma sintering, Metall. Mater. Trans. A 45(3) (2014) 1485-1497.
[34] G. Ji, N. Bozzolo, T. Grosdidier, S. Launois, The mechanisms of microstructure formation in a nanostructured oxide dispersion strengthened FeAl alloy obtained by spark plasma sintering, Intermetallics 15(2) (2007) 108-118.
[35] H.U. Hong, B.S. Rho, S.W. Nam, Correlation of the M 23 C 6 precipitation morphology with grain boundary characteristics in austenitic stainless steel, Mater. Sci. Eng., A 318(1–2) (2001) 285-292.
[36] T. Hayashi, K. Matsuura, M. Ohno, TiC coating on titanium by carbonization reaction using spark plasma sintering, Materials Transactions (2013) L-M2013829.

5

Microstructure and mechanical properties of SPS-produced and heat-treated ODS Eurofer[1]

[1] This chapter is based on the scientific papers:
J. Fu, J. Brouwer, R. Hendrikx, I. Richardson, M. Hermans, Microstructure characterisation and mechanical properties of ODS Eurofer steel subjected to designed heat treatments, Mater. Sci. Eng., A 770 (2020) 138568.
J. Fu, T. Davis, A. Kumar, I. Richardson, M. Hermans, Characterisation of the influence of vanadium and tantalum on yttrium-based nano-oxides in ODS Eurofer steel, Mater. Charact. 175 (2021) 111072.
J. Fu, J. Brouwer, I. Richardson, M. Hermans, Microstructure Characterisation and Microhardness of ODS Eurofer Subjected to Designed Heat Treatments, The 10th Pacific Rim International Conference on Advance Materials and Processing Proceedings, 2019, pp. 136-141.

5.1 Introduction

ODS Eurofer steel was successfully produced via a powder metallurgy route, *i.e.* mechanical alloying (MA) followed by spark plasma sintering (SPS) technique, as presented in chapter 4. Spark plasma sintering has the characteristic of utilising uniaxial force and a pulsed direct electrical current under low atmospheric pressure to perform high speed consolidation of powders [1]. However, the short duration of the deformation process will cause a significant change of properties and an increased number of defects in the material, leading to a deformed microstructure [2]. Meanwhile, after the SPS process, the cooling (below 673 K) of the material in the mould is relatively slow, leading to coarsening of the prior austenite grains, which will probably cause degradation of the mechanical properties [3]. Therefore, a post heat treatment is usually applied after SPS to recover the initial microstructure and improve the mechanical performance [4, 5].

The application of a heat treatment is crucial for the formation of martensite and ferrite in dual phase steels like ODS Eurofer. In particular for the study reported in chapter 4, the mechanical properties of the as-produced material are not homogenous due to a difference in the cooling rate and carbon content between the surface area and the centre of the material. There is very limited literature available concerning the heat treatment effects on the microstructure and mechanical properties of mechanically alloyed and SPS produced ODS Eurofer. For this purpose, a post heat treatment route was designed based on the results of differential scanning calorimetry (DSC) and Vickers microhardness measurements. The microstructure and mechanical properties of as-produced and heat-treated ODS Eurofer were investigated and are discussed in detail in this chapter.

5.2 Experimental details

5.2.1 Materials

ODS Eurofer was produced with the optimal condition F as mentioned in Table 4.1, by which the highest density of the material was obtained. The chemical composition of the as-produced steel, obtained through X-Ray Fluorescence (for heavy elements) and combustion analysis (for carbon), is listed in Table 5.1.

Table 5.1 Chemical composition of the bulk steel in wt%.

	Cr	W	Mn	V	Ta	Y	Al	C	Fe
As-produced steel (wt%)	8.92	0.99	0.45	0.20	0.15	0.21	0.09	0.09	Bal.

5.2.2 Methods

Thermal analysis of the as-produced ODS Eurofer was conducted by means of differential scanning calorimeter (DSC) to obtain the DSC profile and phase transformation temperatures. A heat treatment route was applied to the as-produced steel in order to homogenise the chemical composition and mechanical properties based on the result of the DSC measurements. The steel

was subjected to a normalisation treatment for 1 h at 1323 K, 1423 K or 1523 K, respectively. In the case of a normalisation treatment at 1423 K, a tempering treatment was subsequently applied at 873 K, 973 K or 1073 K for 1 h, respectively. All specimens were air cooled to room temperature. Vickers microhardness was measured from the top surface to the bottom surface of the heat-treated samples, with a load of 0.3 kg and a step size of 0.5 mm (Figure 5.1 (a)).

The microstructural features were studied by means of optical microscopy (OM), scanning electron microscopy (SEM), electron backscattered diffraction (EBSD), X-Ray diffraction (XRD), transmission electron microscopy (TEM) and atom probe tomography (APT). For characterisation of carbides in the steel, precipitates were electrolytically extracted using a solution of 10% hydrochloric acid, 1% citric acid and balance ethanol, with a current density of 0.1 A/cm^2 at room temperature. The residues were separated using a centrifuge rotating at 18 000 rpm for 3 min. The extracted residues were then analysed by X-Ray diffraction (XRD). To elucidate the mechanism of the formation of carbides precisely, computation of the phase diagram of ODS Eurofer was performed, using the Thermo-Calc code and TCFE6 database.

The specimens for tensile testing were machined by wire electrical discharge machining (WEDM) according to Figure 5.1 (b). Specimens cut from the top to bottom were labelled from 1 to 7, the same as the approach used in chapter 4.

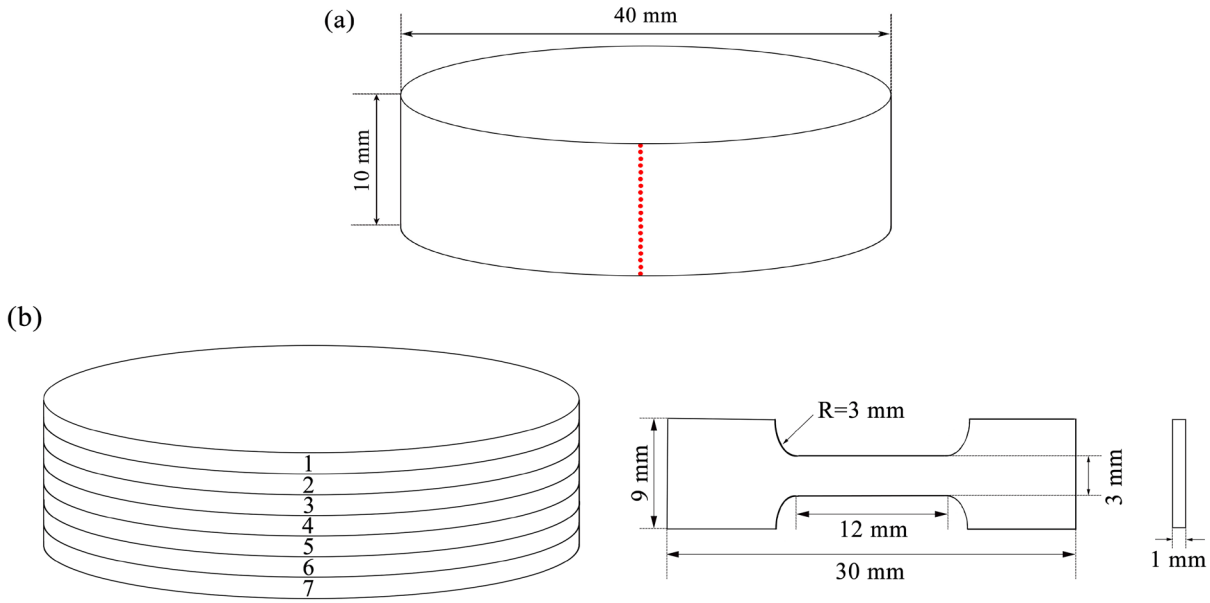


Figure 5.1. (a) The position of the hardness measurements and (b) the position, shape and dimensions of tensile samples.

5.3 Results and discussion

5.3.1 Design of a heat treatment route

The DSC profile of the as-produced steel obtained during the heating and cooling processes can be seen in Figure 5.2. The onset and offset of the peaks were determined by the intersection point of the tangents of the curve. In the heating stage, two distinct endothermic peaks are

identified. The first one is caused by the Curie transition and the second is related to the ferrite to austenite transformation. The starting temperature (Ac1) and finishing temperature (Ac3) of the austenite transformation are determined as 1096 K and 1142 K, respectively. Two peaks at the start and end of the holding stage at 1523 K can be seen, which are probably associated with a rapid change of the heat input. In the cooling stage, two exothermic peaks can be observed, which are related to the Curie transition and the martensite transformation, respectively. The change of the heat flow of the second peak is small, probably because the cooling rate is not high enough to achieve a fully martensitic transformation. The starting temperature (M_s) and finishing temperature (M_f) of martensite transformation are 661 K and 612 K, respectively. Peaks corresponding to the γ/δ-ferrite transformation are hardly distinguishable in the curve. As the range of the γ+δ two-phase region is wide, the change of heat flow per unit time is too small to be accurately measured [6].

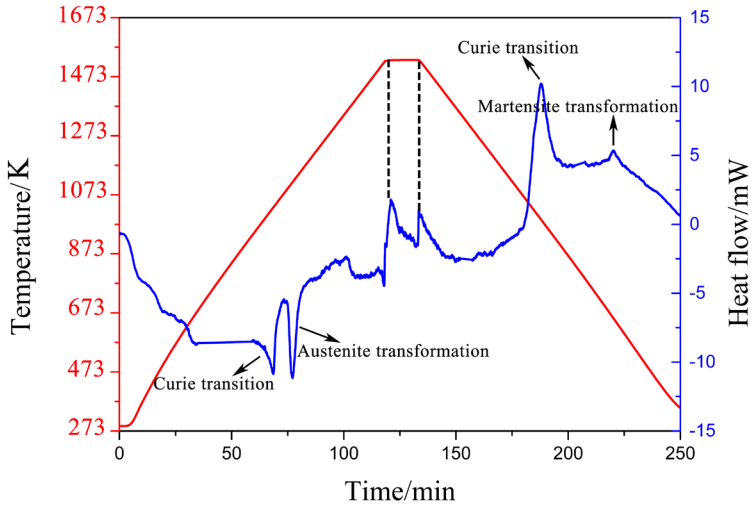


Figure 5.2. DSC profile of the as-produced steel obtained during heating and cooling schedule.

In order to obtain a recovered microstructure as well as relatively uniform mechanical properties of the material, a two-step heat treatment route including normalising and tempering treatment was designed. The main goal of normalising treatment is to enhance the mechanical properties of the material by refining the microstructure, which is realised by solid state phase transformation. The normalising temperature should be higher than Ac3 (1142 K). Moreover, according to the study of normalising treatment on ODS Eurofer by Lu *et al.* [7], the temperature should be lower than 1573 K to avoid coarsening of the microstructure. Therefore, three normalising temperatures were chosen: 1323 K, 1423 K and 1523 K. As the steel is air cooled after normalising, the microstructure is partially transformed to a brittle martensite with high dislocation density. To relieve the residual stress and achieve the desired balance of mechanical properties, a high temperature tempering step should be applied [8]. The tempering temperature should be below Ac1 (1096 K) to avoid the formation of fresh martensite, which otherwise would cause a decrease in the material toughness [9]. Tempering temperatures were chosen to be at 873 K, 973 K or 1073 K.

Figure 5.3 shows a Vickers hardness profile of the cross section of the as-produced and heat-treated samples. It can be seen that there is a large variation in the hardness profile of the as-produced sample. The top and bottom surfaces have a higher hardness of approximately 650 $HV_{0.3}$ whereas the middle area has a lower hardness of approximately 400 $HV_{0.3}$. After a normalising heat treatment at 1323 K for 1 h, the hardness of the material does not change significantly. This could be ascribed to a competitive effect of grain growth and martensite transformation in this condition. After a normalising treatment at 1423 K and 1523 K for 1 h, the hardness of the materials is increased remarkably, indicating the occurrence of the martensite transformation. It was observed that part of the material was detached after normalising at 1523 K. Therefore, 1423 K was selected as a more appropriate normalising temperature. Upon tempering, defect recovery, carbon diffusion and carbide precipitation will usually occur in dual phase steels [8]. It can be seen that after tempering at 873 K for 1 h, the variation of the hardness in the material has been partially eliminated. After tempering at 973 K and 1073 K for 1 h, the average hardness of the samples is 348.1 ± 17.7 and 334.6 ± 20.4 $HV_{0.3}$, respectively. A more homogenous microstructure and mechanical properties compared to the as-produced material are obtained. The hardness of the sample tempered at 1073 K is slightly lower than the one tempered at 973 K, probably due to carbide coarsening and grain growth, which will affect the strength of the material. The condition of normalising at 1423 K and tempering at 973 K was therefore determined as a more suitable heat treatment route. The microstructure and mechanical properties of the steel subjected to this condition were investigated and the steel is referred to as "tempered steel" in the following text.

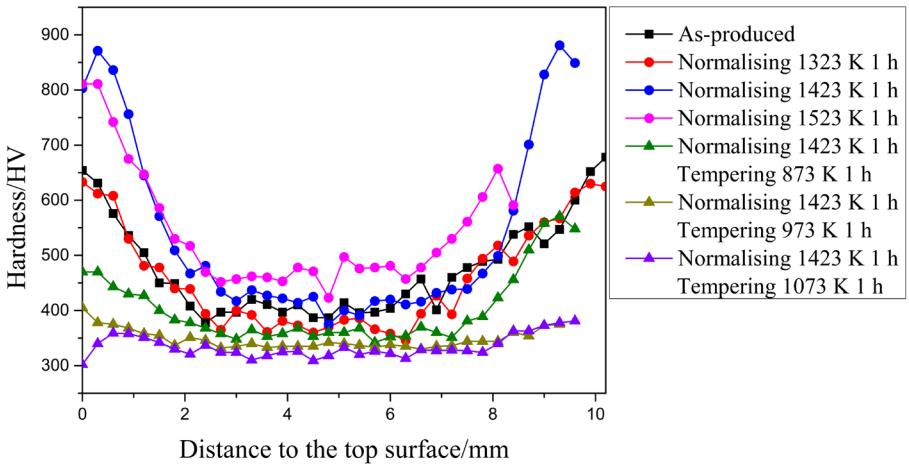


Figure 5.3. Vickers hardness profile of the cross section of the as-produced and heat-treated samples.

5.3.2 Microstructure characterisation

The optical micrographs of the as-produced and tempered steel can be seen in Figure 5.4. Martensite (dark regions) and residual δ-ferrite (white regions) are revealed in both conditions. The formation of residual ferrite in Figure 5.4 (b) is unusual, as after a normalising treatment, a fully martensitic microstructure is expected to form. Yamamoto *et al.* [10] and Cayron *et al.* [11] also reported the presence the residual ferrite after a normalising treatment of ODS Fe–

9Cr steels. This phenomenon arises probably because the phase transformation is partly suppressed in the material, as the δ-ferrite–austenite interface motion is strongly pinned by finely dispersed oxide particles during the heat treatment.

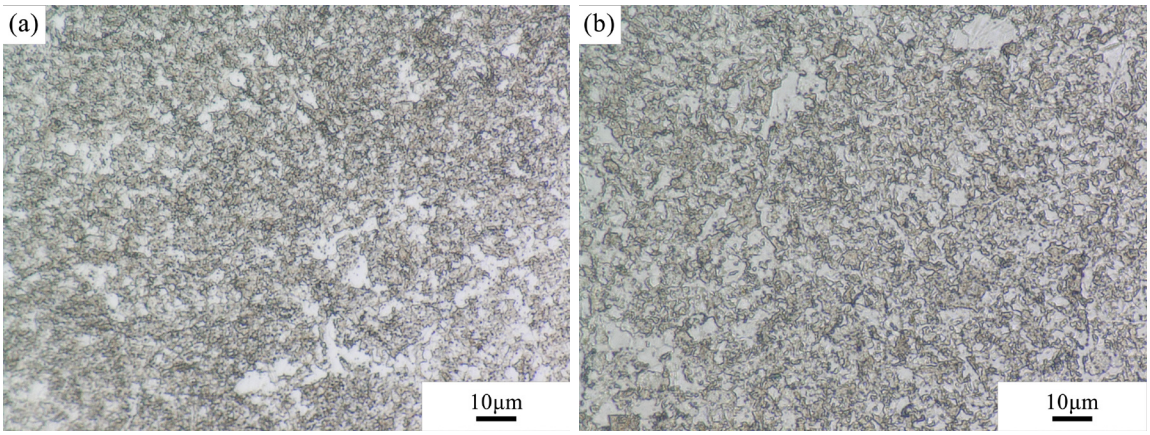


Figure 5.4. Optical micrographs of the (a) as-produced and (b) tempered steel.

Figure 5.5 shows the EBSD maps of ODS Eurofer under different conditions, with grain colours related to grain orientation expressed in the standard triangle. TSL OIM analysis software was used to determine the grain size. The effective grain boundaries were chosen as the high angle grain boundaries with misorientations larger than 15°. It can be seen from Figure 5.5 (a) that the microstructure of as-produced ODS Eurofer consists of fine grains and coarse grains. The grain size distribution is bimodal, with peaks at 0.29 and 2.62 μm. Finer grains smaller than 0.29 μm could not be indexed, causing the non-indexed (black) areas in the figure. Similar bimodal grain size distributions have been widely reported for powder metallurgy prepared ODS steels. As described in chapter 4, this microstructure could result from heterogenous recrystallisation due to an inhomogeneous dislocation density after the milling process [12-14], combined with a spatial variation in the pinning force by a nonuniform distribution of nanoparticles [13-15].

Table 5.2 shows the average grain size obtained from the EBSD data for the different conditions in Figure 5.5. High standard deviations of the average grain size were found in all conditions due to a bimodal grain size distribution. To characterise the grain size distribution more accurately, the grains were separated into fine grains and coarse grains; the average grain sizes were calculated separately and are presented in Table 5.2. It can be seen that after a normalising treatment, the grain sizes of both fine grains and coarse grains slightly decrease. This phenomenon could be ascribed to a competition between martensite transformation and grain growth due to a high temperature normalising treatment (according to the result of the TSL OIM software, the average grain size of martensite is smaller than ferrite). Moreover, according to the studies of Zilnyk *et al.* [16] and Lu *et al.* [7], there is a significant increase in the grain size of Eurofer 97 after a normalising treatment above 1273 K for 1 h. This confirms that the pinning effect on the grain boundaries by Y_2O_3 nanoparticles is very effective even at

high temperatures. Grain growth occurs during the tempering treatment, due to a lack of martensite transformation during the tempering process.

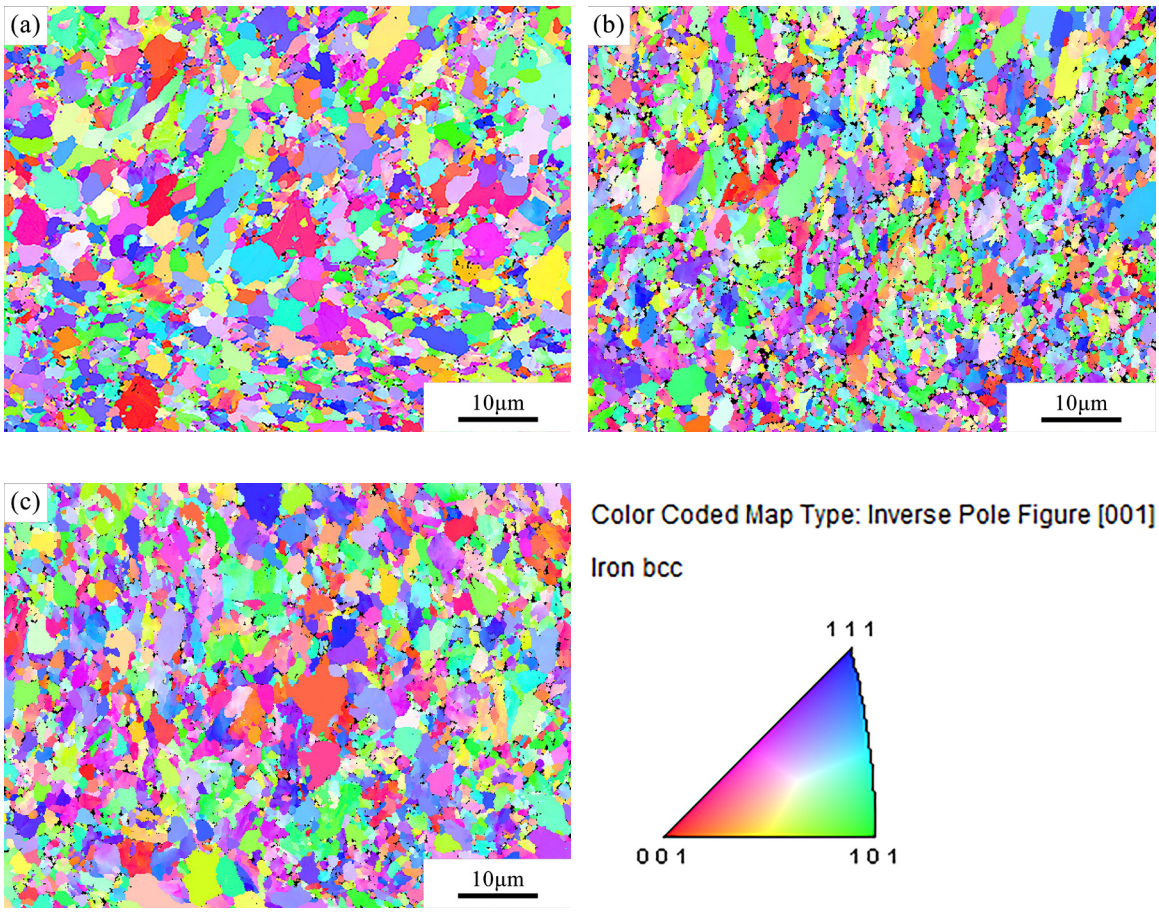


Figure 5.5. EBSD maps of ODS Eurofer at different conditions: (a) as-produced, (b) Normalising at 1423 K and (c) Normalising at 1423 K and tempering at 973 K.

Table 5.2 Average grain size obtained from EBSD data for different conditions.

Conditions	Average grain size/μm	Fine grain size/μm	Coarse grain size/μm
As-produced	2.08 ± 1.31	0.61 ± 0.30	2.49 ± 1.22
Normalised steel (1423 K)	1.64 ± 1.04	0.59 ± 0.22	2.06 ± 1.13
Tempered steel	1.92 ± 1.10	0.62 ± 0.33	2.25 ± 1.16

The SEM micrographs of the as-produced and tempered steel are shown in Figure 5.6. Precipitates rich in Fe, Cr and C are confirmed by energy dispersive spectrometer (EDS). Based on the particle size (50–200 μm) and chemical composition, they appear to be Fe–Cr carbides. It is notable that after the heat treatment, they are more preferentially located on the grain boundaries. The carbides dissolve and reprecipitate during the normalising and tempering treatment, and tend to precipitate along the prior austenite grain boundaries due to a decrease in volume free energy [17]. The presence of small Fe–Cr carbides is beneficial for the

mechanical strength, as they are effective in inhibiting the motion of grain boundaries, acting as obstacles to block the dislocation motion and subgrain formation [18].

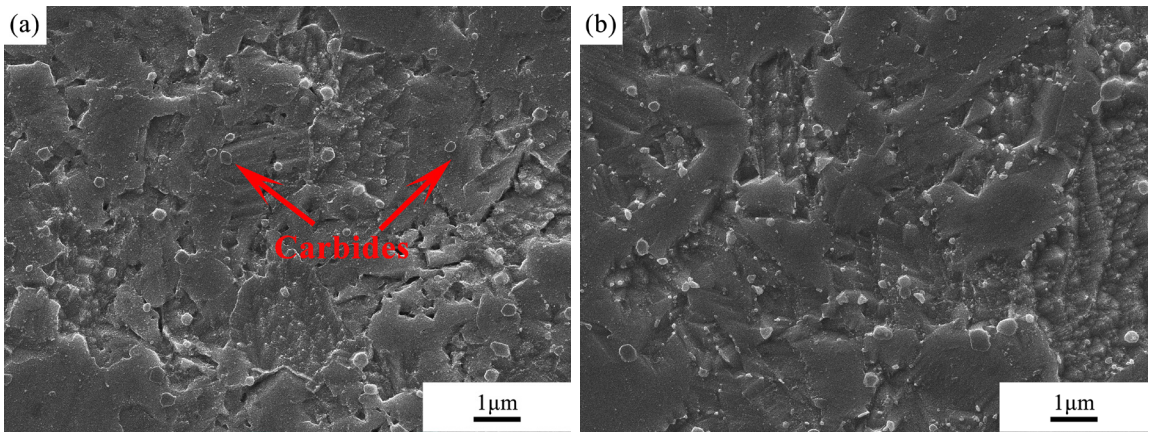


Figure 5.6. SEM micrographs of the (a) as-produced and (b) tempered steel.

In order to characterise the carbides more precisely, the particles were electrolytically extracted and analysed by XRD, as shown in Figure 5.7. The presence of $(Fe_3W_3)C$, referred to as M_6C and $(Cr_{15.58}Fe_{7.24})C_6$, referred to as $M_{23}C_6$ were confirmed in the as-produced steel, while only $M_{23}C_6$ carbides were observed in the tempered steel. The lattice constants obtained from different 2θ values were plotted as a function of $cos2(\theta)/sin(\theta) + cos2(\theta)/\theta$, the Nelson-Riley function, and extrapolated to $\theta = 90°$ to minimise absorption errors [19]. After calculation, the lattice constants of the M_6C and $M_{23}C_6$ carbides in the as-produced sample are 11.081 Å and 10.577 Å, respectively; the lattice constant of the $M_{23}C_6$ carbides in the tempered sample is 10.616 Å.

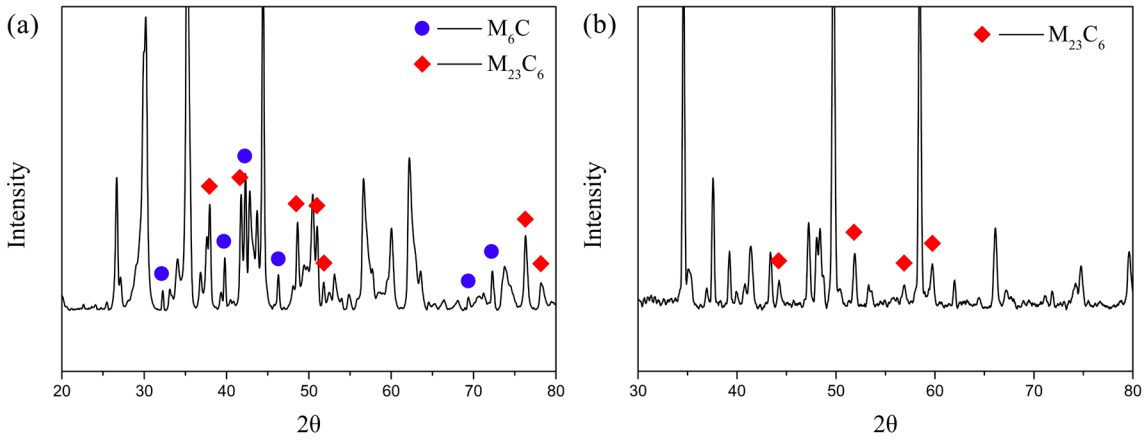


Figure 5.7. XRD patterns of the extracted carbides from the (a) as-produced and (b) tempered steel.

The phase diagram of ODS Eurofer with respect to the carbon content was calculated using Thermo-Calc software and is shown in Figure 5.8. The computations were performed using a defined composition of Fe–9Cr–1.1W–0.4Mn–0.2V–0.12Ta–$0.3Y_2O_3$ (wt%). Note that the

calculations did not consider the impeding effect of Y_2O_3 on the phase transformations. The dash line indicates a carbon content of 0.09 wt%, corresponding to the chemical composition shown in Table 5.1. The starting temperature of the austenite transformation predicted by the phase diagram is 1099.8 K, very close to that obtained by the DSC measurement, which is 1096 K. At room temperature, for a carbon content of more than 0.07 wt%, $M_{23}C_6$ carbides would form in the α-Fe matrix, whereas M_6C carbides are predicted to form at a carbon content of less than 0.07 wt%. The formation of carbides is probably due to carbon diffusion from the graphite mould during the SPS process, as no carbon powder was added to the precursor powder for mechanical alloying. The diffusion results in an inhomogeneous distribution of carbon in the bulk steel. Higher carbon levels are formed near the surface area and less carbon near the centre area. Therefore, in the as-produced sample (carbon content equals 0.09 wt%), it is likely that the $M_{23}C_6$ carbides tend to form near the surface area where the carbon content is more than 0.07 wt%, and the M_6C carbides tend to form near the centre area where the carbon content is less than 0.07 wt%. As for the tempered sample, carbon becomes more homogenous due to the heat treatment process. It is safe to assume that the carbon content in the sample is approximately 0.09 wt% on the macroscopic scale. Therefore, only $M_{23}C_6$ carbide would form in the bulk steel at room temperature. Tantalum carbides predicted by the software were not observed in this study, possibly due to the exhaustion of tantalum forming nanoclusters, which will be addressed in the next section. Laves Phase was not observed in the microstructure, either. Laves Phase in 9–12 wt% Cr steels is a microconstituent with a hexagonal structure and a composition of $(Fe, Cr)_2(W, Mo)$, however, it appears only after long time exposure at temperatures up to 900 K [20].

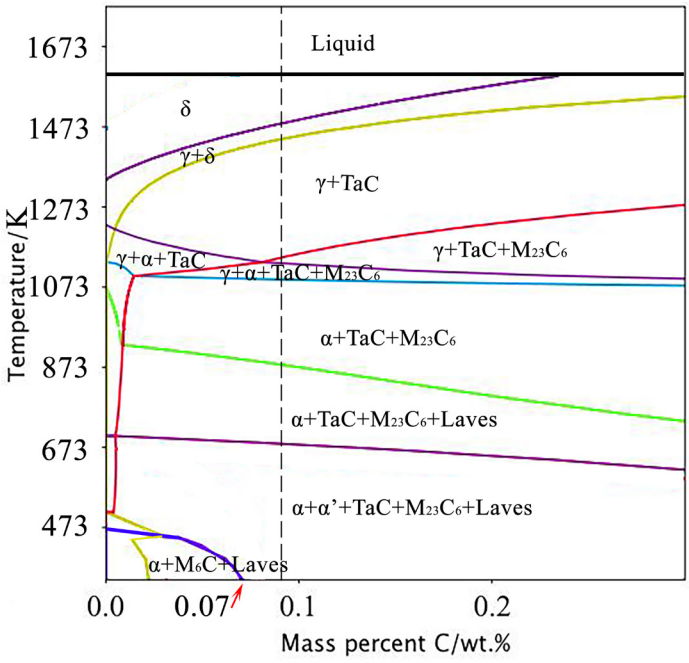
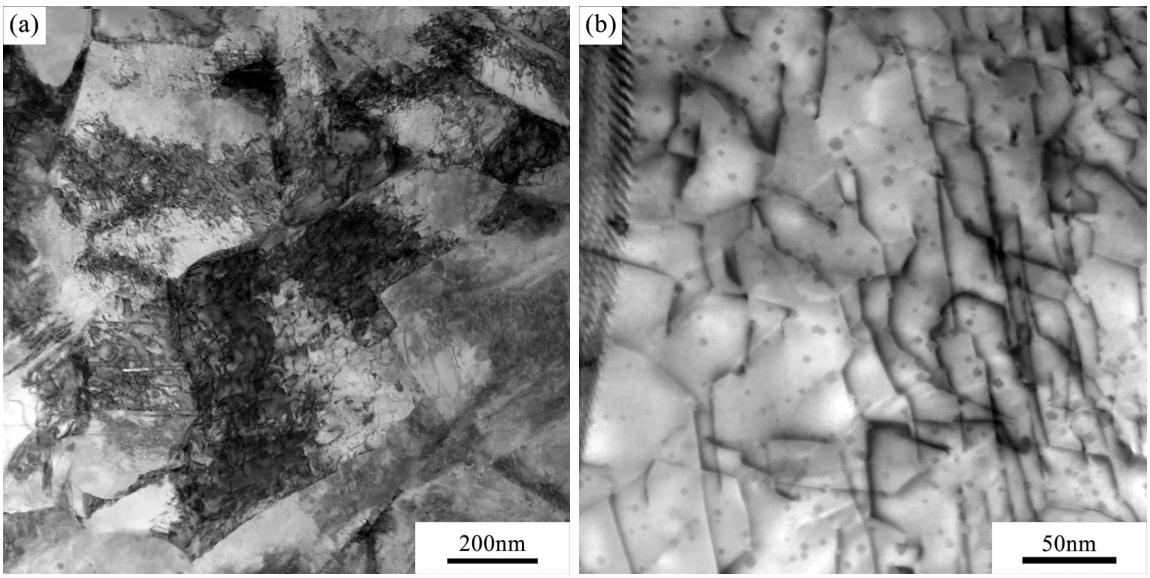


Figure 5.8. Computed phase diagram with respect to the carbon content for Fe–9Cr–1.1W–0.4Mn–0.2V–0.12Ta–0.3Y_2O_3 (wt%).

TEM images of the microstructure features of the as-produced and tempered steels are shown in Figure 5.9. A high density of dislocations is evident in the microstructure of the as-produced steel (Figure 5.9 (a)), related to the mechanical alloying process. Meanwhile, a large number of Y_2O_3-rich nanoparticles, confirmed by EDS, are observed in the steel matrix (Figure 5.9 (b)). Some particles are pinning the dislocation lines, which would lead to an increased creep resistance compared to non-ODS steels [21]. The average size of the particles in the as-produced steel is 8 nm. The starting size of the Y_2O_3 powder is 25–50 nm, indicating that the mechanical alloying process has a refinement effect on the Y_2O_3 particles. In the tempered steel, dislocation-free areas and martensite laths are observed (Figure 5.9 (c)), showing the effect of the normalising and tempering treatment. Figure 5.9 (d) shows a dark field image of Y_2O_3 particles pinning the grain boundaries, which is beneficial for enhancing the mechanical properties and extending the operating temperature range [22]. The average size of Y_2O_3 is slightly increased to 11 nm after the heat treatment. Figure 5.9 (e) and (f) exhibit the presence of $M_{23}C_6$ carbides along grain boundaries and the diffraction pattern of $M_{23}C_6$, respectively.



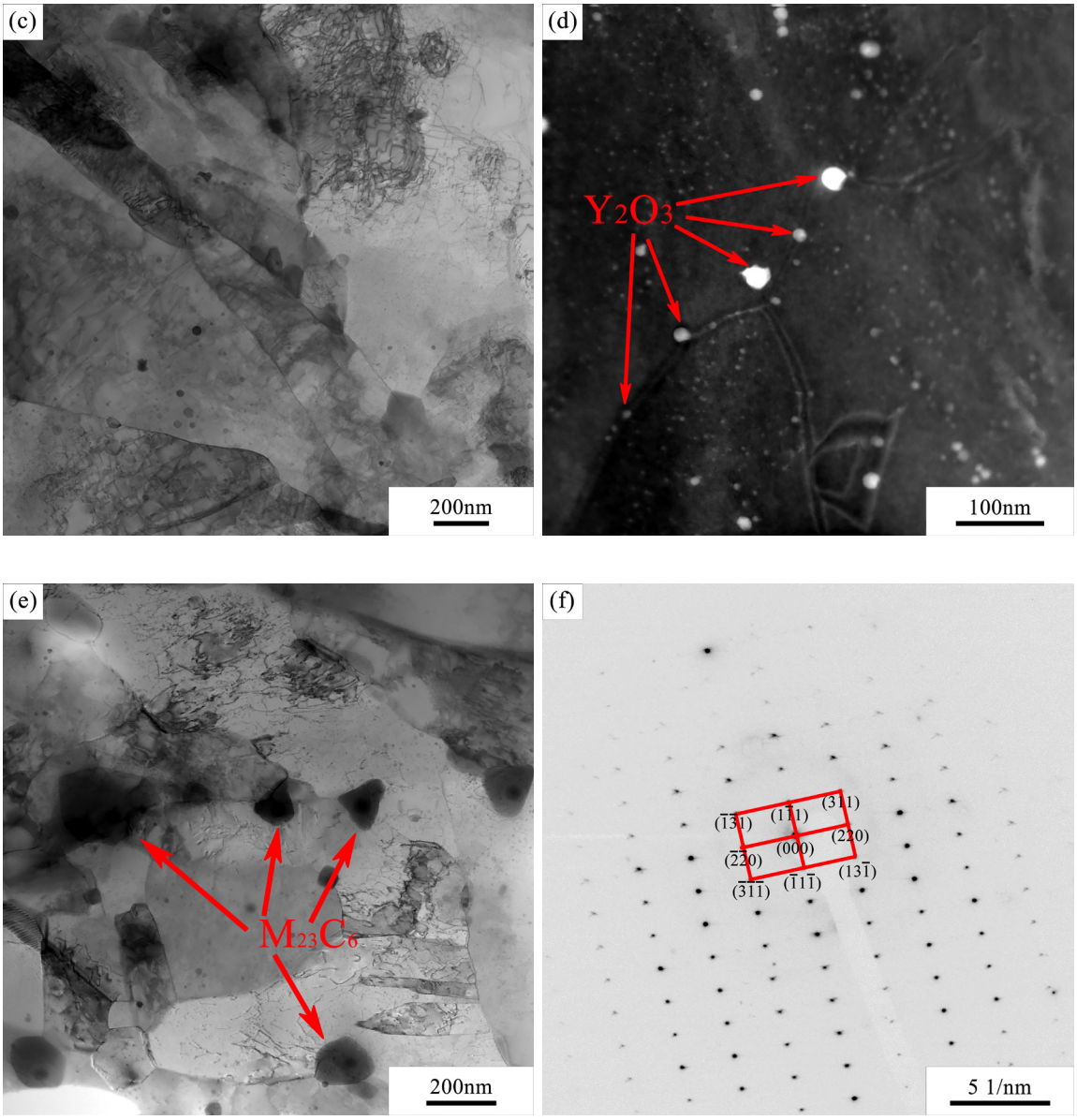


Figure 5.9. TEM images of the microstructural features of the (a), (b) as-produced and (c), (d), (e), (f) tempered steel: (a) high density dislocations, (b) dispersed Y_2O_3, (c) tempered martensite lath and clean grains, (d) Y_2O_3 pinning the grain boundaries (e) $M_{23}C_6$ carbides and (f) diffraction pattern of $M_{23}C_6$ carbides.

Considering the important role that the oxide particles play in affecting the performance of ODS Eurofer, it is crucial that their characteristics, such as size distribution, chemical composition, morphology and number density, are well understood. Previous investigations on the oxide particles in ODS steels were conducted by means of different techniques, the results, however, were not completely consistent with each other. For example, Williams *et al.* [23] found a core/shell structure in the nanoclusters in ODS Eurofer via atom probe tomography (APT), where the core is primarily composed of Y and O enriched with Mn and Si, while C, N, Ta, W, V and Cr were predominantly found in the shell. Klimenkov *et al.* [24] reported TEM investigations of ODS Eurofer steel, suggesting that the nanoparticles were more than 10 nm with a complex structure. The core of the particle consisted of a phase with a composition of

$(Y_{1.8}Mn_{0.2})O_3$, which was surrounded by a shell of V and Cr with 0.5 – 1.5 nm thickness. Such a complex composition of the ODS particles led to the assumption that their nucleation and dispersion was associated with the concentrations of Mn and Y. An APT study on ODS Eurofer from Aleev *et al.* [25] revealed that the core of nanoclusters was rich in V, Y and O while the concentration of Mn was negligible in the clusters. A model Fe–12Cr–0.4Y_2O_3 (wt%) alloy was investigated by Castro *et al.* [26] using electron energy loss spectroscopy (EELS), after annealing at 1023 K up to 96 h, the nanoparticles either had a core/shell structure with a Cr-enriched shell or evolved into complex oxides such as $YCrO_3$. Furthermore, studies on Ti containing ODS steels gave even more complex findings. Ohnuma *et al.* [27] used small angle scattering using neutrons (SANS) and X–rays (SAXS) to study a number of 9Cr–ODS steels containing Ti and found that the finest oxide nanoparticles have a chemical composition close to $Y_2Ti_2O_7$. Recent APT analysis of a Fe–18Cr–1W–0.3Ti–0.3Y_2O_3 (wt%) ODS steel [28] showed that the Y–O–Ti nanoparticles exhibited a core–shell structure consisting of a complex Cr-rich shell with 1.2 – 1.5 nm thickness. The particle stoichiometry evolved from $YTiO_2$ for the small particles (<2 nm) to Y_2TiO_5 for the big ones (>8 nm). Templeman *et al.* [29] used a combined investigation method of TEM, APT and electron diffraction tomography (EDT) to characterise a Fe–14Cr–1W–0.3Ti–0.25Y_2O_3 (wt%) ODS steel. Three populations of particles were identified: highly dispersed, 3–20 nm Fe(Cr,Ti,Y)O particles, 50–150 nm $YTiO_3$ and 100–200 nm TiC particles. In summary, there have been considerable uncertainties in terms of characterising and understanding the nature of nanoclusters in ODS Eurofer/ODS steels. Part of the inconsistency undoubtedly comes from the differences in alloy compositions, processing routes employed, and techniques and interpretation methods used for the characterisation. A thorough understanding of the nano-oxide characteristics is needed for a better control of microstructure and mechanical properties for ODS steels and their nuclear applications.

In order to accurately characterise the finely dispersed nano-oxide particles in ODS Eurofer, APT was conducted to perform cluster analysis on the atomic scale. Table 5.3 summarises the concentrations of elements averaged over 5 analysed tips irrespective of their spatial distribution. The matrix composition was estimated from data that excluded the atoms of clusters in the volumes. In general, there is a good agreement between the XRF and LECO analysis measured chemical composition and the APT measured results, indicating that the identifications of ion species within the APT mass-spectrum is reasonable. The measured C content is lower than the chemical composition. Due to the low solubility of C in BCC iron, it can be assumed that the majority of C is likely to have segregated and formed carbides (such as $M_{23}C_6$) and is not captured in the APT datasets due to the small volume probed. The matrix composition is depleted with Y and O, probably due to the formation and segregation of the Y–O clusters. More importantly, according to Ref. [23] and [25] on the structure of nanoclusters in ODS steels, V and Ta can play an important role in affecting the formation of nano-oxides. Due to the low level of V and Ta detected by APT, a Fe–9Cr–1.1W–0.4Mn–2V–1.2Ta–0.3Y_2O_3 (wt%) alloy with increased V and Ta levels was made and analysed to further investigate their influences on the nature of nanoclusters. The chemical and APT measured compositions of the modified material (referred to as ODS Eurofer–2V–1.2Ta) are also presented in Table 5.3.

Table 5.3 X-ray fluorescence and LECO analysis measured and APT measured compositions of ODS Eurofer and ODS Eurofer–2V–1.2Ta.

Element	ODS Eurofer by XRF/LECO (at%)	ODS Eurofer bulk by APT (at%)	ODS Eurofer matrix by APT (at%)	ODS Eurofer–2V–1.2Ta by XRF/LECO (at%)	ODS Eurofer–2V–1.2Ta bulk by APT (at%)	ODS Eurofer–2V–1.2Ta matrix by APT (at%)
C	0.42	0.02	0.08	0.43	0.05	0.11
Si	0.02	0.04	0.05	0.02	0.04	0.05
Cr	9.16	9.03	9.14	9.52	9.01	9.17
Fe	89.05	89.99	90.11	86.47	88.56	88.94
W	0.28	0.30	0.25	0.31	0.24	0.30
N	–	0.04	0.02	–	0.07	0.03
V	0.19	0.18	0.13	2.1	1.06	0.98
Y	0.12	0.06	0.02	0.13	0.14	0.05
O	0.21	0.20	0.06	0.22	0.60	0.19
Mn	0.53	0.13	0.16	0.45	0.14	0.14
Ta	0.03	0.01	0.01	0.33	0.08	0.03

Three dimensional elemental maps of ODS Eurofer and ODS Eurofer–2V–1.2Ta were obtained by APT and are shown in Figure 5.10. In ODS Eurofer (Figure 5.10 (a)), elements of Fe, Cr, Mn, W, C and Si were relatively homogeneously distributed in the analysed volume. The elemental distribution of Fe is shown as an example with a uniform distribution. Elemental maps of V, O, and Y show non-homogenous distribution (*i.e.* clustering) features, indicating an enrichment of these solute elements in the nanoclusters. In addition, molecular ions of VO, YO and TaO_2 have been identified from the mass spectrum and overlap with previously mentioned clusters, providing confidence that they contribute towards the cluster analysis. In the case of ODS Eurofer–2V–1.2Ta (Figure 5.10 (b)), the ion point cloud maps quantitively reveal a higher density of nanoclusters in the sample. The averaged number density of the clusters is 5.15×10^{23} m^{-3} compared to 2.44×10^{23} m^{-3} found in ODS Eurofer. Moreover, it is notable that the size and spatial distributions of the nanoclusters are not homogenous in either condition (a common feature in ODS steels [30]). The corresponding size distribution of nanoclusters is shown in Figure 5.11. The gyration diameter (d) of nanoclusters varies from 1.8–12.2 nm, with the average value of 4.13 nm in ODS Eurofer, while that in ODS Eurofer–2V–1.2Ta ranges from 1.2–14 nm, with the average value of 2.96 nm. The experimental results suggest that the addition of V and Ta appears to affect and promote the formation of small, high density nanoclusters.

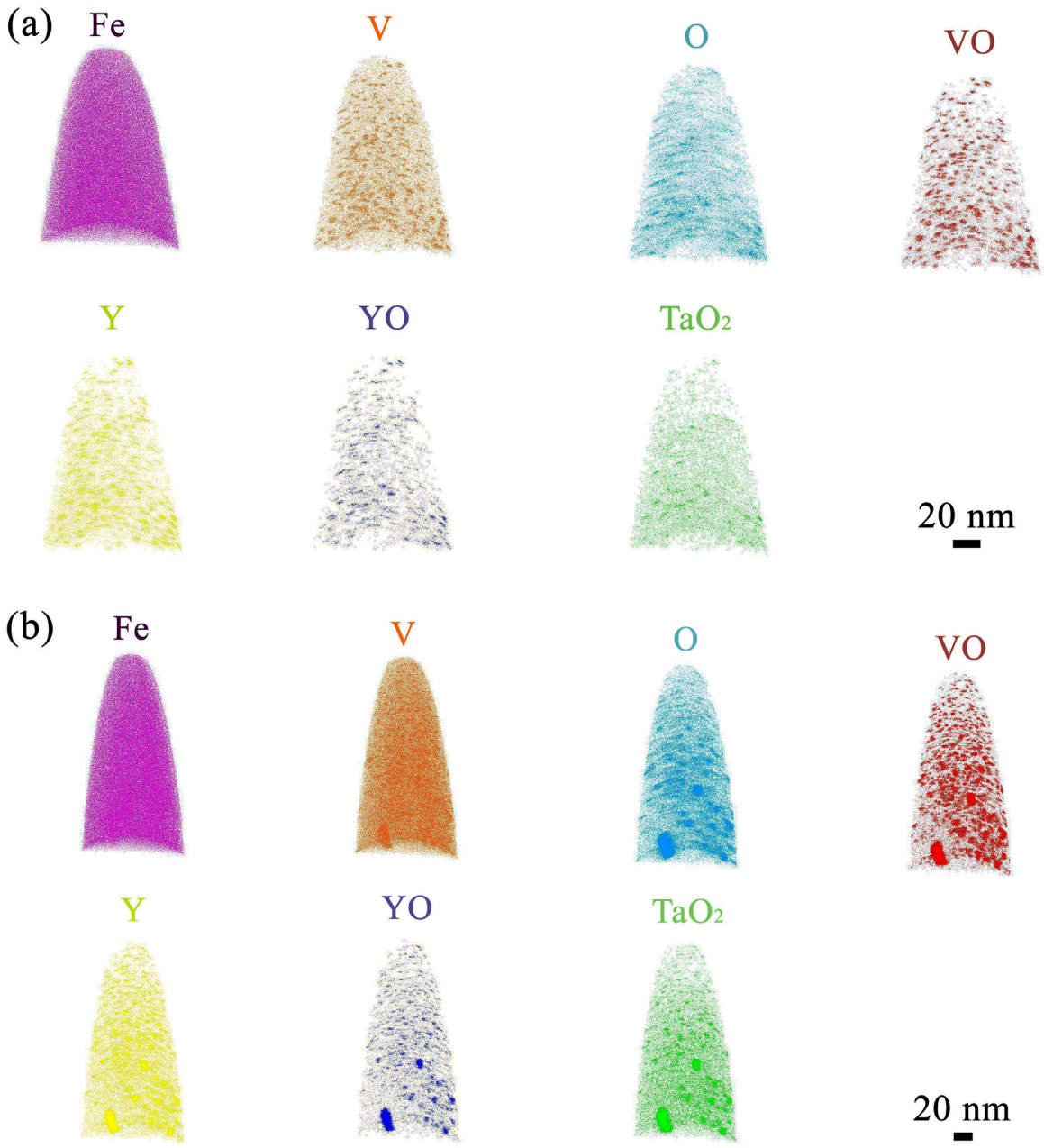


Figure 5.10. APT 3D reconstruction of (a) ODS Eurofer and (b) ODS Eurofer–2V–1.2Ta.

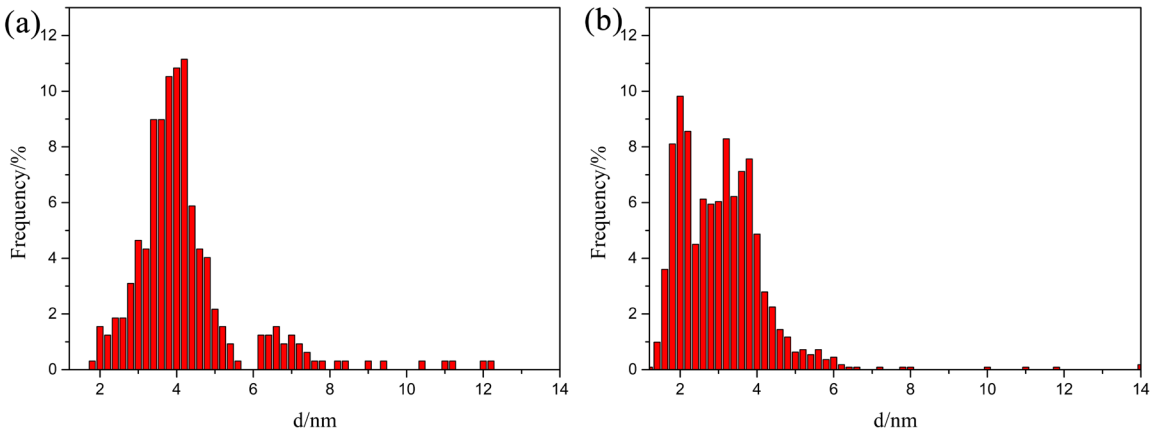


Figure 5.11. Size distribution of nanoclusters in (a) ODS Eurofer and (b) ODS Eurofer–2V–1.2Ta.

The averaged chemical composition of the nanoclusters in ODS Eurofer is shown in Table 5.4. The measured Fe by APT is around 36.56 at%, which is probably the result of trajectory aberrations [23]. Although it is possible that nano-oxides contain Fe, it is very unlikely that such a high level of Fe is present in the core of the particles, due to a very low solubility of Fe in Y_2O_3 [31]. The exact quantity of Fe in the clusters is not addressed in this study. Instead, following the method proposed by Williams *et al.* [23], the Fe contribution in the clusters was artificially set to zero. The Fe level was used to estimate the quantity of the other matrix elements introduced by trajectory aberrations, which were removed from the raw composition. The obtained cluster composition is quoted as "matrix corrected" in Table 5.4. It can be seen that the clusters in ODS Eurofer are mainly composed of V, Y and O and enriched with other alloying elements. The averaged chemical composition of the nanoclusters in ODS Eurofer–2V–1.2Ta were measured and corrected by the same method. Of noted interest, the Ta level is significantly higher, while the V level is lower compared to the clusters in ODS Eurofer. This could be due to the addition of Ta in the material. Considering that Ta has a higher affinity for O than V [32], it is possible that Ta combines with O in Y_2O_3 and pushes V to the outside of the particle core.

To further investigate the composition difference in small and large clusters, the averaged chemical composition of clusters larger than 6 nm in ODS Eurofer and clusters larger than 4 nm in ODS Eurofer–2V–1.2Ta were measured and are shown in Table 5.4. It can be seen that in both cases, the Ta and Cr level increase and the Y level slightly decreases for the large clusters. This indicates that there are more Ta and Cr atoms contributing to the formation of large nanoclusters, leading to a lower level of Y in the clusters.

Table 5.4 Averaged chemical composition of the nanoclusters in ODS Eurofer and ODS Eurofer–2V–1.2Ta.

Element	Nanoclusters in ODS Eurofer		Clusters larger than 6 nm in ODS Eurofer		Nanoclusters in ODS Eurofer–2V–1.2Ta		Clusters larger than 4 nm in ODS Eurofer–2V–1.2Ta	
	Measured (at%)	Matrix corrected (at%)	Measured (at%)	Matrix corrected (at%)	Measured (at%)	Matrix corrected (at%)	Measured (at%)	Matrix corrected (at%)
C	0.04	0.02	0.08	0.09	0.05	0.03	0.09	0.07
Si	0.08	0.10	0.16	0.30	0.04	0.04	0.10	0.13
Cr	6.19	4.18	8.97	8.76	2.96	1.19	5.25	2.83
Fe	36.56	0.00	50.4	0.00	19.70	0.00	33.93	0.00
W	0.13	0.05	0.21	0.16	0.09	0.03	0.19	0.12
N	4.18	6.95	2.87	6.49	7.77	9.97	4.99	8.05
V	16.72	28.13	11.21	25.29	15.42	19.53	13.23	20.79
Y	13.27	22.22	9.02	20.45	19.72	25.32	12.67	20.45
O	22.60	37.99	16.62	37.66	29.26	37.53	25.03	40.35
Mn	0.08	0.13	0.13	0.09	0.05	0.03	0.14	0.15
Ta	0.15	0.24	0.32	0.72	4.94	6.34	4.38	7.06

The Y/O ratio of nanoclusters in ODS Eurofer and ODS Eurofer–2V–1.2Ta are plotted in Figure 5.12. In both cases, the smaller clusters have a variable stoichiometry, while in the larger clusters, the Y/O ratio shows a relatively constant value of around 0.51 ± 0.16. (It is worth mentioning that, while no crystallographic measurements were conducted to determine the stoichiometry, the compositional measurements indicate what the stoichiometry would be.) In addition, the Y/O ratio of the larger clusters in ODS Eurofer–2V–1.2Ta is slightly lower than that in ODS Eurofer, probably due to a higher number of molecular ions of VO and TaO_2 in the clusters.

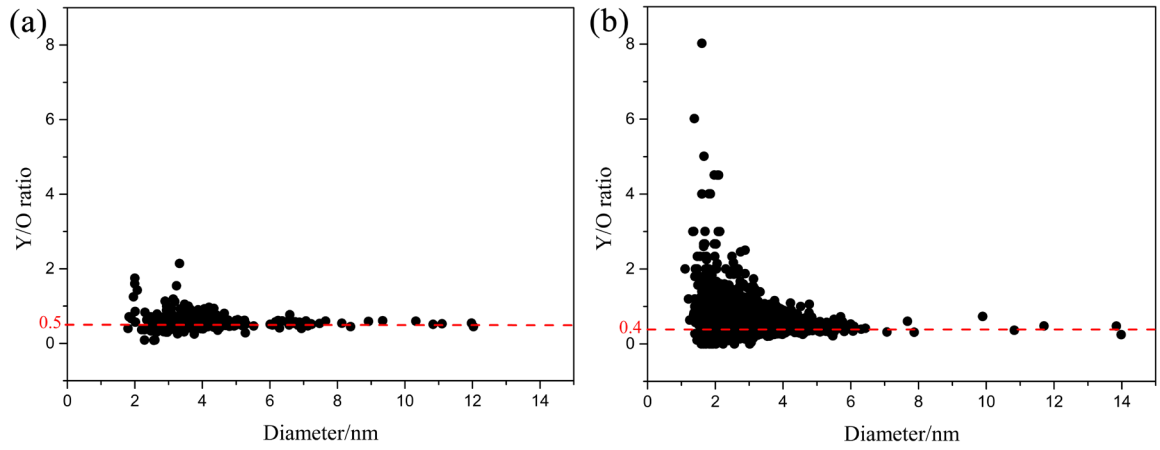


Figure 5.12. Y/O ratio of nanoclusters in (a) ODS Eurofer and (b) ODS Eurofer–2V–1.2Ta.

Two one-dimensional concentration profiles obtained from a cylinder of 2 nm diameter and intercepting a particle of interest are shown in Figure 5.13. One particle of around 2.5 nm gyration diameter in ODS Eurofer (Figure 5.13 (a)) and one particle of around 8 nm gyration diameter in ODS Eurofer–2V–1.2Ta (Figure 5.13 (b)) were analysed. By examining the cross-sectional composition profiles, it appears that the particles have a pronounced core/shell structure. It can be seen that Cr and V have higher levels near the particle–matrix interface, forming the shell, whereas Y, O and Ta are more concentrated at the core. The level of other alloying elements (excluding Fe) in the shell and core of the particles is lower than 0.5 at% and does not seem to play an important role in affecting the structure of nanoclusters. The formation of the core/shell structure in our study is possibly due to a segregation of elements to the particle/matrix interface. As Ta and Y have a higher affinity for O than Cr and V, Ta and Y tend to bind with O in the particle core, while some of the Cr and V are pushed to the surrounding shell. Another possible reason proposed by Williams *et al.* [23] is that the shell can act as an interfacial phase in nanoparticles, lowering the surface energy and promoting the formation of nanoparticles.

The composition of ODS steels should be carefully designed to fulfil the requirements for the cladding structure in nuclear power plants. For example, the addition of Cr was to achieve a better corrosion resistance while W was used to replace Mo, Nb, and Ni in conventional ferritic steels to obtain low activation capability [22]. In this study, the important role of V and Ta in cluster formation is confirmed by an analysis of the mass spectrum of the evaporated particles. It has been revealed that, apart from ions and isotopes such as Cr^{+2}, V^{+2}, Y^{+3}, and O^{+}, a number of molecular ions, such as CrO_2^{+3}, YO^{+2}, VO^{+2}, VO_2^{+1}, TaO_2^{+1} and TaO_2^{+2}, were identified from the mass spectrum. It should be noted that the evaporation of such ions is possible only if there is a large affinity between the atoms [33]. It is likely that there is a competition effect between Cr, Y, V and Ta binding with O when forming nanoclusters, suggesting how and why Cr, V and Ta solute elements enter the core of Y_2O_3 particles. However, whether the formation of Y_2O_3 particles occurs before or after the oxidation of vanadium and tantalum is beyond the scope of this study. Considering the high level of V and Ta in the nanoclusters irrespective of size and composition, at least it cannot be excluded that V and Ta can act as nucleation sites for Y_2O_3 clusters.

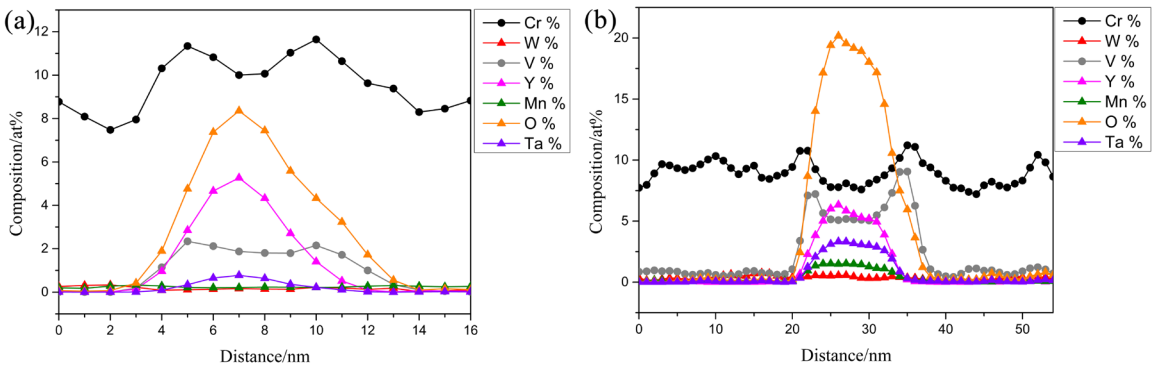


Figure 5.13. Composition profiles along the direction of analysis, intercepting a representative particle in (a) ODS Eurofer and (b) ODS Eurofer–2V–1.2Ta.

By subtracting the O atoms in molecular ions composed of Cr, V, Ta and O, the calculated Y/O ratios at the core of the small and large particle in Figure 5.13 are around 1.58 and 0.69, respectively. According to Williams *et al.* [23] and Miller *et al.* [34], oxygen atoms in the clusters in ODS steels generally have a greater radius of gyration than the segregated metal atoms. This could cause a slightly underestimated oxygen level when using the maximum separation method to define clusters. Therefore, the core of the larger particle is likely to have Y_2O_3 stoichiometry, assuming that the actual Y/O ratio is close to 0.67. This finding is consistent with the results found by Sakasegawa *et al.* [35] and He *et al.* [36], which concluded that the composition of nanoclusters could be affected by their size and the larger particles tend to have a stable phase of yttrium oxide (Y_2O_3).

5.3.3 Dislocation density measurement

The dislocation density of the as-produced, normalised (1423 K) and tempered steels was calculated from XRD measurements. Assuming that peak broadening is caused by dislocations only, the full width at half maximum (FWHM) of the diffraction profiles can be given by a modified Williamson-Hall plot in quadratic form [37, 38]:

$$\Delta K \cong \frac{0.9}{D} + \left(\frac{\pi M^2 b^2}{2}\right)\rho^{\frac{1}{2}} K^2 \overline{C} + O(K^4 \overline{C}^2), \qquad (5.1)$$

where ΔK is the full width at half maximum, D is the average grain size, $K = 2sin\theta/\lambda$, θ is the diffraction angle, λ is the wavelength of the X-rays, M is a constant parameter depending on the effective outer cut-off radius of dislocations and is taken as 2 [39], b is the Burgers vector, ρ is the dislocation density and O indicates non-interpreted higher order terms. $\overline{C}$ is an average contrast factor of dislocations and is estimated by [40]:

$$\overline{C} = \overline{C_{h00}}\left[1 - q\frac{h^2k^2 + h^2l^2 + k^2l^2}{\left(h^2 + k^2 + l^2\right)^2}\right], \qquad (5.2)$$

where $\overline{C_{h00}}$ is the average dislocation contrast factor for the (h00) reflection and is taken as 0.332 [39], q is a parameter that depends on the elastic constants of the crystal and the edge or screw character of dislocations.

To estimate the dislocation density, equation (5.1) can be approximated to [37]:

$$\Delta K^2 \cong \left(\frac{0.9}{D}\right)^2 + \left(\frac{\pi M^2 b^2}{2}\right) \rho K^2 \overline{C}. \tag{5.3}$$

Combining equations (5.2) and (5.3), the following relationship can be obtained:

$$\frac{\Delta K^2 - \left(\frac{0.9}{D}\right)^2}{K^2} \cong \left(\frac{\pi M^2 b^2}{2}\right) \rho \overline{C_{h00}} \left[1 - q \frac{h^2k^2 + h^2l^2 + k^2l^2}{\left(h^2 + k^2 + l^2\right)^2}\right]. \tag{5.4}$$

The dislocation density ρ can therefore be determined by the intercept of equation (5.4), plotting the left-hand side against the factor which is multiplied by q. The result of the estimated dislocation density of the materials at different conditions is presented in Table 5.5.

As expected, the dislocation density of the normalised steel is significantly increased compared to the as-produced steel due to the martensite transformation. Meanwhile, the dislocation density in the tempered steel is notably lower than the as-produced steel and normalised steel, which can be ascribed to static recovery during the tempering treatment. In the recovery process, the stored energy in the material decreases due to the change in the dislocation structure and growth of the subgrains [41]. Additionally, according to a study of Sandim *et al.* [42] on the annealing behaviour of ODS Eurofer, dislocation annihilation and/or rearrangement occurs when the heat treatment temperature is in the α-ferritic regime, resulting in a decrease in dislocation density.

Table 5.5 Dislocation density of the materials at different conditions.

	As-produced steel	Normalised steel (1423 K)	Tempered steel
Dislocation density/m^{-2}	2.2×10^{14}	9.4×10^{14}	8.9×10^{13}

5.3.4 Tensile properties investigation

5.3.4.1 Results of tensile properties measurement

The tensile properties of the tempered steel are presented in Figure 5.14 (a). Compared to the results of the as-produced material (Figure 4.11), the strength of the heat-treated samples is decreased, while the elongation is increased after annealing and tempering. Meanwhile, the tensile properties of all specimens are relatively uniform, indicating a more homogenous mechanical behaviour of the material. These results can be explained by the redistribution of

carbon atoms, recovery of dislocations and decomposition of brittle martensite during the heat treatment. This is supported by the results of carbon content obtained by combustion analysis. As can be seen in Figure 5.14 (b), the difference of the carbon content in the tempered tensile specimens has almost been eliminated. A more homogenous microstructure and thereby mechanical properties can be achieved under this condition.

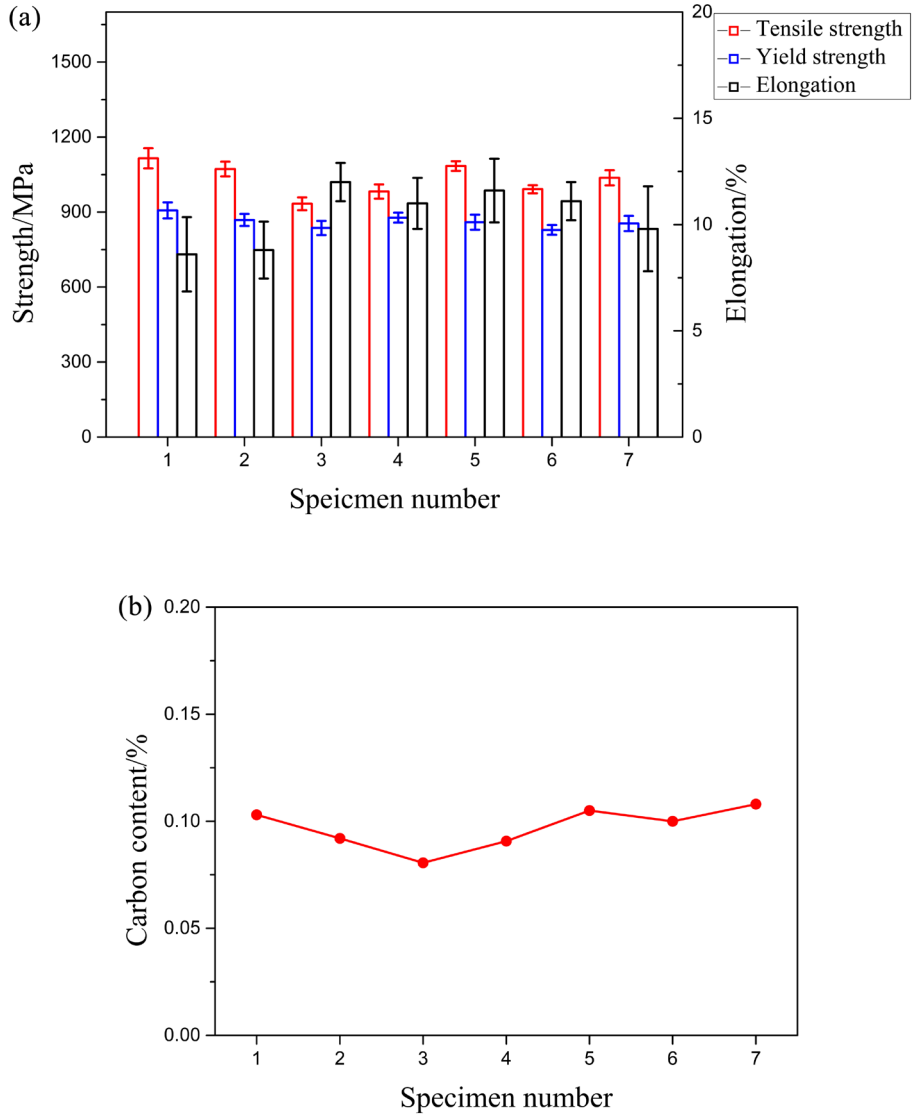


Figure 5.14. (a) Ultimate tensile strength, yield strength and elongation of the tempered steel at the location indicated in Figure 5.1 (b). (b) Carbon content of the tempered steel.

The fracture surfaces from tensile testing observed by SEM are presented in Figure 5.15. The fracture of the tempered steel shows larger dimples compared to that of the as-produced samples (Figure 4.13), showing the benefits of the heat treatment. It is notable that the size of the dimples observed in the fractures also appears to be bimodal, which can probably be ascribed to the bimodal grain structure. In recent studies, it has been demonstrated that materials having bimodal microstructures yield balance between strength and ductility, where the

ultrafine grains induce high strength as expected from an extrapolation of the Hall-Petch relationship, and the coarse grains provide substantial strain-hardening, therefore ensure retained ductility [43-45]. In the early stages of tensile loading, the coarse grain regions experienced yielding prior to the ultrafine grain regions. This would cause a slight decrease of the yield strength compared to fully ultrafine grain samples. However, due to the high work hardening capacity of the coarse grain material, the strength of the bimodal structure is not significantly weakened [46]. As shown in Figure 5.15 (b), the cracks initiated more easily at the fine grain/coarse grain interfaces due to stress mismatch. The cracks started to propagate until reaching the ductile coarse grain region with additional plastic deformation, leading to the inhibition or even termination of crack growth. Consequently, plastic strain accumulates in the structure and the strain hardening stage is extended before fracture occurs. The ductility of the specimen is therefore improved through this ductile-phase toughing mechanism [47].

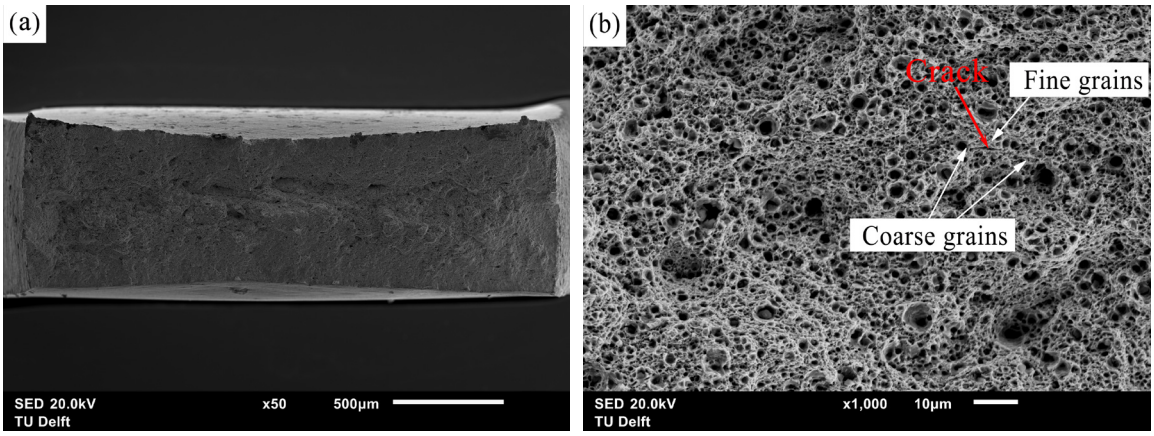


Figure 5.15. Fracture surfaces of the tempered steel after tensile testing.

Figure 5.16 summarises the elongation as a function of tensile strength of the as-produced and heat-treated ODS Eurofer compared to those reported in references. Results of the ODS Fe–9Cr steel were also collected and compared due to the limited amount of data available on ODS Eurofer. It can be seen that all of the published results of the SPS-produced steels are on the left side of the figure (black and green symbols), showing either poor strength or elongation. In comparison, the results in this study reveal a good combination between high strength and reasonable ductility. From the figure, it is also evident that the results of this study are comparable to the HIP and HE prepared ODS Eurofer. Considering the remarkably lower pressure and time needed for consolidation, SPS shows significant potential as a cost-effective technique to produce high performance ODS Eurofer.

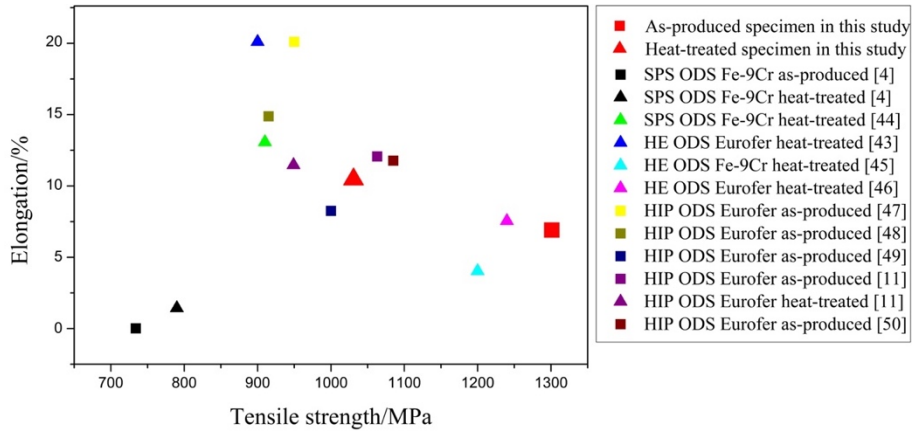


Figure 5.16. Elongation versus tensile strength of the as-produced and heat-treated ODS Eurofer compared to those in references [4, 48-51].

5.3.4.2 Yield strength modelling

From the results of the microstructure characterisation, it is shown that ODS Eurofer consists of steel matrix, precipitates, a bimodal grain size distribution, dislocations and nanoparticles. All of these features contribute to the mechanical properties of the material. To further quantify the contributions of each microstructural component, the following equation is used to estimate the yield strength of the steel at room temperature [52]:

$$\sigma_y=\sigma_0+\sigma_{ss}+\sigma_{GB}+(\sigma_{Dis}^n+\sigma_P^n)^{1/n}, \quad (5.5)$$

where σ_y is the yield strength of the material, σ_0 is friction stress of a single crystal of pure iron, σ_{ss} is the solid solution contribution, σ_{GB} is the grain boundary contribution, σ_{dis} is the forest dislocation hardening contribution, σ_p is the nano-sized oxide particles contribution and n is taken as 2 [52].

σ_{ss} is classically estimated with the following equation:

$$\sigma_{ss}=\sum_i K_i \cdot X_i^Z, \quad (5.6)$$

where K_i a hardening constant, X_i is the atomic fraction of element I, and z equals 0.75 for substitutional solid solution elements *i.e.* Cr and W [53].

σ_{GB} is usually expressed by the Hall-Petch equation [54, 55]:

$$\sigma_{GB}=\frac{k_{GB}}{\sqrt{D}}, \quad (5.7)$$

where k_{GB} is the Hall-Petch coefficient and D is the mean grain size of the material, as shown in Table 5.2.

σ_{dis} can be described according to Taylor [56] with the following equation:

$$\sigma_{dis}=M\alpha Gb\sqrt{\rho}, \tag{5.8}$$

where M is the Taylor factor that depends on the crystallographic structure and the texture of the material, α is a numerical constant, G is the shear modus for iron, b is the Burgers vector and ρ the dislocation density.

The contribution of nano-sized oxide particles σ_p is estimated by Ashby-Orowan equation [57]:

$$\sigma_p=\frac{0.81MGb}{2\pi(1-\nu)^{1/2}}\frac{\ln(2r_s/r_0)}{\lambda-2r_s} \tag{5.9}$$

$$\lambda=2\sqrt{\frac{2}{3}}r\left[\left(\frac{\pi}{4f}\right)^{1/2}-1\right], \tag{5.10}$$

where r is the radius of oxide particles obtained by TEM, $r_s = 0.816 \times r$ is the mean planar radius of the cross-section of nano-sized oxides, r_0 is the inner cut-off radius of a dislocation core, which is assumed to be the magnitude of the Burgers vector, λ is the average inter-particle spacing, υ is the Possion ratio and f is the volume fraction of nano-sized oxides, which is estimated by the following equation [5]:

$$f=1.5618\times10^{-2}\times(\text{wt.\% } Y_2O_3). \tag{5.11}$$

Using the above equations for each strengthening component and the parameters listed in Table 5.6, the experimentally obtained and theoretically estimated yield strength of the as-produced and tempered steels are presented in Figure 5.17. The estimated value of the as-produced steel is within the deviation range of the experimental result, indicating a good agreement. A small deviation between the estimated and experimental values of the tempered steel is found, which may be due to the neglect of the contribution of coarsened carbides. Another possible explanation is that, as mentioned in section 5.3.2, finer grains smaller than 0.29 μm were neglected when calculating the average grain size, which will cause a slightly underestimated strength. It is evident that the oxide dispersion strengthening, dislocation strengthening and grain boundary strengthening are the major contributions to the yield strength of the as-produced ODS Eurofer at room temperature. The contributions of nanoparticles, dislocations and grain size are 36%, 22% and 27%, respectively. In the tempered steel, as the dislocation density in the material is decreased considerably, while the average size of the oxide particles and the mean grain size do not change significantly, the contributions of nanoparticles, dislocations and grain size are 37%, 15% and 31%, respectively. The oxide dispersion strengthening and grain boundary strengthening are the dominant strengthening mechanisms in the tempered ODS Eurofer.

Table 5.6 Parameters used for the yield strength model.

Parameters	Values and references
σ_0/MPa	53.9 [58]
K_{Cr}/(MPa·at%$^{-3/4}$)	9.95 [59]
K_W/(MPa·at%$^{-3/4}$)	75.79 [56]
k_{GB}/(MPa·μm$^{1/2}$)	210 [60]
M	3.06 [58]
α	0.38 [58]
G/GPa	81.6 [58]
b/nm	0.25 [5]
υ	0.334 [58]

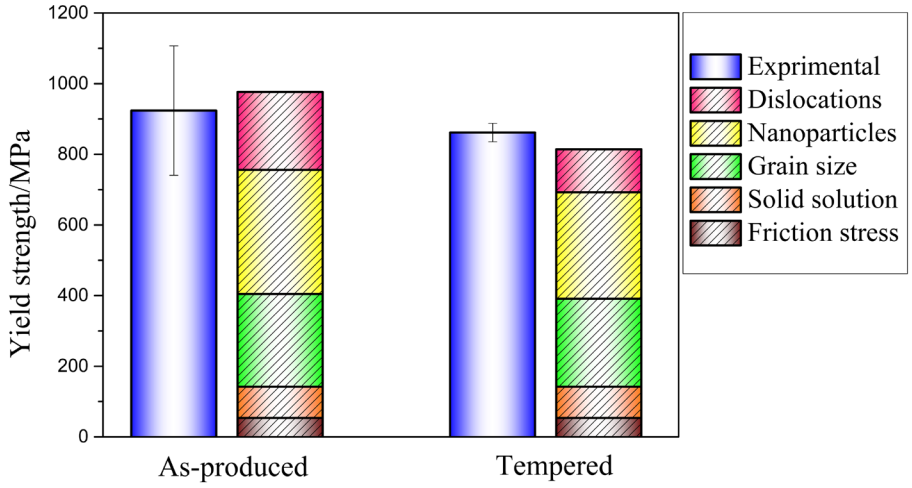


Figure 5.17. The experimental and estimated yield strength of the as-produced and tempered ODS Eurofer.

5.4 Conclusions

A heat treatment route was designed for powder metallurgy prepared ODS Eurofer steel. The microstructure and mechanical properties of the as-produced and heat-treated steel were investigated in detail. The following conclusions can be drawn:

1. The condition of normalising at 1423 K for 1 h and tempering at 973 K for 1 h is determined to be a suitable heat treatment route for the as-produced steel to homogenise the microstructure and microhardness.

2. The material has a bimodal grain size distribution and a dual phase microstructure in both as-produced and tempered conditions. High-density Y_2O_3-rich nanoparticles remain dispersed in the steel matrix after the heat treatment, acting as obstacles for the motion of dislocations and grain boundaries.

3. The nanoclusters have a number density of 2.44×10^{23} m^{-3} with an average gyration diameter of 4.13 nm in ODS Eurofer in comparison with a number density 5.15×10^{23} m^{-3} with an average diameter of 2.96 nm in ODS Eurofer–2V–1.2Ta. The addition of V and Ta appears to influence and promote the formation of small, high density nanoparticles. There is a

difference in composition between the small particles (< 4 nm) and large particles (around 5–15 nm). The small particles have a variable stoichiometry while the large particles are likely to have Y_2O_3 stoichiometry. Cross-sectional composition measurements show that the nanoparticles have a core/shell structure. Yttrium, O and Ta are found to be enriched in the core whereas Cr and V are predominantly present in the shell, which is possibly due to a competition of elements binding with O.

4. The as-produced steel has a high dislocation density of 2.2×10^{14} m^{-2}, with $M_{23}C_6$ and M_6C carbides in the microstructure. Comparatively, the tempered steel has a lower dislocation density of 8.9×10^{13} m^{-2}, with $M_{23}C_6$ carbides decorating the grain boundaries.

5. The heat-treated ODS Eurofer exhibits a good combination of high strength and reasonable ductility and a relatively uniform mechanical behaviour compared to the as-produced material. Fracture analysis shows a ductile failure with well-defined dimples. SPS has shown advantages as a cost-effective consolidation approach to produce ODS Eurofer with comparable quality to HIP and HE at significantly lower pressures and times.

6. Oxide dispersion strengthening, dislocation strengthening and grain boundary strengthening are the major contributions to the yield strength of the as-produced ODS Eurofer, while oxide dispersion strengthening and grain boundary strengthening are the dominant strengthening mechanisms in the tempered ODS Eurofer.

References

[1] M. Suárez, A. Fernández-Camacho, J.L. Menéndez, R. Torrecillas, Challenges and opportunities for spark plasma sintering: a key technology for a new generation of materials, InTech2013.

[2] X. Boulnat, M. Perez, D. Fabregue, T. Douillard, M.H. Mathon, Y.D. Carlan, Microstructure evolution in nano-reinforced ferritic steel processed by mechanical alloying and spark plasma sintering, Metall. Mater. Trans. A 45(3) (2014) 1485-1497.

[3] S. Noh, A. Kimura, T.K. Kim, Diffusion bonding of 9Cr ODS ferritic/martensitic steel with a phase transformation, Fusion Eng. Des. 89(7-8) (2014) 1746-1750.

[4] Q.X. Sun, Y. Zhou, Q.F. Fang, R. Gao, T. Zhang, X.P. Wang, Development of 9Cr-ODS ferritic-martensitic steel prepared by chemical reduction and mechanical milling, J. Alloys Compd. 598 (2014) 243-247.

[5] X. Zhou, Y. Liu, L. Yu, Z. Ma, Q. Guo, H. Yuan, H. Li, Microstructure characteristic and mechanical property of transformable 9Cr-ODS steel fabricated by spark plasma sintering, Mater. Des. 132 (2017) 158-169.

[6] E. Wielgosz, T. Kargul, Differential scanning calorimetry study of peritectic steel grades, J. Therm. Anal. Calorim. 119(3) (2015) 1547-1553.

[7] Z. Lu, R.G. Faulkner, N. Riddle, F.D. Martino, K. Yang, Effect of heat treatment on microstructure and hardness of Eurofer 97, Eurofer ODS and T92 steels, J. Nucl. Mater. 386-388(C) (2009) 445-448.

[8] S.S. Wang, D.L. Peng, L. Chang, X.D. Hui, Enhanced mechanical properties induced by refined heat treatment for 9Cr–0.5Mo–1.8W martensitic heat resistant steel, Mater. Des. 50(17) (2013) 174-180.
[9] B. Silwal, L. Li, A. Deceuster, B. Griffiths, Effect of postweld heat treatment on the toughness of heat-affected zone for grade 91 steel, Weld. J. 92 (2013) 80-87.
[10] M. Yamamoto, S. Ukai, S. Hayashi, T. Kaito, S. Ohtsuka, Formation of residual ferrite in 9Cr-ODS ferritic steels, Mater. Sci. Eng., A 527(16) (2010) 4418-4423.
[11] C. Cayron, E. Rath, I. Chu, S. Launois, Microstructural evolution of Y_2O_3 and $MgAl_2O_4$ ODS EUROFER steels during their elaboration by mechanical milling and hot isostatic pressing, J. Nucl. Mater. 335(1) (2004) 83-102.
[12] X.L. Wang, C.T. Liu, U. Keiderling, A.D. Stoica, L. Yang, M.K. Miller, C.L. Fu, D. Ma, K. An, Unusual thermal stability of nano-structured ferritic alloys, J. Alloys Compd. 529 (2012) 96-101.
[13] N. Sallez, X. Boulnat, A. Borbély, J.L. Béchade, D. Fabrègue, M. Perez, Y. de Carlan, L. Hennet, C. Mocuta, D. Thiaudière, Y. Bréchet, In situ characterization of microstructural instabilities: Recovery, recrystallization and abnormal growth in nanoreinforced steel powder, Acta Mater. 87 (2015) 377-389.
[14] I. Hilger, F. Bergner, T. Weißgärber, Bimodal Grain Size Distribution of Nanostructured Ferritic ODS Fe-Cr Alloys, J. Am. Ceram. Soc. 98(11) (2015) 3576-3581.
[15] N. Sallez, P. Donnadieu, E. Courtois-Manara, D. Chassaing, C. Kübel, F. Delabrouille, M. Blat-Yrieix, Y. de Carlan, Y. Bréchet, On ball-milled ODS ferritic steel recrystallization: From as-milled powder particles to consolidated state, J. Mater. Sci. 50(5) (2015) 2202-2217.
[16] K.D. Zilnyk, V.B. Oliveira, H.R. Sandim, A. Möslang, D. Raabe, Martensitic transformation in Eurofer-97 and ODS-Eurofer steels: A comparative study, J. Nucl. Mater. 462 (2015) 360-367.
[17] M. Taneike, K. Sawada, F. Abe, Effect of carbon concentration on precipitation behavior of $M_{23}C_6$ carbides and MX carbonitrides in martensitic 9Cr steel during heat treatment, Metall. Mater. Trans. A 35(4) (2004) 1255-1262.
[18] L. Zheng, X. Hu, X. Kang, D. Li, Precipitation of $M_{23}C_6$ and its effect on tensile properties of 0.3C-20Cr-11Mn-1Mo-0.35N steel, Mater. Des. 78 (2015) 42-50.
[19] B. Peng, H. Zhang, J. Hong, J. Gao, H. Zhang, Q. Wang, J. Li, The effect of $M_{23}C_6$ on the high-temperature tensile strength of two austenitic heat-resistant steels: 22Cr–25Ni–Mo–Nb–N and 25Cr–20Ni–Nb–N, Mater. Sci. Eng., A 528(10) (2011) 3625-3629.
[20] V. Pereira, H. Schut, J. Sietsma, A study of the microstructural stability and defect evolution in an ODS Eurofer steel by means of Electron Microscopy and Positron Annihilation Spectroscopy, J. Nucl. Mater. 540 (2020) 152398.
[21] M. Ohnuma, J. Suzuki, S. Ohtsuka, S.W. Kim, T. Kaito, M. Inoue, H. Kitazawa, A new method for the quantitative analysis of the scale and composition of nanosized oxide in 9Cr-ODS steel, Acta Mater. 57(18) (2009) 5571-5581.
[22] R. Lindau, A. Möslang, M. Rieth, M. Klimiankou, E. Materna-Morris, A. Alamo, A.-A. Tavassoli, C. Cayron, A.-M. Lancha, P. Fernandez, Present development status of EUROFER and ODS-EUROFER for application in blanket concepts, Fusion Eng. Des. 75 (2005) 989-996.

[23] C.A. Williams, E.A. Marquis, A. Cerezo, G.D. Smith, Nanoscale characterisation of ODS–Eurofer 97 steel: an atom-probe tomography study, J. Nucl. Mater. 400(1) (2010) 37-45.
[24] M. Klimenkov, R. Lindau, A. Möslang, TEM study of internal oxidation in an ODS-Eurofer alloy, J. Nucl. Mater. 386 (2009) 557-560.
[25] A. Aleev, N. Iskandarov, M. Klimenkov, R. Lindau, A. Möslang, A. Nikitin, S. Rogozhkin, P. Vladimirov, A. Zaluzhnyi, Investigation of oxide particles in unirradiated ODS Eurofer by tomographic atom probe, J. Nucl. Mater. 409(2) (2011) 65-71.
[26] V. De Castro, E. Marquis, S. Lozano-Perez, R. Pareja, M. Jenkins, Stability of nanoscale secondary phases in an oxide dispersion strengthened Fe–12Cr alloy, Acta Mater. 59(10) (2011) 3927-3936.
[27] M. Ohnuma, J. Suzuki, S. Ohtsuka, S.-W. Kim, T. Kaito, M. Inoue, H. Kitazawa, A new method for the quantitative analysis of the scale and composition of nanosized oxide in 9Cr-ODS steel, Acta Mater. 57(18) (2009) 5571-5581.
[28] C. Hatzoglou, B. Radiguet, P. Pareige, Experimental artefacts occurring during atom probe tomography analysis of oxide nanoparticles in metallic matrix: Quantification and correction, J. Nucl. Mater. 492 (2017) 279-291.
[29] Y. Templeman, S. Rogozhkin, A. Khomich, A. Nikitin, M. Pinkas, L. Meshi, Characterization of nano-sized particles in 14% Cr oxide dispersion strengthened (ODS) steel using classical and frontier microscopy methods, Mater. Charact. 160 (2020) 110075.
[30] A. Das, P. Chekhonin, E. Altstadt, F. Bergner, C. Heintze, R. Lindau, Microstructural characterization of inhomogeneity in 9Cr ODS EUROFER steel, J. Nucl. Mater. (2020) 152083.
[31] D. Murali, B. Panigrahi, M. Valsakumar, S. Chandra, C. Sundar, B. Raj, The role of minor alloying elements on the stability and dispersion of yttria nanoclusters in nanostructured ferritic alloys: An ab initio study, J. Nucl. Mater. 403(1-3) (2010) 113-116.
[32] Y.-R. Luo, Comprehensive handbook of chemical bond energies, CRC press2007.
[33] S. Rogozhkin, A. Aleev, A. Zaluzhnyi, N. Iskanderov, A. Nikitin, P. Vladimirov, R. Lindau, A. Möslang, Atom probe tomography of nanoscaled features of oxide-dispersion-strengthened ODS Eurofer steel in the initial state and after neutron irradiation, The Physics of Metals and Metallography 113(1) (2012) 98-105.
[34] M. Miller, E. Kenik, K. Russell, L. Heatherly, D. Hoelzer, P. Maziasz, Atom probe tomography of nanoscale particles in ODS ferritic alloys, Mater. Sci. Eng., A 353(1-2) (2003) 140-145.
[35] H. Sakasegawa, F. Legendre, L. Boulanger, M. Brocq, L. Chaffron, T. Cozzika, J. Malaplate, J. Henry, Y. de Carlan, Stability of non-stoichiometric clusters in the MA957 ODS ferrtic alloy, J. Nucl. Mater. 417(1-3) (2011) 229-232.
[36] J. He, F. Wan, K. Sridharan, T.R. Allen, A. Certain, V. Shutthanandan, Y. Wu, Stability of nanoclusters in 14YWT oxide dispersion strengthened steel under heavy ion-irradiation by atom probe tomography, J. Nucl. Mater. 455(1-3) (2014) 41-45.
[37] T. Ungár, J. Gubicza, P. Hanák, I. Alexandrov, Densities and character of dislocations and size-distribution of subgrains in deformed metals by X-ray diffraction profile analysis, Mater. Sci. Eng., A 319 (2001) 274-278.

[38] Z. Arechabaleta, P. van Liempt, J. Sietsma, Quantification of dislocation structures from anelastic deformation behaviour, Acta Mater. 115 (2016) 314-323.
[39] R.A. Renzetti, H.R.Z. Sandim, R.E. Bolmaro, P.A. Suzuki, A. Möslang, X-ray evaluation of dislocation density in ODS-Eurofer steel, Mater. Sci. Eng., A 534 (2012) 142-146.
[40] T. Ungár, G. Tichy, The Effect of Dislocation Contrast on X-Ray Line Profiles in Untextured Polycrystals, Phys. Status Solidi 171(2) (1999) 425-434.
[41] B. Kim, D. Sanmartin, P.E.J. Riveradíazdelcastillo, Modelling recovery kinetics in high-strength martensitic steels, Philos. Mag. Lett. 97(7) (2017) 280-286.
[42] H.R.Z. Sandim, R.A. Renzetti, A.F. Padilha, D. Raabe, M. Klimenkov, R. Lindau, A. Möslang, Annealing behavior of ferritic–martensitic 9%Cr–ODS–Eurofer steel, Mater. Sci. Eng., A 527(15) (2010) 3602-3608.
[43] D. Zhao, L. Yong, L. Feng, Y. Wen, L. Zhang, Y. Dou, ODS ferritic steel engineered with bimodal grain size for high strength and ductility, Mater. Lett. 65(11) (2011) 1672-1674.
[44] G. Dirras, J. Gubicza, S. Ramtani, Q.H. Bui, T. Szilágyi, Microstructure and mechanical characteristics of bulk polycrystalline Ni consolidated from blends of powders with different particle size, Mater. Sci. Eng., A 527(4-5) (2010) 1206-1214.
[45] Z. Zhang, S.K. Vajpai, D. Orlov, K. Ameyama, Improvement of mechanical properties in SUS304L steel through the control of bimodal microstructure characteristics, Mater. Sci. Eng., A 598 (2014) 106-113.
[46] J.G. Sevillano, J. Aldazabal, Ductilization of nanocrystalline materials for structural applications, Scripta Mater. 51(8) (2004) 795-800.
[47] Z. Lee, V. Radmilovic, B. Ahn, E.J. Lavernia, S.R. Nutt, Tensile Deformation and Fracture Mechanism of Bulk Bimodal Ultrafine-Grained Al-Mg Alloy, Metall. Mater. Trans. A 41(4) (2010) 795-801.
[48] X. Zhou, Y. Liu, L. Yu, Z. Ma, Q. Guo, Y. Huang, H. Li, Microstructure characteristic and mechanical property of transformable 9Cr-ODS steel fabricated by spark plasma sintering, Mater. Des. 132 (2017) 158-169.
[49] P. Olier, A. Bougault, A. Alamo, Y. De Carlan, Effects of the forming processes and Y_2O_3 content on ODS-Eurofer mechanical properties, J. Nucl. Mater. 386 (2009) 561-563.
[50] S. Ukai, S. Mizuta, M. Fujiwara, T. Okuda, T. Kobayashi, Development of 9Cr-ODS martensitic steel claddings for fuel pins by means of ferrite to austenite phase transformation, J. Nucl. Sci. Technol. 39(7) (2002) 778-788.
[51] E. Lucon, Mechanical tests on two batches of oxide dispersion strengthened RAFM steel (EUROFER97), Fusion Eng. Des. 61 (2002) 683-689.
[52] J. Shen, Y. Li, F. Li, H. Yang, Z. Zhao, S. Kano, Y. Matsukawa, Y. Satoh, H. Abe, Microstructural characterization and strengthening mechanisms of a 12Cr-ODS steel, Mater. Sci. Eng., A 673 (2016) 624-632.
[53] P. Susila, D. Sturm, M. Heilmaier, B.S. Murty, V.S. Sarma, Effect of yttria particle size on the microstructure and compression creep properties of nanostructured oxide dispersion strengthened ferritic (Fe–12Cr–2W–0.5Y_2O_3) alloy, Mater. Sci. Eng., A 528(13) (2011) 4579-4584.

[54] E.O. Hall, The Deformation and Ageing of Mild Steel: III Discussion of Results, Proc. Phys. Soc. Sect. B 64(9) (1951) 747-753.
[55] N.J. Petch, The Cleavage Strength of Polycrystals, J. Iron Steel Inst. 174 (1953) 25-28.
[56] G.I. Taylor, The Mechanism of Plastic Deformation of Crystals. Part I. Theoretical, Proc. Roy. Soc. A 145(855) (1934) 362-387.
[57] J.W. Martin, Micromechanisms in particle-hardened alloys, Cambridge University1980.
[58] F.B. Pickering, Physical metallurgy and the design of steels, Applied Science Publishers, London, 1978.
[59] M. Couvrat, Fabrication d'aciers ODS à haute performance: relation procédé, microstructure, propriétés mécaniques, University of Rennes 1, 2013.
[60] D. Preininger, Effect of particle morphology and microstructure on strength, work-hardening and ductility behaviour of ODS-(7–13)Cr steels, J. Nucl. Mater. 329(1) (2004) 362-368.

6

Additive manufacturing of ODS Eurofer by direct metal deposition

6.1 Introduction

As presented in chapter 4 and 5, ODS Eurofer with desired microstructures and good mechanical properties can be prepared by the conventional powder metallurgy route. However, the complex mechanical alloying process has the drawbacks of long manufacturing times, high costs, an inhomogeneous distribution of nanoparticles within the steel, etc [1]. These drawbacks hinder the widespread application of ODS steels despite their promising high temperature performance. Moreover, spark plasma sintering (SPS) was reported in the previous chapters to realise an efficient consolidation of ODS Eurofer powder at a lower temperature and pressure compared to conventional techniques. However, SPS is only capable of producing simple symmetrical shapes such as cylindrical designs and disks. Upscaling of material production with complex geometry is therefore not feasible. Furthermore, element diffusion from the mould material could cause the final microstructure and mechanical properties to be heterogeneous [2]. Therefore, the evaluation and development of alternative methods to produce ODS steels is under intense investigations with the aim of achieving both scalable and consistent properties [3].

Laser additive manufacturing processing provides a potential alternative for the fabrication of ODS steels. The localised heat input facilitates the generation of surface tension gradients (Marangoni effect) and a very high cooling rate (around 10^6 K s^{-1}) in the melt pool [4], thereby facilitating the retention of nano-oxide particles in the build. Additionally, it offers potential benefits over conventional techniques, including short manufacturing times, low manufacturing costs, high material utilisation and high flexibility in terms of fabricating large and complex parts. In particular, direct metal deposition (DMD, also referred to as laser engineered net shaping) is one of the most widely used laser additive manufacturing techniques. In this process, metal powders or wires are fed on the surface of a solid substrate in a controlled manner by continuous injection through coaxial nozzles [5]. A focused laser heat source is used to melt the metallic feedstock and produce three-dimensional near-net-shape metal parts [6]. Direct metal deposition provides a high deposition rate and a relatively wide process window to fabricate large items compared to other metal-based additive manufacturing techniques.

Previous work on using DMD to produce metals and alloys has been mainly focused on titanium alloys [7], steels (low carbon, mild, stainless, duplex, and etc.) [8] and nickel-based superalloys [9]. Research on fabricating ODS alloys is very limited and still in an early stage. A Zr-containing ODS-FeCrAl alloy was manufactured by Shi *et al.* [10] using DMD and post heat treatment. Slag-like layers containing coarse oxides were observed at the surface of the deposited material. Post heat treatment was found to promote the reprecipitation of nanoscale oxides $Y_4Zr_3O_{12}$, leading to an increase of tensile properties. The feasibility of DMD for producing an ODS steel with a nominal composition of Fe–13.8Cr–0.45Si–0.21Mn–0.2Ti–0.3 Y_2O_3 (wt%) was studied by Euh *et al.* [11]. No significant pore formation was observed under all laser deposition conditions. However, the alloy fabricated by DMD exhibited larger Y_2O_3 clusters (around 45 μm) and grain size (100–200 μm) and lower microhardness than bulk ODS steel produced by a typical powder metallurgy route. Kenel *et al.* [12] reported the microstructure features of an ODS Ti–45Al–3Nb alloy processed by DMD and spark plasma

sintering, respectively. The material prepared by DMD revealed a microstructure with coarser grains. Meanwhile, only 41% of the dispersoids were retained in the material, compared to the alloy fabricated by spark plasma sintering.

In the present study, ODS Eurofer steel was fabricated by the DMD technique, however, with limited processing conditions due to time limitation. The effect of laser power on the microstructure and mechanical properties of the printed steels were investigated. The feasibility of DMD was revealed by comparing to the results obtained from the powder metallurgy route.

6.2 Experimental details

ODS Eurofer powders were prepared in a Retsch planetary ball milling machine under an argon atmosphere for 16 h at 300 rpm. Subsequently, the powders were sieved and had a size distribution within the range of 50–100 μm. The mechanical alloyed powders were characterised by differential scanning calorimetry (DSC) to study their thermal behaviour upon heating and cooling. The powders were heated to 1273 K at a rate of 10 K/min and held for 20 min. Subsequently, the powder was cooled to room temperature at a rate of 10 K/min. The test was operated in an argon atmosphere with a flow rate of 100 ml/min.

ODS Eurofer was produced by the DMD process as described in chapter 3. Three different laser powers were used: 600 W, 800 W and 1000 W. The steels printed using these conditions are referred to as DMD_600 W, DMD_800 W and DMD_1000 W in the following text. In order to consolidate the internal pores within the build, DMD_800 W alloy was further treated by hot isostatic pressing (HIP) at a temperature of 1373 K and a pressure of 100 MPa for 2 h.

The printed steels were characterised by various means of microscopy analysis, including optical microscopy (OM), electron backscatter diffraction (EBSD) and transmission electron microscopy (TEM). The density and microhardness of the steels produced by different conditions were measured. In order to evaluate local micromechanical properties of different phases in the microstructure, nanoindentation experiments were conducted using MTS Nano Indenter XP with a Berkovich tip using the continuous stiffness measurement mode. Load controlled indentations with an applied force of 10 mN and spacing of 10 μm between the indents were employed. This spacing value was chosen based on the grain size of ODS Eurofer to collect enough statistical data over the microstructural components.

6.3 Results and discussion

6.3.1 Powder characterisation

Figure 6.1 shows the SEM morphology of the mechanical alloyed powders before and after sieving. As seen in Figure 6.1(a), after 16 h of mechanical alloying, the powders have a size variation between 10–120 μm. In order to meet the flowability requirement for the DMD and have a stable injection into the melt pool, the powders were sieved and have a size distribution between 50–100 μm (Figure 6.1(b)). The powders show an irregular shape and a severe deformation at the surface, due to repeated fracturing and cold welding during the ball milling process.

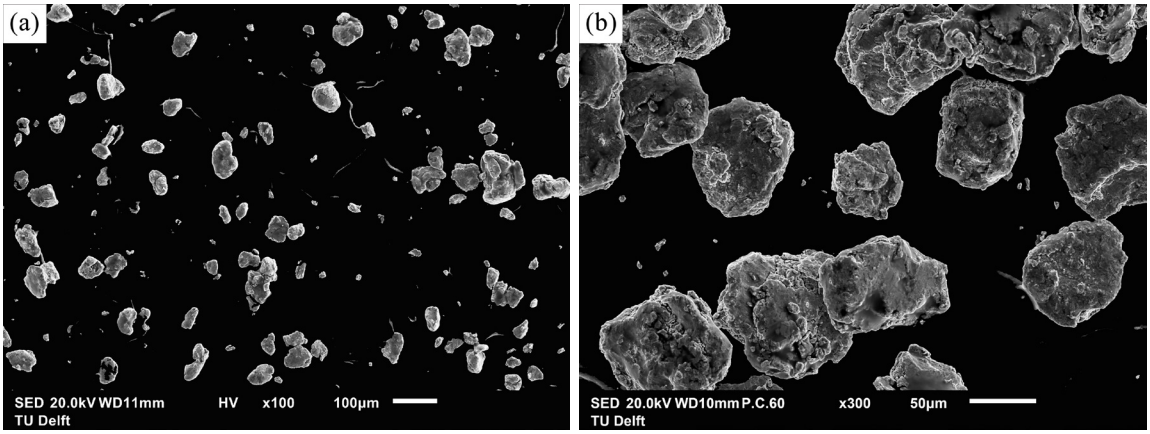


Figure 6.1. SEM morphology of the mechanical alloyed powders: (a) before sieving and (b) after sieving.

The DSC profile of mechanical alloyed powders obtained during heating and cooling is shown in Figure 6.2. In the heating stage, the first endothermic peak is related to the magnetic transformation at the Curie temperature. The second peak is associated with austenite transformation, with the starting temperature (Ac1) and finishing temperature (Ac3) of about 1130 K and 1207 K, respectively. In the cooling stage, the first exothermic peak is caused by the Curie transition. The second peak is due to martensite transformation, with the starting temperature (M_s) and finishing temperature (M_f) of 747 K and 541 K, respectively. The DSC result confirmed that martensite can be formed at a cooling rate of 10 K/min. It is well known that DMD process has the characteristics of rapid cooling, which may promote the austenite–martensite transformation. However, the presence of nano-oxide particles in the steel matrix may suppress phase transformations. The microstructural constituents of the printed steel were therefore confirmed by EBSD analysis.

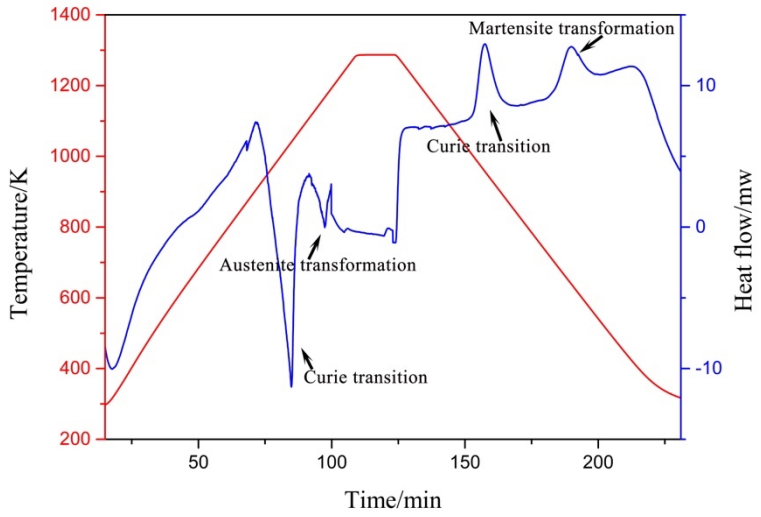


Figure 6.2. DSC profile of the mechanical alloyed powder obtained during heating and cooling schedule.

6.3.2 Microstructure characterisation

Direct metal deposition was carried out using the mechanical alloyed powders with different laser powers of 600 W, 800 W and 1000 W. The chemical composition of the powder and printed steels was analysed by X-ray fluorescence, as shown in Table 1. Results of carbon were omitted due to its lightweight nature. It can be seen that the chemical composition of the DMD_600 W and DMD_800 W samples are very close to that of the powder. The yttrium content in these conditions is slightly lower than that in the powder. However, no yttrium was found in the DMD_1000 W sample, indicating a complete loss of Y_2O_3 during the printing process. A higher laser power would cause a larger melt pool as well as a slower solidification rate. This will lead to a coarsening and floating of Y_2O_3 particles to the top of the melt pool, and consequently a Y_2O_3-depleted material. A small amount of Ni was found in all conditions, which is probably due to a partial melting of the substrate.

Table 6.1 Chemical composition of the ball milled powder and printed material in wt%.

	Cr	W	Mn	V	Ta	Y	Ni	Fe
Powder	9.10	1.05	0.43	0.20	0.15	0.22	–	Bal.
DMD_600 W	10.06	0.78	0.56	0.15	0.22	0.20	0.45	Bal.
DMD_800 W	10.91	0.84	0.55	0.20	0.36	0.19	0.18	Bal.
DMD_1000 W	11.42	0.79	0.54	0.12	–	–	1.97	Bal.

Optical micrographs of the steels produced by different conditions can be seen in Figure 6.3. In the condition of DMD_600 W (Figure 6.3 (a)), some narrow voids caused by partially melted powders can be observed, indicating an insufficient bonding of the powders. This finding reveals that an inadequate laser power may adversely affect the densification behaviour. Such a phenomenon is avoided with higher laser powers of 800 W and 1000 W (Figure 6.3 (c)). However, a large number of pores can be seen in these conditions, with a size of around 10–100 μm and 5–50 μm, respectively. Residual porosity in DMD manufactured steels could be caused either by the unfilled voids in the powders or trapped gas bubbles during printing [13]. Different forms of porosity may occur due to inappropriate process parameters, scan strategies, powder feedstock properties, etc., leading to an unstable building process.

Porosity in additive manufactured materials should be minimised to limit the adverse effect on mechanical properties and to ensure the consistency of produced parts [14]. Optimising processing conditions or using finer powders with less irregular particles were found to be effective for the reduction of porosity in the additive manufactured parts [15]. However, despite the best optimisation of the manufacturing process, the presence of small pores in additive manufactured parts seems to be inevitable. Post treatment is known to be effective to further reduce the porosity in additive manufactured builds. In particular, hot isostatic pressing (HIP) is a process in which materials are subjected to high temperature and pressure simultaneously to realise efficient consolidation [16]. Hot isostatic pressing has been widely accepted and used

to reduce porosity in the production chain of additively manufactured parts for aerospace applications [17, 18].

As the retaining of Y_2O_3 precipitates is crucial for the mechanical properties of ODS Eurofer, a laser power of 800 W is assumed to be a suitable printing condition. A subsequent HIP treatment was conducted to minimise the residual pores in the steel. As HIP is a solid-state consolidation technique, the distribution of Y_2O_3 nanoparticles in the material will not be significantly changed after the treatment. As can be seen in Figure 6.3 (d), the size of the pores has been reduced to 1–10 µm after HIP, which would be beneficial for the mechanical properties of the steel.

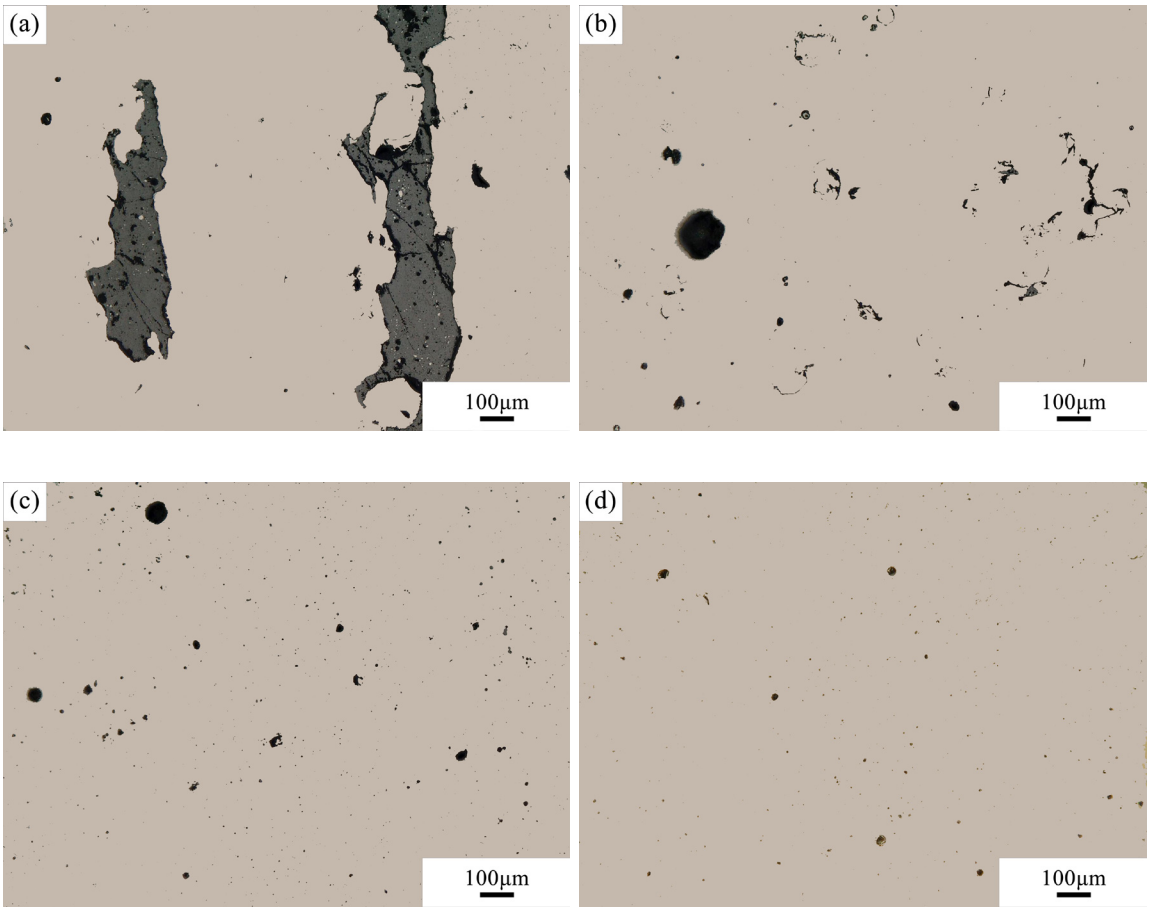


Figure 6.3. Optical micrographs of the printed material, (a): DMD_600 W, (b): DMD_800W, (c) DMD_1000W and (d): HIP DMD_800W.

The relative density and microhardness of the printed samples were measured and are shown in Table 6.2. As a comparison, the result of a spark plasma sintering (SPS) produced ODS Eurofer is also included in this table. It can be seen that the density and microhardness of the printed steels are lower than the SPS produced sample, probably due to a higher porosity and grain growth in the microstructure. The density of the printed steels increases with laser power, which agrees with the optical observation. The microhardness of the DMD_1000 W steels is significantly lower than other conditions, which can be ascribed to a combined effect of grain

growth as well as a lack of dispersion strengthening by Y_2O_3. Meanwhile, the DMD_800 W steel has the highest density and microhardness after the HIP treatment, demonstrating that HIP is an effective method to remove the residual pores without disrupting the microstructural features in the material.

Table 6.2 Relative density and microhardness of SPS and DMD produced material.

Conditions	Relative density/%	Microhardness/$HV_{0.3}$
SPS produced	99.2	477.1 ± 88.5
DMD_600 W	93.5	416.5 ± 34.7
DMD_800 W	95.7	410.9 ± 22.4
DMD_1000 W	96.9	331.5 ± 20.6
HIP DMD_800 W	98.5	422.1 ± 19.4

Figure 6.4 shows TEM images of the microstructural features of ODS Eurofer produced by different conditions. A high number density of nanoprecipitates (indicated by the arrows) can be observed in the SPS produced ODS Eurofer, with a size of 1–15 nm (Figure 6.4(a)). Finely dispersed nano-oxide particles can be obtained in the steel, thanks to the solid-state characteristic of SPS. The nanoparticles in the DMD_800 W steel are coarsened and have a size of 5–30 nm (indicated by the arrows in Figure 6.4(b)). Coarsening of Y_2O_3 is commonly found in additive manufactured ODS steels [14]. As soon as a molten pool is created, nanoparticle agglomeration will be aggressively promoted by the inter-particle forces in the liquid state. During DMD, repeated heating from the previously and subsequently deposited layers induces further particle coarsening. Moreover, compared to selective laser melting (another laser additive manufacturing technique), the solidification and cooling rates of DMD are generally lower (10^3–10^5 versus 10^4–10^6 K s^{-1}) [19, 20], providing a longer period of time for the agglomeration or motion of nano-precipitates. Nonetheless, the particle size distribution obtained in this study are comparable to that of selective laser melting prepared ODS steels (around 20–30 nm) [21, 22]. However, if the solidification rate is too slow, for instance, due to the employment of a high laser power, the nano-oxides tend to be removed from the microstructure due to the buoyancy effect and slag off to the surface of the melt pool. As shown in the Figure 6.4(c), most of the observed regions in the DMD_1000 W sample are depleted with Y_2O_3, which would be detrimental to its high temperature mechanical properties. A large yttrium-rich cluster of around 100 nm is shown in the figure.

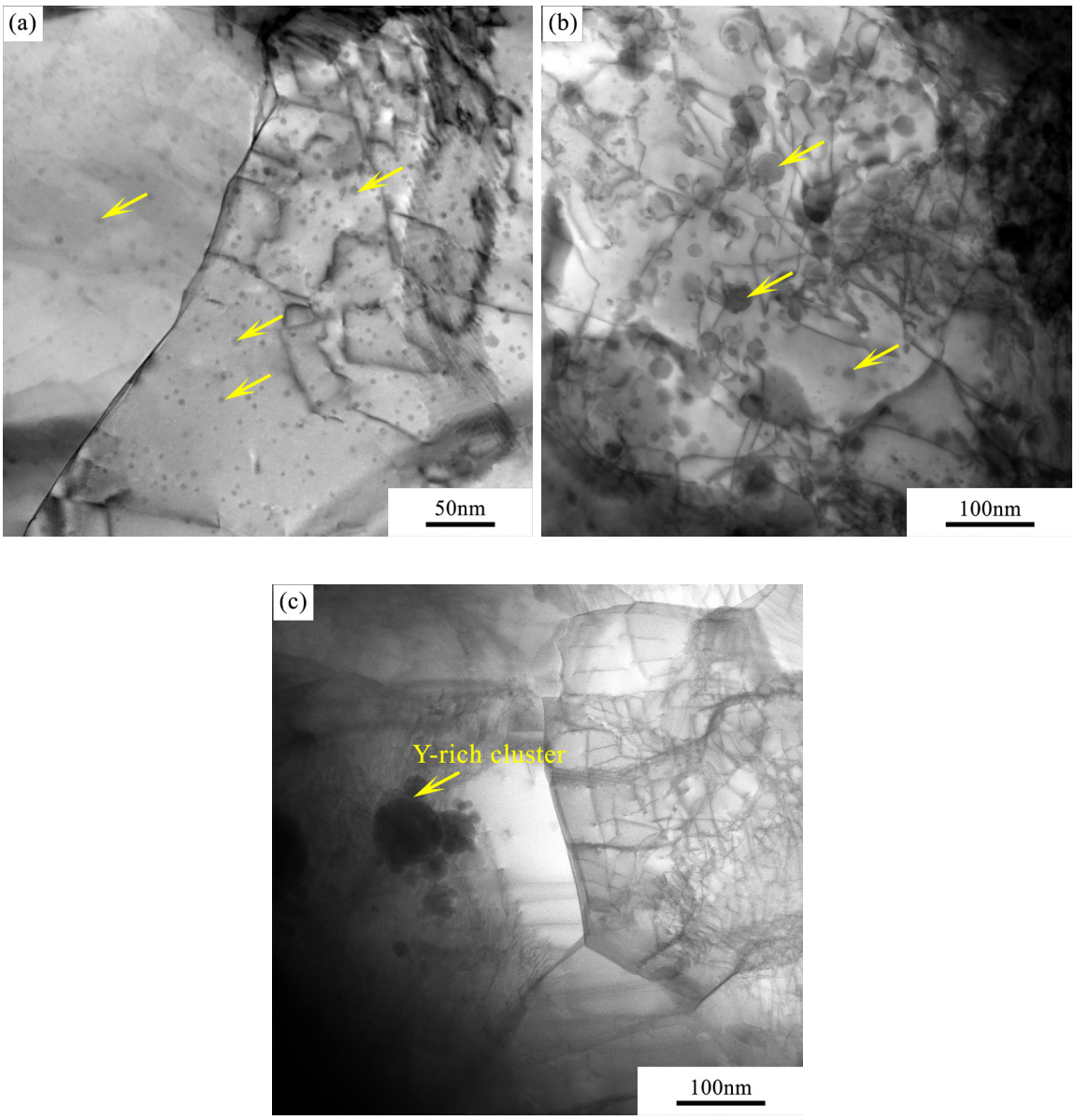


Figure 6.4. TEM images of the microstructural features of ODS Eurofer produced by (a) SPS (b) DMD_800 W and (c) DMD_1000 W.

Figure 6.5 (a), (b) and (c) present inverse pole figure (IPF) maps of ODS Eurofer steel processed by different conditions, with grain colours related to grain orientation expressed in the standard triangle. The average grain sizes obtained from the EBSD maps are given in Table 6.4. Compared to the SPS produced ODS Eurofer, the grains in the steel produced by DMD seem to be elongated and perpendicular to the scanning direction due to the rapid directional solidification behaviour. Similar observation was reported by Guo *et al.* [23], who found that the temperature gradient along the vertical direction of the molten pool border was higher than other directions. As a result, the grains preferentially grow along the direction of maximum temperature gradient. The grain size of the sample produced by DMD_1000 W is much larger compared to the other two conditions. This can be ascribed to a higher heat input and a lack of pinning effect of Y_2O_3 in the material. Due to the rapid heating and cooling process of DMD,

it is possible that there is not sufficient time to complete the phase transformations. The fractions of the FCC phases in DMD_800 W and DMD_1000 W are determined to be 3.73% and 2.9%, respectively. Therefore, it is likely that the microstructure of both steels consists of martensite, δ-ferrite and a small fraction of retained austenite. The differentiation and quantification of martensite and ferrite can be realised by EBSD observation, since martensite grains generally have a lower image quality and higher misorientation angle than ferrite due to a more distorted lattice [24]. Detailed methodology is described in the next chapter in section 7.3.2.2. The fractions of different phases in the printed steels are summarised in Table 6.3.

Rapid cooling rates employed in the thermo-mechanical processes of steel productions can cause disparities between the two constituent phases of dual phase steels, leading to reduced formability and ductility. Therefore, a tempering heat treatment process is often used to soften the microstructure through carbon diffusion and to homogenise the supersaturated martensitic microstructures [25]. In addition, tempering is known to be effective for the relief of residual stresses generated during manufacturing, which otherwise would cause cracks or catastrophic failures. In this study, the SPS and DMD produced samples were further treated by a standard heat treatment proposed in chapter 5 to study their microstructure stability. The treatment started with normalising at 1423 K for 1 h, air cooling to room temperature and then tempering at 973 K for 1 h, followed by air cooling to room temperature. The corresponding IPF maps and grain sizes can be seen in Figure 6.5 and Table 6.4, respectively. The grain size of the SPS produced steel shows no significant change after heat treatments. However, the grains grow to a size of 5.29 μm and 10.50 μm in the DMD_800 W and DMD_1000 W samples, respectively. This indicates that the pinning effect of Y_2O_3 is partially lost in the condition of 800 W and completely lost in the condition of 1000 W. It also reveals the role of Y_2O_3 as potential inoculants in facilitating the heterogeneous nucleation and formation of finer grains. The fractions of the FCC phases in the heat-treated DMD_800 W and DMD_1000 W are determined to be 3.6% and 0%, respectively. It suggests that the microstructure of heat-treated DMD_800 W is tempered martensite, δ-ferrite and retained austenite, while heat-treated DMD_1000 W has a fully tempered martensitic microstructure, due to an absence of Y_2O_3 inhibiting the phase transformations. The fractions of different phases in the heat-treated steels can be seen in Table 6.3.

Table 6.3 Fractions of different phases in the printed and heat-treated ODS Eurofer.

Conditions	Martensite/%	δ-ferrite/%	Retained austenite%
DMD_800 W	14.4	81.8	3.73
DMD_1000 W	22.3	74.8	2.9
DMD_800 W heat-treated	32.4	64.0	3.6
DMD_1000 W heat-treated	100	0	0

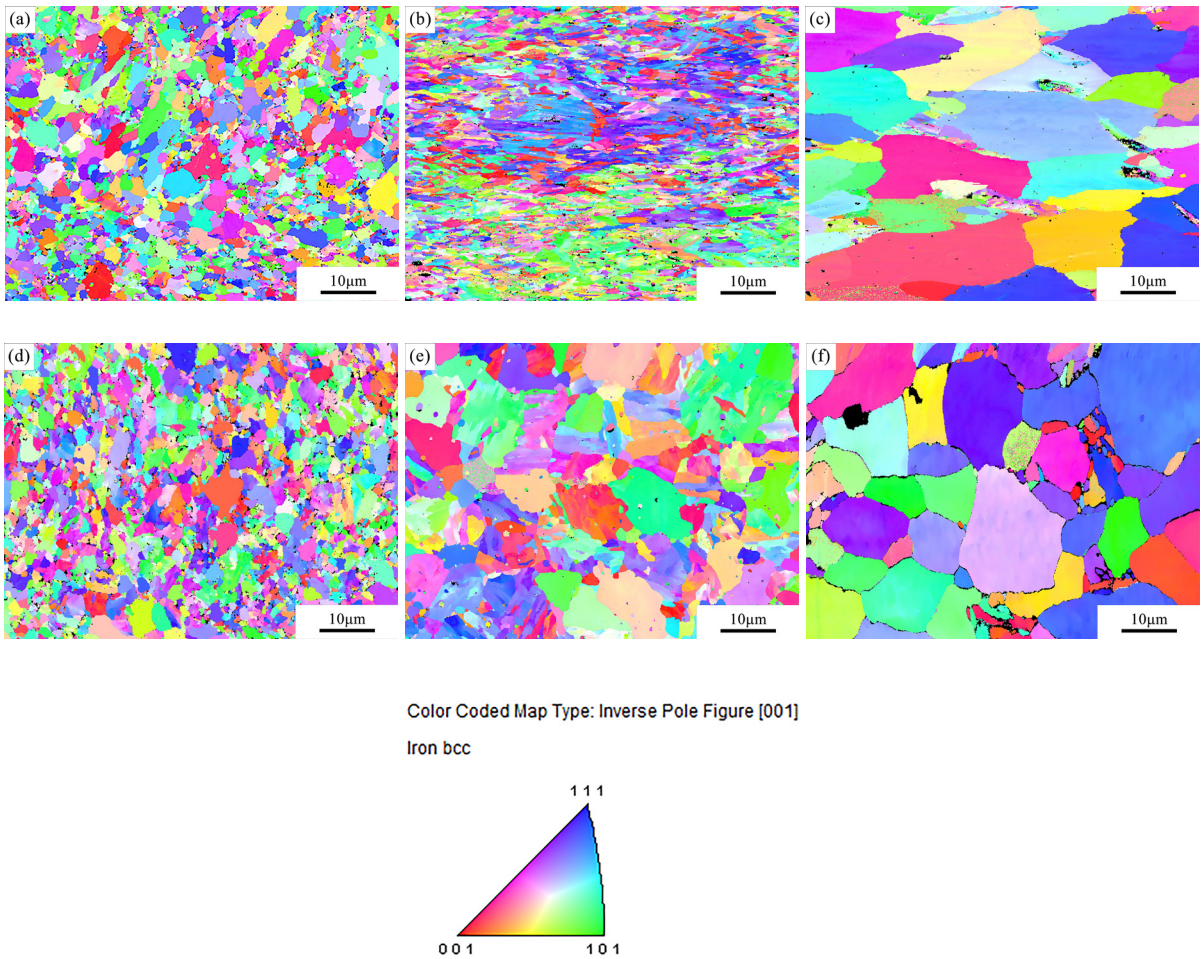


Figure 6.5. EBSD maps of ODS Eurofer produced by different conditions: (a) SPS, (b) DMD_800 W, (c) DMD_1000 W, (d) heat-treated SPS, (e) heat-treated DMD_800 W and (f) heat-treated DMD_1000 W.

Table 6.4. The average grain sizes obtained from EBSD data in Figure 6.5.

Conditions	Grain size/μm
SPS produced	2.08 ± 1.31
DMD_800 W	3.52 ± 2.40
DMD_1000 W	9.53 ± 5.15
SPS heat-treated	1.92 ± 1.10
DMD_800 W heat-treated	5.29 ± 2.98
DMD_1000 W heat-treated	10.50 ± 4.87

Figure 6.6 (a) and (c) present the grain boundary misorientation maps superimposed on the image quality maps of DMD_800 W and DMD_1000 W, respectively. The green lines represent high angle grain boundaries (grain boundary misorientation angle >15°) and the blue lines represent low angle grain boundaries (grain boundary misorientation angle <15°). It can be observed that in both conditions, high angle boundaries predominantly packet and block boundaries (65.6% and 78.9% of the total grain boundaries for DMD_800 W and

DMD_1000 W, respectively). Meanwhile, low angle boundaries can be noticed subdividing blocks, *i.e.* they can be associated with either lath boundaries or substructures. It should be mentioned that only misorientations above 2° were taken into account in the misorientation distribution results depicted in the figures. This is an intrinsic limitation of the EBSD technique. It is very likely that a significant amount of dislocation boundaries with lower misorientations are present in the material, but its quantification is not straightforward [26].

The kernel average misorientation (KAM) maps which characterise the average angular misorientation between a data point and its neighbour points, are shown in Figure 6.6 (b) and (d). A comparison between Figure 6.6 (a) and (b) as well as (c) and (d) indicates that a higher misorientation tends to be concentrated close to the high angle grain boundaries, implying a higher dislocation density at these locations.

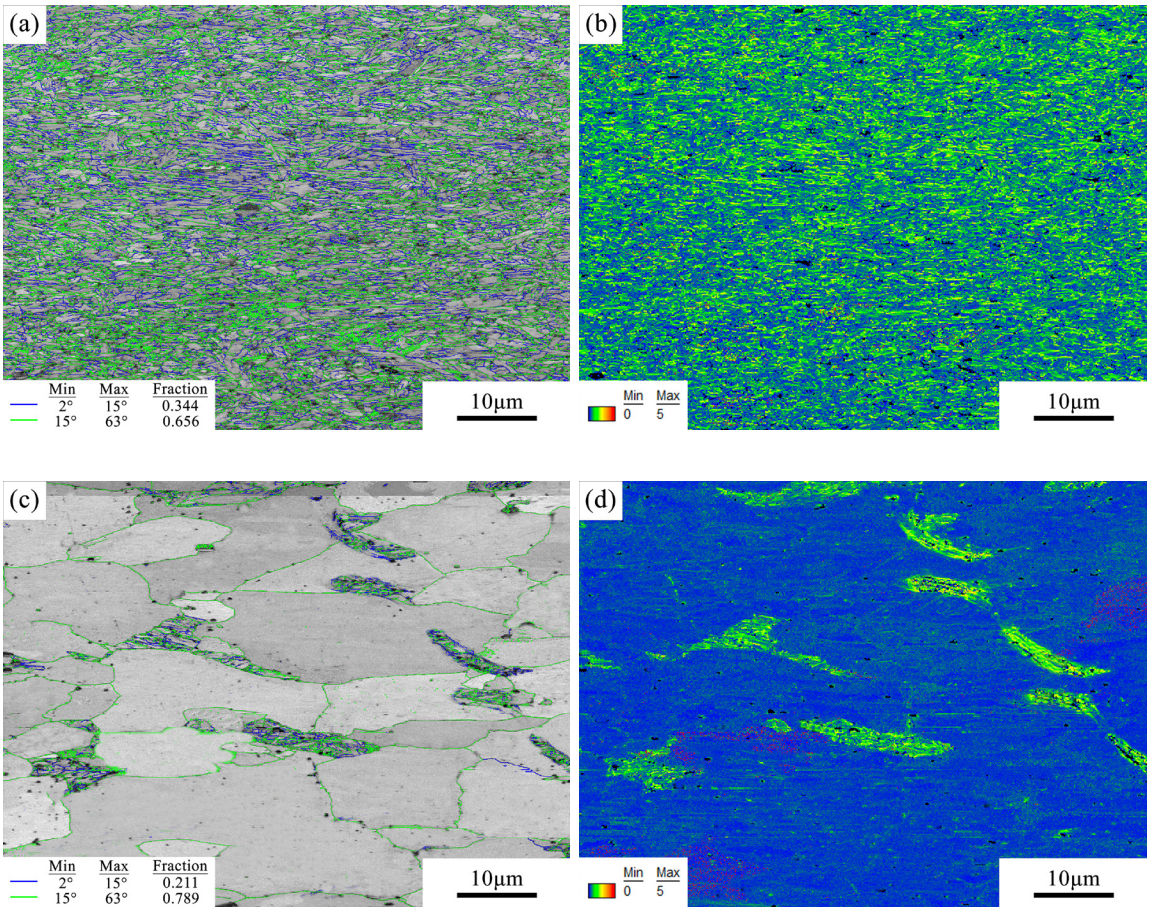


Figure 6.6. (a) and (c): Grain boundary misorientation maps superimposed on image quality maps for DMD_800 W and DMD_1000 W, respectively. (b) and (d): Kernel average misorientation (KAM) maps, measured in degrees for DMD_800 W and DMD_1000 W, respectively.

6.3.3 Nanoindentation measurement

The hardness of martensite and ferrite in ODS Eurofer processed by different conditions was obtained from nanoindentation measurements and is shown in Table 6.5. The result of austenite was omitted from the raw data, due to its small amount in all conditions. It can be seen from

the table that martensite has a higher hardness than ferrite in all conditions, related to a higher dislocation density. Meanwhile, the hardness of martensite and ferrite unsurprisingly decreases from the SPS produced steel to DMD_800 W to DMD_1000 W, which agrees with the microhardness result. The distribution of grain size and oxide particles in ODS steels has a strong impact on their hardness (mechanical properties). A fine-grained microstructure implies a high density of grain boundaries, which can act as obstacles for dislocation movement. Therefore, the hardness of fine-grained zones is usually higher than that of coarse-grained zones in the same material (Hall-Petch effect). Additionally, nano-oxide particles can also hinder the dislocation migration, leading to an increased hardness compared to non-ODS steels. However, Davis *et al.* [27] recently found that the dominant strengthening mechanism of an ODS steel was grain boundary hardening, rather than dislocation pinning of nano-particles. The hardening effect of oxide particles on ODS steels was actually through an indirect grain refinement.

The hardness of martensite and ferrite in the heat-treated ODS Eurofer is also summarised in Table 6.5. Irrespective of processing conditions, there is a significant decrease in the hardness of martensite after tempering. This can be attributed to grain growth and an alteration of the internal structures of tempered martensite grains [28, 29]. Such a phenomenon is commonly observed in tempered dual phase steels including carbide precipitation in the microstructures of martensite, as well as a reduction of residual stresses and dislocation density [25]. In comparison, ferrite grains have less carbon content than martensite, therefore the softening in ferrite is minor [30]. This explains a lower reduction of hardness in ferrite after tempering.

Table 6.5. Hardness of martensite and ferrite in ODS Eurofer obtained from nanoindentation measurements.

Conditions	Hardness of martensite/GPa	Hardness of ferrite/GPa
SPS produced	8.5 ± 0.6	6.3 ± 0.8
DMD_800 W	4.8 ± 0.2	3.0 ± 0.5
DMD_1000 W	3.2 ± 0.4	1.8 ± 0.4
SPS heat-treated	6.7 ± 0.5	5.7 ± 0.9
DMD_800 W heat-treated	3.0 ± 0.5	2.1 ± 0.5
DMD_1000 W heat-treated	2.1 ± 0.4	–

6.4 Conclusions

ODS Eurofer was successfully produced by the laser-based direct metal deposition technique. The following conclusions can be drawn, based on a limited set of processing conditions in this feasibility study.

1. The laser power plays an important role in affecting the microstructure and properties of the printed steel. The relative density increases while the microhardness decreases with the laser power. A laser power of 800 W was determined to be a suitable printing condition, as a lower power does not provide sufficient heat input while a higher power leads to a depletion of Y_2O_3 nanoparticles in the steel. The nanoparticles in the DMD_800 W steel are coarsened and have

a size of 5–30 nm. A subsequent HIP treatment was found to be effective to consolidate the residual pores in the deposit.

2. Compared to SPS produced ODS Eurofer, the grains in the steel produced by DMD seem to be elongated and perpendicular to the scanning direction due to the rapid directional solidification behaviour. After a normalising and tempering treatment, the grain size of the SPS produced steel shows no obvious change, while the grains in the DMD_800 W and DMD_1000 W samples grow significantly due to a (partial) loss of Y_2O_3 pinning. High angle grain boundaries predominantly packet and block boundaries, where a higher misorientation tends to be concentrated.

3. Nanoindentation results show that the hardness of martensite and ferrite decreases from the SPS produced steel to DMD_800 W to DMD_1000 W, which is associated with the grain size and nano-oxide distribution. After a tempering treatment, there is a decrease in the hardness of martensite and ferrite, which is related to carbide precipitation as well as residual stress and dislocation density reduction.

References

[1] Y. Xu, Z. Zhou, M. Li, P. He, Fabrication and characterization of ODS austenitic steels, J. Nucl. Mater. 417(1-3) (2011) 283-285.

[2] T. Vanherck, G. Jean, M. Gonon, J. Lobry, F. Cambier, Spark plasma sintering: homogenization of the compact temperature field for non conductive materials, International Journal of Applied Ceramic Technology 12 (2015) E1-E12.

[3] J.R. Rieken, I.E. Anderson, M.J. Kramer, G. Odette, E. Stergar, E. Haney, Reactive gas atomization processing for Fe-based ODS alloys, J. Nucl. Mater. 428(1-3) (2012) 65-75.

[4] H. Ali, L. Ma, H. Ghadbeigi, K. Mumtaz, In-situ residual stress reduction, martensitic decomposition and mechanical properties enhancement through high temperature powder bed pre-heating of Selective Laser Melted Ti6Al4V, Mater. Sci. Eng., A 695 (2017) 211-220.

[5] J. Mazumder, Past present and future of art to part by Direct Metal Deposition, Pacific International Conference on Applications of Lasers and Optics, Laser Institute of America, 2004, p. P703.

[6] X. Wu, A review of laser fabrication of metallic engineering components and of materials, Mater. Sci. Technol. 23(6) (2007) 631-640.

[7] N. Hrabe, R. White, E. Lucon, Effects of internal porosity and crystallographic texture on Charpy absorbed energy of electron beam melting titanium alloy (Ti-6Al-4V), Mater. Sci. Eng., A 742 (2019) 269-277.

[8] Z. Wang, A.M. Beese, Stress state-dependent mechanics of additively manufactured 304L stainless steel: Part 1–characterization and modeling of the effect of stress state and texture on microstructural evolution, Mater. Sci. Eng., A 743 (2019) 811-823.

[9] S. Gribbin, S. Ghorbanpour, N.C. Ferreri, J. Bicknell, I. Tsukrov, M. Knezevic, Role of grain structure, grain boundaries, crystallographic texture, precipitates, and porosity on fatigue behavior of Inconel 718 at room and elevated temperatures, Mater. Charact. 149 (2019) 184-197.

[10] Y. Shi, Z. Lu, L. Yu, R. Xie, Y. Ren, G. Yang, Microstructure and tensile properties of Zr-containing ODS-FeCrAl alloy fabricated by laser additive manufacturing, Mater. Sci. Eng., A 774 (2020) 138937.
[11] K. Euh, B. Arkhurst, I.H. Kim, H.-G. Kim, J.H. Kim, Stability of Y-Ti-O nanoparticles during laser deposition of oxide dispersion strengthened steel powder, Metals and Materials International 23(6) (2017) 1063-1074.
[12] C. Kenel, K. Dawson, J. Barras, C. Hauser, G. Dasargyri, T. Bauer, A. Colella, A.B. Spierings, G.J. Tatlock, C. Leinenbach, Microstructure and oxide particle stability in a novel ODS γ-TiAl alloy processed by spark plasma sintering and laser additive manufacturing, Intermetallics 90 (2017) 63-73.
[13] Y. Shi, Z. Lu, H. Xu, R. Xie, Y. Ren, G. Yang, Microstructure characterization and mechanical properties of laser additive manufactured oxide dispersion strengthened Fe-9Cr alloy, J. Alloys Compd. 791 (2019) 121-133.
[14] A. Sola, A. Nouri, Microstructural porosity in additive manufacturing: The formation and detection of pores in metal parts fabricated by powder bed fusion, Journal of Advanced Manufacturing and Processing 1(3) (2019) e10021.
[15] C. Zhong, A. Gasser, T. Schopphoven, R. Poprawe, Experimental study of porosity reduction in high deposition-rate Laser Material Deposition, Optics & Laser Technology 75 (2015) 87-92.
[16] A. Du Plessis, E. Macdonald, Hot isostatic pressing in metal additive manufacturing: X-ray tomography reveals details of pore closure, Additive Manufacturing 34 (2020) 101191.
[17] M. Seifi, M. Gorelik, J. Waller, N. Hrabe, N. Shamsaei, S. Daniewicz, J.J. Lewandowski, Progress towards metal additive manufacturing standardization to support qualification and certification, JOM 69(3) (2017) 439-455.
[18] M. Ahlfors, F. Bahbou, A. Eklund, U. Ackelid, HIP for AM-optimized material properties by HIP, Hot Isostatic Press HIP 17 (2019) 10.
[19] J.C. Walker, K.M. Berggreen, A.R. Jones, C.J. Sutcliffe, Fabrication of Fe–Cr–Al oxide dispersion strengthened PM2000 alloy using selective laser melting, Adv. Eng. Mater. 11(7) (2009) 541-546.
[20] F. Bergner, I. Hilger, J. Virta, J. Lagerbom, G. Gerbeth, S. Connolly, Z. Hong, P.S. Grant, T. Weissgärber, Alternative fabrication routes toward oxide-dispersion-strengthened steels and model alloys, MMTA 47(11) (2016) 5313-5324.
[21] J.S. Park, M.-G. Lee, Y.-J. Cho, J.H. Sung, M.-S. Jeong, S.-K. Lee, Y.-J. Choi, D.H. Kim, Effect of heat treatment on the characteristics of tool steel deposited by the directed energy deposition process, Metals and Materials International 22(1) (2016) 143-147.
[22] T. Boegelein, S.N. Dryepondt, A. Pandey, K. Dawson, G.J. Tatlock, Mechanical response and deformation mechanisms of ferritic oxide dispersion strengthened steel structures produced by selective laser melting, Acta Mater. 87 (2015) 201-215.
[23] P. Guo, B. Zou, C. Huang, H. Gao, Study on microstructure, mechanical properties and machinability of efficiently additive manufactured AISI 316L stainless steel by high-power direct laser deposition, J. Mater. Process. Technol. 240 (2017) 12-22.

[24] G. Cheng, F. Zhang, A. Ruimi, D. Field, X. Sun, Quantifying the effects of tempering on individual phase properties of DP980 steel with nanoindentation, Mater. Sci. Eng., A 667 (2016) 240-249.
[25] M.D. Taylor, Effect of microstructure on the fracture response of advanced high strength steels, Colorado School of Mines, 2016.
[26] K. Zilnyk, V.B. Oliveira, H.R.Z. Sandim, A. Möslang, D. Raabe, Martensitic transformation in Eurofer-97 and ODS-Eurofer steels: A comparative study, J. Nucl. Mater. 462 (2015) 360-367.
[27] T.P. Davis, J.C. Haley, S. Connolly, M.A. Auger, M.J. Gorley, P.S. Grant, P.A. Bagot, M.P. Moody, D.E. Armstrong, Electron microscopy and atom probe tomography of nanoindentation deformation in oxide dispersion strengthened steels, Mater. Charact. 167 (2020) 110477.
[28] K.S. Choi, Z. Zhu, X. Sun, E. De Moor, M.D. Taylor, J.G. Speer, D.K. Matlock, Determination of carbon distributions in quenched and partitioned microstructures using nanoscale secondary ion mass spectroscopy, Scripta Mater. 104 (2015) 79-82.
[29] V.B. Hernandez, S. Nayak, Y. Zhou, Tempering of martensite in dual-phase steels and its effects on softening behavior, MMTA 42(10) (2011) 3115.
[30] A.A. Sayed, S. Kheirandish, Affect of the tempering temperature on the microstructure and mechanical properties of dual phase steels, Mater. Sci. Eng., A 532 (2012) 21-25.

7

Welding of ODS Eurofer via solid state diffusion bonding and non-traditional fusion welding[1]

[1] This chapter is based on the scientific papers:
J. Fu, I. Richardson, M. Hermans, Microstructure Study of Pulsed Laser Beam Welded Oxide Dispersion-Strengthened (ODS) Eurofer Steel, Micromachines 12(6) (2021) 629.
J. Fu, J. van Slingerland, H. Brouwer, V. Bliznuk, I. Richardson, M. Hermans, Applicability Study of Pulsed Laser Beam Welding on Ferritic–Martensitic ODS Eurofer Steel, Metals 10(6) (2020) 736.
J. Fu, J. Brouwer, I. Richardson, M. Hermans, Solid State Diffusion Bonding of ODS Eurofer Steel by Spark Plasma Sintering, TMS 2020 149th Annual Meeting & Exhibition Supplemental Proceedings, Springer, 2020, pp. 2095-2102.

7.1 Introduction

Due to their good high-temperature strength, corrosion resistance and radiation resistance, oxide dispersion strengthened (ODS) steels are promising candidates for structural materials employed in elevated-temperature and nuclear applications [1]. Favourable properties of ODS steels are mainly attributed to the fine grains and dispersed nano-oxide particles in the steel matrix [2]. These fine and thermally stable dispersoids hinder the motion of dislocations and grain boundaries, acting as trapping sites for both point defects and helium atoms generated during irradiation, resulting in an increased resistance to irradiation damage.

Despite the promising behaviour of ODS steels for use in advanced nuclear systems, joining these materials remains one of the major technological challenges limiting their deployment [3]. The welding of ODS steels by traditional, fusion-based welding techniques such as gas metal arc welding and tungsten inert gas welding is problematic. As soon as a molten zone is produced, the oxide particles rapidly agglomerate and float to the top of the molten weld pool resulting in a significant loss of strength [4]. By employing solid state joining methods such as hot isostatic pressing (HIP) and friction stir welding (FSW), the degradation of featured microstructures and mechanical properties can be minimised since these techniques do not create a molten zone in the joint area [5]. However, the cost of HIP is relatively high due to a long processing time (1–5 h) [6]. The application of FSW is limited due to geometrical restrictions [4]. The tool wear in FSW may reduce the tool life and deteriorate the microstructure and mechanical properties of the joint [7]. In addition, high residual stresses can be generated in the thermo-mechanically affected zone of the joining area, which will cause a reduction in the fatigue strength [8].

Spark plasma sintering (SPS) is mainly used as a powder consolidation technique but it can also be applied as a solid state diffusion bonding method. In the latter case, SPS has the advantages of a low joining temperature and a short processing time [9]. More importantly, it does not create a molten zone at the joining interface, therefore permitting retention of the featured microstructures including nanostructures and nanoparticles in the joint [10]. Recently, the SPS technique has been employed for joining similar and dissimilar materials. Yang *et al.* [11] joined 316L stainless steel samples using SPS. Parameters including heating power, heating time, pressure, pulse sequence, particle size and powder quantity were found to affect the joining process and joint behaviour. Miriyev *et al.* [12] successfully joined 4330 steel and Ti–6Al–4V alloy where a maximum tensile strength of about 250 MPa was obtained when joining at 1223 K for 1 h. TiAl intermetallics were successfully joined using SPS by Zhao *et al.* [6]. Examination of the effects of bonding conditions on the microstructure and mechanical properties of the joints showed that metallurgical bonding could be obtained at lower pressures and shorter times compared to traditional bonding techniques. So far, little information is available on using SPS to join ODS steels.

Additionally, unlike traditional fusion welding techniques, laser beam welding [13-15] can potentially be employed for joining ODS steels due to its highly concentrated energy input, leading to the melting of a small amount of base material, and consequently a small heat affected zone (HAZ). The study of Lemmen *et al.* [15] showed that PM1000 had a relatively good laser weldability with a wide range of welding parameters. However, yttrium oxide clustering was

found in all conditions, causing a reduction of strength in the weld. Similar results were obtained by Liang *et al.* [16] who indicated that the nanoprecipitates in ODS steels were larger in the laser welded metal than in the base material. In summary, a new laser welding method needs to be developed for joining ODS steels to address the issue of microstructure and mechanical behaviour degradation.

In this chapter, SPS and pulsed laser beam welding were successfully employed to join ODS Eurofer. The welding parameters were investigated and optimised to improve the microstructure of the joint. Microstructure characterisation and investigation of mechanical properties were undertaken to evaluate the feasibility of SPS and pulsed laser welding to join ODS Eurofer.

7.2 Experimental details

7.2.1 Material preparation

ODS Eurofer steel was fabricated via a powder metallurgy route with the optimal condition as shown in chapter 4. The production process started with mechanical alloying, where the precursor powders were mixed in a Retsch planetary ball milling machine under an argon atmosphere for 30 h at 300 rpm. The resultant powders were subsequently consolidated by spark plasma sintering (SPS, FCT group, Germany) at a pressure of 60 MPa and a sintering temperature of 1373 K with a heating rate of 100 K min^{-1}. Disks with a 20 mm diameter and 17 mm thickness (for SPS joining) and a 40 mm diameter and 10 mm thickness (for laser welding) were produced.

For SPS joining, two disks were placed with faces adjacent to each other with ODS Eurofer powder added in between. Based on the study of SPS producing ODS Eurofer presented in chapter 4, the specimens were joined by sintering at 1373 K with a heating rate of 100 K min^{-1}, a pressure of 80 MPa and holding times in the range of 10–40 min. For pulsed laser welding, spot-on-plate experiments were initially conducted to study the effect of a laser beam on the microstructure of ODS Eurofer. The focusing optic projects a laser spot with a diameter of 0.4 mm or 0.6 mm for different purposes. The work pieces were treated by a pulsed laser beam with a power (P) of 2500 W and pulse durations (t) ranging from 2 ms to 200 ms. Subsequently, ODS Eurofer plates were welded by a pulsed laser beam with a designed pattern (Figure 3.6) and filler material. For both welding methods, a post heat treatment was conducted to improve the mechanical performance by normalising at 1423 K for 1 h, air cooling to room temperature and then tempering at 973 K for 1 h, followed by air cooling to room temperature. Detailed conditions and strategies of SPS joining and laser welding are presented in chapter 3.

7.2.2 Material characterisation

The microstructure of the joints was characterised using a Keyence Digital Microscope VHX-5000, a JEOL 6500F scanning electron microscope (SEM) equipped with an energy dispersive spectrometer (EDS) and electron backscattered diffraction (EBSD) and a JEM-2200FS transmission electron microscope (TEM) equipped with an EDS system. TSL OIM software

was used for EBSD data processing and analysis. EBSD maps, including inverse pole figure (IPF), grain average image quality (GAIQ) and kernel average misorientation (KAM) were implemented and analysed in the study.

Vickers microhardness was measured across the joint, with a load of 0.2 kg and a step size of 0.5 mm (for SPS joints) or 0.1 mm (for laser welded joints). Flat tensile specimens were cut from the SPS and laser welded samples, with the weld seam located at the centre of sample and perpendicular to the applied tensile force. The tensile properties were determined using an Instron 5500R, with a nominal strain rate of 2.5×10^{-4} s^{-1} at room temperature. At least five measurements were made per condition.

7.3 Results and discussion

7.3.1 Joining by SPS

7.3.1.1 Microstructure characterisation

Figure 7.1 shows optical macrographs of the joints for different joining conditions. Large cavities and cracks can be observed for the condition of 10 min holding time with 0.32 g cm^{-2} powder layer in between (Figure 7.1 (a)). Cracks initiate at the edge of the sample, probably due to the mismatch between the interfaces as they are not perfectly flat before joining. With more powder added, the number of cavities and the length of cracks are reduced significantly (Figure 7.1 (b)). A thicker powder layer is beneficial for the joining process as the resistance of the powder is much higher than the bulk material with the same shape, therefore promoting a much higher heating rate in the powder layer [11]. With a powder layer of 1.27 g cm^{-2}, no crack is observed in the microstructure, indicating a better joint at this condition (Figure 7.1 (c)). After a holding time of 40 min, almost all of the cavities are eliminated (Figure 7.1 (d)). A joint almost free of macroscopic defects is obtained with this condition. No evident interface is observed in the microstructure.

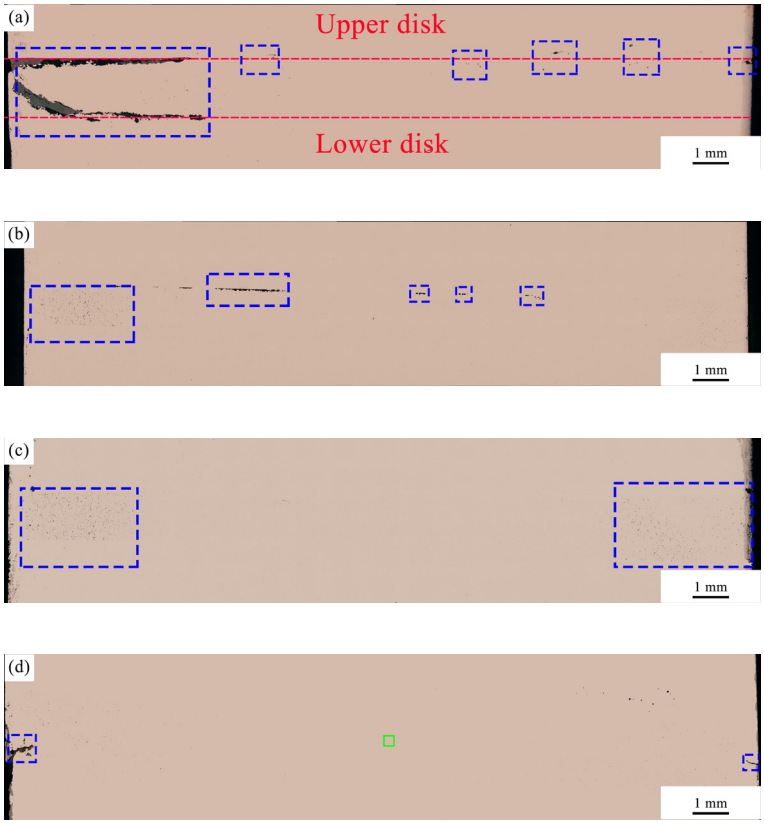


Figure 7.1. Morphology of cross-sectioned joints under conditions of: (a) 10 min holding time, 0.32 g cm^{-2} powder layer, (b) 10 min holding time, 0.64 g cm^{-2} powder layer, (c) 20 min holding time, 1.27 g cm^{-2} powder layer and (d) 40 min holding time, 1.27 g cm^{-2} powder layer (the green frame indicates the position of EBSD and TEM measurements). The dashed blue frames indicate the joining defects.

Figure 7.2 (a) and (b) respectively show the EBSD maps taken from the weld centre of the as-joined and heat-treated specimen, at the location illustrated in Figure 7.1 (d). The average grain sizes are determined to be 1.95 ± 1.21 µm and 2.02 ± 1.39 µm, respectively. The grain size of the base material [17] is 2.08 ± 1.31 µm, indicating that the fine grained feature of ODS Eurofer is fully retained. The grain size of the material does not change significantly after the heat treatment, probably because of the strong pinning effect of Y_2O_3 on the grain boundaries. TEM micrographs of the microstructure features of the as-joined and heat-treated specimen are shown in Figure 7.2 (c) and (d). Finely dispersed Y_2O_3-rich nanoparticles, confirmed by EDS, are observed in the steel matrix. The particle size varies within a small range of 1–15 nm. No clustering of nanoparticles is evident in the microstructure. The results reveal that the fine-grained feature and distribution of Y_2O_3 particles are not affected by the solid state joining process, which is crucial for the mechanical properties of the joints.

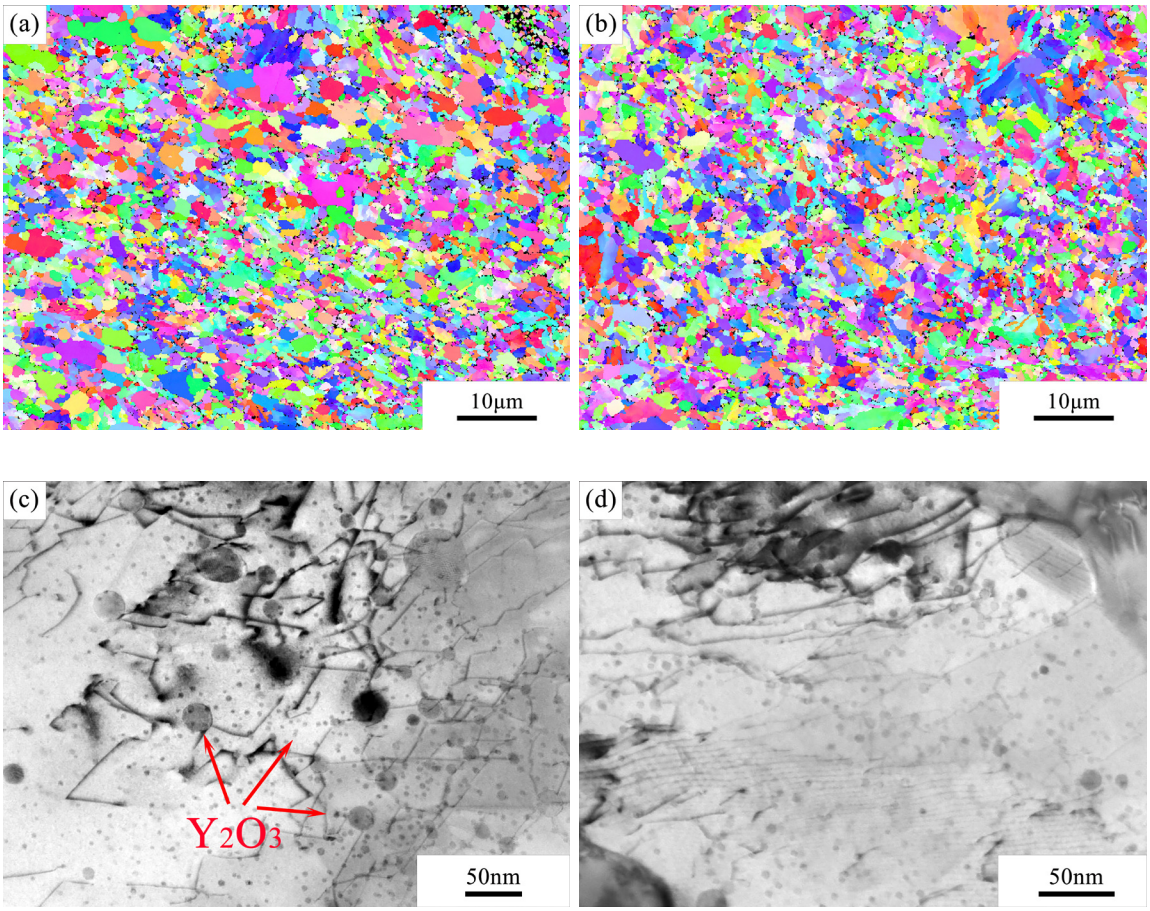


Figure 7.2. EBSD maps of the (a) as-joined and (b) heat-treated specimen and TEM images of the (c) as-joined and (d) heat-treated specimen.

7.3.1.2 Mechanical properties

The microhardness of the cross-sections of the samples can be seen in Figure 7.3. For the as-produced disk (thickness 17 mm), the hardness of the surface area is higher than the middle area due to a higher carbon content, resulting from the carbon diffusion from the graphite mould [18]. The hardness of the as-joined sample is slightly higher than the as-produced disk at the same location, which could be ascribed to an additional thermal cycle and a rapid cooling during the joining procedure. In addition, the hardness of the interface region has a higher hardness than the majority of the base material, indicating that the interface is not the weakest point of the as-produced joint. After a heat treatment of normalising and tempering, the hardness profile of the joined material becomes more uniform, due to carbon diffusion and dislocation recovery.

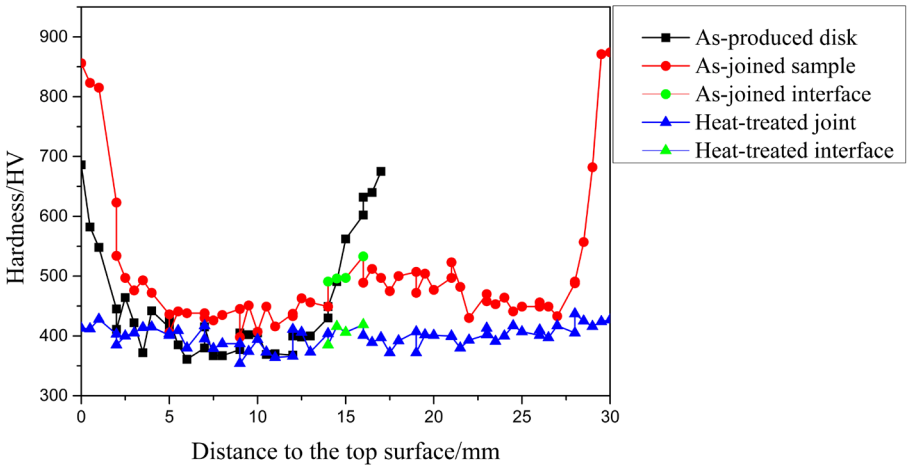


Figure 7.3. Microhardness of the cross-sections of the as-produced disk and joined samples.

The tensile properties of the as-joined and heat-treated specimens are shown in Table 7.1. The tensile properties of the base material as reported in chapter 5 are also listed in this table; it should be emphasised that the direction of the applied tensile force for the base material is perpendicular to that employed here due to the location of the joint. It can be seen that the strength of the joined specimens is slightly higher while the elongation is lower than that of the base material, which is consistent with the microhardness result. After a heat treatment of normalising and tempering, the strength of the material slightly decreases, while the elongation increases compared to the as-joined specimen. All of the tested specimens fractured in the base material region, indicating that the strength of the joint is at least comparable to that of the base material.

Table 7.1 Tensile testing results of the joined material and base material.

	Tensile strength/MPa	Yield strength/MPa	Elongation/%
Base material	1301.2 ± 144.5	923.7 ± 183.1	6.86 ± 2.69
Heat-treated base material	1030.8 ± 64.7	861.6 ± 26.2	10.4 ± 1.40
As-joined specimen	1342.3 ± 51.2	973.9 ± 18.5	3.75 ± 1.61
Heat-treated joint	1112.3 ± 19.5	944.5 ± 17.5	5.55 ± 2.30

Fractographic examinations were performed on the fracture surfaces from tensile testing by SEM (Figure 7.4). It can be seen that the fracture of the as-joined sample exhibits many small and smooth facets, indicating an intergranular fracture mode. In contrast, the heat-treated joint shows a typical ductile fracture mode with numerous dimple features, showing an enhanced ductility compared to the as-joined sample. In summary, SPS shows potential to be employed as a joining technique for ODS steels, considering the advantages of short processing time, ease of operation and good mechanical properties of the joints obtained.

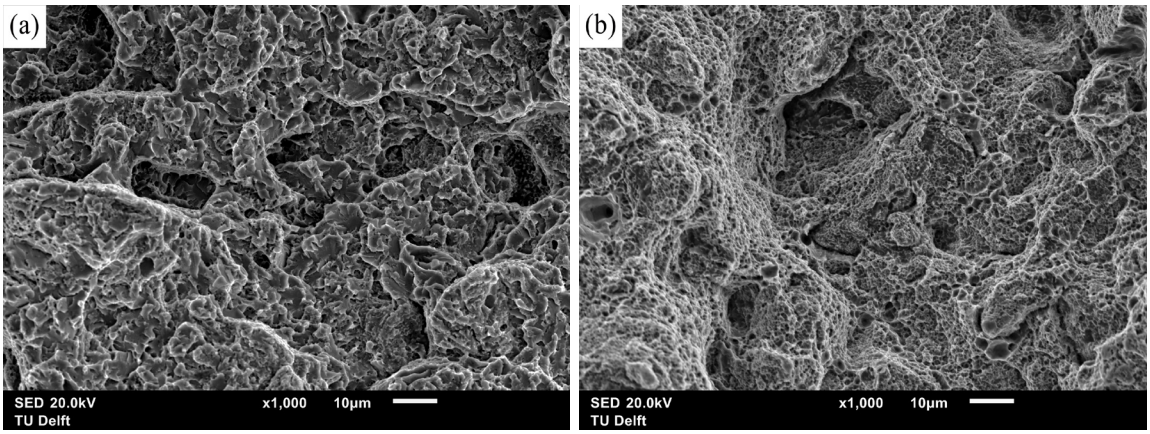


Figure 7.4. SEM micrographs of the fractures for specimens after tensile testing: (a) as-joined sample and (b) heat-treated joint.

7.3.2 Joining by pulsed laser beam welding

7.3.2.1 Parameter optimisation

To study the effect of a pulsed laser beam on the microstructure of ODS Eurofer, a number of spots were created on a plate with varying parameters. Since melting is inevitable during pulsed laser beam treatment, a short melt pool lifetime would be favourable for retaining the Y_2O_3 particles in the material. Therefore, a balance of a high laser power of 2500 W in combination with short pulse durations were chosen to have sufficient heat input. As can be seen from Figure 7.5, a spot was created on a 5 mm thick plate by a pulsed laser beam with a beam size of 0.4 mm (P = 2500 W, t = 50 ms). Material loss was observed at the top surface due to metal evaporation during the high-temperature treatment. Partial penetration is obtained in this condition. The width of the top of the fusion zone is around 0.55 mm, which is close to the beam size, indicating a concentrated heat input. A large number of pores can be observed in the fusion zone, probably due to the trapped gas during the melting process. In particular, there are more pores located at the bottom of the melt pool failing to escape. It can be deduced that a wider fusion zone created by a larger beam size and full penetration realised by a longer pulse duration could be beneficial for the elimination of residual pores in the spot.

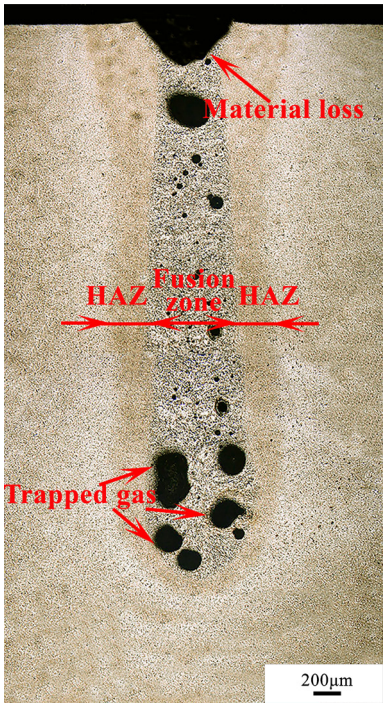


Figure 7.5. Optical micrograph of a spot on a 5 mm plate with a beam size of 0.4 mm (P = 2500 W, t = 50 ms).

A number of spots were created on the plate with a beam size of 0.6 mm to have a less concentrated heat source. From the optical macrographs shown in Figure 7.6, it can be seen that the width of the fusion zone is wider compared to the previous condition. In the case of pulse durations of 20 ms and 50 ms, a large number of pores can be observed in the spot due to partial penetration. For a pulse duration of 150 ms, full penetration is obtained, with a V-shaped fusion zone. The bottom of the fusion zone is so narrow that the large pore did not manage to escape. Solidification cracks can be seen around the edge of the pore, which are detrimental to the mechanical properties of the material as they can lead to catastrophic failure. Joints with a V-shaped melt pool are generally unfavourable as the asymmetrical morphology results in a non-uniform load transfer. In addition, the welding process is unstable due to an insufficient heat input, leading to an incomplete joint [15]. In the case of a longer pulse duration of 200 ms, it can be seen that the bottom of the melt pool becomes wider and it is easier for the pores to escape in this open keyhole condition. However, the morphology of the spot seems heavily affected, with severe material loss at both the top and bottom surfaces.

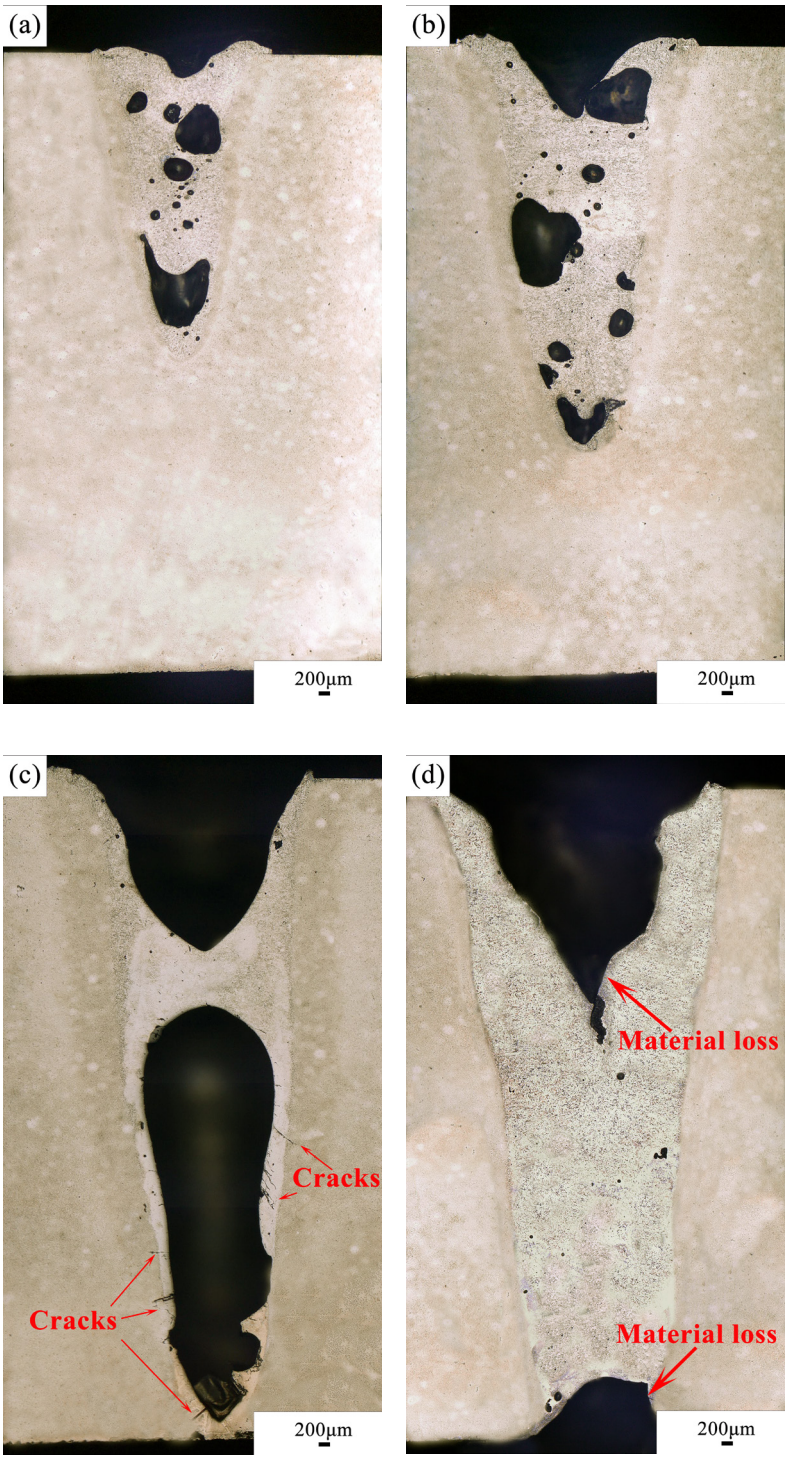


Figure 7.6. Optical macrographs of spots on a 5 mm plate with a beam size of 0.6 mm, P = 2500 W, (a) t = 20 ms, (b) t = 50 ms (c) t = 150 ms and (d) t = 200 ms.

Figure 7.7 (a) shows an SEM image of the microstructure morphology of the fusion zone shown in Figure 7.6 (d). It can be seen that the microstructure consists of elongated structures, with ultrafine grains (around 0.1–1 µm) and coarse grains (around 5–10 µm). As mentioned before, the average grain size of the parent material is around 2 µm. Considerable grain growth occurs due to a significant increase of temperature and the following solidification process. An

enlarged image of the fusion zone (Figure 7.7 (b)) shows a large number of precipitates (0.1–0.5 μm) in the microstructure. EDS analysis indicates that the precipitates are rich in Fe, Cr, W and C, which can be identified as $M_{23}C_6$ carbides (M = Fe, Cr and W) based on their size and chemical composition. The presence of $M_{23}C_6$ carbides is commonly found in chromium containing steels. These carbides can play an important role affecting the mechanical properties of the materials, including toughness, tensile strength and ductility, depending on their size and morphology [19]. It is notable that besides the presence of carbides, the grains seem to be very clean and without Y_2O_3 nano-precipitates. An EDS map of the fusion zone is presented in Table 7.2. It appears that no yttrium is revealed in the scanned area (around 500×700 μm^2), indicating a complete loss of nano-Y_2O_3, presumably attributed to the agglomeration and floating of Y_2O_3 due to a lower density compared to the liquid steel matrix.

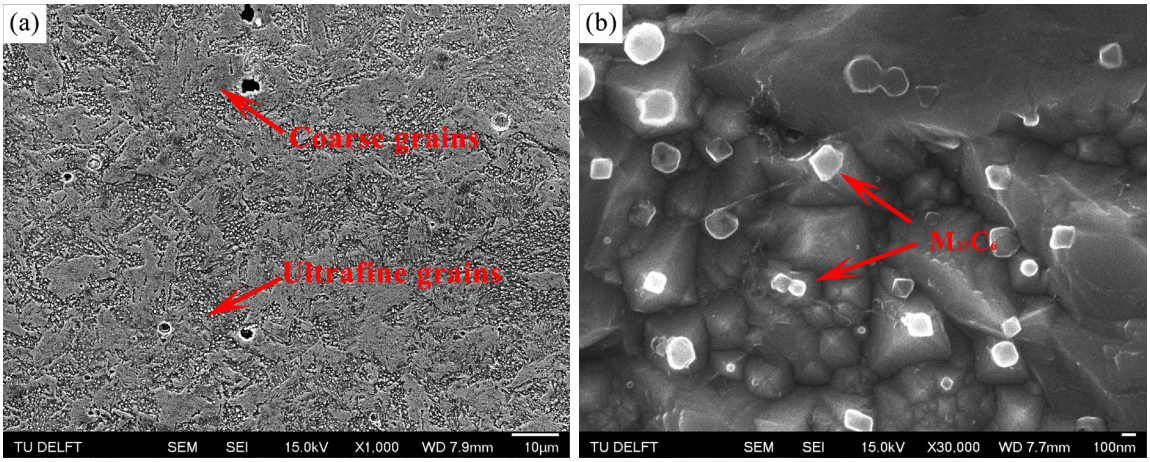


Figure 7.7. (a) and (b) SEM morphology of the fusion zone in Figure 7.6 (d).

Table 7.2. Chemical composition of base material and a scanned area in the fusion zone.

Elements (wt./%)	Cr	W	Mn	Y	V	Ta	Fe
Base material	9	1.1	0.4	0.24	0.2	0.12	Bal.
Fusion zone	8.83 ± 0.08	1.20 ± 0.19	0.36 ± 0.05	–	0.22 ± 0.02	–	Bal.

In order to further shorten the pulse durations while maintaining full penetration of the melt pool, a 1 mm thick plate was used for the following study. Cross sectional optical macrographs of the molten spots created by different pulse durations are illustrated in Figure 7.8. It can be seen that partial penetration is obtained with a pulse duration of 2 ms, while full penetration is realised with a pulse duration of 3 ms. Almost all of the large pores were eliminated in the open key-hole condition in Figure 7.8 (b). However, the residual thickness of the fusion zone is only about half of the parent material. A severely uneven thickness would be detrimental to the mechanical properties of the joint due to the influence of stress concentrations, resulting in an early failure under mechanical loading.

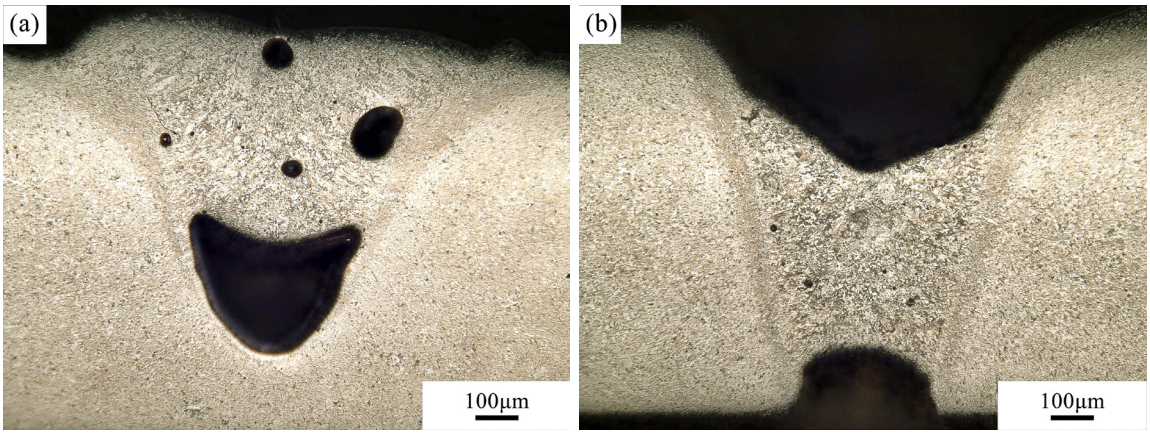


Figure 7.8. Optical macrographs of spots on a 1 mm plate, P = 2500 W, (a) t = 2 ms and (b) t = 3 ms.

To overcome the loss of material, two rectangular bars of ODS Eurofer, with a dimension of 30×1×0.5 mm^3, were attached to the top and bottom surfaces of the work piece acting as filler material. A pulse duration of 5 ms was used to realise full penetration. From the cross section of the spot shown in Figure 7.9, it can be seen that the material loss in the specimen is fully compensated by the use of filler material. In other words, the mechanical properties of the material will not be degraded by the reduction of thickness. In addition, the morphology of the material is not severely affected by the heat input compared to Figure 7.6 (d), due to a much shorter pulse duration.

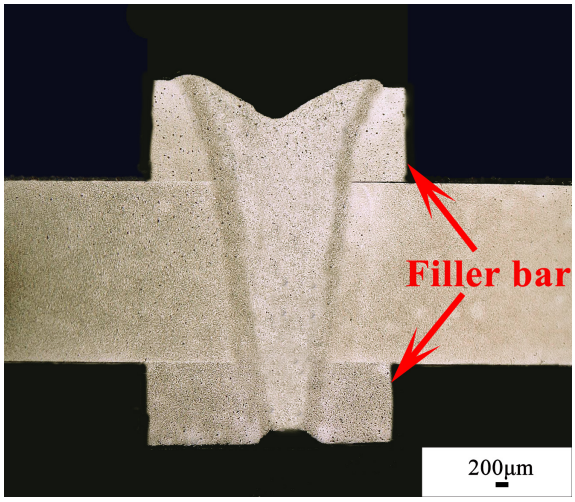


Figure 7.9. An optical micrograph of a spot on a 1 mm thick plate (P = 2500 W, t = 5 ms, with filler material).

Figure 7.10 (b) shows an SEM image of the morphology of the fusion zone in Figure 7.9. The microstructure seems to be similar to that shown in Figure 7.7 (a), with ultrafine grains, coarse grains as well as microvoids (0.5–3 µm) distributed in the material. The microstructure contains both martensite grains (dark regions) and ferrite grains (bright regions). Martensite is formed during the cooling process, since both the SPS sintering temperature and laser welding temperature are higher than Ac1 (around 1096 K). The presence of residual ferrite is possibly

the result of partial suppression of the phase transformation, as the motion of ferrite–austenite interface can be strongly blocked by finely dispersed oxide particles [20]. Therefore, the dual phase microstructure could be an indication that the Y_2O_3 particles are retained in the fusion zone. Another possible reason is that since the ferrite–austenite transformation is a diffusion–controlled process, the rapid solidification does not offer sufficient time to complete the phase transformation [21]. Consequently, residual ferrite is observed in the microstructure. Table 7.3 presents the result of chemical composition of a scanned area (around 500×700 μm^2) of the fusion zone. It can be seen that about 0.17 wt.% of yttrium was retained in the material. An enlarged image shown in Figure 7.10 (d) indicates that a large number of nanoprecipitates (Y_2O_3) can be observed in the steel matrix. The nanoparticles are not homogeneously distributed in the steel matrix. It seems that the smaller grains have a higher number of Y_2O_3 precipitates than the larger grains. This can be explained as follows: The distribution of Y_2O_3 is not perfectly homogenous even after a long-period of mechanical alloying. Since Y_2O_3 nanoprecipitates have a strong effect on impeding grain growth through a Zener-type pinning [22], grains having a higher density of Y_2O_3 are presumably more resistant to recovery and growth. Retaining Y_2O_3 nanoparticles is critical for the mechanical properties of ODS Eurofer joints, as they have a strong pinning effect on grain boundary motion and dislocations even at high temperatures, leading to a considerably enhanced mechanical behaviour compared to Y_2O_3-depleted joints. Based on the above findings, the condition employed (P = 2500 W, t = 5 ms with filler material) can be considered suitable for pulsed laser beam welding procedure for ODS Eurofer.

The grain size of the HAZ is smaller compared to that of the base material and clearly smaller than that of the fusion zone (Figure 7.10 (c)). This could be due to martensite transformation and a much lower temperature compared to the fusion zone. An enlarged image of the HAZ (Figure 7.10 (e)) shows a large number of $M_{23}C_6$ precipitates with a size ranging from 0.1 to 0.5 μm decorating the grain boundaries.

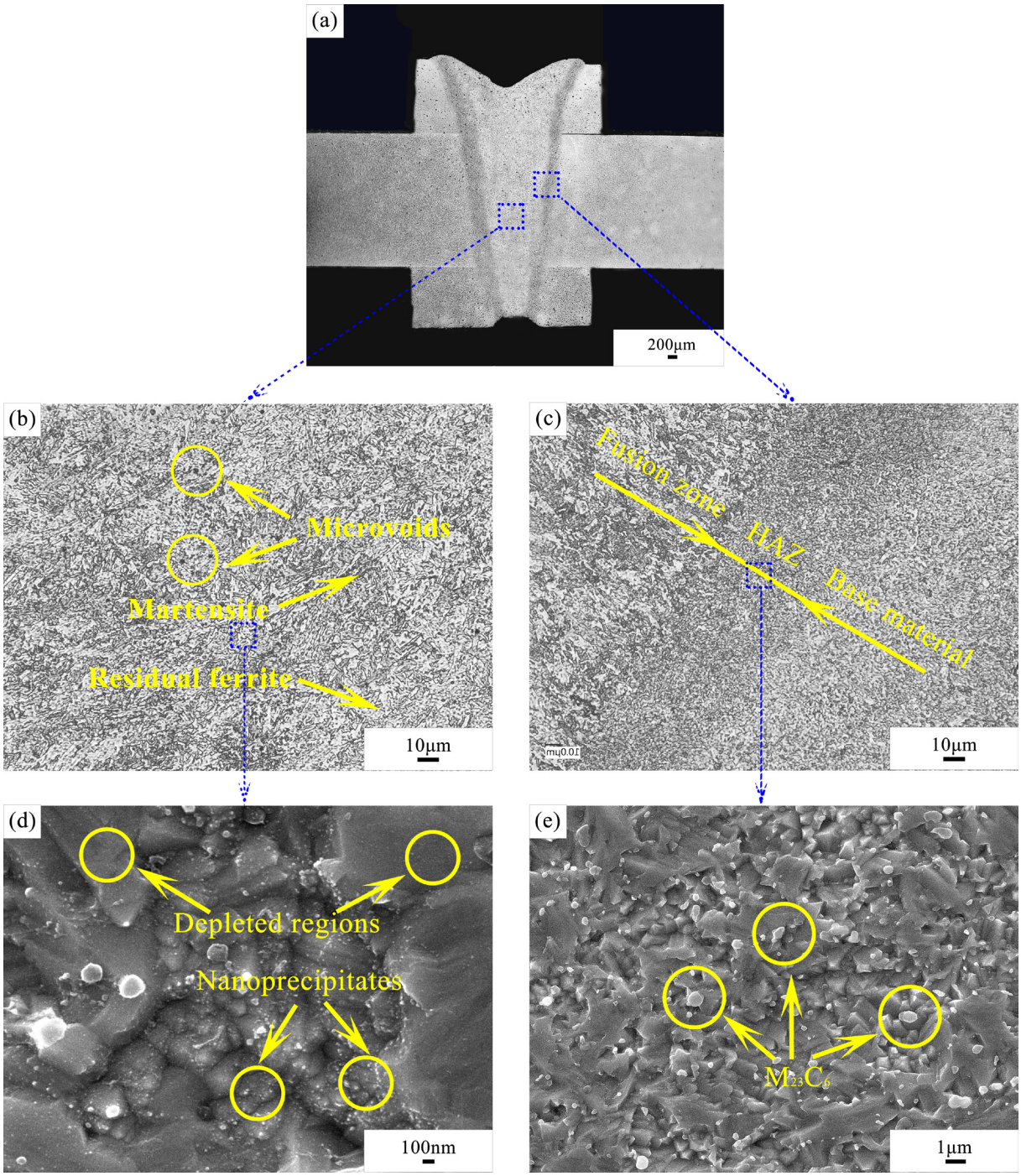


Figure 7.10. SEM morphologies and microhardness of the weld seam with filler material (P = 2500 W, t = 5 ms): (a) morphology of the weld seam, (b) fusion zone, (c) fusion line, (d) enlarged fusion zone and (e) enlarged HAZ.

Table 7.3. Chemical composition of base material and a scanned area of the fusion zone.

Elements (wt./%)	Cr	W	Mn	Y	V	Ta	Fe
Base material	9	1.1	0.4	0.24	0.2	0.12	Bal.
Fusion zone	8.82 ± 0.08	1.13 ± 0.20	0.64 ± 0.06	0.17 ± 0.06	0.20 ± 0.02	0.18 ± 0.16	Bal.

7.3.2.2 Microstructure characterisation

Based on the results reported above, ODS Eurofer was successfully welded using the pattern indicated in section 3.3.2 with filler material (P = 2500 W, t = 5 ms). To further investigate the microstructural features in the weld seam, samples taken from the fusion zone and base material were characterised by TEM. As can be seen in Figure 7.11 (a), a large number of $M_{23}C_6$ carbides, confirmed by the diffraction pattern shown in Figure 7.11 (b), are found to be present in the fusion zone. Meanwhile, finely dispersed Y_2O_3-rich nanoparticles, confirmed by EDS (Figure 7.12), are observed in both samples (Figure 7.11 (c) and (d)). The particle sizes vary between 1 and 30 nm and do not show a significant difference in distribution between the fusion zone and base material. In addition, no evident clustering of Y_2O_3 is observed in the microstructure of the fusion zone, which is crucial for the required mechanical properties of the joint.

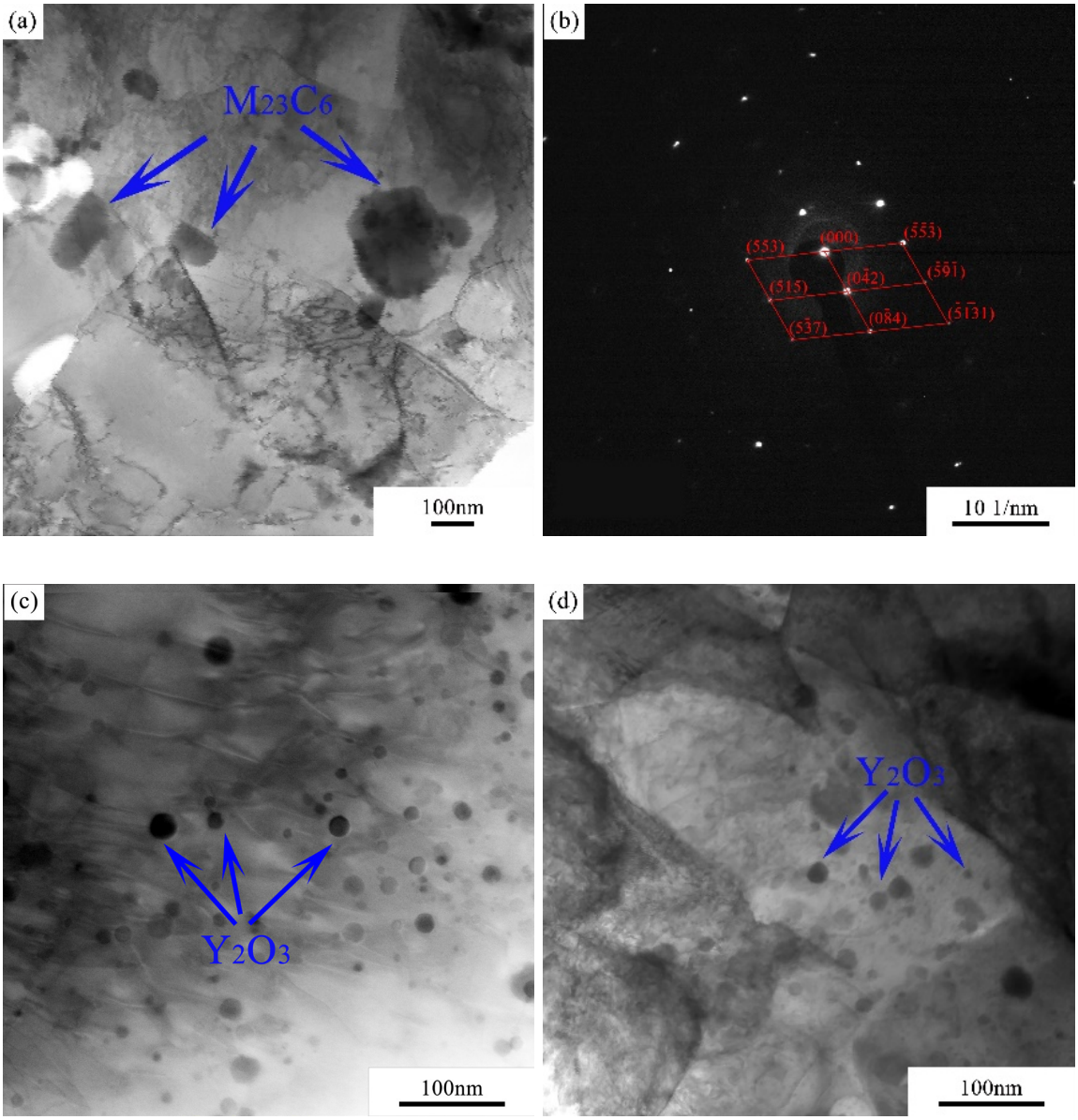


Figure 7.11. TEM images of the microstructural features: (a) $M_{23}C_6$ carbides in the fusion zone, (b) diffraction pattern of $M_{23}C_6$ carbides, (c) Y_2O_3-rich nanoparticles in the fusion zone and (d) Y_2O_3-rich nanoparticles in base material.

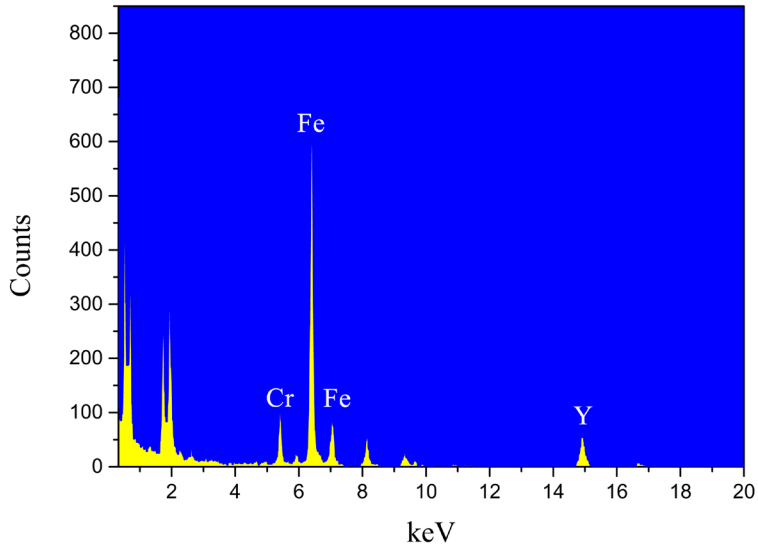


Figure 7.12. TEM-EDS analysis of nanoprecipitates in Figure 7.11 (c).

Figure 7.13 shows inverse pole figure (IPF) maps of different regions in the weld (P = 2500 W, t = 5 ms, with filler material) obtained by EBSD, with grain colours related to grain orientation expressed in the standard triangle. It can be observed that the maps exhibit grain sizes ranging from the nanometre scale to a few micrometres. The microstructure of the fusion zone consists of elongated structures, while that of HAZ shows equiaxed grains. None of the regions show preferential grain orientation.

From the IPF maps of different regions, the average grain sizes were measured and are shown in Table 7.4. The grain size distribution was determined under the assumption that the minimum misorientation characterising grain boundaries is 15°. It can be seen that in the as-joined condition, the average grain size of different regions decreases from fusion zone to base material to HAZ, which agrees with the observation from SEM. In the heat-treated condition, the average grain size of the fusion zone is still the largest, and that of the HAZ remains the smallest, but with smaller differences compared to the as-joined condition. Additionally, compared to the as-joined condition, there is a decrease in the grain size of the fusion zone, which could be ascribed to a refinement effect due to martensite transformation. Grain growth occurs in the HAZ, presumably resulting from the release of stored energy due to phase transformation and distortion during laser welding. In general, the grain sizes of the joint overall do not grow significantly after the heat treatment, probably because of the strong pinning effect of Y_2O_3 on the motion of grain boundaries.

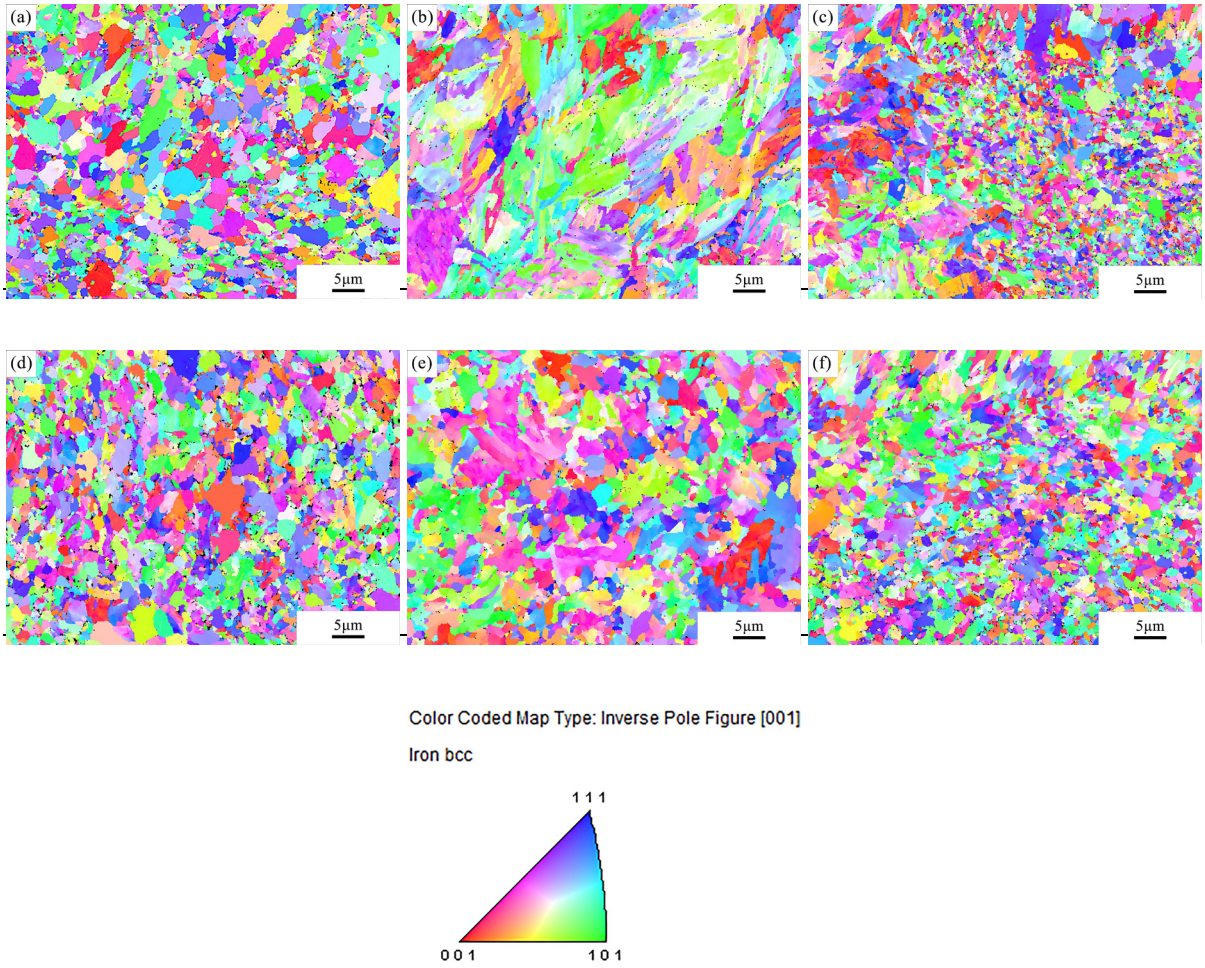


Figure 7.13. Inverse pole figure (IPF) maps of different regions (P = 2500 W, t = 5 ms): (a) base material, (b) fusion zone, (c) HAZ, (d) heat-treated base material, (e) heat-treated fusion zone and (f) heat-treated HAZ.

Table 7.4. Average grain size obtained from EBSD data for different regions in Figure 7.13.

Conditions	Regions	Grain size/µm
As-joined	Base material	2.08 ± 1.31
	Fusion zone	4.33 ± 2.89
	HAZ	1.64 ± 1.25
Heat treated	Base material	1.92 ± 1.10
	Fusion zone	2.20 ± 1.50
	HAZ	1.72 ± 1.07

From Table 7.4, it can also be noted that the standard deviations of all conditions are high. This is due to a bimodal grain size distribution of the material. Taking the fusion zone in the heat-treated joint (Table 7.4) as an example, the grain size distribution has two peaks at 1.42 and 7.20 µm, respectively, as can be seen in Figure 7.14. Similar bimodal grain size distributions have been widely reported for powder metallurgy prepared ODS steels [23-25]. In

martensitic–ferritic steels, which generally contain 0.1–0.2 wt% C and 9–11 wt% Cr [26], this phenomenon could be due to the dual phase nature of the material. To further differentiate martensite from ferrite in the studied material, the EBSD image quality maps are depicted and shown in Figure 7.15. Image quality describes the quality of diffraction property of the analysed Kikuchi patterns. It can be used to differentiate martensite from ferrite in dual-phase steels, since martensite exhibits lower image quality due to its highly distorted lattice [27]. Figure 7.15 (a), (c), (e) respectively present a chart of image quality of 60, 65 or 70. The corresponding phases in the microstructure are highlighted and shown in Figure 7.15 (b), (d), (f), respectively. It can be seen that if an image quality of 60 is chosen, the martensite grains are underestimated (see the disconnected dots in the figure). Meanwhile, if an image quality of 70 is chosen, the martensite grains are overestimated (some of the ferrite grains are highlighted in the figure). Therefore, an image quality of 65 is assumed to be an appropriate threshold value to estimate the martensite and ferrite phases in this case. It can be noted that the smaller martensite grains are mainly located between the larger ferrite grains. This finding supports the dual phase microstructure of the material, and consequently a high standard deviation of the grain size distribution. Recently, it has been shown that dual phase steels with fine martensite distributed uniformly in the ferrite matrix provide a better combination of strength and ductility compared with those having martensite islands along the grain boundaries of ferrite grains [28]. As can be seen from Figure 7.15 (b), martensite seems to be randomly distributed in the steel matrix, which would be beneficial for a high mechanical strength and reasonably ductility.

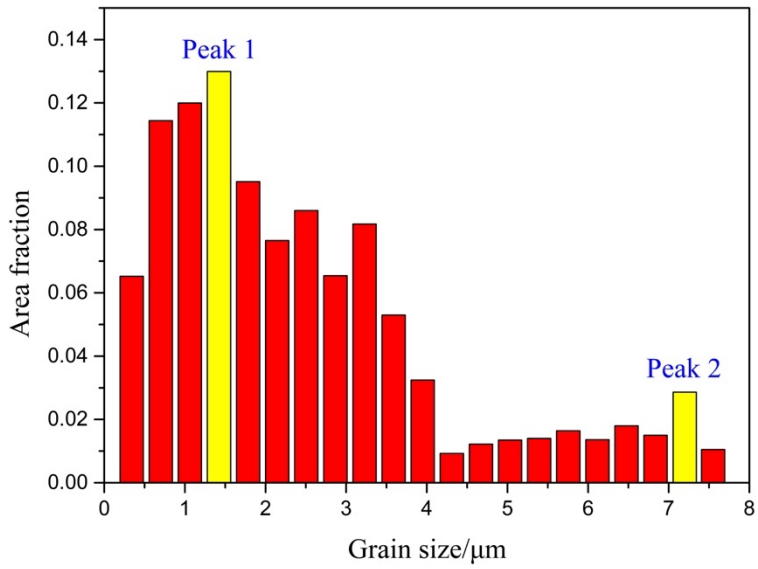


Figure 7.14. Grain size distribution of the fusion zone in the heat-treated joint (P = 2500 W, t = 5 ms).

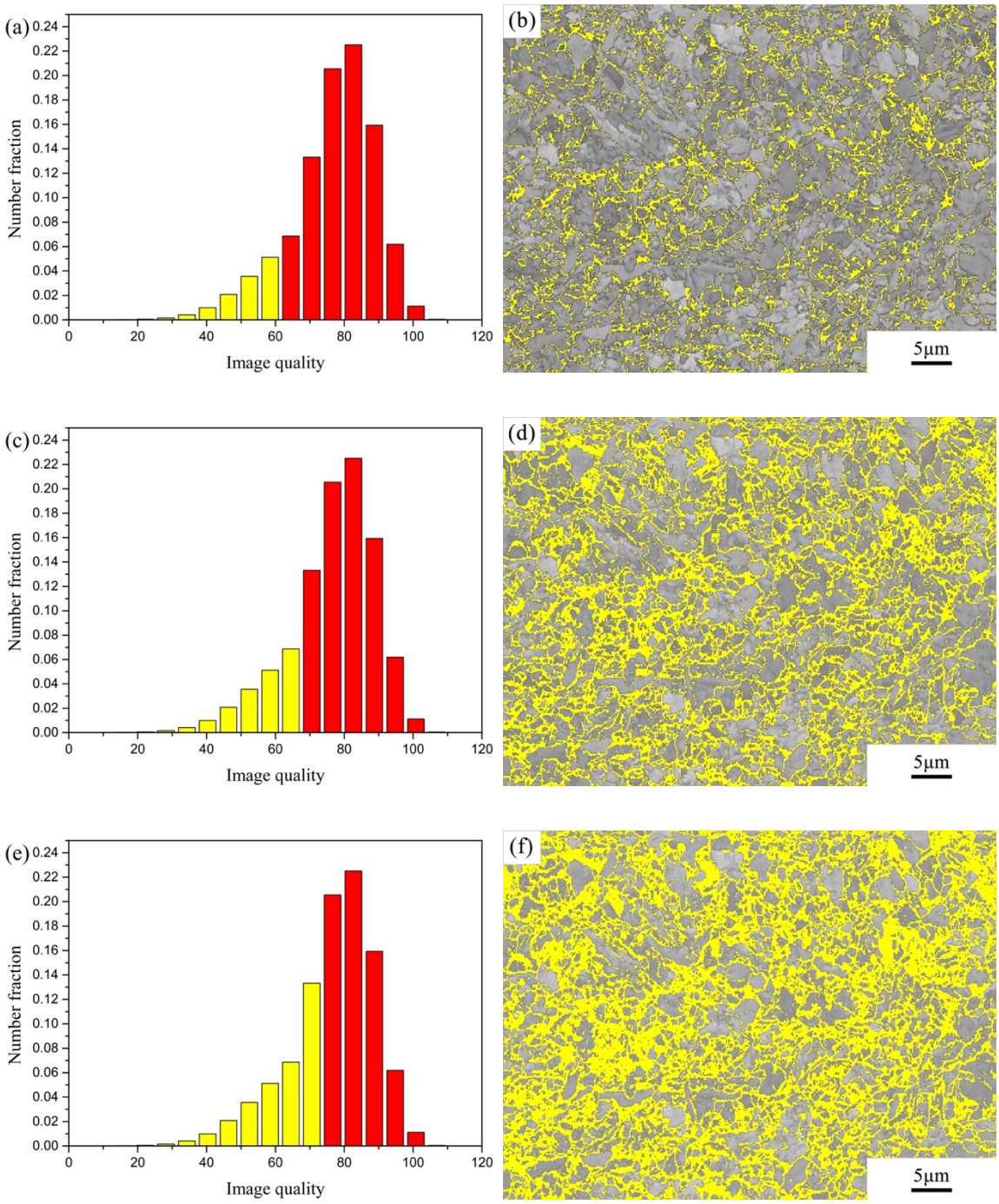


Figure 7.15. Fusion zone in the heat-treated joint (P = 2500 W, t = 5 ms): (a), (c) and (e): Image quality in percentage showing highlighted low image quality. (b), (d) and (f): Image quality map showing highlighted phases.

The kernel average misorientation (KAM), which represents the numerical misorientation average of a given point with its nearest neighbours, was used to characterise local misorientations. The maps were calculated using a maximum misorientation of 5°. Figure 7.16 (a) shows the KAM map of the fusion zone in the heat-treated joint. It can be observed that the grains standing out from the rest due to a larger size, show almost no misorientation, *i.e.* no local lattice distortion. In addition, misorientations between 0.5° to 2° are observed near the

grain boundaries. These small grain regions having higher misorientations, can be linked to the areas with lower image quality. As shown in Figure 7.16 (b), the KAM map combined with the IQ map reveals overlapping regions, where martensite grains (yellow) have a higher misorientation and ferrite grains (dark blue) generally have a lower misorientation. By comparing KAM of different regions in the joint, it indicates whether the microstructure is changed significantly after welding or the heat treatment. The fusion zone and HAZ have a higher KAM than the base material, indicating a more distorted microstructure and probably a higher martensite fraction due to an additional thermal cycle (Figure 7.17). Meanwhile, in the heat-treated condition, the KAM values are smaller than those of the as-joined condition and show no significant difference in different regions, demonstrating that the microstructure is substantially recovered and homogenous after the normalising and tempering treatment, which would be beneficial for the mechanical properties.

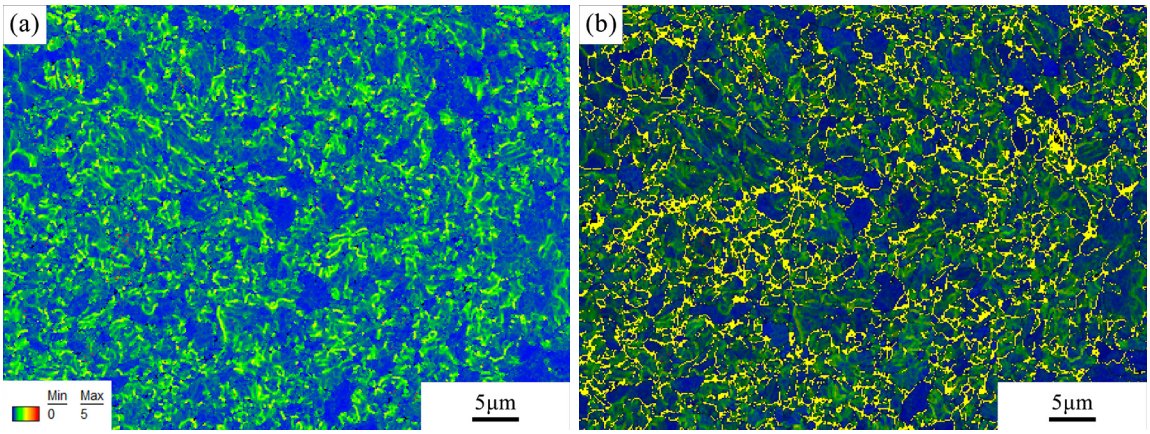


Figure 7.16. (a) Kernel average misorientation (KAM) map of the fusion zone in the heat-treated joint (P = 2500 W, t = 5 ms) and (b) Kernel average misorientation (KAM) map combined with image quality (IQ) map shown in Figure 7.15 (b).

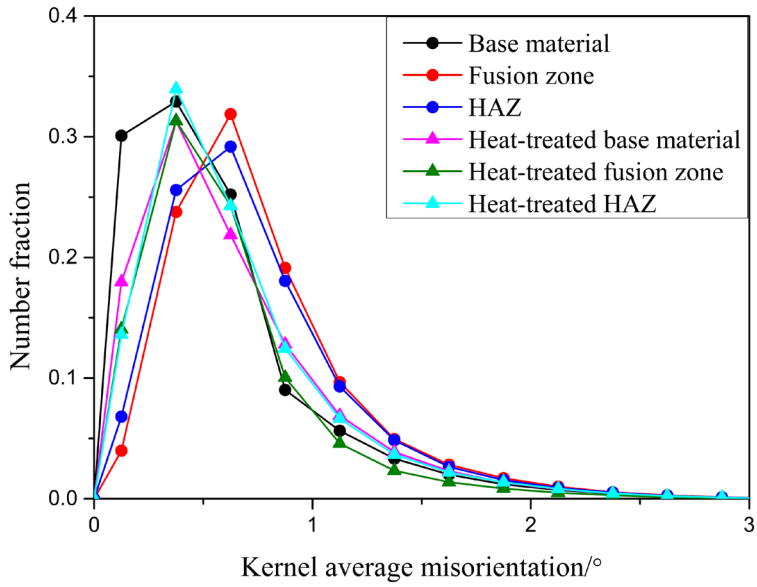


Figure 7.17. Distribution of kernel average misorientation (KAM) of different regions in the as-joined and heat-treated joint.

7.3.2.3 Mechanical properties

A hardness profile over a cross section of the weld (P = 2500 W, t = 5 ms, with filler material) is shown in Figure 7.18. In the as-joined condition, as can be seen from the red line, the average microhardness of the base material is approximately 465 $HV_{0.3}$. The hardness profile in the joint region is roughly symmetric. The weld centre has the lowest hardness value due to grain growth, indicating the weakest region of the joint. Meanwhile, there is a slight increase in the HAZ hardness compared to the base material due to a finer grain size. In the case of the heat-treated condition, the average microhardness of the base material is around 345 $HV_{0.3}$, showing an obvious softening effect. In addition, the difference of the hardness in the material has almost been eliminated, although the hardness of the fusion zone is still the lowest. It can be deduced that the joint is more homogenous in microstructure and more ductile after the heat treatment.

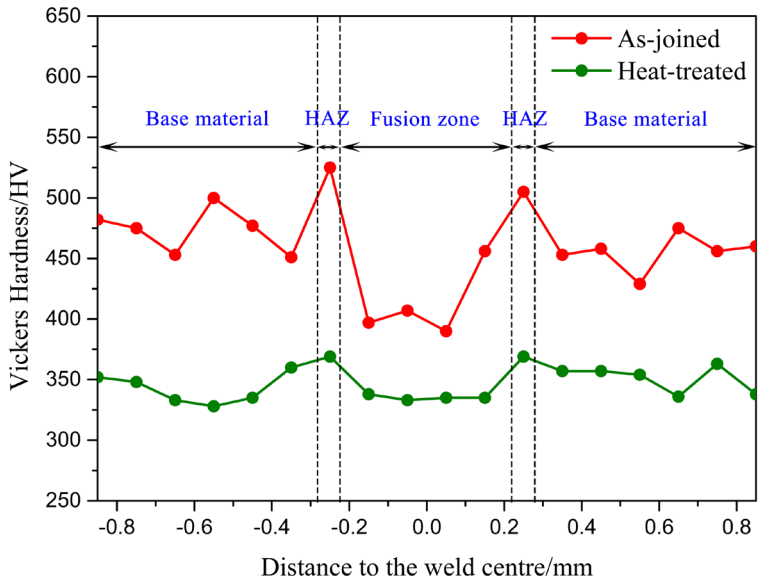


Figure 7.18. Microhardness profile along the cross section of the weld (P = 2500 W, t = 5 ms).

Specimens for tensile testing were machined flat to remove the excess filler metal block, in order to have a consistent stress across the joint. All of the tested specimens fractured in the fusion zone, indicating the weakest point of the joint due to microvoids and grain growth, which agrees with the softer material observed in the hardness profile. The tensile properties of the joined specimens are shown in Table 7.5. This table also shows the tensile properties of the base material obtained from chapter 4. It can be seen that the standard deviations of the tensile properties of the joints are relatively high. Welding defects in the fusion zone can act as preferential sites for crack initiation. As a result, specimens having a larger number of defects such as microvoids will have significantly lower strength and ductility. Nonetheless, the average tensile strength and yield strength of the as-joined specimens are as high as approximately 89% of those of the base material. After a heat treatment of normalising and tempering, as expected, the strength of the joint decreases while the elongation increases compared to the as-joined specimen. The tempering treatment favours the recovery of dislocations and residual stress generated during the powder metallurgy and joining process, leading to enhanced ductility. However, the elongation of the joint is not increased significantly compared to that of the base material after heat treatment. This indicates that even though the microstructure of the steel is generally recovered and homogenous, the welding defects (microvoids) have an important influence on the tensile properties of the heat-treated joints.

Table 7.5. Tensile testing results of the base material and joined material.

	Tensile strength/MPa	Yield strength/MPa	Elongation/%
Base material	1301.2 ± 144.5	923.7 ± 183.1	6.86 ± 2.69
Heat-treated base material	1030.8 ± 64.7	861.6 ± 26.2	10.40 ± 1.40
As-joined specimen	1156.0 ± 154.1	821.0 ± 143.2	5.54 ± 1.72
Heat-treated joint	825.4 ± 100.2	725.2 ± 123.3	6.68 ± 1.63

Fractographic examinations were performed on the fracture surfaces from tensile testing by SEM (Figure 7.19). It can be seen that the fracture of the as-joined sample exhibits many small dimples and some smooth facets, indicating a mixed ductile and intergranular fracture mode. In contrast, the heat-treated joint shows a typical ductile fracture mode with numerous dimple features. The dimples are larger and deeper compared to those in the as-joined sample, showing an enhanced ductility of the material. It is notable that large precipitates were observed in the dimples. The chemical composition of some precipitates at the fracture surface was determined by EDS, as shown in Table 7.6. Compared to point 4 (base material, Figure 7.19), there is an obvious increase of Cr, Mn and C in the precipitates, which could be identified as $M_{23}C_6$ carbides due to their size and chemical composition. Brittle precipitates such as $M_{23}C_6$ can act as initial crack sources due to the stress concentration at their non-slip lattice plane [29], leading to an early fracture during tensile testing.

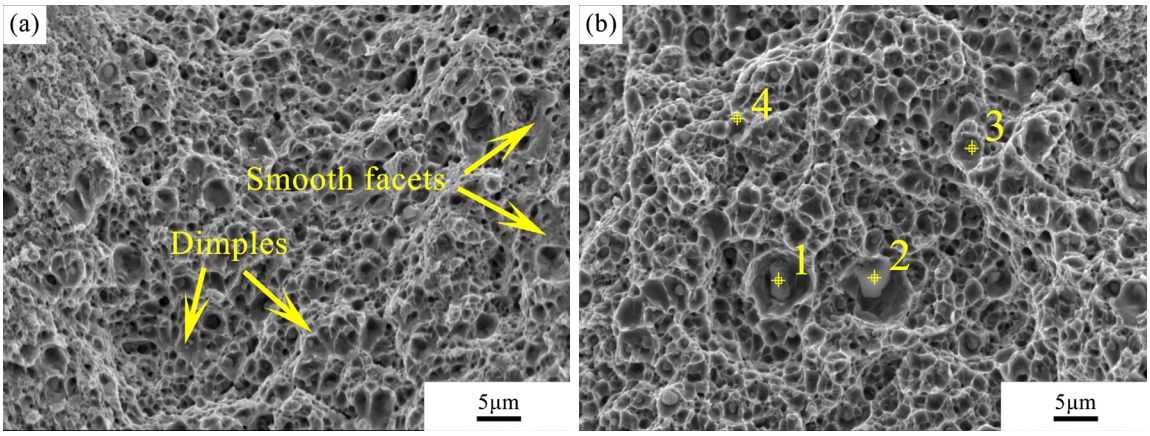


Figure 7.19. SEM micrographs of the fractures for specimens after tensile testing: (a) as-joined specimen and (b) heat-treated joint.

Table 7.6. Chemical composition of the points indicated in Figure 7.19 (b).

	Cr	W	Mn	V	Ta	Y	C	Fe
1	17.92	0.56	0.22	0.33	–	–	1.78	Bal.
2	17.65	1.46	8.98	0.45	0.07	–	1.11	Bal.
3	13.45	1.68	4.41	0.28	–	0.18	1.78	Bal.
4	8.84	1.01	0.49	0.23	–	0.15	0.42	Bal.

With controlled welding conditions including an optimised laser power, a short pulse duration and a small overlap rate, a fully penetrated and not overheated spot weld was obtained. The welding defects observed in the joint are mainly material loss and microvoids. The material loss is generally caused by metal evaporation and spattering. This could be improved by tuning the focal position and the divergence angle [30, 31]. With a reduced power density around the keyhole aperture, the speed of the melt flow as well as the instability of the keyhole will be decreased, therefore the evaporation and spattering phenomenon will be limited. As for the porosity defects, it has been found that porosity can be effectively inhibited at the optimum frequency and duty cycle of the employed laser pulse [32]. In addition, the keyhole stability and material evaporation also have a large effect on the generation of porosity [33]. The use of nitrogen instead of inert shielding gas was found to be effective to supress the formation of porosity defects, due to the occurrence of the on-and-off cycle of nitrogen plasma prior to the initiation of keyhole instability [33]. All of these could be used to reduce the welding defects and thus improve the mechanical performance of the weld in future work.

The melt pool lifetime during fusion welding is crucial for retaining the microstructure and mechanical properties of ODS steel joints. Upon welding, the oxide particles will quickly float to the top of the melt pool and consequently form a depleted area, leading to significantly reduced mechanical properties. With traditional "continuous" welding, the heat will accumulate in the weld. Even though techniques such as laser beam welding has a very high cooling rate, the melt pool lifetime is still too long for ODS steels. The temperature of the fusion zone usually stays above the melting point for a relatively long period of time. It is therefore difficult, if not impossible, to obtain an undisturbed microstructure. For instance, Lindau *et al.* [4] studied the joining of ODS Eurofer via electron beam welding, which also has a characteristic of high power density. The results showed that the nano-dispersoids in the fusion zone unsurprisingly agglomerated to larger particles, causing a weak weld seam. Conversely, with the distributed pulsed spot welding procedure proposed in this study, the melt pool lifetime of each spot is reduced to the order of milliseconds, which is favourable for the retention of the microstructure and mechanical properties of the joint. It is shown in chapter 5 that the strengthening mechanisms of ODS Eurofer are mainly based on grain boundary strengthening and dispersion strengthening, as neither the grain size nor the nanoparticle distribution is changed significantly after joining, the strength of the joint is not therefore unduly reduced.

7.4 Conclusions

ODS Eurofer was joined successfully by SPS and pulsed laser beam welding. The welding parameters were optimised based on their effect on the microstructure. The microstructure and mechanical properties of the as-joined and heat-treated specimens were investigated in detail. The main conclusions are as follows.

1. The SPS joining was conducted at 1373 K with a heating rate of 100 K min^{-1} and a pressure of 80 MPa. Under the condition of a holding time of 40 min, with a powder layer of 1.27 g cm^{-2} between the steel disks, an almost defect-free joint was obtained.

2. The fine-grained feature and nanoparticles in the material are fully retained after SPS joining, thanks to the solid state welding process. The tensile properties of the joints are comparable to the base material in both as-produced and heat-treated condition.

3. For pulsed laser beam welding, spot-on-plate experiments show that full penetration is beneficial to avoid trapped gas in the material. A short pulse duration is crucial for retaining Y_2O_3 nano-precipitates in ODS Eurofer. With a laser power of 2500 W and a pulse duration of 5 ms, the result of a spot created on a 1 mm plate with filler material is satisfactory, yielding a slightly modified microstructure without macroscopic welding defects in the material.

4. In the as-joined condition (P = 2500 W, t = 5 ms, with filler material), the fusion zone consists of elongated grains, while the HAZ has refined grains compared to the base material. The nanoprecipitates are retained in the fusion zone, although not homogenously distributed in the steel matrix. $M_{23}C_6$ carbides are observed in the microstructure and found to be preferentially located at the grain boundaries.

5. EBSD results reveal that the joined material has a bimodal and dual phase microstructure. Martensite grains show a lower image quality and a higher misorientations compared to ferrite grains. The microstructure is generally recovered and homogenous after the heat treatment, which is beneficial for the mechanical properties.

6. The microhardness and tensile properties of the as-joined specimens are slightly compromised compared to those of the base material. The material becomes more ductile after the heat treatment; however, mechanical properties remain largely influenced by microvoids in the size up to about 3 μm.

This study shows that both SPS and pulsed laser beam welding can be potentially employed as an effective method for the joining of ODS Eurofer steel. This study will contribute to the weldability research on ODS steels, with the aim of extending their application in advanced nuclear reactors.

References

[1] A.N. Ashong, M.Y. Na, H.C. Kim, S.H. Noh, T. Park, H.J. Chang, J.H. Kim, Influence of manganese on the microstructure and mechanical properties of oxide-dispersion-strengthened steels, Mater. Des. 182 (2019) 107997.

[2] M.K. Dash, R. Mythili, R. Ravi, T. Sakthivel, A. Dasgupta, S. Saroja, S.R. Bakshi, Microstructure and mechanical properties of oxide dispersion strengthened 18Cr-ferritic steel consolidated by spark plasma sintering, Mater. Sci. Eng., A 736 (2018) 137-147.

[3] B. Baker, L. Brewer, Joining of oxide dispersion strengthened steels for advanced reactors, JOM 66(12) (2014) 2442-2457.

[4] R. Lindau, M. Klimenkov, U. Jäntsch, A. Möslang, L. Commin, Mechanical and microstructural characterization of electron beam welded reduced activation oxide dispersion strengthened–Eurofer steel, J. Nucl. Mater. 416(1-2) (2011) 22-29.

[5] S. Noh, R. Kasada, A. Kimura, Solid-state diffusion bonding of high-Cr ODS ferritic steel, Acta Mater. 59(8) (2011) 3196-3204.

[6] K. Zhao, Y. Liu, L. Huang, B. Liu, Y. He, Diffusion bonding of Ti-45Al-7Nb-0.3 W alloy by spark plasma sintering, J. Mater. Process. Technol. 230 (2016) 272-279.
[7] U. Acharya, B.S. Roy, S.C. Saha, A study of tool wear and its effect on the mechanical properties of friction stir welded AA6092/17.5 Sicp composite material joint, Materials Today: Proceedings 5(9) (2018) 20371-20379.
[8] L.N. Brewer, M.S. Bennett, B. Baker, E.A. Payzant, L. Sochalski-Kolbus, Characterization of residual stress as a function of friction stir welding parameters in oxide dispersion strengthened (ODS) steel MA956, Mater. Sci. Eng., A 647 (2015) 313-321.
[9] D. He, Z. Fu, W. Wang, J. Zhang, Z.A. Munir, L. Ping, Temperature-gradient joining of Ti–6Al–4V alloys by pulsed electric current sintering, Mater. Sci. Eng., A 535(7) (2012) 182-188.
[10] S. Noh, A. Kimura, T.K. Kim, Diffusion bonding of 9Cr ODS ferritic/martensitic steel with a phase transformation, Fusion Eng. Des. 89(7-8) (2014) 1746-1750.
[11] J. Yang, J. Trapp, Q. Guo, B. Kieback, Joining of 316L stainless steel by using spark plasma sintering method, Mater. Des. 52(24) (2013) 179-189.
[12] A. Miriyev, A. Stern, E. Tuval, S. Kalabukhov, Z. Hooper, N. Frage, Titanium to steel joining by spark plasma sintering (SPS) technology, J. Mater. Process. Technol. 213(2) (2013) 161-166.
[13] T. Kelly, Pulsed YAG laser welding of ODS alloys, AIP Conf. Proc., American Institute of Physics, 1979, pp. 215-220.
[14] P. Molian, Y. Yang, P. Patnaik, Laser welding of oxide dispersion-strengthened alloy MA754, J. Mater. Sci. 27(10) (1992) 2687-2694.
[15] H. Lemmen, K. Sudmeijer, I. Richardson, S. van der Zwaag, Laser beam welding of an Oxide Dispersion Strengthened super alloy, J. Mater. Sci. 42(13) (2007) 5286-5295.
[16] S. Liang, Y. Lei, Q. Zhu, The filler powders laser welding of ODS ferritic steels, J. Nucl. Mater. 456 (2015) 206-210.
[17] J. Fu, H. Brouwer, I. Richardson, M. Hermans, Microstructure characterisation and mechanical properties of ODS Eurofer subject to designed heat treatments, Mater. Sci. Eng., A (2019) Submitted.
[18] J. Fu, J.C. Brouwer, I.M. Richardson, M.J.M. Hermans, Effect of mechanical alloying and spark plasma sintering on the microstructure and mechanical properties of ODS Eurofer, Mater. Des. 177 (2019) 107849.
[19] L. Zheng, X. Hu, X. Kang, D. Li, Precipitation of $M_{23}C_6$ and its effect on tensile properties of 0.3C-20Cr-11Mn-1Mo-0.35N steel, Mater. Des. 78 (2015) 42-50.
[20] M. Yamamoto, S. Ukai, S. Hayashi, T. Kaito, S. Ohtsuka, Formation of residual ferrite in 9Cr-ODS ferritic steels, Mater. Sci. Eng., A 527(16) (2010) 4418-4423.
[21] J. Yan, M. Gao, X. Zeng, Study on microstructure and mechanical properties of 304 stainless steel joints by TIG, laser and laser-TIG hybrid welding, OptLE 48(4) (2010) 512-517.
[22] K.D. Zilnyk, H.R.Z. Sandim, R.E. Bolmaro, R. Lindau, A. Möslang, A. Kostka, D. Raabe, Long-term microstructural stability of oxide-dispersion strengthened Eurofer steel annealed at 800 °C, J. Nucl. Mater. 448(1-3) (2014) 33-42.

[23] N. Sallez, P. Donnadieu, E. Courtois-Manara, D. Chassaing, C. Kübel, F. Delabrouille, M. Blat-Yrieix, Y. de Carlan, Y. Bréchet, On ball-milled ODS ferritic steel recrystallization: From as-milled powder particles to consolidated state, J. Mater. Sci. 50(5) (2015) 2202-2217.
[24] I. Hilger, F. Bergner, T. Weißgärber, Bimodal Grain Size Distribution of Nanostructured Ferritic ODS Fe-Cr Alloys, J. Am. Ceram. Soc. 98(11) (2015) 3576-3581.
[25] N. Sallez, X. Boulnat, A. Borbély, J.L. Béchade, D. Fabrègue, M. Perez, Y. de Carlan, L. Hennet, C. Mocuta, D. Thiaudière, Y. Bréchet, In situ characterization of microstructural instabilities: Recovery, recrystallization and abnormal growth in nanoreinforced steel powder, Acta Mater. 87 (2015) 377-389.
[26] G. Odette, M. Alinger, B. Wirth, Recent developments in irradiation-resistant steels, Annu. Rev. Mater. Res. 38 (2008) 471-503.
[27] A. Laureys, M. Pinson, T. Depover, R. Petrov, K. Verbeken, EBSD characterization of hydrogen induced blisters and internal cracks in TRIP-assisted steel, Mater. Charact. 159 (2020) 110029.
[28] D. Das, P.P. Chattopadhyay, Influence of martensite morphology on the work-hardening behavior of high strength ferrite–martensite dual-phase steel, J. Mater. Sci. 44(11) (2009) 2957-2965.
[29] S. Wang, X. Chang, J. Key, New insight into high-temperature creep deformation and fracture of T92 steel involving precipitates, dislocations and nanovoids, Mater. Charact. 127 (2017) 1-11.
[30] Y. Kawahito, K. Nakada, Y. Uemura, M. Mizutani, K. Nishimoto, H. Kawakami, S. Katayama, Relationship between melt flows based on three-dimensional X-ray transmission in situ observation and spatter reduction by angle of incidence and defocussing distance in high-power laser welding of stainless steel, Welding International 32(7) (2018) 485-496.
[31] J.-P. Weberpals, P. Krueger, P. Berger, T. Graf, Understanding the influence of the focal position in laser welding on spatter reduction, International Congress on Applications of Lasers & Electro-Optics, Laser Institute of America, 2011, pp. 159-168.
[32] J. Dowden, P. Kapadia, A mathematical investigation of the penetration depth in keyhole welding with continuous CO2 lasers, J. Phys. D: Appl. Phys. 28(11) (1995) 2252.
[33] A. Matsunawa, M. Mizutani, S. Katayama, N. Seto, Porosity formation mechanism and its prevention in laser welding, Welding international 17(6) (2003) 431-437.

8

Conclusions and recommendations for future work

8.1 General conclusions

Oxide dispersion strengthened (ODS) steels are considered as promising candidate materials for advanced nuclear applications, due to their good swelling resistance under irradiation and high temperature mechanical properties. Favourable properties are mainly attributed to the dispersed nano-oxide particles, acting as effective barriers for dislocations and stable sinks for point defects. However, the fabrication and joining of ODS steels are the major bottlenecks limiting their further use. In this study, experimental efforts have been made to pursue and optimise the powder metallurgy, additive manufacturing and welding procedures of ODS Eurofer steel. The effects of different processes on the microstructure and mechanical properties of ODS Eurofer were investigated. The following conclusions are drawn.

ODS Eurofer was initially prepared by a powder metallurgical route. The influences of mechanical alloying, sintering temperature, pressure and heating rate were investigated to obtain optimised process parameters, based on their effect on the mechanical properties of the produced steel. It was found that the effect of mechanical alloying is not only refinement of the (grain) size of the powders and introduction of high deformation stresses and a high dislocation density, but also the homogenous incorporation of the alloying elements into the steel matrix. After 30 h of milling, the powders have a minimum average size (approximately 10.7 μm) and a homogeneous chemical composition. The sintering temperature, which determines the efficiency of SPS, is crucial for the production chain. A high heating rate in SPS is found to promote a dense material, possibly due to a higher electric current density passing through the powders, leading to the generation of higher Joule heat and a more effective sintering. The applied pressure in SPS appears to be an extra driving force for densification. With higher pressure applied, the particles are sintered more efficiently, resulting in limited grain growth and less porosity. SPS prepared ODS Eurofer steel shows the highest density when milled for 30 h, sintered at 1373 K with a heating rate of 100 K min^{-1} at a pressure of 60 MPa. The top and bottom surfaces of the as-produced sample present a higher microhardness and tensile strength and a lower elongation associated with a higher carbon content. Therefore, a subsequent heat treatment is required to homogenise the chemical composition and improve the mechanical performance.

The condition of normalising at 1423 K for 1 h and tempering at 973 K for 1 h was determined to be a suitable heat treatment route for the SPS-produced ODS Eurofer. The heat-treated material has a relatively uniform microhardness due to carbon diffusion and carbide reprecipitation. The material has a bimodal grain size distribution and a dual phase (martensite and δ-ferrite) microstructure in both SPS-produced and heat-treated conditions. The bimodal grain size distribution could result from heterogenous recrystallisation due to an inhomogeneous dislocation density after the milling process, combined with a spatial variation in the pinning force by a nonuniform distribution of nanoparticles. The dual phase microstructure probably arises because the phase transformation is partly suppressed in the material, as the ferrite–austenite interface motion is strongly pinned by finely dispersed oxide particles. The SPS-produced steel has a high dislocation density of 2.2×10^{14} m^{-2}, with $M_{23}C_6$

and M_6C carbides in the microstructure. Comparatively, the heat-treated steel has a lower dislocation density of 8.9×10^{13} m^{-2}, with $M_{23}C_6$ carbides decorating the grain boundaries. A yield strength model was proposed based on the strengthening contributions of solid solutes, grain size, dislocation density and nanoparticles. Oxide dispersion strengthening, dislocation strengthening and grain boundary strengthening are the major contributions to the yield strength of the SPS-produced ODS Eurofer, while oxide dispersion strengthening and grain boundary strengthening are the dominant strengthening mechanisms in the heat-treated material. Mechanical alloying combined with SPS are effective to produce ODS Eurofer with a desired microstructure and dispersed nano-Y_2O_3 particles. Moreover, SPS shows advantages as a cost-effective consolidation approach to produce ODS Eurofer with comparable mechanical properties to conventional consolidation techniques at significantly lower pressures and times.

The nature and formation mechanism of nanoclusters in the SPS prepared ODS Eurofer were revealed by atom probe tomography. With the addition of vanadium and tantalum in ODS Eurofer, the nanoclusters exhibit a higher number density with a decreased average diameter, indicating that vanadium and tantalum are beneficial for the formation of small, high density distribution clusters. The small particles (< 4 nm) have a variable stoichiometry, while the larger particles (around 5–15 nm) are likely to have a Y_2O_3 stoichiometry. The nanoparticles tend to have a core/shell structure. Yttrium, oxygen and tantalum are found to be enriched in the core, whereas chromium and vanadium are predominantly present in the shell, which is possibly due to a competition of elements binding with oxygen. It is deduced that tantalum tends to combine with oxygen in the core (Y_2O_3) of the clusters due to a higher affinity, and pushes vanadium and chromium to the surrounding shell during the formation of nanoclusters.

ODS Eurofer was produced by an alternative route, *i.e.* laser-based direct metal deposition (DMD) followed by hot isostatic pressing. A laser power of 800 W was determined to be a suitable printing condition, which guaranteed a sufficient heat input meanwhile avoided a depletion of Y_2O_3 nanoparticles in the steel. The nanoparticles in the steel were coarsened and had a size of 5–30 nm. After a normalising and tempering treatment, compared to the SPS produced steel, the grains in the DMD_800 W and DMD_1000 W samples grow significantly due to a (partial) loss of Y_2O_3 pinning. Nanoindentation results show that the hardness of martensite and ferrite decreases from the SPS produced steel to DMD_800 W to DMD_1000 W, which could be ascribed to grain growth as well as coarsening and a partial loss of Y_2O_3. After a tempering treatment, there is a decrease in the hardness of martensite and ferrite, which is related to carbide precipitation as well as residual stress and dislocation density reduction.

Solid-state diffusion bonding of SPS was used to join ODS Eurofer. The joining was conducted at 1373 K with a heating rate of 100 K min^{-1} and a pressure of 80 MPa. Employing a powder layer between the steel disks is beneficial for the joining process as the resistance of the powder is much higher than the bulk material with the same shape, therefore promoting a much higher heating rate in the powder layer. The condition of a 40 min holding time with a 1.27 g cm^{-2} powder layer ensures a sufficient time and energy to close the gap through diffusion bonding, leading to an almost defect-free joint. The microstructural features and mechanical properties of the joints are fully retained compared to the parent material.

ODS Eurofer was welded successfully using a pulsed laser beam welding technique with a distributed pulse pattern to minimise the heat accumulation in the melt pool. With a laser power of 2500 W and a pulse duration of 5 ms, the joint using 1 mm thick plates with filler material is satisfactory, showing a slightly modified microstructure without macroscopic welding defects. Y_2O_3 nano-precipitates are retained in the fusion zone due to the short pulse duration applied. The microhardness and tensile properties of the joined specimens are slightly compromised (around 10%) compared to those of the base material, due to microvoids and grain coarsening. The experimental results indicate that joints with reasonable microstructures and mechanical properties can be achieved via pulsed laser beam welding with filler material and post heat treatments.

8.2 Recommendations for future work

Based on the results of this study, the following recommendations are given for future research:

1. Numerical simulation could be used in the future work to help better understand the effect of various processes on the microstructure of ODS steels. For instance, modelling of SPS, laser welding, laser additive manufacturing or heat treatment cycles would help to establish a link between the thermal profiles of different processes and microstructural evolution of ODS steels.

2. ODS steels are regarded as potential structural materials for future nuclear reactors that comprise different subsystems and modules that utilising different materials to meet the challenging requirements. Therefore, the study of welding of dissimilar materials, such as ODS steels to non-ODS steels or ODS steels to tungsten alloys, is essential for the successful development of advanced nuclear systems.

3. Besides the direct metal deposition technique investigated in this thesis, additive manufacturing techniques such as selective laser melting, selective laser sintering and binder jetting also provide promising methods for the fabrication of ODS steels. A further study on these techniques would help to extend the fabrication possibilities of ODS steels.

4. In order to be employed in the harsh working environment of nuclear reactors, the properties of ODS Eurofer need to be thoroughly investigated. This includes high-temperature creep properties, neutron radiation resistance, corrosion resistance, fracture toughness, etc.

5. Artificial intelligence and machine learning, which are being developed rapidly, could help to identify improved chemical compositions of ODS Eurofer/ODS steels to obtain desired microstructures and mechanical properties in the future.

Acknowledgements

First and foremost, I would like to express my deepest appreciation to my daily supervisor Dr. Marcel Hermans for his dedicated support and guidance. Marcel continuously provided encouragement and was always willing and enthusiastic to assist in any way he could throughout the research project. I was truly honoured and lucky to work under his supervision.

I am deeply indebted to my promoter Dr. Ian Richardson. The meetings and conversations with Ian were always inspiring, especially in helping me form a comprehensive and objective knowledge network from multiple perspectives. Ian is my role model as a gentleman, scientist and mentor.

Apart from TU Delft, I am also registered as a PhD student at Dutch Institute for Fundamental Energy Research (DIFFER). I would like to extend my sincere thanks to my supervisor Prof. Marco de Baar from DIFFER for his big support throughout my PhD.

This project was carried out under project number T16010f in the framework of the Partnership Program of the Materials Innovation Institute (M2i) and the Netherlands Organisation for Scientific Research (NWO). I would like to thank M2i and NWO for the financial support in this project. Nuclear Research and Consultancy Group (NRG) as the industrial partner is thanked for the useful collaboration. I would like to acknowledge the collaboration of Mr. Frank Rohrink and Ms. Astrid Loite from Nedclad for direct metal deposition experiments.

I am grateful to all respected professors and researchers for their tremendous help during the last four years: Dr. Wim Sloof and Hans Brouwer (powder metallurgy and thermal analysis), Dr. Vitaliy Bliznuk (TEM measurements), Prof. Rouman Petrov (EBSD analysis), Dr. Thomas Davis and Dr. Ankit Kumar (APT measurement and analysis), Dr. Vera Popovich (plasma spheroidisation), Prof. Moataz Attallah (HIP), Dr. Yaiza Gonzalez-Garcia (atomic force microscopy), Prof. Jilt Sietsma (general advice and discussions), Prof. Yutao Pei and Dr. Ali Chabok (nanoindentation measurements) and Dr. Xukai Zhang (TEM sample preparation).

I wish to thank experienced technicians from TU Delft for their help and contribution in the project: Sander van Asperen (microscopy), Ruud Hendrikx (XRF and XRD), Kees Kwakernaak (SEM and EBSD), Elise Reinton (tensile testing), Jurriaan van Slingerland (welding), Remko Seijffers (sample preparation), Richard Huizenga (thermal calculations), Agnieszka Kooijman (etching) and Michel van den Brink (particle analysis).

The administrative assistance is acknowledged to the secretaries from TU Delft: Ellen Vendrig, Saskia Brandt Corstius, Prisca Koelman and Saskia van der Meer as well as the staff members from DIFFER: Ans Vermeer, Wilko Mensink, Henk Tamsma, Bebe van de Vils and Jolanda van Achthoven.

I thank all group members from Joining and Additive Manufacturing: Konstantinos, He, Parisa, Gautam, Amin, Vamsi, Xiaohui, Aravind and Emiliano, for creating such a nice working

atmosphere. Thanks should also go to my colleagues and friends from Department of Materials Science and Engineering: Zhiyuan, Prakash, Wei, Jun, Aytac, Jianing, Virginia, Vibhor, Jaji and many more. A special thanks to my project partner and dear friend Viviam. I will certainly miss the invaluable discussions and cheerful laughter we had. Thanks also to my best friends in China: Jiong, Tao and Xiaohua. I am so glad that distance did not drift us apart.

Last but not least, I wish to thank my mother, who has sacrificed her everything for me. I am nothing without her. I would also like to thank my partner Cedric, whose unconditional love and support has been the extra strength and motivation for me.

List of publications

Journal publications:

- J. Fu, I. Richardson, M. Hermans, Microstructure Study of Pulsed Laser Beam Welded Oxide Dispersion-Strengthened (ODS) Eurofer Steel, Micromachines 12(6) (2021) 629.
- J. Fu, T. Davis, A. Kumar, I. Richardson, M. Hermans, Characterisation of the influence of vanadium and tantalum on yttrium-based nano-oxides in ODS Eurofer steel, Mater. Charact. 175 (2021) 111072.
- J. Fu, J. van Slingerland, H. Brouwer, V. Bliznuk, I. Richardson, M. Hermans, Applicability Study of Pulsed Laser Beam Welding on Ferritic–Martensitic ODS Eurofer Steel, Metals 10(6) (2020) 736.
- J. Fu, J. Brouwer, R. Hendrikx, I. Richardson, M. Hermans, Microstructure characterisation and mechanical properties of ODS Eurofer steel subjected to designed heat treatments, Mater. Sci. Eng., A 770 (2020) 138568.
- J. Fu, J. Brouwer, I. Richardson, M. Hermans, Joining of oxide dispersion strengthened Eurofer steel via spark plasma sintering, Mater. Lett. 256 (2019) 126670.
- J. Fu, J. Brouwer, I. Richardson, M. Hermans, Effect of mechanical alloying and spark plasma sintering on the microstructure and mechanical properties of ODS Eurofer, Mater. Des. 177 (2019) 107849.
- M. Laot, B. Rich, I. Cheibas, J. Fu, J.N. Zhu, V. Popovich, Additive Manufacturing and Spark Plasma Sintering of Lunar Regolith for Functionally Graded Materials, SPOOL 8.2 (2021) 7-29.
- J. Fu, F. Rohrink, A. Chabok, M. Attallah, I. Richardson, M. Hermans, Elaboration of oxide dispersion strengthened Eurofer steel by direct metal deposition, to be submitted.

Conference publications:

- J. Fu, J. Brouwer, I. Richardson, M. Hermans, Solid State Diffusion Bonding of ODS Eurofer Steel by Spark Plasma Sintering, TMS 2020 149th Annual Meeting & Exhibition Supplemental Proceedings, Springer, 2020, pp. 2095-2102.
- J. Fu, J. Brouwer, I. Richardson, M. Hermans, Microstructure Characterisation and Microhardness of ODS Eurofer Subjected to Designed Heat Treatments, The 10th Pacific Rim International Conference on Advance Materials and Processing Proceedings, 2019, pp. 136-141.
- J. Fu, I. Richardson, M. Hermans, Effect of a pulsed laser beam on the microstructure of oxide dispersion strengthened (ODS) Eurofer steel, to be submitted.

Curriculum Vitae

Jia Fu

8, September, 1991 — Born in Qitaihe, China

Education

Mar. 2017 – Jun. 2021	Ph.D. in Materials Science and Engineering Delft University of Technology, Delft, The Netherlands Thesis title: On the powder metallurgy, additive manufacturing and welding of oxide dispersion strengthened Eurofer steel Promotors: Dr. I.M. Richardson and Dr.ir. M.J.M. Hermans
Sep. 2013 – Mar. 2016	M.Sc. in Materials Science and Engineering Beihang University, Beijing, China Thesis title: Microstructure and fatigue properties of laser and friction stir welded AA2060 Al-Li alloy
Sep. 2009 – Jul. 2013	B.Sc. in Materials Science and Engineering Beihang University, Beijing, China Thesis title: Microstructure and fracture toughness study of a 2A14 aluminium alloy rocket tank